ALMA MATER STUDIORUM
UNIVERSITÀ DI BOLOGNA

DOTTORATO DI RICERCA IN

INGEGNERIA ELETTRONICA, TELECOMUNICAZIONI E TECNOLOGIE DELL'INFORMAZIONE

Ciclo 37

Settore Concorsuale: 09/F2 - TELECOMUNICAZIONI

Settore Scientifico Disciplinare: ING-INF/03 - TELECOMUNICAZIONI

LOCALIZATION AND COMMUNICATION IN SMART RADIO ENVIRONMENTS

Presentata da:

Marina Lotti

Supervisore:

Chiar.mo Prof. Ing.
Davide Dardari

Coordinatore Dottorato:

Chiar.mo Prof. Ing.
Davide Dardari

Co-supervisore:

Prof. Ing.
Gianni Pasolini

Esame finale anno 2025

Keywords

Reconfigurable intelligent surface

Metasurface

Smart Radio Environments

Localization

Communication

5G & Beyond Wireless Systems

"Nella vita non c'è nulla da temere, solo da capire." Margherita Hack

"Se ho visto più lontano, ho potuto farlo stando in piedi sulle spalle di giganti." Isaac Newton

Ai miei amati figli Isacco e Margherita.

Abstract

In recent years, the concept of the *Smart Radio Environment (SRE)* has emerged as a transformative approach in wireless communications. This innovative paradigm shifts the perception of the wireless environment from a passive, uncontrollable entity to an active, programmable component. By enabling dynamic programming and optimizing the radio propagation environment, the SRE paradigm aims to revolutionize the field, addressing challenges posed by next-generation wireless networks. Aligned with this vision, the focus of this thesis is on advanced "smart" methods exploiting the possibility to sense and modify radio propagation environments to enable advanced communication, localization, and mapping applications.

The initial chapters thoroughly explore the technologies employed in smart radio environment applications. One of these key technologies is Reconfigurable Intelligent Surfaces (RISs) which are adaptable surfaces that can be programmed to manipulate the propagation of radio waves. By adjusting how signals are reflected, a RIS can effectively shape the wireless environment, leading to improved coverage and enhanced signal strength. Another promising technology discussed is the frequency-selective metasurfaces. These metasurfaces are engineered to interact selectively with different frequency components of a signal. This selective interaction enables precise control over the signal's angle of reflection response, allowing for customized improvements in signal processing and propagation. The chapters also delve into self-conjugating metasurfaces that exploit the retrodirectivity propriety, appealing to reduce the beamforming time in Multiple-Input Multiple-Output (MIMO) systems while reducing the system complexity.

The thesis proceeds with the description of practical experiments carried out during this Ph.D., including the validation of two RIS devices oper-

ating at frequencies of 3.47 GHz and 5.3 GHz. It also details a measurement campaign that provided the world's first successful validation of radio-simultaneous localization and mapping (SLAM) algorithms at 300 GHz. Additionally, the thesis covers a ultra wideband (UWB) localization application conducted as an experimental analysis of an automatic docking system for the retrieval of large objects in harsh environments.

The manuscript continues with the description of the algorithms developed during the doctoral research, exploiting the technologies investigated in the first part of the thesis. In particular, regarding the use of frequency-selective surfaces, algorithms that leverage a Orthogonal Frequency-Division Multiplexing (OFDM) signals and a frequency-modulated continuous-wave (FMCW) signals to enhance localization accuracy through the use of frequency-selective metasurfaces are shown. Then, algorithms that exploit the self-conjugating metasurfaces have been developed. These address communication, beam tracking, channel access, and localization purposes. Finally, radio-SLAM algorithms, integral to the measurement campaign discussed earlier, are designed for simultaneous localization and mapping in high-frequency environments.

This thesis offers a detailed examination of these cutting-edge technologies, tailored signal processing methods, and their application in advancing the Smart Radio Environment concept.

Contents

Abstract **vii**

Acronyms **1**

1 Introduction **7**
1.1 Main Contributions and Thesis Organization 11
1.2 Notation 14

2 Enabling technologies for SREs **15**
2.1 Reconfigurable intelligent surfaces 15
2.2 Frequency-selective surfaces (metaprism) 25
2.3 Self-conjugating metasurfaces 29

3 Experimental results **37**
3.1 Experimental characterization of a RIS 38
3.1.1 5.3 GHz RIS 38
3.1.2 3.47 GHz RIS 55
3.2 Backscatter THz measurements 59
3.3 Localization measurements using UWB devices 66
3.3.1 Measurement campaign 71

4 Communication and localization algorithms for SREs **83**
4.1 NLOS Localization using metaprism 84
4.1.1 OFDM-based beamsteering design 84
4.1.2 FMCW radar-based beamsteering design 97
4.2 SCMs for communication, media access control and localization purposes 107

4.2.1 MU-MIMO communication using SCM 109
4.2.2 Grant-free Random Access with SCMs 134
4.2.3 Real-time Localization Based on SCMs 147
4.3 Radio-Simultaneous Localization and Mapping at THz 175
4.3.1 R-SLAM Experimental Performance 190

Conclusion **197**

Appendix **203**

List of Figures **218**

Bibliography **219**

Acknowledgements **241**

Acronyms

AF array factor

AoA Angle of Arrival

AoD Angle of Departure

ADC Analog-to-Digital converter

AP Access Point

AWGN additive white Gaussian noise

BS Base Station

CDL Clustered Delay Line

CDF Cumulative Density Function

CDMA Code Division Multiple Access

CFAR constant false alarm rate

CFR channel frequency response

CIR channel impulse response

CRB Cramer Rao Bound

CRLB Cramer Rao Lower Bound

CSI channel state information

DAC Digital-to-Analog Converter

DFT Discrete Fourier Transform

DoA Direction of Arrival

EM electromagnetic

FF Far Field

GEM ghost-effect mitigation

GDOP Geometric Dilution of Precision

GFRA grant-free random access

GSL Generalized Snell's law

GUI Graphical User Interface

HPBW Half Power Beam Width

H-RIS Hybrid RIS

ID identifier

i.i.d. independent, identically distributed

IIoT Industrial Internet of Things

IoT Internet of Things

IP Internet Protocol

ISAC Integrated Sensing and Communication

Lidar laser-based radar

LFM Linear Frequency Modulated

LOS Line of Sight

MU-MIMO Multi-User MIMO

MIMO Multiple-Input Multiple-Output

Acronyms

MIMO TRX MIMO transceiver

ML Maximum Likelihood

mMTC massive Machine Type Communication

mmWave millimeter-Wave

NOMA non-orthogonal multiple access

NM noise-masking

NLOS Non Line of Sight

NF Near Field

OFDM Orthogonal Frequency-Division Multiplexing

PCB Printed Circuit Board

PEB Position error bound

PEP packet error probability

PER packet error rate

PN pseudo noise

RAA Retrodirective Antenna Array

RCS Radar Cross Section

RFID radio frequency identification

RIS Reconfigurable Intelligent Surface

RMS root mean square

RMSE root-mean-square error

R-SLAM radio-SLAM

RSS Receive Signal Strength

RSSI Received Signal Strength Indicator

RTLS real time locating system

RTT Rount-Trip Time

RX Receiver

R-RIS Receiving-RIS

RV random variable

SCM Self-Conjugating Metasurface

SIC successive interference cancellation

SIMO single-input multiple-output

SINR signal-to-interference-noise ratio

SLAM simultaneous localization and mapping

SNR Signal-to-Noise Ratio

SRE Smart Radio Environment

STAR-RIS Simultaneous Transmitting And Reflecting RIS

SVD singular-value decomposition

TOA Time of Arrival

TDOA Time-difference of Arrival

THz Terahertz

TX Transmitter

TWR Two-way Ranging

T-RIS Transmissive RIS

UAV unmanned aerial vehicle

Acronyms

UE User Equipment

ULA Uniform Linear Array

UPA Uniform Planar Array

UWB ultra wideband

VNA Vector Network Analyzer

V2X Vehicular-to-Everything

5G fifth generation

6G sixth generation

RF radio frequency

SFCW stepped-frequency continuous-wave

FMCW frequency-modulated continuous-wave

PDP power delay profile

ECDF empirical cumulative distribution function

PADP power angular delay profile

Chapter 1

Introduction

The exponential growth in data traffic is pushing the boundaries of wireless connectivity, transforming it into an essential pillar of modern society. As we look ahead to 2030, forecasts predict a staggering 55% annual increase in global Internet Protocol (IP) data traffic, culminating in an unprecedented 5,016 exabytes [1]. This explosive growth underscores the urgency for future wireless networks not only to deliver ultra-high data rates, potentially up to 1 Tb/s [2], but also to support a diverse array of services such as sensing, localization, low-latency, and ultra-reliable communications. However, the fifth generation (5G) networks, constrained by their inherent design limitations, fall short of meeting these emerging demands.

To address these challenges, a revolutionary concept gained attraction in the last few years: the SRE [3, 4]. This paradigm shift proposes that, instead of treating the wireless environment as a static and uncontrollable element, it should be actively programmed and optimized. By doing so, the SRE can transform the wireless communication landscape, mitigating power wastage, reducing interference, and enhancing security. As reported in Fig. 1.1, the SRE exploits the inputs received by the wireless environment and optimizes the signals in it.

The traditional design assumptions of wireless networks, which have remained largely unchanged through five generations of cellular systems, are now being questioned. These assumptions held that the wireless environment between communicating devices is dictated by nature and cannot be modi-

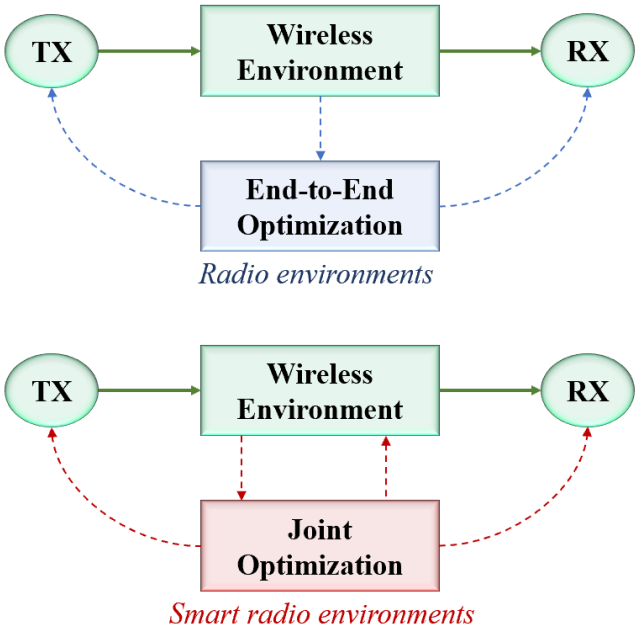

Figure 1.1: Radio Environment vs Smart Radio Environement concept.

fied, with compensation only achievable through sophisticated transmission and reception schemes. This outdated view is increasingly inadequate for the stringent requirements of future networks. The sixth generation (6G) networks envision a holistic architectural platform that seamlessly integrates communication [5], sensing [6–8], localization [9–11], and computing [12], delivering ultra-high throughput, ultra-low latency, and ultra-high reliability, all dynamically and flexibly customized in real-time [13, 14].

Central to the SRE concept is Reconfigurable Intelligent Surface (RIS), a breakthrough technology that enables the wireless environment to become an optimization variable [15]. RISs are meta-surfaces embedded with programmable electronic circuits capable of altering incoming electromagnetic fields. These surfaces are typically two-dimensional structures composed of composite material layers with metallic or dielectric patches, known as unit cells or scattering particles, that can be designed to be either locally passive or active. Through balanced absorptions and gains, RISs can transform incident electromagnetic fields to desired outcomes [16].

RIS technology offers significant energy savings by forwarding signals without the need for traditional power amplifiers, relying instead on precise phase shifts applied by each reflecting element. This makes RISs far more energy-efficient than conventional Amplify-and-Forward relay transceivers. Furthermore, their minimal hardware footprint allows for easy deployment in diverse environments, from building facades to room ceilings and even wearable devices. Although the absence of amplifiers means RISs may achieve lower gains compared to traditional Amplify-and-Forward relays with equivalent antennas, properly designed phase shifts can still ensure superior energy efficiency.

Recent research has demonstrated the impressive capabilities of RISs in indoor environments [17], showing substantial enhancements in received signal power and the ability to control various electromagnetic phenomena such as dynamic polarization [18], scattering, and beamforming [19]. These studies highlight the potential of RIS technology to improve indoor coverage and optimize communication environments. As investigations continue, RISs are poised to play a pivotal role in the evolution of wireless networks, driving the transition towards smarter, more efficient communication systems [20].

Besides the deployment of RIS, the SRE concept is further advanced by incorporating radio-simultaneous localization and mapping (SLAM) applications. These applications, along with advanced localization techniques, enhance environment awareness by dynamically mapping and localizing wireless nodes within the network without the need for deploying any infrastructure [21]. This integration allows the SRE to adapt more precisely to the environmental conditions, thereby optimizing communication performance and reliability. Radio-SLAM and localization techniques provide real-time data on the positions and movements of devices, enabling the network to make informed adjustments to signal paths and resource allocations. Traditionally, SLAM is based on the concept that a robot, moving in an unknown environment, recognizes the surrounding objects being then able to reconstruct a 2D/3D map of the area. This is typically done by steering a laser beam across a dense number of test directions and estimating the Rount-Trip Time (RTT) of the signal reflected by the obstacles (targets) for each test direction. In such a way, from RTT estimates, the distance of targets can

be inferred and, consequently, an accurate map of the environment can be built [22, 23]. This level of environment awareness is crucial for meeting the stringent requirements of next-generation wireless networks, such as ultra-low latency and high reliability, by ensuring that the network can proactively respond to changes and potential disruptions in the wireless environment.

In recent years, the concept of personal mobile radar has been developed [24, 25], leveraging the antennas of smartphones. The availability of numerous antennas on mobile devices enables the creation of narrow beams with electronically driven steering capabilities, which are crucial for high-accuracy mapping. This presents a cost-effective and energy-efficient alternative to laser technology.

In this context, a key step is the digital representation (mapping) of the physical world into the so-called smart space, a space that facilitates cooperation and interaction among smart objects. These developments contribute to the creation of smart radio environments. Fig. 1.2 illustrates how the concept of personal radar can become a reality. By utilizing antennas' smartphones, radio-SLAM can be employed to map the environment and geolocate within it, enabling the creation of an image of the surrounding environment without using laser radar and any wireless infrastructure.

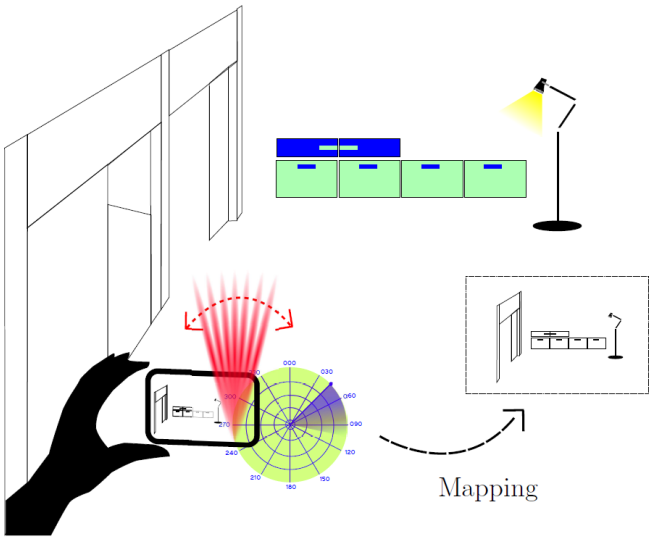

Figure 1.2: Personal radar concept [26].

Smart environments, such as SRE, in future generations of wireless systems, will not only leverage innovative technologies like RIS or radio-SLAM algorithms, but also technologies previously developed for earlier generations, such as ultra wideband (UWB) localization algorithms. The vision is to shift toward higher frequencies [27, 28], given the current congestion of the spectrum, which allows for the use of increasingly higher frequency bands. This shift offers several benefits, including high localization accuracy due to the use of wide bandwidths, enhanced resistance to interference, and low power consumption—crucial for applications where battery life is critical [29]. In addition to the aforementioned benefits, operating at high frequencies introduces coverage issues, particularly in Non Line of Sight (NLOS) scenarios, where technologies based on RIS can provide assistance.

1.1 Main Contributions and Thesis Organization

The above-mentioned topics are thoroughly addressed in this thesis. After a survey on conventional RISs illustrated in Chapter 2.1, Chapter 2.2 introduces a particular type of metasurface that is not reconfigurable but is frequency selective, referred to as *metaprism*. With metaprism, the frequency components of the impinging signal are reflected toward different angles depending on how the metaprism has been designed. The innovative aspect treated in this thesis includes the design of an algorithm capable of estimating the position of a target in NLOS by leveraging the frequency-angle mapping of the metaprism and near-field propagation. Two types of incident signal impinging on the metaprism were investigated: the first excited by an OFDM signal, and the second by an FMCW-chirp signal, both of which are modeled in general in Chapter 2.2. Subsequently, the metaprism is applied to high-frequency localization algorithms, with details and numerical results presented in Chapter 4.1.1 for the OFDM-metaprism and Chapter 4.1.2 for the FMCW one. This research has also led to the publication of the following scientific articles:

- **M. Lotti**, G. Calesini, D. Dardari, "LOS Localization Exploiting

Frequency-selective Metasurfaces", IEEE International Conference on Communications Workshops (ICC Workshops), Denver, CO, USA, Jun. 2024, pp. 1012-1016 [30].

- **M. Lotti**, D. Dardari, "Metaprism-aided NLOS Target Localization" 31st European Signal Processing Conference (EUSIPCO), Helsinki, Finland, Sep. 2023, pp. 895-899 [31].

The second type of metasurface studied in this thesis is the *Self-Conjugating Metasurface (SCM)*, also referred to as Retrodirective Antenna Array (RAA). This metasurface reflects the signal back towards the angle of arrival of the incident signal, leveraging the retro-directivity property. The general model of this type of metasurface is described in Chapter 2.3, and it has various applications. These include establishing efficient communication and beam tracking with multiple users equipped with SCMs, as discussed in Chapter 4.2.1, enabling grant-free channel access for users seeking to communicate with an access point, detailed in Chapter 4.2.2, and achieving high-accuracy localization of users equipped with SCMs, as presented in two different architectures in Chapter 4.2.3. The innovative aspect of this technology is that it enables beamforming between two arrays in an ultra-short time without the need for channel state information (CSI), using a node of extremely low complexity. It fully exploits path loss compensation due to the array configuration and can also amplify the backscattered signal if desired. These investigations have also resulted in the publication of several scientific papers:

- D. Dardari, **M. Lotti**, N. Decarli, G. Pasolini, "Establishing MIMO communications automatically using self-conjugating metasurfaces", IEEE International Conference on Communications (ICC), Rome, Italy, Jun. 2023, pp. 1286-1292 [32].

- D. Dardari, **M. Lotti**, N. Decarli, G. Pasolini, "Establishing multi-user MIMO communications automatically using retrodirective arrays", IEEE Open Journal of the Communications Society, vol. 4, pp. 1396-1416, Jun. 2023 [33].

- D. Dardari, **M. Lotti**, N. Decarli, G. Pasolini, "Grant-Free Random Access With Backscattering Self-Conjugating Metasurfaces", IEEE Transactions on Cognitive Communications and Networking, vol. 10, no. 5, pp. 1620-1634, Oct. 2024 [34].

- **M. Lotti**, N. Decarli, G. Pasolini, D. Dardari, "Real-time Localization Based on MIMO Backscattering from Retro-Directive Antenna Arrays," in IEEE Transactions on Vehicular Technology, Feb. 2025 [35].

It is worth noting that paper [32] received the Best Paper Award at the 2023 ICC conference in the selected area of communication "Reconfigurable Intelligent Surfaces and Smart Environments".

Chapter 3 is dedicated to the experimental activities conducted over the three years of the PhD program. Specifically, Chapter 3.1 presents the results obtained from the validation of two RIS prototypes operating at 5.3 GHz and 3.47 GHz. Subsequently, the measurement campaign for the world's first validation of a radio-SLAM application at Terahertz (THz) frequencies is described in Chapter 3.2, with numerical results reported following the description of the custom-developed SLAM algorithms for these frequencies, which are detailed in Chapter 4.3. Lastly, an experimental UWB localization analysis of an automatic docking system for the retrieval of large objects in harsh environments, for which application details cannot be disclosed due to a confidentiality agreement with the commissioning company, is presented in Chapter 3.3.

Regarding the SLAM activities, these have resulted in the following scientific publications:

- **M. Lotti**, G. Pasolini, A. Guerra, F. Guidi, M. Caillet, R. D'Errico, D. Dardari, "Radio simultaneous localization and mapping in the terahertz band", WSA 2021; 25th International ITG Workshop on Smart Antennas, Sophia-Antipolis, Nov. 2021 [36].

- **M. Lotti**, G. Pasolini, A. Guerra, F. Guidi, M. Caillet, R. D'Errico, D. Dardari, "Radio SLAM for 6G systems at THz frequencies: Design and experimental validation", IEEE Journal of Selected Topics in Signal Processing, vol. 17, no. 4, pp. 834-849, July 2023 [37].

1.2 Notation

In this thesis, boldface lower-case letters denote vectors (e.g., $\mathbf{x}$), whereas boldface capital letters represent matrices (e.g., $\mathbf{A}$ or $\mathbf{H}$). $\mathbf{I}_N$ and $\mathbf{0}_N$ are used to indicate the identity and zero matrices of size $N \times N$, respectively, while $\mathbf{0}_{M\times N}$ represents the zero matrices of size $M \times N$. The notation $a_{n,m} = [\mathbf{A}]_{n,m}$ is used to denote the (n, m)th element of the matrix $\mathbf{A}$. The operators $(\cdot)^T$ and $(\cdot)^*$ indicate the transpose and complex conjugate, respectively.

Furthermore, $\|\mathbf{x}\|$ represents the Euclidean norm of vector $\mathbf{x}$, and $\mathbf{x}^*$ denotes its complex conjugate. For matrices, $\mathbf{H}^*$, $\mathbf{H}^\top$, and $\mathbf{H}^\dagger$ represent, respectively, the complex conjugate, the transpose, and the conjugate transpose (Hermitian) of the matrix $\mathbf{H}$.

The notation $x \sim \mathcal{CN}(m, \sigma^2)$ describes a complex circular symmetric Gaussian random variable with mean m and variance σ^2, while $\mathbf{x} \sim \mathcal{CN}(\mathbf{m}, \mathbf{C})$ refers to a complex Gaussian random vector with mean $\mathbf{m}$ and covariance matrix $\mathbf{C}$.

Chapter 2

Enabling technologies for SREs

As previously described, one of the key technologies for shifting the perception of the wireless environment from a passive, uncontrollable entity to an active, programmable component is RISs. These are adaptable surfaces that can be programmed to manipulate the propagation of radio waves, beyond nature's law.

This chapter first outlines the general model of RISs, including their properties, governing principles, and applications. It then explores two types of metasurfaces. Specifically, a study of a frequency-selective metasurface, referred to as metaprism, is carried out and then examines a metasurface capable of reflecting the incident signal along the same direction as the impinging signal, referred to as SCM.

2.1 Reconfigurable intelligent surfaces

Reconfigurable intelligent surfaces and *metasurfaces* both manipulate electromagnetic waves, but they differ in their design, technology, and functionality. RISs are engineered surfaces that can dynamically adjust their properties in real-time through external control signals, enabling adaptive beamforming and improved signal propagation in wireless communications. Metasurfaces, on the other hand, are generally passive structures composed of subwavelength elements, designed to produce fixed electromagnetic responses such as anomalous reflection or focusing. While RISs can alter their behavior based

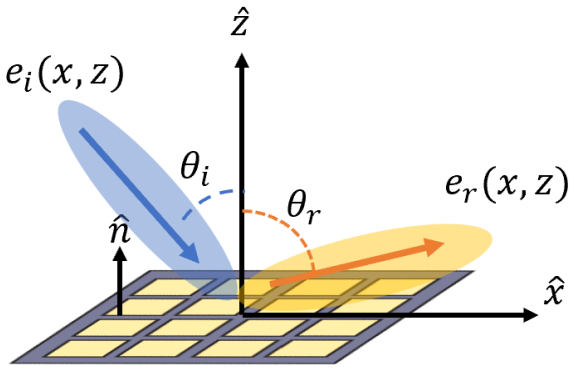

Figure 2.1: Schematic representations of the desired behavior for the anomalous reflection.

on environmental changes or specific requirements, metasurfaces typically maintain a static configuration once fabricated. In this thesis and from here on, the distinction between a RIS and a metasurface lies in the reconfigurability and adaptability of RIS compared to the static nature of conventional metasurfaces.

RISs have garnered significant interest for several reasons [3, 38]. Firstly, for millimeter-Wave (mmWave) [39] or THz [40, 41] frequencies, they offer a promising solution to critical coverage challenges, i.e., areas where traditional signal propagation is insufficient, often due to obstacles or environmental factors [42, 43]. RISs can address this by directing the signal straight to the receiver without dispersing it in the environment, effectively overcoming the limitations of traditional propagation methods. This capability goes beyond Snell's law, enabling RISs to create anomalous reflections of the incident signal, thus ensuring more reliable and efficient signal transmission [44, 45]. The Generalized Snell's law (GSL) can be defined considering the scenario illustrated in Fig. 2.1 where the incident and reflected waves propagate in a homogeneous medium with density ρ and light speed c, assuming time-harmonic dependence $e^{j\omega t}$, the incident and reflected electromagnetic (EM) fields can be written as [46]:

$$e_i(x,z) = p_0 e^{-jk\sin\theta_i x} e^{jk\cos\theta_i z}, \tag{2.1}$$

$$e_r(x,z) = Ap_0 e^{-jk\sin\theta_r x} e^{-jk\cos\theta_r z}, \tag{2.2}$$

where p_0 is the amplitude of the incident plane wave, $k = \omega/c$ is the wavenumber in the background medium at the operation frequency, θ_i and θ_r are the incidence and reflection angles, and A is a constant which relates the amplitudes of the incident and reflected waves.

Assuming that the field beyond the RIS is zero (an impenetrable surface), the system can be conveniently modeled by the equivalent circuit, as shown later in the Sec. 2.2 in Fig. 2.5, with an impedance Z_s that models the specific impedance of the RIS. According to the GSL, to obtain a reflected wave toward direction θ_r when the impinging angle is θ_i, the RIS's reflection phase profile must be characterized by the following gradient

$$\frac{\partial\Psi(x)}{\partial x} = k(\sin\theta_r - \sin\theta_i)$$

corresponding to a reflection phase profile $\Psi(x) = k(\sin\theta_r - \sin\theta_i)x$. In other words, the RIS is characterized by the local reflection coefficient with unit amplitude, which can be written as

$$\Gamma(x) = \frac{e^{-jk\sin\theta_r x}}{e^{-jk\sin\theta_i x}} = e^{jk(\sin\theta_i - \sin\theta_r)x} = e^{j\Psi_x}. \tag{2.3}$$

This reasoning is made assuming for the moment that along the $x-z$ plane the RIS is not discretized into unit cells, but continuous. Then, the reflection coefficient is related to the surface impedance as $\Gamma(x) = \frac{Z_s(x)-Z_i}{Z_s(x)+Z_i}$, where $Z_i = \frac{Z_0}{\cos\theta_i}$ represents the specific impedance of the incident wave at the RIS. From this expression, the impedance which models the RIS can be found as

$$Z_s(x) = j\frac{Z_0}{\cos\theta_i}\cot(\Psi_x/2). \tag{2.4}$$

Therefore, by changing the spatial evolution of the impedance, the reflection properties of the surface are altered, and consequently, the reflection angle of the incident signal is modified.

RISs can also exploit favorable propagation characteristics to enhance spatial multiplexing gains. Spatial multiplexing is a technique used in wireless communication to transmit multiple data streams simultaneously over the same

frequency channel. This is achieved by using multiple antennas, which significantly increases the capacity and efficiency of the communication system. RISs can further augment these gains by dynamically controlling the signal's propagation environment, thereby improving the separation and quality of the multiple data streams [12].

Furthermore, RISs finds applications in various advanced wireless technologies. In localization, RISs can enhance the accuracy and reliability of positioning systems by manipulating signal paths to improve signal strength and reduce multipath interference [47]. In sensing applications, RISs can be used to improve the detection and monitoring of objects or environments by optimizing the reflection and scattering of signals [48]. In terms of security, RISs provide physical layer security in wireless networks by controlling the signal propagation to minimize eavesdropping risks and enhance confidentiality. This makes RISs a versatile and powerful tool for enhancing the performance and security of modern wireless communication systems [49,50].

Therefore, RISs are a transformative technology used across communications, localization, and also Integrated Sensing and Communication (ISAC) applications. RIS leverages the ability to dynamically adjust the properties of surfaces to control and enhance radio wave propagation, making them highly valuable in these domains.

In communications, as pointed out above, RIS optimizes the signal transmission and reception by adjusting the reflective and refractive properties of surfaces in real-time. This capability improves coverage and connectivity in wireless networks, reduces interference, and enhances overall network performance. By configuring the surfaces to direct signals more efficiently, RIS enables higher data rates and more reliable connections, which are crucial for modern communication systems [51].

For localization, RIS provides advanced solutions for precise object and user tracking. By manipulating radio waves to create favorable conditions for signal propagation, RIS can significantly enhance the accuracy of location-based services. This is particularly beneficial in environments such as smart buildings and industrial settings, where precise localization of assets and individuals is essential for operational efficiency and safety.

In ISAC applications, RISs integrate sensing and communication capabil-

ities to enable more intelligent and adaptive systems. The ability to reconfigure surfaces allows for dynamic environmental sensing and data collection, which enhances situational awareness and decision-making. RISs contribute to the development of smart environments where real-time data acquisition and analysis support improved responses to various conditions and scenarios [52, 53].

Overall, RIS are pivotal in advancing communications by optimizing signal characteristics, improving localization accuracy through enhanced tracking, and supporting intelligent sensing and communication systems, driving innovation and efficiency across diverse applications.

From the technological viewpoint, RISs can be implemented of surfaces that use tunable sub-wavelength structures, like microstrip patches, to modulate the phase and/or amplitude of reflected waves. Two main approaches to implement RISs have been mainly discussed in the literature, which are either based on traditional *antenna arrays* or *metasurfaces*. The antenna-array-based RIS uses unit cells that have resonant size close to half-wavelength while the metasurface-based RISs are composed of a large number of closely spaced sub-wavelength unit cells.

Each sub-wavelength unit cell within the RIS receives the incident signal and re-emits it with altered amplitude and/or phase. This modulation is achieved by tuning the electromagnetic properties of the unit cell, such as through a switch placed at the feed of a resonant metallic patch, which changes the path of the electric current (open or short termination) and thus modulates the re-radiated field's amplitude and phase. More switches can provide multi-bit wavefront modulation, enhancing beam control and efficiency. Various topologies exist, employing single or multiple active devices and single or multi-layered substrates. All these designs require a biasing circuit and control unit (e.g., microcontroller) to manage the tunable devices by adjusting the biasing voltage.

RIS are typically two-dimensional structures, with lateral dimensions that are multiple wavelengths and thickness only a fraction of a wavelength, allowing seamless installation on building surfaces, both indoors and outdoors, and even on curved surfaces. With reference to Fig. 2.2, consider a surface in the $x-y$ plane with center at coordinates $\mathbf{p}_0 = (0, 0, 0)$, consisting

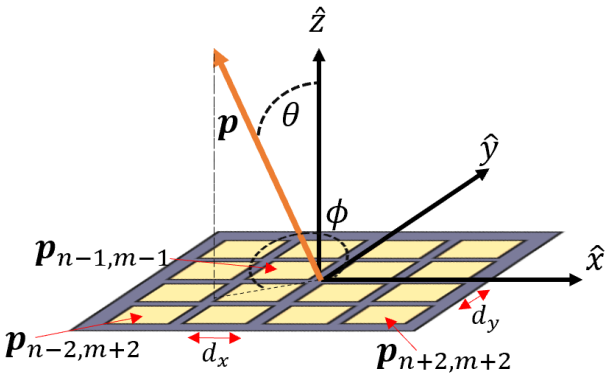

Figure 2.2: 3D geometry explanation of a reconfigurable surface composed of elementary cells.

of $N \times M$ cells of size $d_x \times d_y$ distributed in a grid of points with coordinates $\mathbf{p}_{nm} = (x_n, y_m, 0)$, where $x_n = n\,d_x - N\,d_x/2$, $n = 0, 1, \ldots N-1$, and $y_m = m\,d_y - M\,d_y/2$, $m = 0, 1, \ldots M-1$. The total surface's size is $L_x \times L_y$, with $L_x = N\,d_x$ and $L_y = M\,d_y$. The cell's size d_x, d_y, respectively, in the x and y directions, may be smaller than the wavelength λ, typically $d_x, d_y \approx \lambda/2 - \lambda/10$ [54, 55].

In mmWave and THz NLOS paths, if the user is not in the direction of specular reflection, communication relies on diffuse scattering from rough surfaces like walls and terrain. In such cases, enabling anomalous reflection can create viable propagation paths and enhance the received signal strength. The phase distribution Ψ_{nm} of the RIS, where n and m index the geometric position of the $x-y$ cells in the array, is characterized by the following design project equation [56]:

$$\Psi_{nm} + \Psi_i(x_n, y_m) = \Psi_r(x_n, y_m), \tag{2.5}$$

where $\Psi_i(x_n, y_m)$ and $\Psi_r(x_n, y_m)$ represent the phase distributions of the incident and (desired) reflected waves at the position x_n, y_m of the nm-th cell, respectively. The incident wave is generated by the Transmitter (TX) antenna illuminating the RIS. The radiation pattern $E(\theta, \phi)$ produced by the RIS configured to a specific state can be approximated as the radiation

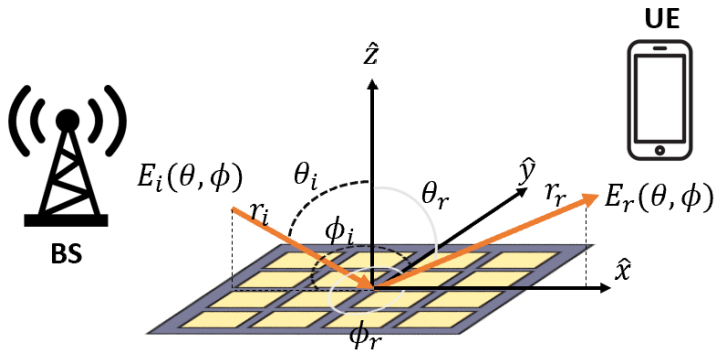

Figure 2.3: Overview of the signal's cascade channel from the TX (Base Station (BS)) to the Receiver (RX) (User Equipment (UE)).

pattern created by an array of patch-like antennas, and is given by [39, 57]:

$$E_r(\theta,\phi) = \cos(\theta) \sum_{n,m=1}^{N} \Gamma_{nm} E_i(x_n, y_m) \cos(\theta_{nm}) \times \exp\left(-jk\sin(\theta)\left(x_n\cos(\phi) + y_m\sin(\phi)\right)\right), \tag{2.6}$$

where $\cos(\theta)$ represents the radiation pattern of each individual antenna in the array, Γ_{nm} is the local reflection coefficient of the nm-th cell, $E_i(x_n, y_m)$ is the electric field of the incident wave at the nm-th cell, and θ_{nm} is the angle θ at which the nm-th cell views the TX antenna. The phase quantization varies with the number of bits; for instance, with 1-bit quantization, the phase can be 0 or π; with 2-bit quantization, it can be 0, $\pi/2$, π, $3\pi/2$ etc. It is important to distinguish between three cases: if the TX antenna (denoted as the BS in Fig. 2.3) is close to the RIS, a near-field configuration occurs [39]. Conversely, if the TX antenna is far from the RIS, a far-field configuration is established. It can be also considered the possibility of operating the RIS not only for beamforming but also for focusing, meaning concentrating the energy of the reflected wave at a specific point - with known distance and angle - rather than just along a direction. This is, of course, only feasible in the receiver-near-field case, not only for the transmitter - Near Field (NF) assumption as case I, where one has information about the RIS-receiver distance in addition to the angle. The latter will be described as the third case.

Near-field scenario: the first scenario resembles a classical reflectarray antenna configuration. The incident wave radiated by the TX (in practical setup is usually a horn) antenna is modeled as a spherical wave

$$\Psi_{\mathrm{i}} = \frac{\exp\left(-jk\sqrt{x_{Tx}^2 + y_{Tx}^2 + z_{Tx}^2}\right)}{\sqrt{x_{Tx}^2 + y_{Tx}^2 + z_{Tx}^2}}, \tag{2.7}$$

where $z_{Tx} = r_i \cos(\theta_i)$, $x_{Tx} = r_i \sin(\theta_i)\cos(\varphi_i)$, $y_{Tx} = r_i \sin(\theta_i)\sin(\varphi_i)$ and $k = \frac{2\pi}{\lambda}$ is the wavenumber. However, more elaborate models can be used to account for antenna parameters such as directivity. The reflected wave is considered a plane wave $\exp(-jk\mathbf{rn})$, propagating towards the RX antenna in the direction (θ_r, ϕ_r) defined by the vector $\mathbf{n}$. Under this configuration, (2.5) takes the following form:

$$\begin{aligned}\Psi_{nm,\,NF} = &- k\sin(\theta_r)\left(x_n\cos(\phi_r) + y_m\sin(\phi_r)\right) \\ &+ k\sqrt{(x_n - x_{Tx})^2 + (y_m - y_{Tx})^2 + z_{Tx}^2}.\end{aligned} \tag{2.8}$$

Far-field scenario: in the second case, the TX antenna is assumed to be sufficiently far from the RIS such that $r_i \gg L_x \times L_y$, where r_i is the distance between the TX and the RIS and $L_x \times L_y$ is the RIS's size, allowing the impinging wave to be approximated as a plane wave. The phase profile along the RIS is thus calculated using the following formula:

$$\begin{aligned}\Psi_{nm,\,FF} = &- k\sin(\theta_r)\left[x_n\cos(\phi_r) + y_m\sin(\phi_r)\right] \\ &+ k\sin(\theta_i)\left[x_n\cos(\phi_i) + y_m\sin(\phi_i)\right].\end{aligned} \tag{2.9}$$

Focusing scenario: as described above, focusing requires precise knowledge of the receiver's location, i.e., where the wave is to be re-radiated. In this case, the phase profile along the RIS is calculated using the following formula:

$$\Psi_{nm,\,Foc} = -k\sqrt{(x_n - x_{Rx})^2 + (y_m - y_{Rx})^2 + z_{Rx}^2} + k\sqrt{(x_n - x_{Tx})^2 + (y_m - y_{Tx})^2 + z_{Tx}^2}. \tag{2.10}$$

where $z_{Rx} = r_r \cos(\theta_r)$, $x_{Rx} = r_r \sin(\theta_r)\cos(\phi_r)$, $y_{Rx} = r_r \sin(\theta_r)\sin(\phi_r)$ and r_r is the distance between the RIS and the RX.

In the following, RISs are characterized based on their operation modes:

- **Signal Reflection**: This mode, typically referred to as RIS, involves the RIS acting as a reconfigurable reflector (Fig. 2.4 (a)), optimally steering the incoming EM waves.

- **Signal Reception (R-RIS)** [16] (Fig. 2.4 (b)): In this mode, the RIS is used for sensing the environment, acquiring channel state information, and localization. Reception with Receiving-RIS (R-RIS) may involve conventional radio frequency (RF) chain reception, but it can also include other technologies, such as signal intensity detectors [58].

- **Signal Transmission** Transmissive RIS (T-RIS) [59] (Fig. 2.4 (c)): This mode is used in conjunction with signal feeding units, such as spatial feeding [59] or RF chains [60].

- **Simultaneous Signal Reflection and Reception**: The Hybrid RIS (H-RIS) mode (Fig. 2.4 (d)) [61] combines the benefits of reflection and reception by allocating part of the impinged signal power for reception while reflecting the remainder.

- **Simultaneous Signal Transmission and Reflection Simultaneous Transmitting And Reflecting RIS (STAR-RIS)** [62] (Fig. 2.4 (e)): This mode involves refracting incoming EM waves and can operate in three different ways:

  1. A portion of the impinged EM wave's power is refracted while the rest is reflected.
  2. Different elements switch between reflecting and refracting modes.

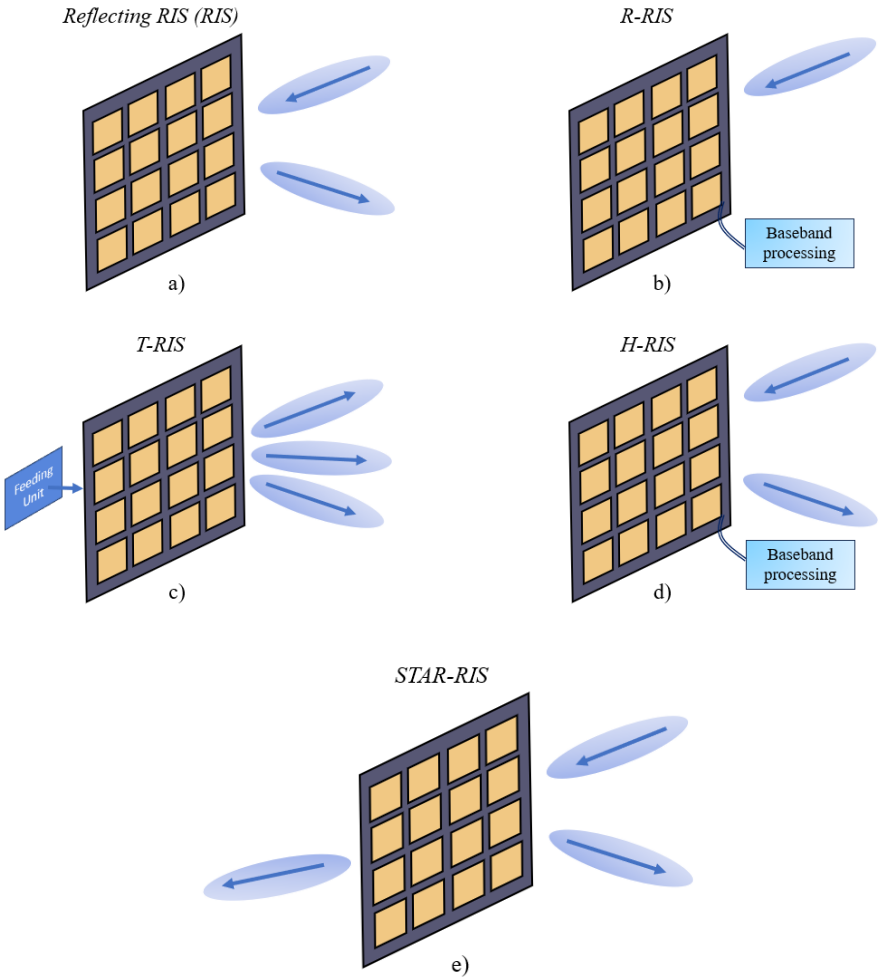

Figure 2.4: Schematic drawings of different operations with an RIS.

3. Alternating between reflecting and refracting over time.

2.2 Frequency-selective surfaces (metaprism)

Despite being promising solutions, RIS-based systems have some disadvantages which could make them less competitive than expected. In fact, to reconfigure a RIS in real-time, a dedicated control channel is needed, which might entail certain signaling overhead and, above all, additional complexity and cost. Although RIS was initially proposed as a passive component, coordinating a large number of elements still requires a certain amount of electrical energy [63]. When multiple RISs are deployed, establishing a dedicated physical link for each one would lead to significant resource consumption. Furthermore, RISs require power, which may not always be feasible or practical in many scenarios, in addition to not being entirely "green". A fundamental challenge when using an RIS is the estimation of the CSI [64]. In fact, the optimal configuration of the RIS's reflection coefficients, i.e., how the RIS reflects the impinging EM wave, is a function of the state of the channel between the RIS and BS / TX as well as between the RIS and the mobile user / RX (local CSIs). Its estimation is quite challenging because it may require additional hardware at the RIS to perform sensing (semi-passive RIS) or ad hoc CSI protocols and methods. Another solution is given by smart skins that are passive surfaces and do not suffer from the disadvantages of RISs. However, they always reflect the impinging signal toward the direction for which they have been designed and hence they do not offer the flexibility of a RIS. To overcome the main limitations of RISs and smart skins, in this thesis a novel solution has been investigated named metaprism, which is defined as a static frequency selective surface properly designed to reflect the various frequency components of the impinging signal toward different angles. It has to be noticed that there are several technologies to realize a metasurface. A rough classification can be done between metasurfaces whose cells can be seen as small radiating elements with tunable load impedance as described in Sec. 2.1 [65–68], i.e., using volumetric metamaterials with several wavelengths thick, and subwavelength metasurfaces producing a modification of the EM field which can be modeled as impedance sheets [69–73]. To facilitate the explanation and analysis, I focus on the first class even though the metaprism concept introduced in this section can be applied to the second

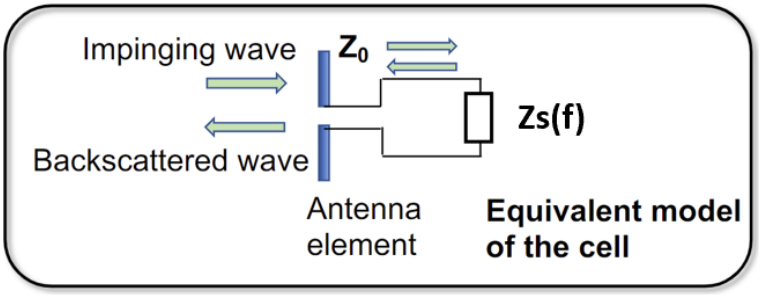

Figure 2.5: Equivalent model of the cell.

class as well.

A quite general equivalent model of the nm-th cell of the metasurface at position $\mathbf{p}_{nm}$ is shown in Fig. 2.5, which consists of a radiation element (antenna) above a ground screen loaded with a cell-dependent and frequency-dependent impedance $Z_s(f)$, with $n = 0, 1, \dots N-1$, $m = 0, 1, \dots M-1$, and f being the frequency. $Z_s(f)$ is nothing other than (2.4) discretized in the $x-y$ space, but here it is also frequency-dependent. The impedance is designed in such a way it is not matched to the antenna impedance Z_0, thus determining a reflected wave that is irradiated back by the radiation element. The corresponding frequency-dependent reflection coefficient in the presence of an incident plane wave with 3D angle $\mathbf{\Theta}^{\text{inc}} = (\theta^{\text{inc}}, \phi^{\text{inc}})$ and observed at angle $\Theta = (\theta, \phi)$ is[1] [65, 66]

$$\begin{aligned} r_{nm}(\mathbf{\Theta}^{\text{inc}}, \Theta; f) =& \sqrt{F(\mathbf{\Theta}^{\text{inc}})\, F(\Theta)}\, G_{\text{c}}\, \Gamma_{nm}(f) \\ =& \beta_{nm}(\mathbf{\Theta}^{\text{inc}}, \Theta; f)\, e^{\jmath\, \Psi_{nm}(f)} \end{aligned} \tag{2.11}$$

where $F(\Theta)$ is the normalized power radiation pattern that accounts for possible non-isotropic behavior of the radiation element, which can be considered, as a first approximation, frequency-independent within the bandwidth of interest, G_{c} is the boresight antenna gain, $\Gamma_{nm}(f)$ is the frequency-dependent load reflection coefficient, $\beta_{nm}(\mathbf{\Theta}^{\text{inc}}, \Theta; f)$ is the reflection amplitude and $\Psi_{nm}(f)$ is the reflection phase.[2] For instance, in [66] the following

[1] The conventional spherical coordinate system where $\phi \in [0, 2\pi)$ (azimuth) and $\theta \in [0, \pi)$ (inclination) is adopted.

[2] A more rigorous model should also account for the signal reflected back by the antenna

parametric shape for $F(\Theta)$ is proposed

$$F(\Theta) = \begin{cases} \cos^q(\theta) & \theta \in [0, \pi/2]\,, \phi \in [0, 2\pi] \\ 0 & \text{otherwise} \end{cases} . \tag{2.12}$$

Parameter q depends on the specific technology adopted as well as on the dimension of the cell and it is related to the boresight gain $G_\mathrm{c} = 2\,(q+1)$. Following an approach similar to that in [66], one possibility is to set G_c so that the effective area of the cell is equal to the geometric area of the cell $A_\mathrm{c} = d_x\, d_y$, i.e., $G_\mathrm{c} = A_\mathrm{c}\, 4\pi/\lambda^2$, assuming an ideal radiation efficiency. Considering a cell with $d_x = d_y = \lambda/2$, it follows that $G_\mathrm{c} = \pi \simeq 5\,\mathrm{dBi}$, and $q = 0.57$. A similar model is presented in [65] with $q = 3$. The load reflection coefficient, as described in the general case in Sec. 2.1, is given by

$$\Gamma_{nm}(f) = \frac{Z_s(f) - Z_0}{Z_s(f) + Z_0}\,. \tag{2.13}$$

By properly designing the impedance $Z_s(f)$ at each cell it is possible to realize different reflecting behaviors of the metasurface. Regardless of the specific technology adopted, it is proposed to design the reflection phase shift of the metasurface, $\Psi_{nm}(f)$, so that it exhibits a linear behavior with the frequency f, i.e.,

$$\Psi_{nm}(f) \approx \alpha_{nm} \cdot (f - f_\mathrm{r}) + \gamma(f) \tag{2.14}$$

for f within the signal bandwidth W, where α_{nm} is a cell-dependent coefficient and $\gamma(f)$ is a (possibly present) frequency-dependent phase shift.[3] In particular, $\gamma(f)$ represents a common (among cells) phase offset which is irrelevant to beamsteering and focusing operations. For this reason, in the remaining text, it will be neglected. Note that α_{nm} refers to the nm-th cell located at position $\mathbf{p}_{nm}$. According to the desired reflection behavior, the reference frequency f_r can be chosen either equal to the center frequency f_0 of the signal or equal to the lowest frequency edge of the signal band, i.e.,

according to its structural Radar Cross Section (RCS) component [74].

[3] From the practical point of view, the phase profile can be implemented equivalently according to a 2π modulo operation.

$f_\mathrm{r} = f_0 - W/2$. It will be shown that, thanks to the form in (2.14), it is possible to obtain a metasurface with the desired reflection properties allowing for frequency-dependent beamsteering and focusing; for this reason, it is named *metaprism*.

It is now shown an example of how the phase response (2.14) can be approximated starting from the equivalent model in Fig. 2.5 described by (2.11), (2.12), and (2.13). To this purpose, it can be considered a purely reactive impedance $Z_s(f) = \jmath X_{nm}(f)$ and a purely resistive antenna impedance $Z_0 = R_0$. The phase profile is

$$\Psi_{nm}(f) = \arg \Gamma_{nm}(f) = -2 \arctan \frac{X_{nm}(f)}{R_0} \,. \tag{2.15}$$

Suppose the reactive impedance consists of a resonating series LC circuit, with cell-dependent inductive and capacitive values L_{nm} [H] and C_{nm} [Farad], respectively. The corresponding impedance is

$$Z_s(f) = \jmath X_{nm}(f) = -\jmath \frac{1 - (2\pi f)^2 L_{nm} C_{nm}}{2\pi f C_{nm}} \tag{2.16}$$

where L_{nm} and C_{nm} are chosen to satisfy $(2\pi\sqrt{L_{nm}C_{nm}})^{-1} = f_\mathrm{r}$. To obtain the form in (2.14), it is convenient to derive the first-order Taylor series expansion in f for the reflection coefficient phase with respect to the reference frequency f_r. In particular, for the LC load, it results

$$\Psi_{nm}(f) \simeq -\frac{8\pi L_{nm}}{R_0}(f - f_\mathrm{r}) \,. \tag{2.17}$$

From (2.17) it is possible to obtain the desired coefficient $\alpha_{nm} = -8\pi L_{nm}/R_0$ in (2.14) by properly designing L_{nm} and C_{nm} in each cell. From the technological point of view, examples of metasurfaces whose elementary cells can be modeled as a purely reactive impedance can be found in [72, 75]. In particular, in [75] a cell made of a ring-loaded square patch with a single varactor diode connected across the gap between the ring and the patch is proposed and modeled using both a full-wave solver and an equivalent LC circuit.

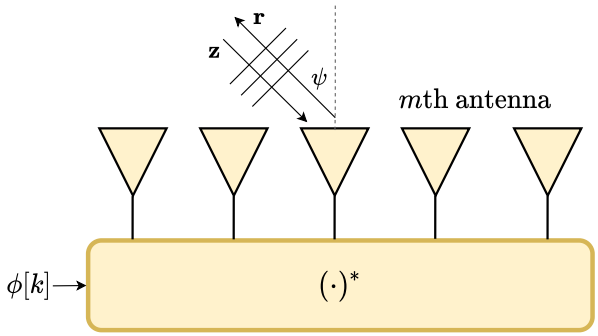

Figure 2.6: Schematic representation of a SCM.

2.3 Self-conjugating metasurfaces

So far, RISs have been studied mainly as reflectors deployed in the environment to create favorable propagation conditions for communications between the BS and the UEs [63, 76]. To cope with the large attenuation experienced by signals when reflected by passive RISs, the advantages of introducing amplifying (or active) RISs have recently been discussed [77–79]. Notable advancements have been achieved in architectures where data is incorporated into the reflected signals by modifying the reflection characteristics of the RIS, enabling spectrum sharing with legacy systems, as well as architectures supporting conventional backscatter communications [80–84].

Another advancement in the field of metasurfaces focuses on the realization of retrodirective devices. Several studies, accompanied by prototypical implementations, have demonstrated that achieving this objective is feasible [85–88]. For instance, the design of a metasurface is presented in [88] which exhibits a high level of retrodirectivity for 17 different angles of incidence. This result is achieved by realizing the metasurface according to a periodic grating, whose surface impedance is engineered such that retro-reflective property is obtained. In the following, it will be denoted as SCMs those metasurfaces capable of retro-directing the impinging signal and that can be able to incorporate data into the reflected signal.

A schematic representation of a SCM is reported in Fig. 2.6, where it is considered M antennas organized, for simplicity of explanation, as a Uniform Linear Array (ULA). From a technological point of view, the possibility of

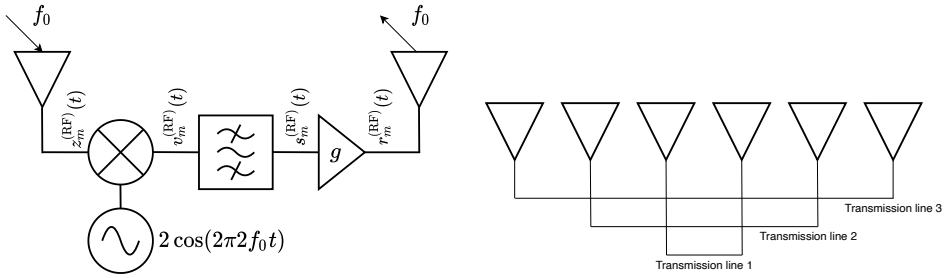

(a) Heterodyne technique for phase conjugation at the m-th antenna.

(b) Van Atta passive retrodirective array [92].

Figure 2.7: Schematic representation and principle of active and passive retrodirective arrays proposed as TX/RX antenna by the UE.

realizing ULAs capable of conjugating the phase of the impinging signal has been investigated for many years [89]. The main methods to achieve retrodirectivity are phase conjugating arrays, exploiting heterodyne mixing, and Van Atta arrays [90–92]. Phase conjugating arrays are based on the heterodyne mixing of the incoming wave, centered at frequency f_0, with a locally generated sinusoid oscillating at $2f_0$ [90,93]. The principle behind this solution is sketched in Fig. 2.7(a), which refers to the m-th phase-conjugating antenna of the array. For the sake of clarity, in Fig. 2.7(a) it is depicted as two separate transmit and receive antennas, which however correspond to a single antenna of the ULA shown in Fig. 2.6.

Consider a plane wave impinging the ULA, with an angle Ψ with respect to its normal direction, as shown in Fig. 2.6. At the m-th antenna, the impinging wave accumulates a phase shift θ_m, with respect to the first antenna, given by

$$\theta_m = \frac{2\pi}{\lambda} m\Delta \sin\Psi \tag{2.18}$$

for $m = 0, 1, \ldots, M-1$, where Δ is the inter-antenna separation.

Concerning Fig. 2.7(a), the analytical expressions of the signals at each port of the m-th antenna can be easily derived. In this regard, since the theoretical foundation of the phase conjugation process is illustrated, this subsection does not consider the presence of noise, which will be taken into account afterward. In particular, at the output of the m-th receiving antenna,

the RF signal $z_m^{(\mathrm{RF})}(t)$ can be written as

$$\begin{aligned} z_m^{(\mathrm{RF})}(t) &= x(t)\cos(2\pi f_0 t + \theta_m) - y(t)\sin(2\pi f_0 t + \theta_m) \\ &= \Re\Big(z_m(t) e^{\jmath 2\pi f_0 t} \Big) \end{aligned} \tag{2.19}$$

where $x(t)$ and $y(t)$ denote the in-phase and quadrature components of the received signal, respectively, and

$$z_m(t) = \Big(x(t) + \jmath y(t) \Big) e^{\jmath \theta_m} \tag{2.20}$$

represents its complex envelope. After the heterodyne mixing of $z_m^{(\mathrm{RF})}(t)$ with a sinusoid at $2f_0$, it results

$$\begin{aligned} v_m^{(\mathrm{RF})}(t) = {} & x(t)\cos(2\pi f_0 t - \theta_m) + x(t)\cos(2\pi 3 f_0 t + \theta_m) \\ & + y(t)\sin(2\pi f_0 t - \theta_m) - y(t)\sin(2\pi 3 f_0 t + \theta_m). \end{aligned} \tag{2.21}$$

The bandpass filter shown in Fig. 2.7(a) is designed to remove the spectral components centered at $3f_0$, so the signal entering the transmitting antenna is

$$\begin{aligned} r_m^{(\mathrm{RF})}(t) &= g\, x(t)\cos(2\pi f_0 t - \theta_m) + g\, y(t)\sin(2\pi f_0 t - \theta_m) \\ &= \Re\Big(r_m(t) e^{\jmath 2\pi f_0 t} \Big) \end{aligned} \tag{2.22}$$

with g denoting the amplitude gain of the power amplifier and

$$r_m(t) = g\Big(x(t) - \jmath y(t) \Big) e^{-\jmath \theta_m} \tag{2.23}$$

being the complex envelope of $r_m^{(\mathrm{RF})}(t)$. Comparing (2.20) with (2.23) it is evident that the final result of the processing carried out by the antenna is the phase conjugation of the signal, as expected. It is worth noting that, assuming that the modulated signal $z_m^{(\mathrm{RF})}(t)$ is narrowband (i.e., its bandwidth W is such that $W \ll f_0$), the exponential terms $e^{-\jmath \theta_m}$ in (2.23), for

$m = 0, 1, \ldots M-1$, form the beam direction vector

$$\left[1,\, e^{-\frac{2\pi}{\lambda}\Delta \sin\Psi},\, \ldots,\, e^{-\frac{2\pi}{\lambda}(M-1)\Delta \sin\Psi}\right]^{\mathrm{T}} \tag{2.24}$$

which is required to steer the array beam back to Ψ, that is, to have the impinging wave reflected in the same direction of arrival (retrodirectivity).

An example of the experimental effectiveness of this technique can be found in [93], where a testbed consisting of an antenna array with eight slot antennas, each of which connected to a Schottky diode performing heterodyne mixing, was realized. The measure of the bistatic RCS of the resulting meta-interface (as it is called in [93]) showed the retrodirectivity property, exhibiting an RCS almost coincident with the array factor for an 8-element array focusing the received signal toward the source. Another relatively simple solution is proposed in [94], in which active split-ring resonators loaded with varactor diodes are demonstrated to act as phase-conjugating elements when pumped with a signal at frequency $2f_0$.

While phase conjugating arrays require active components, Van Atta arrays realize passive retrodirectivity (in this case $g < 1$) [92]. As sketched in Fig. 2.7(b), a Van Atta array consists of an array of antenna elements arranged in symmetrical pairs and connected through transmission lines. Each element of the pair acts as a receiving and transmitting antenna. In particular, the signal received by an element is re-irradiated by its pair after it has traveled through the transmission line whose length is designed to not introduce phase shifts. The elements are deployed in a mirror-symmetric manner to cause an equivalent phase-conjugation effect for the reflected wave compared to the incident wave.

Recently, it has been shown that also metasurfaces can be designed to provide passive retrodirectivity. This property can be achieved by engineering the surface impedance according to a supercell design periodicity that is greater than the wavelength λ [88]. The general principle is that provided that electric or magnetic surface currents are induced at the reflecting boundary, the conventional reflection law does not hold when the surface properties (e.g., the surface impedance) smoothly vary within the wavelength scale [85]. As a result, by properly engineering the induced surface-current gradients,

it is possible to reflect the incident wave in a direction other than specular. One example of implementation at mmWave for Internet of Things (IoT) applications can be found in [95]. Clearly, the main advantage of the heterodyne approach over passive solutions is that by employing active mixing devices, amplitude gain can be achieved in addition to phase conjugation, thereby improving the transmission range at the expense of some power consumption.

One of the primary challenges associated with active SCMs is maintaining a high level of isolation between the transmit (TX) and receive (RX) signal chains during simultaneous transmission and reception. This is typically achieved through various methods, including bistatic configurations (spatial multiplexing), slightly different TX and RX frequencies (frequency multiplexing), and dual-polarized elements (polarization multiplexing). Recently, a co-polarized active SCM has been demonstrated experimentally in [96] with a gain g of 23 dB. Unfortunately, such techniques could lead to a loss of channel reciprocity, which, on the other hand, is assumed in our proposed scheme, due to the unavoidable asymmetry of the circuits. However, the numerical results demonstrate that our communication scheme exhibits strong robustness to channel non-reciprocity.

Another possible issue of heterodyne-based SCMs is the frequency offset Δf between the local oscillator of the SCM and the carrier frequency of the BS because they are not synchronized. This generates an additional phase rotation $\psi(t) = 2\pi\Delta f\, t$ in the reflected signal. The effect of the frequency offset Δf is equivalent to the Doppler shift that would be generated by a moving UE in a dynamic environment. In the following analysis, it is assumed that the phase variation within the transmission of a few symbols is negligible, i.e., $\Delta f \ll 1/T$, being T the symbol interval. However, the impact of the Doppler/frequency offset will be investigated in the numerical results in Sec. 4.2.

Given the bandwidth W of the narrowband signal in (2.19), it is considered the sampled version of its complex low-pass signal in (2.20), $z_m[k] = z_m(kT) = A[k]e^{\jmath\theta_m}$, with sampling time $T = 1/W$ and $A[k] = x(kT)+\jmath y(kT)$ representing the complex symbol received by the m-th antenna in the k-th symbol interval.

By introducing the noise generated by the SCM, the discrete-time signals at the input of the M antennas in the k-th symbol interval can be expressed by the vector

$$\mathbf{z}[k] = A[k]\left[1,\, e^{\jmath\theta_1},\, \ldots,\, e^{\jmath\theta_{M-1}}\right]^{\mathrm{T}} + \boldsymbol{\eta}[k] \tag{2.25}$$

where $\boldsymbol{\eta}[k] \in \mathbb{C}^{M\times 1}$ is the additive white Gaussian noise (AWGN), with $\boldsymbol{\eta}[k] \sim \mathcal{CN}\left(\mathbf{0}, \sigma_\eta^2\, \mathbf{I}_M\right)$. Note that $\sigma_\eta^2 = \kappa T_0 F_{\mathrm{SCM}}\, W$, being κ the Boltzmann constant, $T_0 = 290\,\mathrm{K}$, and F_{SCM} the SCM's noise figure [78, 97]. Thanks to the self-conjugating property of the antenna array, it can be written the vector $\mathbf{r}[k]$ of the signal reflected by the SCM in the same symbol interval as

$$\mathbf{r}[k] = g\, \mathbf{z}^*[k]\,. \tag{2.26}$$

Suppose, now, that the SCM not only performs the conjugation and amplification[4] of the received signal, thus retro-directing the impinging signal as it appears in (2.26), but also introduces, in the k-th symbol interval, a phase shift $\phi[k]$ (the same for all the antennas) that incorporates the information to be transmitted by the UE that is equipped with the SCM in that interval [34]. The vector of the transmitted signal becomes therefore

$$\mathbf{r}[k] = g\, e^{\jmath\phi[k]}\, \mathbf{z}^*[k]\,. \tag{2.27}$$

Equation (2.27) is thus representative of the proposed solution in which the BS transmits a signal to the UE, which (possibly) amplifies and retransmits along the direction of arrival the received signal (retrodirectivity), using it as a carrier to incorporate through the phase $\phi[k]$ the information intended for the BS (see Fig. 2.6). Note that the phase $\phi[k]$ associated with the information affects all the antennas of the array, thus not compromising the retrodirectivity behavior. Most importantly, the implementation of the modulated SCM does not require ADC chains as data directly modulates the phase sequence $\{\phi[k]\}$, thus allowing a low-cost, low-complexity, low-energy consumption multi-antenna device. The principle scheme of a modulating SCM-based MIMO communication is reported in Fig. 2.8, where the signals described in (2.25), (2.26) and (2.27) are shown. In Chapter 4.2, several

[4] If the SCM is passive, then $g \leqslant 1$.

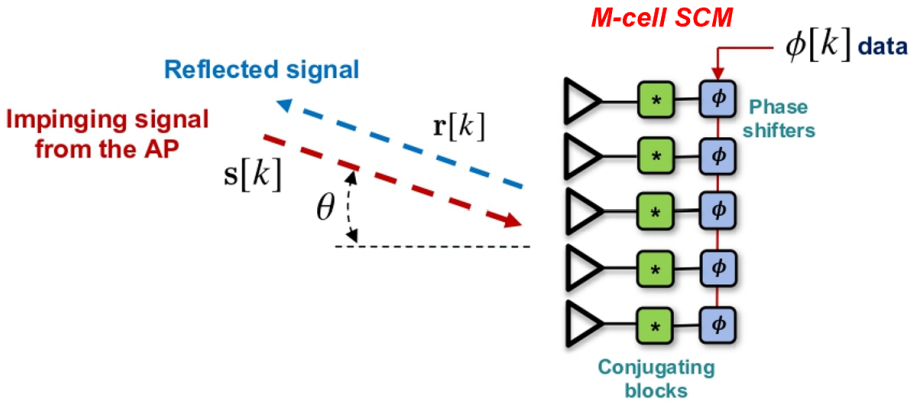

Figure 2.8: Principle scheme of a modulating self-conjugating metasurface (SCM)-based MIMO communication.

solutions leveraging SCM for MIMO communication, both single-user and multi-user, channel access and localization applications are presented.

Chapter 3

Experimental results

During this PhD program, the final objective was to develop algorithms for smart radio environments leveraging reconfigurable intelligent surfaces, followed by field validation of these algorithms through dedicated measurement campaigns. To achieve this, it was necessary first to validate the performance of devices such as reconfigurable surfaces, state-of-the-art antennas like 300 GHz antennas, and understand how to exploit UWB devices. For the RIS, my research team has purchased one RIS, and borrowed another, from the Japanese company NEC, a leader in the field. Being prototypes, one at 3.47 GHz and the other at 5.3 GHz, the objective was first to verify their functionality, as they had never been tested before. Once the RISs were validated, the next step was to use them, for example, in out-of-band operation to exploit the frequency selectivity of the RIS response - which is usually undesired in normal operation - but can instead be leveraged to validate the algorithms developed with metaprisms (Chapter 4), given that real metaprisms have yet to be practically implemented.

After several months spent identifying malfunctions during the configuration and testing phases at the Cesena campus (University of Bologna), the final measurements were conducted in the anechoic chamber in Aalborg, Denmark. All details are provided below.

Moreover, this chapter not only covers the validation of RISs but also presents the world's first validation campaign of the Radio-SLAM concept at 300 GHz and the use of UWB devices for ultra-precise localization applica-

tions; specifically, Sec. 3.1 covers the validation of the RIS, Sec. 3.2 details the measurement campaigns conducted in collaboration with the CEA-Leti research center in France, which led to the world's first validation of a 300 GHz personal radar, and Sec. 3.3 describes an experimental analysis of an automatic docking system for retrieving large objects in harsh environments. Further details on the application cannot be disclosed due to confidentiality agreements with the commissioning company.

3.1 Experimental characterization of a RIS

The purpose of this section is to describe the RIS antenna system supplied by NEC to the University of Bologna. Both RIS antennas (3.47 GHz and 5.3 GHz), which were intended to enhance wireless communication capabilities within our premises, have exhibited significant performance issues since their installation. This section aims to provide a comprehensive overview of the observed problems and potential causes.

3.1.1 5.3 GHz RIS

The NEC RIS 2022 prototype features 100 patch antennas arranged in a 10 $\times$ 10 grid of unit cells, each containing a single antenna. These antennas are implemented using Printed Circuit Board (PCB) technology on a board with a thickness of 0.6 mm. The antennas are separated by a distance equal to $\lambda/2$, both horizontally and vertically, where λ is the wavelength of the supported carrier signals. The operating frequency of the RIS is 5.3 GHz. Thanks to phase shifters based on 3-bit delay lines, 7 different phase shifts, equally spaced between 0° and 360°, can be selected for each unit cell. The 8th state is dedicated to the absorption mode, where the incoming signal is redirected through a 50 Ω resistor, dissipating the signal. The RIS is designed as a modular device, meaning multiple RIS boards can be connected to create a larger RIS, while still maintaining the $\lambda/2$ inter-element distance even across boards. For more details, see [98].

Initially, the work done involved the development of a Graphical User Interface (GUI) (Fig. 3.1) to control the RIS, consistent with the specifica-

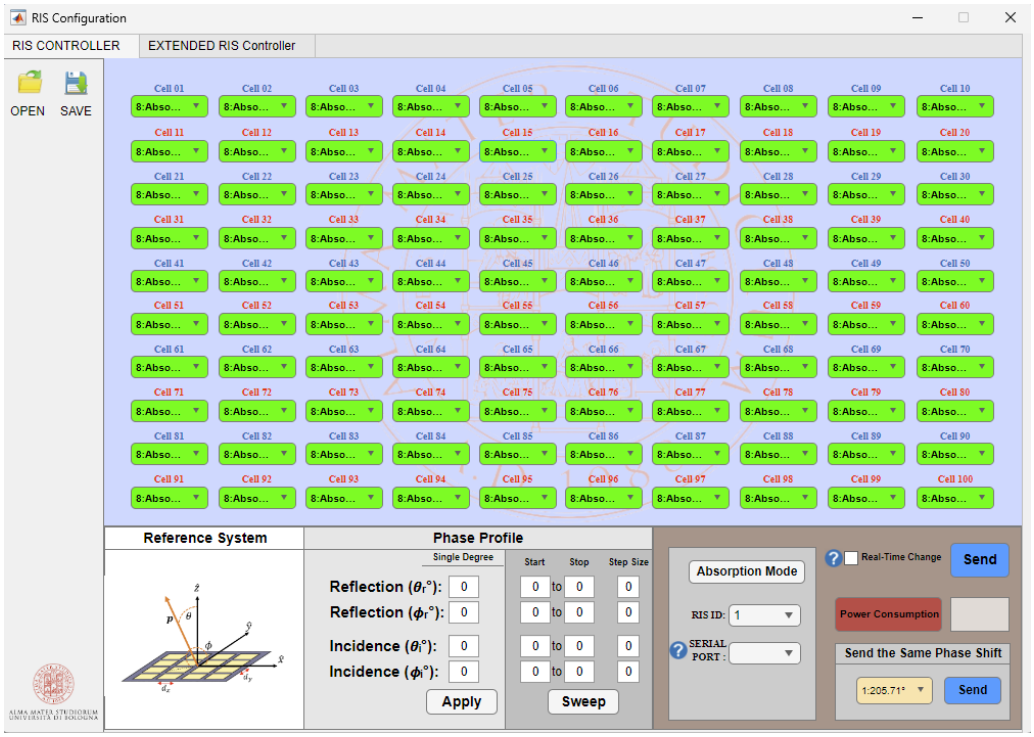

Figure 3.1: RIS Controller layout

tions provided by NEC. In Fig. 3.1, 100 green cells are presented, with each cell representing an individual antenna on the RIS board. To each of these, one of eight possible phase shifts can be assigned, either automatically or by manual selection. The design formulas for the RIS followed those of an array factor (AF) for a planar array under the assumption of incident and reflected plane waves, reported in (2.9) for the Far Field (FF) case or (2.8) for the case where the transmitter is NF with respect to the RIS. An example of the codebook applied in the phase shift design is reported in Fig. 3.2(b).

After the development of the GUI, measurements were conducted in a real-world environment. Initially, tests were carried out in a corridor, where few objects capable of backscattering the signal were present, and theoretically, there should be minimal interference. The parameters used for this measurement campaign are $f_{\text{start}} = 4.3$ GHz, $f_{\text{stop}} = 5.8$ GHz, $f_{\text{center}} = 5.05$ GHz, BW $= 1.5$ GHz which leads to a spatial resolution $\Delta_s = \frac{c}{\text{BW}} = 0.2$ m , $\Delta_f = 750$ kHz, and the number of samples is 2001. These values were also set in the Vector Network Analyzer (VNA) Agilent E5062A [99] during

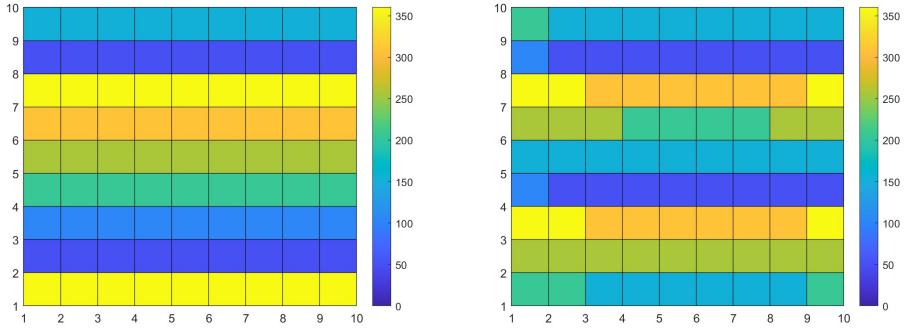

Figure 3.2: Codebook (Ψ_{nm}) for a FF assumption incident wave (a) and for a NF incident wave (b) with TX and RX placed in the same azimuth plane, the RX is normal to the RIS, while the TX is tilted of 30°. ($\theta_i = 30°, \phi_i = 270°, \theta_r = 0°, \phi_r = 0°$)

calibration.

The setup is shown both in the photos in Fig. 3.3 and in the schematic in Fig. 3.4. The transmitter is a Narda 643 Alltest Instrument antenna [100], while the receiver is a TDK HRN-0118 Horn Antenna [101]. The transmitter illuminates the RIS from below with an inclination of $\theta_i = 5°$ and $\phi_i = 270°$, while the receiver is positioned on the same elevation plane as the RIS $\phi_r = 180°$, and displaced at $\theta_r = 30°$. The RIS is placed 1.20 m from the TX (the TX has a height of 89 cm). The RX (with a height of 101 cm) is positioned 4 m from the RIS. The center of the RIS is at a height of 101 cm. From the power delay profile (PDP) shown in Fig. 3.5, it is evident that the main peak is exactly at 5.29 meters, as expected given a spatial resolution of 20 cm. The delay of the PDP is translated into a distance to better understand where the peak is placed. However, varying the configuration of the RIS does not alter the behavior at this distance. Instead, it can be observed that at approximately 5.9 meters, when the configuration is set to the correct angles, there is an increase in power of more than 10 dB compared to when the RIS is configured to re-radiate towards the opposite side of the receiver or even in absorption mode. The peak that does not vary with the configuration can be justified by noting that the highly directive nature of the TX and RX horn antennas already performs spatial filtering. On the other hand, the second peak may be due to a slight misalignment

Figure 3.3: Photos of the setup from the first measurement campaign conducted in the corridor of the Cesena campus at the University of Bologna

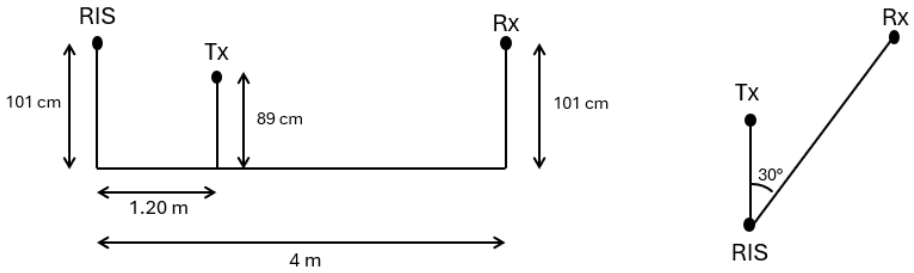

Figure 3.4: Schematic of the geometry for the first measurement campaign

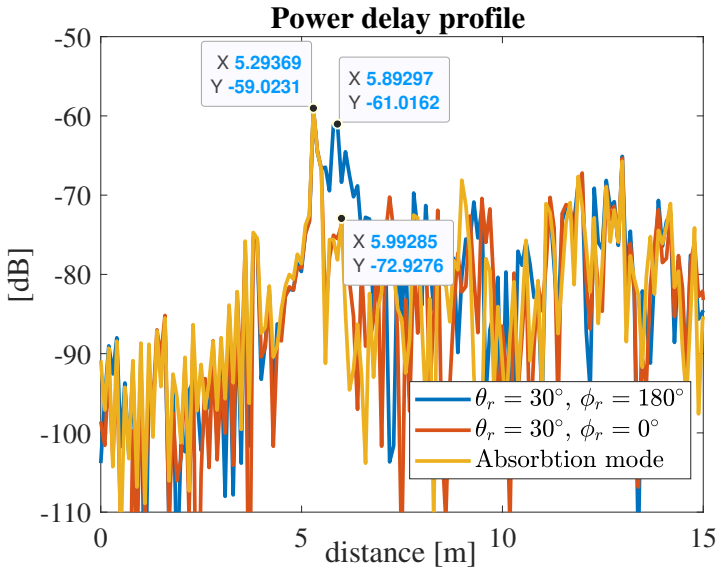

Figure 3.5: Power delay profile first measurement campaign ($\theta_i = 5°, \phi_i = 270°$and $\theta_r = 30°, \phi_i = 180°$)

of the antennas, even though the alignment was carried out using a laser pointer with the utmost precision. These results raised doubts about the RIS functioning as expected, prompting further analysis to investigate the issue in greater depth. The identical behavior shown in Fig. 3.5 was also observed when moving the RX to $\theta = 20°$ and $\theta = 40°$ and adjusting the antenna codebook accordingly. However, the difference between the power levels of the secondary peaks was not as pronounced as in the case of $\theta = 30°$; instead, it was on the order of a few dB (2 to 4 dB).

Due to uncertainties regarding the correct functioning and design of the RIS, and to avoid potential design errors in the codebook design, we requested the company to provide us with the codebook matrix to apply to the RIS for the scenario depicted in Fig. 3.6, which is referenced in their article [98]. We then replicated the same setup in both indoor and outdoor environments to eliminate the possibility of multipath effects impacting the results. The setup pictures are reported in Fig. 3.7 and the schematic in Fig. 3.8. Therefore, for these measurement campaigns, the VNA settings remain the same as in the previous cases. In a top-down view, the RIS, TX, and RX are aligned. The TX is positioned at a height of 90 cm (center of the horn). The RX is

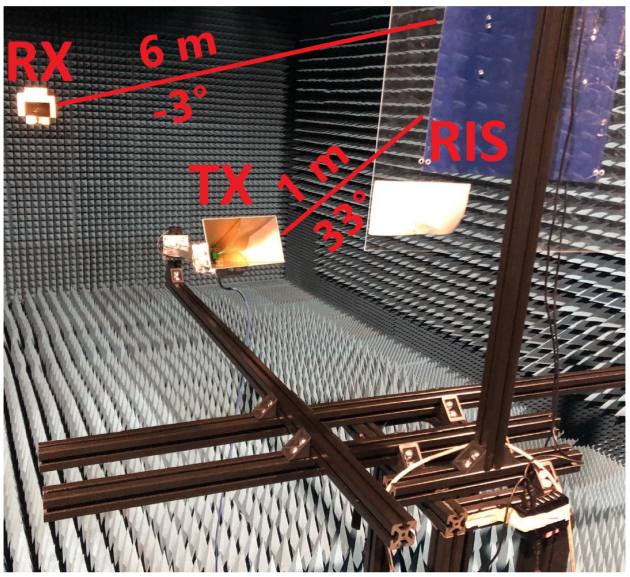

Figure 3.6: Experimental setup tested by NEC [98]

Figure 3.7: Photos of the setup from the second indoor and outdoor measurement campaigns conducted at the Cesena campus of the University of Bologna

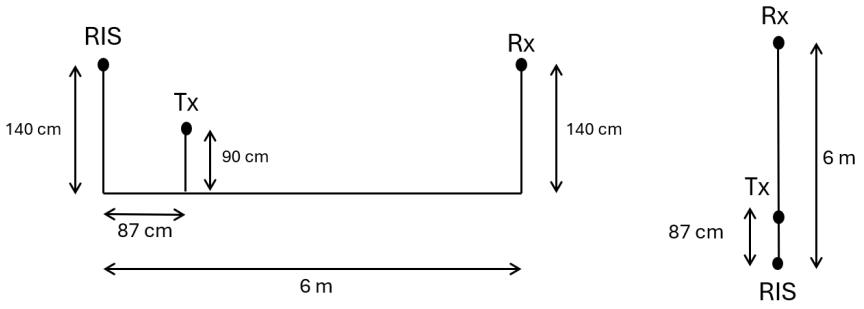

Figure 3.8: Schematic of the geometry for the indoor and outdoor measurement campaigns, resembling the NEC setup

positioned at a height of 140 cm (center of the horn). The RIS is positioned at a height of 140 cm (center of the RIS). The resulting PDPs from the indoor and outdoor measurements are shown in Fig. 3.9 and Fig. 3.10, respectively. From Fig. 3.10, it can be seen that the peak is at 7.29 meters, even though it should be approximately 7 meters; this is still a reasonable value due to the spatial resolution being 20 cm. What raises some doubts is that when the RIS configuration is altered — such that it no longer points 3° upward but instead 30° downward — the peak shows no significant change. On the other hand, when the configuration is set to absorption mode, the main peak is suppressed but only by 3 dB. As for the outdoor measurements, they are certainly cleaner compared to the indoor ones, making it easier to see that the main peak is also at 7.29 meters, and its power level remains unchanged across the three configurations. However, the second peak, located 40 cm further, changes by approximately 8 dB. It is important to note that, in theory, the PDP figures presented in this section could be further processed to accurately filter the direct RIS-RX path, allowing us to study the direct path gain with different codebooks. The issue was that in none of the measurements were we able to distinguish the correct path contributed by the RIS. Even though the TX-RIS and RIS-RX distances were known, varying the codebook did not result in any significant change in the peak corresponding to these distances.

Due to unsatisfactory experimental results and to certify the malfunctions obtained at the Cesena campus of the University of Bologna, it was decided to test the RISs in Aalborg. Aalborg University, which is a part-

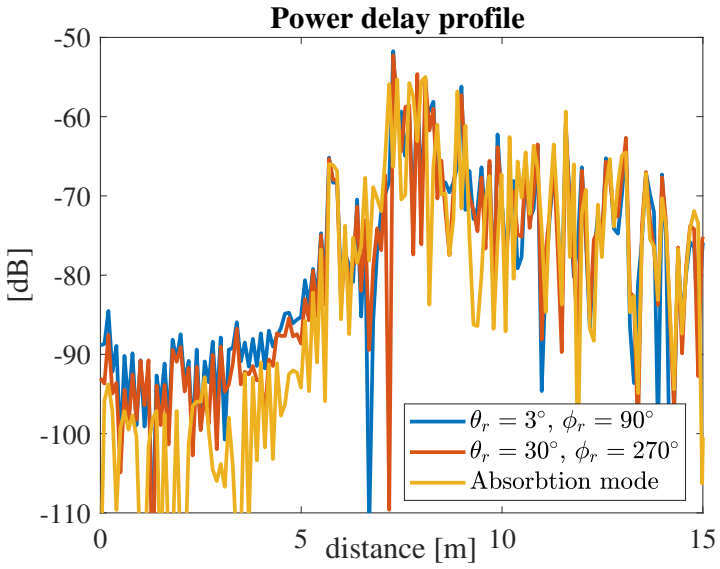

Figure 3.9: Power delay profile indoor measurement campaign with NEC setup ($\theta_i = 33°, \phi_i = 270°$and $\theta_r = 3°, \phi_i = 90°$)

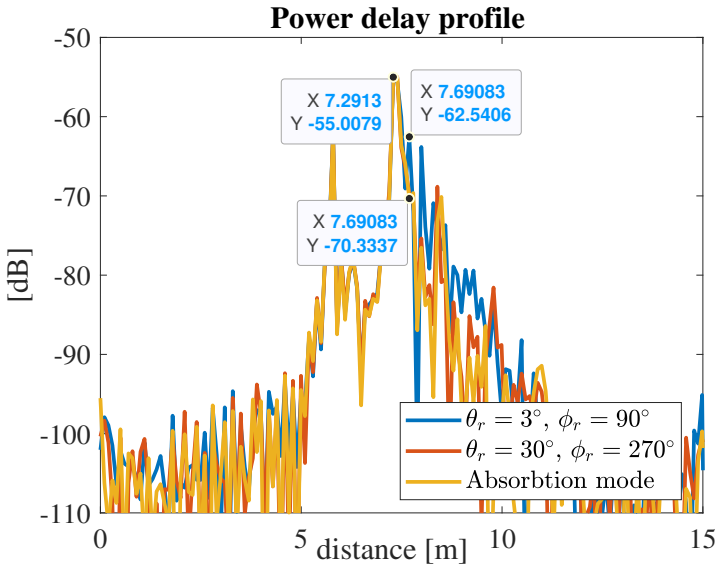

Figure 3.10: Power delay profile outdoor measurement campaign with NEC setup ($\theta_i = 33°, \phi_i = 270°$and $\theta_r = 3°, \phi_i = 90°$)

ner of CNIT (and thus University of Bologna, as part of CNIT) within the 6G-SHINE European project, possesses significant resources allowing for state-of-the-art antenna testing. This would enable the derivation of the antenna's 3D pattern based on the codebook sent through the serial connection to the RIS. The testing instrumentation used, called SATIMO, is shown in Fig. 3.11. SATIMO comprises a rotating and oscillating mast onto which the RIS and the feed antenna are mounted. Receivers (horn antennas) are positioned approximately every 15° along a ring. The system's rotation and oscillation allow for the oversampling of samples and the reconstruction of the 3D radiation pattern.

Initially, a setup composed as shown in Fig. 3.12 was tested. This setup consists of the RIS positioned vertically, correctly oriented, with a horn antenna as the feed. The focal center of the horn antenna is 1.04 meters away from the center of the RIS, with an elevation angle of 14° relative to the center of the RIS. This setup was then tested using both AF approximation for incident and reflected plane waves (setting $\theta_r = 0°$, $\phi_r = 110°$, $\theta_i = 14°$, $\phi_i = 270°$ according to the reference system depicted in Fig. 3.13(a)), and the one with spherical wave assumption. The formulas applied, for the RIS phase shift, are always (2.9) for the FF assumption and (2.8) for the NF one.

The resulting radiation pattern obtained is shown in Fig. 3.14(a) in 3D, while Fig. 3.14(b) represents the elevation cut at $\phi = 90°$ of the anechoic chamber reference system, means that the cut is made along the vertical normal to the RIS. It is important to notice that the reference system of Fig. 3.14(a) is the one of the anechoic chamber depicted in Fig. 3.13(b). It is observed that the peak obtained is not at $\theta_r = 0°$ and $\phi_r = 110°$ as expected, but rather at 15°, resembling the behavior of a specular component, suggesting that the RIS behaves similarly to a metallic plate. Another indication that something was amiss was that behind the RIS, the signal scattered was more intense than in front, suggesting that the transmitted signal was being completely absorbed by the receivers behind the RIS as if the RIS was "transparent" or like some object with its own Radar Cross Section but failed to capture and reradiate the signal effectively.

Figure 3.11: SATIMO testing setup for antenna characterization.

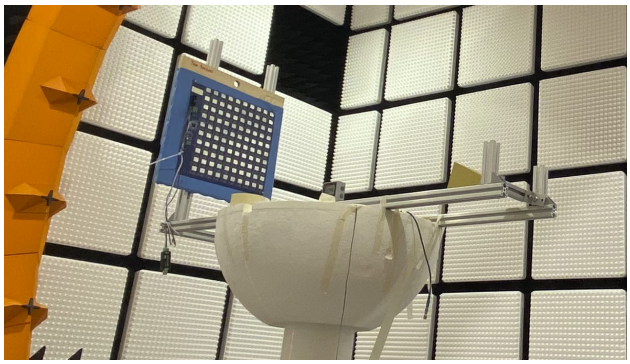

Figure 3.12: Experimental setup for RIS testing.

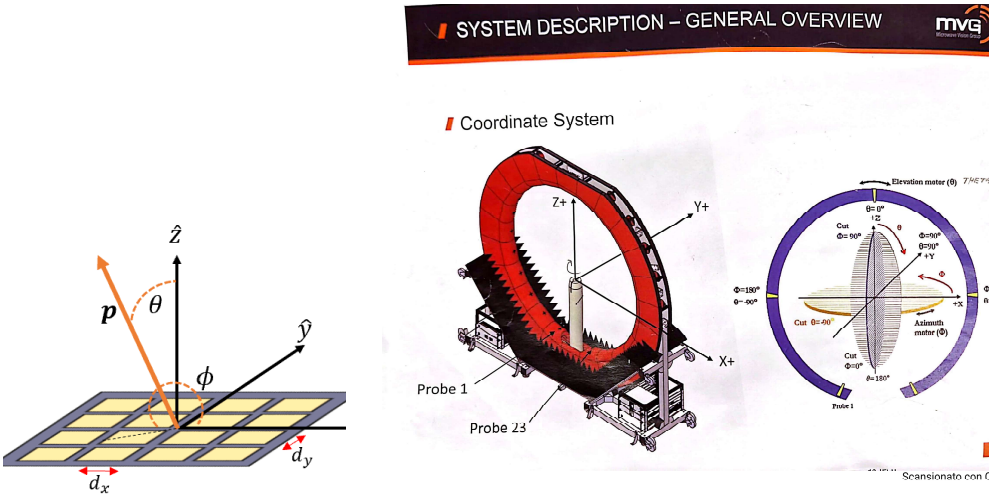

(a) (b)

Figure 3.13: RIS reference coordinate system (a) and anechoic chamber reference system (b).

After realizing that the RIS was not behaving as expected and was unable to capture the transmitted signal, we hypothesized that perhaps we were not configuring the RIS with the correct settings. Therefore, we modified the setup and tested it similarly to that shown in Fig. 3.6, which is detailed in the paper provided by NEC [98].

Previously, we were supplied with the codebook used in this configuration by NEC, ensuring that the combination of setup and codebook was correct. In Fig. 3.15(a), you can find the photo confirming a distance of 1 meter

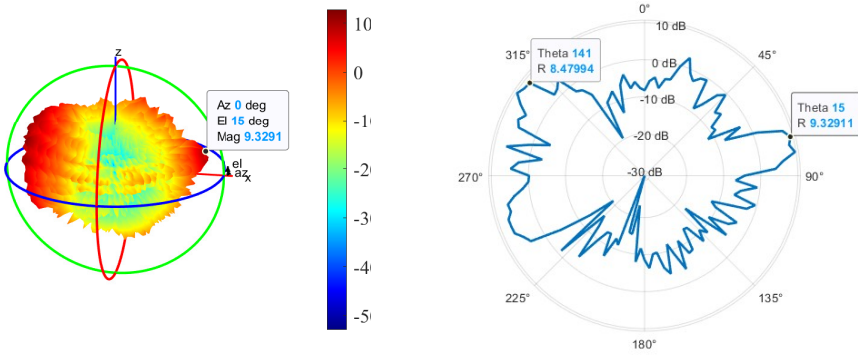

(a) (b)

Figure 3.14: 3D radiation pattern of the RIS setup (a) and elevation cut of the radiation pattern at $\phi = 90°$ (b), setting $\theta_r = 0°$, $\phi_r = 110°$, $\theta_i = 14°$, $\phi_i = 270°$.

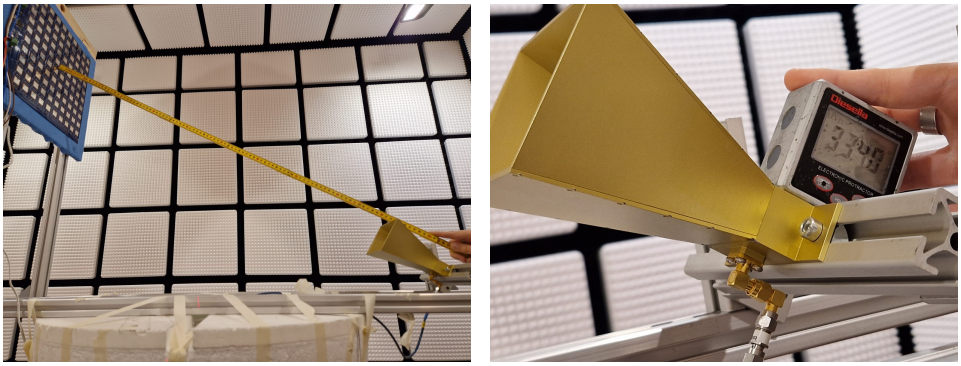

(a) (b)

Figure 3.15: Setup equal to the one tested by NEC.

TX-RX, and in Fig. 3.15(b), the angle of 33° is shown.

The only difference lay in the position of the receiver, which was not placed at 6 meters as in the NEC setup, but rather at 2.5 meters. However, there are several receivers, so there is no issue of not seeing the main lobe of the RIS in this configuration tested by us.

The codebook applied to the RIS is the one precisely provided by NEC, which is identical to ours using the formulas with plane wave incidence and plane wave radiation, setting the design angles as $\theta_i = 33°$, $\phi_i = 271°$, $\theta_r = 3°$, $\phi_r = 90°$. The 3D results and the cut at $\phi = 90°$, thus the vertical 2D graph, can be seen in Fig. 3.16 on the left and right, respectively. What is obtained

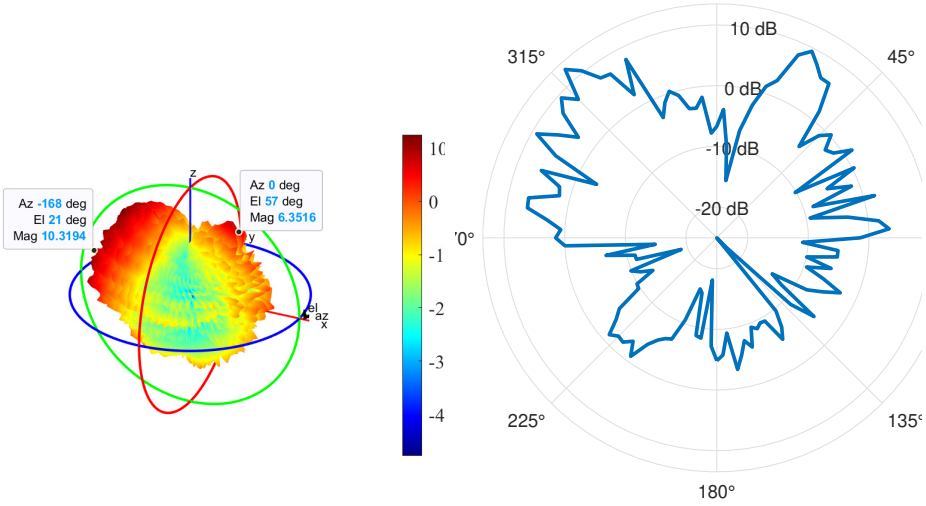

(a) (b)

Figure 3.16: Measurements results obtained with codebook provided by NEC, 3D radiation pattern (a) and 2D cut (b).

is a peak at approximately 60°, still a peak well below the values of 25 dBi as stated in the NEC article [98] and unexplainable as to why it is there, perhaps due to a noise effect.

We also tried different codebooks, for instance setting the design angles as $\theta_i = 33°$, $\phi_i = 271°$, $\theta_r = 10°$, $\phi_r = 180°$. The results are in Fig. 3.17. Essentially, these results show that nothing regarding the main peak has changed, only the effects of the side lobes can be observed changing. We also tried the codebook that put all the cells in absorption mode simultaneously, and again we found the results reported in Fig. 3.18. Here, it can be observed that the main lobe has shifted from the previous 60°, as if the effects of anomalous reflection and specular reflection were adding up in some way. After all these tests, we moved to the workbench, where we used a voltmeter to verify that the orientation of the cells was correct and that each unit cell was fed with the correct delay line, in accordance with Fig. 3.19. The results showed that when the value 1 was sent, the delay line corresponding to the value 1 - i.e, the one measuring 4.85 mm - was indeed at low impedance (3 Ω), while all others were at high impedance (16 KΩ) and the same for all the others values. Therefore, we certified that it was not a problem with

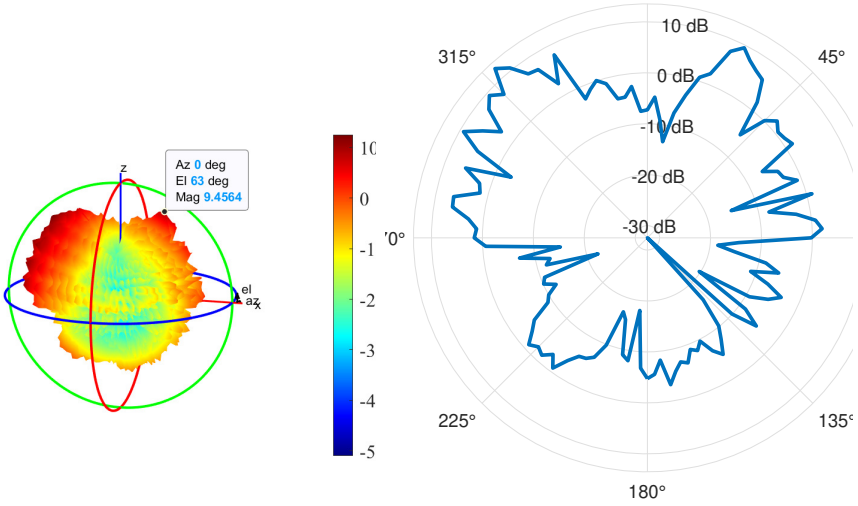

(a) (b)

Figure 3.17: Measurements results, 3D radiation pattern (a) and 2D cut (b) with $\theta_i = 33°$, $\phi_i = 271°$, $\theta_r = 10°$, $\phi_r = 180°$.

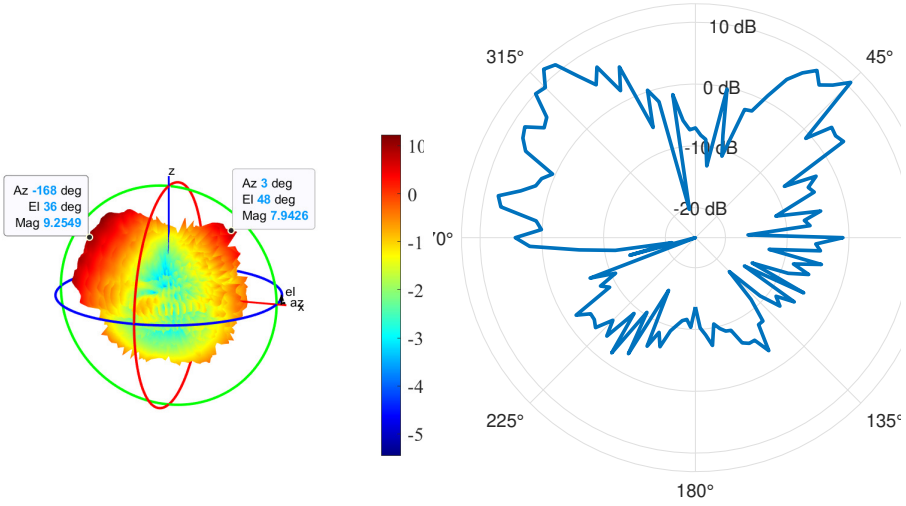

(a) (b)

Figure 3.18: Measurements results obtained with RIS in absorption mode, 3D radiation pattern (a) and 2D cut (b).

the serial connection to the RIS and that the RF switch output ports were functioning correctly.

Once we confirmed that the flip-flop components were functioning, we

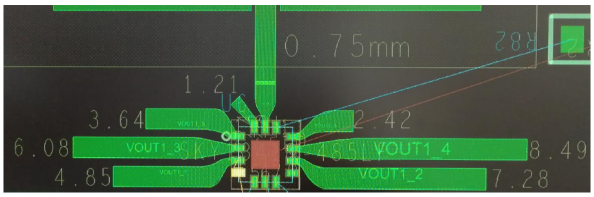

Figure 8: RF switch and microstrips.

Output port	7	6	5	1	3	2	4
φ **(deg)**	51.42	102.85	154.28	205.71	257.14	308.57	360
l **(mm)**	1.21	2.42	3.64	4.85	6.08	7.28	8.49

Figure 3.19: RF switch and microstrips and relative length of the associated delay lines, and the resulting phase shifts [98].

proceeded to test the phase shifters. The only tool we had available was a probe antenna, which illuminated and measured a portion of the RIS, allowing us to verify the phase change occurring in that portion of the antennas through the measurement of S11. For completeness, a photo is attached in Fig. 3.20. The same configuration value was then applied to all cells, and what was observed is that the phase changes expressed in degrees, as the configuration varied, were only a few units of degrees, a maximum of 10°, although there is a phase difference of more than 50° between each configuration. The same test was then tested in the SATIMO anechoic chamber, illuminating the RIS from below with the setup of Fig. 3.15. In Tab. 1 there are the values in degrees of the phase of the S21 signal, at a fixed receiver in $\theta = 90°$ and $\phi = 0°$ (in the reference system of the chamber), this means that we are looking at the receiver in front of the RIS. As you can see from the table the values are not changing a lot between them, showing why even if changing the codebook the RIS was not changing its behavior. In Fig. 3.21, the phases of the $S_{21}(f)$ parameter measured in the operating band declared by the company (5.17-5.44 GHz) are shown. As can be seen, when the phase is changed for all the cells, the measured phase in degrees does not change. While it is certainly not expected to achieve the exact 50 degrees as declared, since the phases in the $S_{21}(f)$ measurement might constructively or destructively add up, the values should not be identical either.

Unfortunately, in Aalborg, we verified that the phase shifters of the RIS,

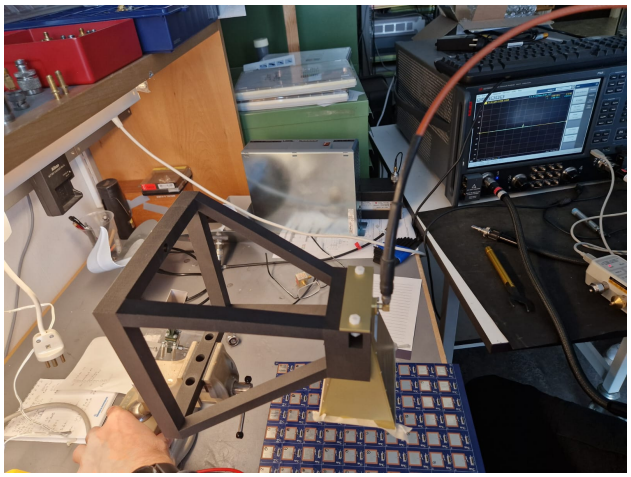

Figure 3.20: Setup in order to test the phase shifter functionality

although correctly set, were not functioning properly. We then contacted the company that provided the RIS, and they explained that the malfunction could be attributed to structural scattering, which likely affected the measurements taken.

Structural scattering refers to the phenomenon where the structure of the RIS itself scatters the incident electromagnetic waves, regardless of the intended phase configuration of the individual elements. This scattering occurs due to the physical and geometric characteristics of the RIS, such as its shape, material properties, and surface irregularities, which cause unintended reflections and diffractions. As a result, the scattered waves can interfere with the desired signal path, leading to inaccurate phase measurements and reduced performance of the RIS.

In our opinion, however, structural scattering is mainly present in the Snell direction, apart from the sidelobes, so if the reflection angle coincides, there is a risk that the reflected signal may be masked by structural scattering. Conversely, if the reflection angle is different, we should clearly see the contribution of the RIS as intended. Contrary to what the company told us, we believe that the fact nothing changed is due to the effective phase shifts of the cells not being as indicated by NEC and possibly varying from cell to cell, making it impossible to program the RIS based on the design formulas. In practice, I have to proceed randomly, trying all possible codebooks.

Value applied to all cells	Corresp. degree angle	Meas. phase shift [°]
4	360	-22.7636
2	308.57	-27.3014
3	257.14	-26.2185
1	205.71	-24.7804
5	154.28	-18.8961
6	102.85	-16.3866
7	51.42	-14.0833
8	abs mode	-16.1861

Table 3.1: Values in degrees of the phase of the S21 signal, at $\theta = 90°$ and $\phi = 0°$ (in the reference system of the chamber)

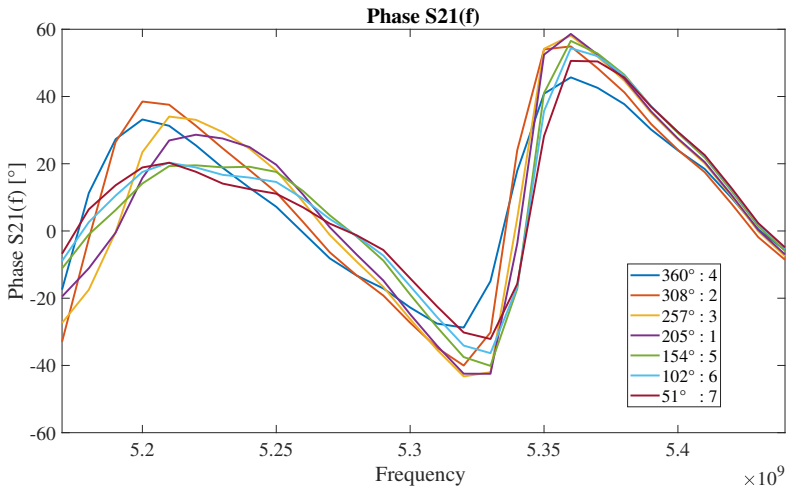

Figure 3.21: Measured phase as a function of the phase configuration applied to all cells

3.1.2 3.47 GHz RIS

The NEC 2023 prototype is a RIS consisting of 256 elements arranged in a 16×16 grid, with a nominal center frequency of 3.47 GHz and a bandwidth of 150 MHz. As in the previous version, each unit cell can achieve seven distinct phase shifts, equally spaced between 0° and 360°, thanks to phase shifters based on 3-bit delay lines. The eighth state is reserved for absorption mode, in which the incoming signal is diverted through a 50 Ω resistor, dissipating the signal.

Initially, it was observed that although the provided documentation specified a spacing of $\lambda/2$ between elements, the actual distance between the elements is 3 cm, corresponding to $\lambda/2.88$. This discrepancy caught us off guard, and despite requesting further clarification from the company, no additional information was provided. Consequently, tests were conducted at both 3.47 GHz, as specified, and at 5 GHz, which corresponds to the anticipated $\lambda/2$ spacing. Additionally, unlike the 2022 prototype, where the patch antennas were square, the current antennas are rectangular, suggesting a preferential vertical polarization. Unfortunately, due to a confidential agreement with the company, we are unable to provide the datasheet or any photographs of the prototype. The formulas used during the design phase are consistent with those corresponding to (2.8) and (2.9) for NF and FF cases, respectively, with the necessary adjustments, such as element spacing and center frequency. For the setup described in Fig. 3.23, the corresponding codebook pictures are reported in Figs. 3.22(a), 3.22(b) for the FF and NF case, respectively. It can be noted that in the FF case, the columns are not perfectly equal between each other, due to the 3° of inclination of the TX. For the NF assumption, it is evident the effect of the spherical incident wave, slightly tilted towards the bottom and the fact that the RX is placed on the left with respect to the RIS. The setup is as described in the previous section, with the VNA calibration performed using the new frequency band. We tested the setup shown in Fig. 3.23, where the distance between the TX and the RIS is 3.75 m, the distance between the RIS and RX is 4 m, and the TX is tilted 3° relative to the center of the RIS.

I would like to point out that working with different inclined planes was

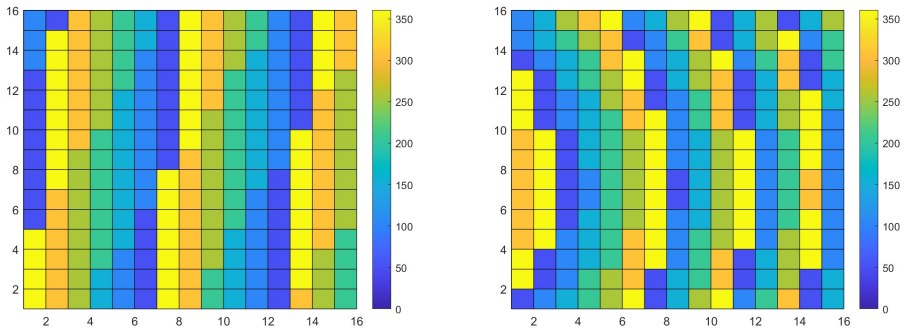

Figure 3.22: Codebook (Ψ_{nm}) for a FF assumption incident wave (a) and for a NF incident wave (b) with TX and RX placed in the same azimuth plane, the RX is 4 m distant to the RIS, with $\theta_r = 30°$, $\phi_r = 180°$ while the TX is tilted of 3° in the elevation plane. ($\theta_i = 3°, \phi_i = 270°$)

Figure 3.23: Picture of the setup for the RIS 3.47 GHz test. The TX is positioned at a distance of $d = 3.75$ m, with $\theta_i = 3°$ and $\phi_i = 270°$. The RX is located 4 meters from the RIS, with $\theta_r = 30°$ and $\phi_r = 180°$.

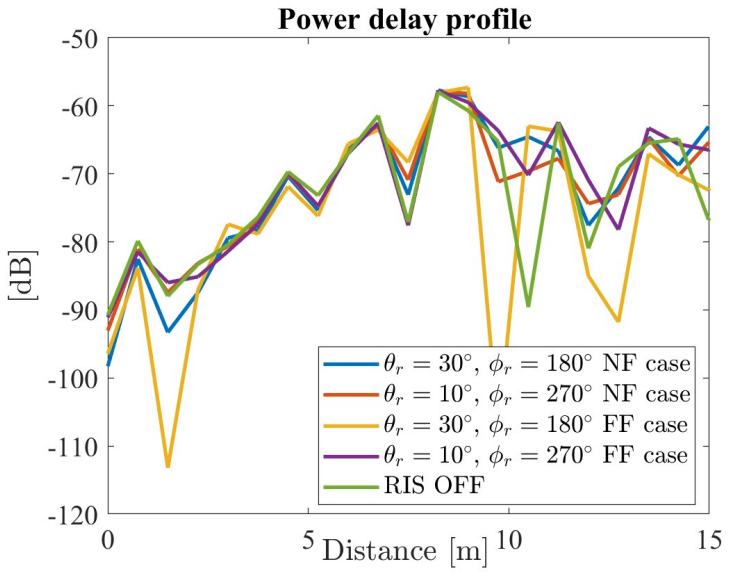

Figure 3.24: Power delay profile for different codebook assumptions in NF and FF cases and RIS turned off.

suggested by the company, although logically it should not have a significant impact. The VNA calibration was performed only on the operational band of the antenna, which is slightly wider, at 200 MHz. As a result, the spatial resolution of the measurements is limited to 1.5 meters. This test was conducted to verify the actual functionality of the antenna, rather than to confirm that the peak precisely corresponded to the exact distance between the TX, RIS, and RX. The results reported in Fig. 3.24 show that there is no impact on the applied codebook, whether under FF or NF assumptions, with a completely random configuration ($\theta_r = 10°$, $\phi_r = 270°$), or even when the RIS is turned off, in which case it should behave like a standard metallic reflector. Please note that even if post-processing is performed at frequencies $[f0-B/2, f0+B/2]$, with $B = 150$ MHz the behavior of the PDP in Fig. 3.24 remains unchanged. These results prompted us to test the RIS at 5 GHz as well, without observing any significant changes compared to what was previously seen in Fig. 3.24. We then questioned whether the programming of the RIS was indeed correct, as no significant changes were observed with different applied configurations. To address this, we tested whether each cell and some configurations correctly received the programmed value. Fig. 3.25

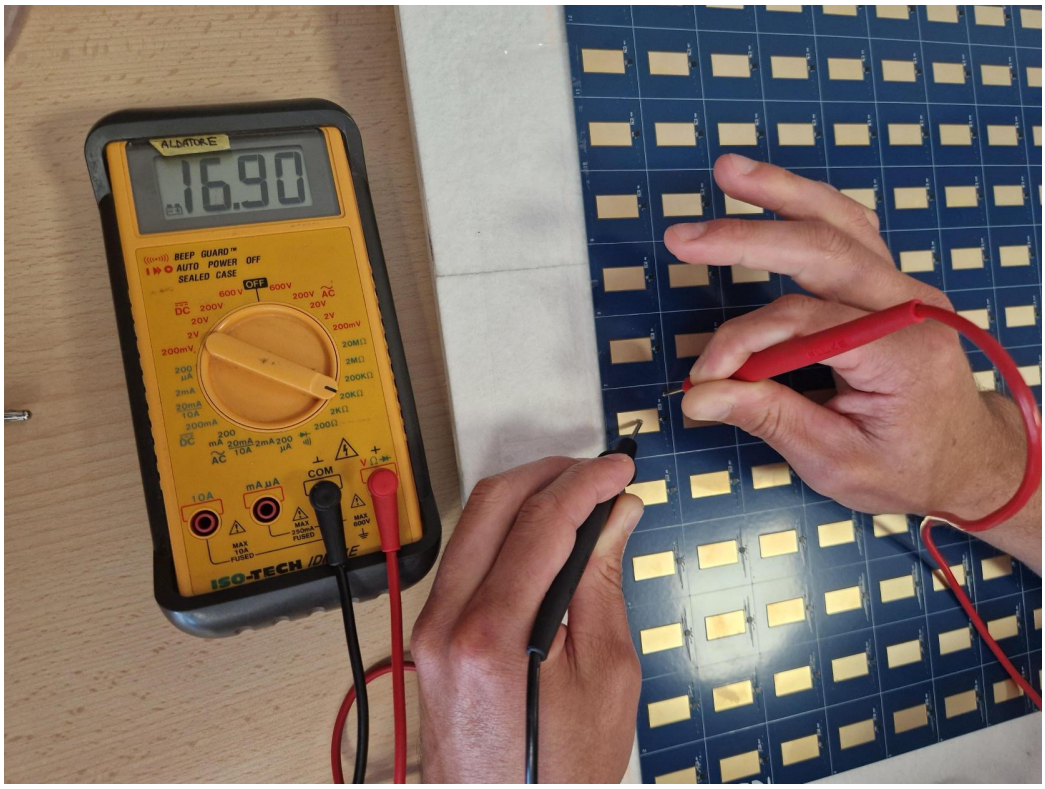

Figure 3.25: Testing each unit cell of the RIS with a voltmeter to ensure that the correct configuration is sent to each cell.

illustrates the testing process. We found that when a specific value is programmed, the corresponding delay line is properly activated. Therefore, it appears that the issue is likely related to the antenna design rather than its programming.

One potential problem identified is related to the so-called ground plane or structural scattering, which was also present in the previous prototype. We contacted the manufacturers, but unfortunately, they were unable to provide any additional information beyond what was previously noted.

3.2 Backscatter THz measurements

In the vision of 6G networks, a transformative shift is anticipated, where handheld devices will seamlessly integrate sensing capabilities, enabling them to perceive and interact with their surrounding 3D environments. This evolution will be significantly empowered by the ability to operate in the THz frequency band. The THz band offers vast bandwidth, facilitating high spatial resolution, and the support for large antenna arrays will enable unmatched angular precision [102].

Building on this foundation, mobile devices are expected to become powerful tools for environmental sensing and monitoring. Their pervasive presence, coupled with the integration of advanced sensors, positions them at the forefront of revolutionizing indoor navigation and environmental awareness. Within the 6G framework, these devices will autonomously generate detailed digital maps of indoor spaces, accurately track their position within these maps, and do so without the need for specialized positioning infrastructure [103]. Motivated by this vision, this chapter explores a comprehensive description of the measurement campaigns carried out at THz frequencies, along with the processing techniques employed for radio-SLAM (R-SLAM) applications. The real-world data were collected at CEA-Leti (France) laboratory, within the European PRIMELOC project collaboration [104], and served as input for the R-SLAM algorithms, that are presented in Sec. 4.3.

To emulate the radar operation, the measurement setup, shown in Fig. 3.26, was based on a four-ports VNA together with converters in order to cover the $[235 - 320]$ GHz band. We employed two linearly polarized horn antennas with gain $G_{\mathrm{TX}} = G_{\mathrm{RX}} = 20\,\mathrm{dBi}$ and Half Power Beam Width (HPBW) of 18°. The backscatter channel acquisition was operated in a quasi-monostatic configuration, as the TX and RX were co-located on a linear - angular positioner, which allowed mechanical steering and displacement over a 2-meter-long X-axis. Acquisitions were managed by an external computer, which was connected to both the VNA and the positioner controller using Ethernet cables. Two measurement campaigns were carried out at CEA-Leti's laboratory room (shown in Fig. 3.27) with a size of $10.2 \times 8.6\ \mathrm{m}^2$. In the first measurement campaign, the radar scanned the laboratory in nine positions

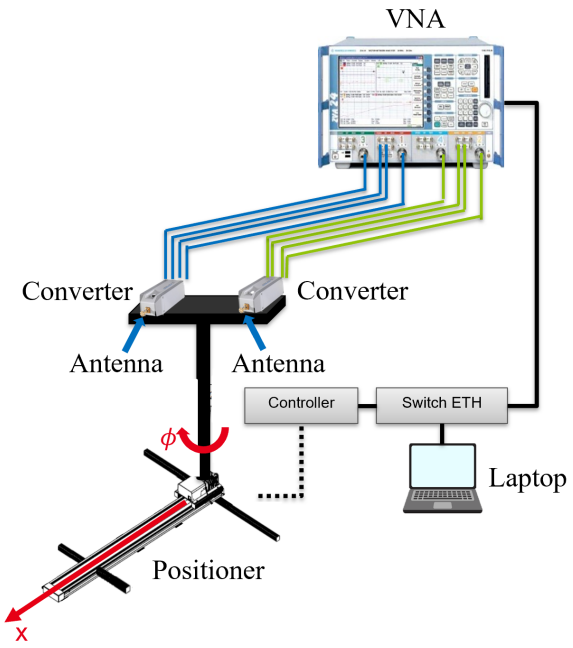

Figure 3.26: Measurement setup scheme.

along a 2-meter straight path with an X-axis step of 0.25 m. This measurement was repeated twice, first with the radar pointed towards the direction of movement (Scenario A), then with the radar pointed perpendicular to the direction of movement (Scenario B). In the second measurement campaign (Scenario C), the radar scanned the environment in 46 positions along an oval path, characterized by diameters of 5 m and 3 m. In the straight segments, the X-axis step size was set at 0.40 m, while in the curved sections, the step sizes varied between 0.23 to 0.27 m to maintain the correlation between the channel responses in adjacent positions. At each radar location, the positioner rotated the antennas with increments of 10° within the steering range of $[-90°, 90°]$. To make it easy to read, the pictures of the three scenarios are reported together with the R-SLAM performance in Sec. 4.3.1. Specifically, the locations where the radar measurements were taken, denoted *positions* in the following, are shown in Figs. 4.43 (top), 4.44 (top) and 4.45 (top), where they appear as red dots. The setup described above emulated a stepped-frequency continuous-waves (SFCWs) radar, with measurements spanning from 235 to 320 GHz and a step size of 10 MHz for each position

(a) (b)

Figure 3.27: Pictures of the environment.

and steering direction. These measurements yielded the channel frequency responses (CFRs), which were further processed to reduce sidelobe ringing by applying frequency domain filtering. To compute the CIRs, an inverse FFT was performed with a time resolution of $T_s = 1.56$ ps. For R-SLAM purposes, the CIRs were computed for 181 steering angles ϕ_n at each position using an interpolation process with a step size of 1° within the $[-90^\circ, 90^\circ]$ range, and then collected to form the Angle-Delay matrix $\mathbf{H}$. Figure 3.28(a) presents an illustrative example of CIRs collected by the radar at position #15 of Scenario C, for 19 steering angles within the range $[-90^\circ, 90^\circ]$ and angular step of 10°. These CIRs, which have been normalized by removing the effect of the TX and RX antenna gains, provide valuable insights into the backscatter characteristics of the surrounding environment and, ultimately, its map. For example, still focusing on the measurements collected at position #15 of Scenario C (see Fig. 3.28(a)), we were able to derive a preliminary (albeit approximate and incomplete) map of the environment by combining the PDPs associated with the CIRs collected from all steering directions [105]. This resulted in the creation of the power angular delay profile (PADP) at the considered position, which allowed an estimate of the map to be derived immediately. In this regard, a visual comparison between the PADP obtained at position #15 and the actual locations of the walls is shown in Fig. 3.28(b). Each point corresponds to a detected path, characterized by a specific delay

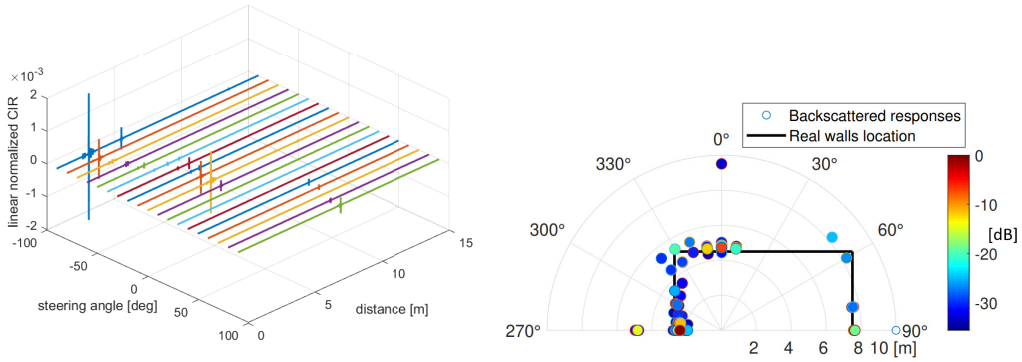

(a) (b)

Figure 3.28: Normalized channel impulse responses (CIRs) for all steering angles at position #15 of Campaign C (a), with delays mapped into distances; polar representation of the normalized power angular delay profile (PADP) at position #15 of Scenario C compared to the actual map of the environment (b).

and arrival angle, with the color indicating the power normalized relative to the highest path power. Notably, the radar echoes detected are consistent with the expected echoes from the primary scatterers in the environment, namely the walls. Interestingly, a part of the horizontal wall depicted in Fig. 3.28(b) shows a lack of backscatter response. It is noted, in this regard, that the wall is made of plasterboard, which has poor reflective properties. Additionally, the undetected part of the wall lacks any objects positioned in front of it that could have triggered radar reflections. It is essential to emphasize, however, that the map depicted in Fig. 3.28(b) was obtained solely from the measurements provided by the radar at position #15. In contrast, the methodology proposed in this paper derives the map by considering measurements collected throughout the entire radar path, resulting in significantly improved outcomes. In fact, the numerical results reported in Sec. 4.3.1 will show that the entire wall is successfully mapped, thanks to the measurement taken when the radar gets closer to it.

In order to characterize the backscatter channel, it is of interest to investigate the root mean square (RMS) delay and the angular spread of the paths detected after the ghost-effect mitigation (GEM) algorithm[1]. Specifically, for

[1]The characterization of the backscatter channel was performed without using the

each position within a given scenario (A, B, or C) and considering all the paths collected in the PADP, which accounts for all steering directions, the RMS delay spread is defined as:

$$\tau_{\text{rms}} = \sqrt{\frac{\sum_{k=1}^{K}(\tau_k - \tau_m)^2\alpha_k^2}{\sum_{k=1}^{K}\alpha_k^2}} \tag{3.1}$$

where τ_m is the mean arrival delay defined as

$$\tau_m = \frac{\sum_{k=1}^{K}\tau_k\alpha_k^2}{\sum_{k=1}^{K}\alpha_k^2} \tag{3.2}$$

and K, α_k^2, τ_k are the number of detected paths, the power, and the arrival delay of the kth path, respectively.

Similarly, the angular spread can be computed at each position of a scenario using Fleury's definition, as in [106]

$$\sigma_\phi = \sqrt{\frac{\sum_{k=1}^{K}|e^{j\phi_k} - \mu_\phi|^2\alpha_k^2}{\sum_{k=1}^{K}\alpha_k^2}} \tag{3.3}$$

where ϕ_k is the arrival angle of the kth path and μ_ϕ is the mean arrival azimuth defined as

$$\mu_\phi = \frac{\sum_{k=1}^{K}e^{j\phi_k}\alpha_k^2}{\sum_{k=1}^{K}\alpha_k^2}. \tag{3.4}$$

Based on the provided definitions, Fig. 3.29 displays the empirical cumulative distribution functions (ECDFs) of the RMS delay spread and angular spread of the paths detected in each scenario after applying the GEM algorithm. Since these metrics are calculated by considering all positions within each of the three scenarios depicted in Fig. 4.43 (top), 4.44 (top), and 4.45 (top), they provide a characterization of their backscattering channels at THz frequencies. A more concise characterization is provided by the average RMS delay spreads, 8.79 ns, 5.67 ns, and 10.86 ns, and the average angular spreads, 61.5°, 76.4°, and 52.6°, for scenarios A, B, and C, respectively.

noise-masking (NM) algorithm to avoid the elimination of weak paths, which could potentially be present.

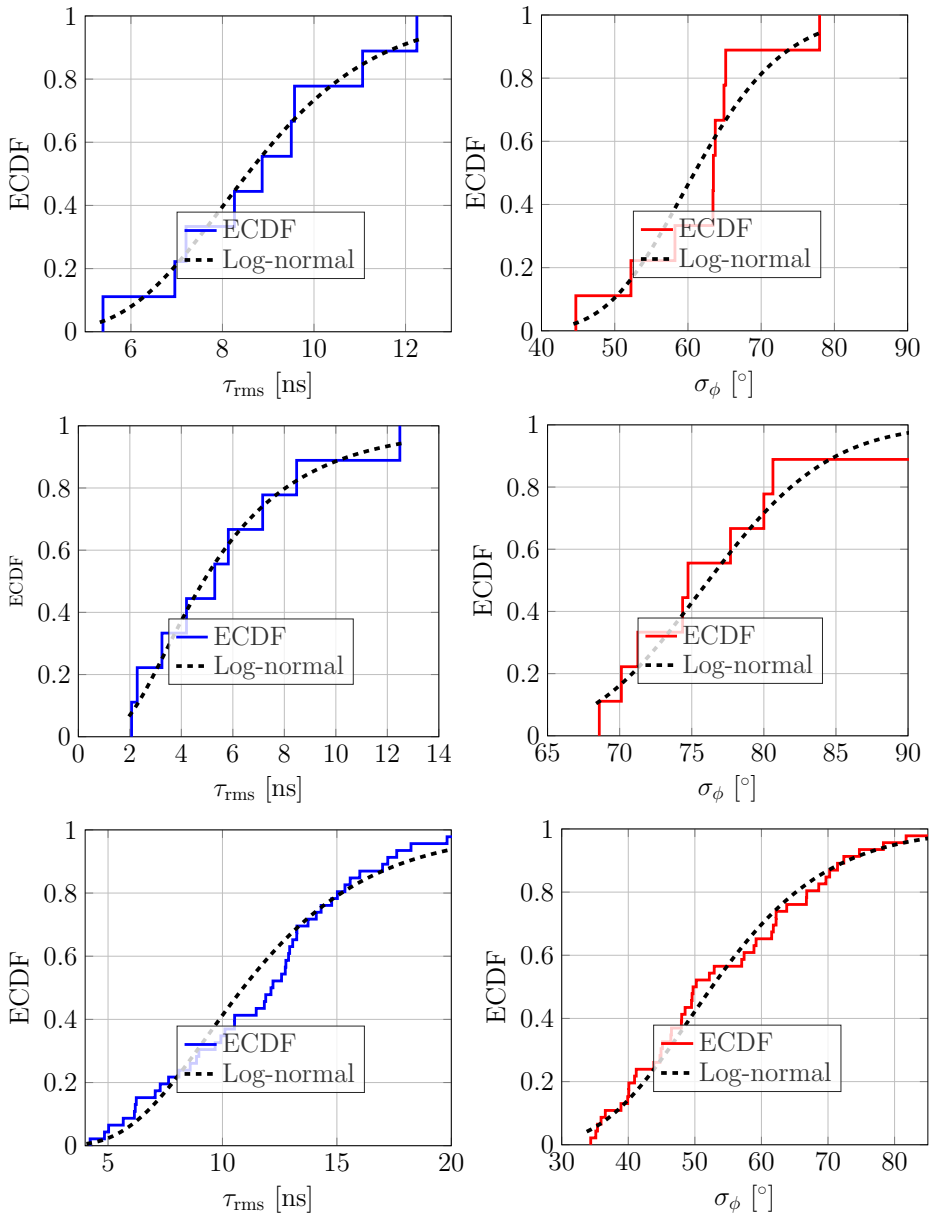

Figure 3.29: Empirical CDFs of the delay spread and angular spread for all the positions of Campaign A (top), Campaign B (middle), and Campaign C (bottom).

The results highlight substantial variations in delays and angular spreads, which are highly dependent on the radar position and steering angle. Interestingly, these variations can be effectively characterized using a log-normal

distribution. Notably, the maximum delay spread is twice the one measured in the classical one-way channel in a similar environment [107], which is in line with the double convolution of the back-scattering channel impulse response.

Finally, it can be noted that the measurement data here discussed are the same used for R-SLAM purposes, which will be the subject of the Sec. 4.3.1. For the reader's convenience, the settings and parameter values adopted during the measurement campaigns are summarized in Table 3.2.

It is important to point out that when operating within the THz frequency range, it could be the case that signal blockage, which becomes increasingly significant at higher frequencies, may impede the detection of objects located further away and potentially obscured by closer ones [108]. In principle, this is a critical issue in the context of environment mapping, as it can result in incomplete representations of the environment. The simplest solution to this problem is to observe the environment from multiple locations and derive the map by leveraging all available measurements, as provided by our methodology. Conversely, the existence of many reflective objects within the sensed area is beneficial for the localization procedure, as it provides the localization algorithm with multiple landmarks that can be utilized to determine the radar's position. This, in turn, enhances the accuracy of mapping, which relies heavily on precise knowledge of the radar's location.

Table 3.2: Measurement campaign: parameters and settings

Description	**Parameter**	**Value**
Measurement setup		
Frequency sweep range	–	235-320 GHz
Frequency sweep step	–	10 MHz
Number of CIR samples	M	8501
Angular range	–	$[-90°, 90°]$
Angular steering step	–	$1°$
Number of steering angles	N	181
Transmit antenna gain	G_{TX}	20 dBi
Receive antenna gain	G_{RX}	20 dBi
Half Power Beam Width	HPBW	$18°$
Detection threshold	–	-100 dB
Delay resolution	T_{s}	1.56 ps
Measurement data processing		
NM algorithm threshold	η_{CF}	10^{-2}
GEM algorithm threshold	η_{CL}	0.4
Scan vector threshold	η_{SV}	0.9
Kalman filter parameters		
Power Spectral Density (PSD) of the linear acceleration noise	w_0	10^{-4}
PSD of the angular acceleration noise	w_θ	10^{-4}
Time step	T_{F}	1 s
Position estimation error std	$\sigma_x = \sigma_y$	$4.7 \cdot 10^{-3}$ m
Angle estimation error std	σ_θ	$1.7 \cdot 10^{-3}$ rad

3.3 Localization measurements using UWB devices

As previously outlined, this thesis aims to investigate communication and localization systems for use in SRE applications. This involves leveraging both cutting-edge technologies, such as those discussed in earlier chapters, and established technologies which are already present in current communication generations. Given that 6G is expected to operate at higher frequencies, it is also pertinent to explore UWB applications, as detailed in this section.

In 2002, the United States Federal Communications Commission (FCC)

defined UWB signals as any signal with a fractional bandwidth (i.e., the absolute bandwidth divided by the center frequency) greater than 20% or a bandwidth of at least 500 MHz, regardless of how it is generated [109]. This definition has been widely adopted by various countries, recognizing the innovative potential of UWB technology. UWB systems offer several key advantages, as they are highly resistant to jamming due to their low power spectral density and compatibility with spread spectrum and Code Division Multiple Access (CDMA) modulation techniques, making UWB signals difficult to detect and interfere with. Additionally, UWB signals exhibit robustness in multipath environments, as the short-duration signals reduce the likelihood of multipath interference. This characteristic makes UWB particularly suitable for indoor localization where high object density challenges other technologies [110].

Localization involves using sensor nodes, or *anchors*, positioned at known locations to determine the position of target nodes, or *tags*. A minimum of four anchors is required for three-dimensional localization. This process often relies on Bayesian filtering techniques [111], which degenerate in the Kalman filters [112] with process noise and measurement noise at statistically zero mean value, or particle filters [113], to improve accuracy by utilizing previous estimates. The localization process can either use single position measurements or leverage previous estimates to predict future positions, enhancing accuracy. The state of the system, including position and velocity, is represented as x_n at discrete time intervals n. The Bayesian filtering approach simplifies the problem by assuming Markov properties, making it computationally feasible to estimate the target's position.

While particle filters offer accuracy in non-linear and non-Gaussian models, they can be computationally intensive. The complexity of updating weights is typically $O(N_p)$, but some formulations, like the resampling at each iteration to increase the low number of samples, can lead to exponential complexity increases with higher N_p.

In indoor environments, the three classical approaches to localization are [114]: Angle of Arrival (AoA) or Direction of Arrival (DoA), Receive Signal Strength (RSS) and Time-Based Methods.

Additionally, hybrid solutions can be employed. In all cases, the main

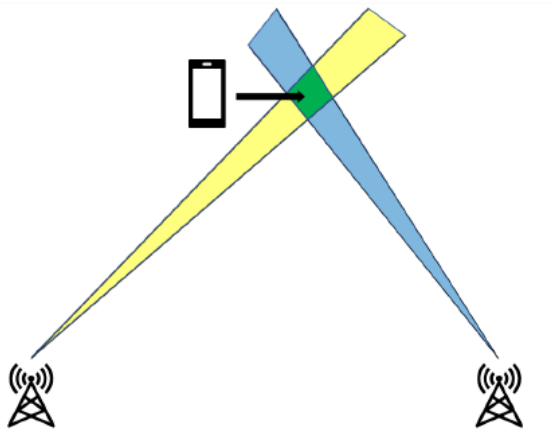

Figure 3.30: Angle of Arrival localization principle.

limitations are due to measurement errors of parameters such as information related to antennas (band, gain, directivity, etc.) and the correct location of anchor nodes and noise. Also, the propagation effects such as multipath, interference, and Line of Sight (LOS) or NLOS conditions limit the performance; in general, geometric effects are summarized in the concept of Geometric Dilution of Precision (GDOP).

For the angle/direction of arrival estimation, the technique employs array antennas. By leveraging the radiation patterns of these antennas, or more precisely, the ability to steer the pattern by manipulating delays and the amplitude of signals to individual elements of the array, it is possible to triangulate the target position with at least two arrays. The principle involves scanning the area with the arrays, and by knowing the direction in which a good signal is obtained and the angles relative to a common reference system, the target's position can be determined, as shown in Fig. 3.30. The accuracy of the system is directly related to the directivity of the antenna, the beamwidth of the main lobe, and the target's distance. Super-resolution algorithms like MUSIC and ESPRIT have been developed to partially compensate for these limitations. Choosing the radiating element for the array impacts the system's performance: the more elements there are, the narrower the beamwidth but the larger the device. Higher frequencies allow for a reduction in the geometric size of the antennas for the same directivity.

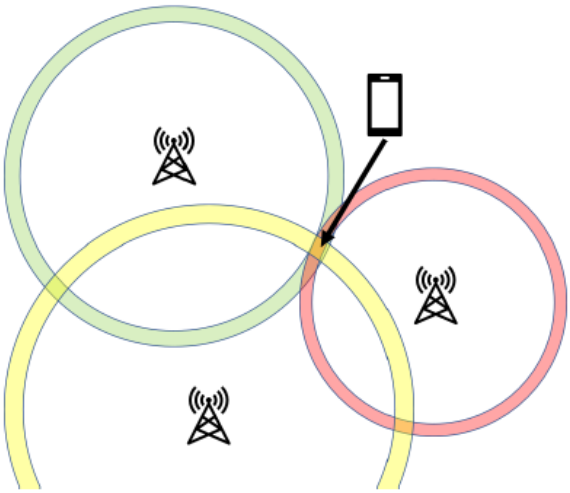

Figure 3.31: Angle of Arrival localization principle, with RSS, TOA and TWR techniques.

This technique works well in LOS conditions, but the quality degrades significantly in NLOS conditions as the antennas report incorrect angles. Another fundamental limitation is the presence of secondary lobes, which in environments with strong multipath can cause precision degradation and inaccurate estimates.

RSS-based techniques estimate the distance between the transmitter and receiver based on the received signal power. The principle relies on the path loss model, which describes how the signal power decreases as the distance increases. However, this method is highly sensitive to environmental conditions, such as obstacles and multipath, making it less reliable in complex indoor environments, the principle is shown in Fig. 3.31. Time-based methods include techniques such as Time of Arrival (TOA), Time-difference of Arrival (TDOA), and Two-way Ranging (TWR). These methods calculate the distance by measuring the time it takes for a signal to travel from the transmitter to the receiver. They are more robust to environmental variations compared to RSS-based methods. In particular, TDOA and TWR are preferred for their higher accuracy in UWB systems, as they leverage precise time measurements to determine the distance. TOA measures the absolute time a signal takes to propagate from the transmitter to the receiver. This requires precise synchronization between the two devices, which can be

challenging to achieve in practice. TDOA measures the difference in arrival times of the same signal at multiple receivers. This technique eliminates the need for synchronization between the transmitter and receivers, making it more practical for real-world applications. TWR involves a round-trip time measurement, where a signal is sent from the transmitter to the receiver and back. This method does not require synchronization and can provide accurate distance measurements by accounting for the round-trip delay.

In order to establish theoretical limits, the Cramer Rao Lower Bound (CRLB) must be defined since it represents a theoretical lower limit on the mean square error of an unbiased estimator. To achieve this, start by defining a vector $\boldsymbol{\theta}$ containing the unknowns (i.e., the tag position $\vec{p} = [x; y; z]$), and denote by $\vec{T}$ the vector of useful measurements. Let $J(\boldsymbol{\theta})$ represent the Fisher information matrix, a function of $\boldsymbol{\theta}$. Then, the CRLB can be expressed as [115]:

$$\text{CRLB}(\boldsymbol{\theta}) = J^{-1}(\boldsymbol{\theta}) = \mathbb{E}\left[\nabla_{\boldsymbol{\theta}}^{T} \ln P(\vec{T}|\boldsymbol{\theta}) \nabla_{\boldsymbol{\theta}} \ln P(\vec{T}|\boldsymbol{\theta})\right]^{-1} \tag{3.5}$$

which in matrix form becomes:

$$\text{CRLB}(\boldsymbol{\theta}) = \begin{bmatrix} \sigma_{xx}^2 & \sigma_{xy}^2 & \sigma_{xz}^2 \\ \sigma_{yx}^2 & \sigma_{yy}^2 & \sigma_{yz}^2 \\ \sigma_{zx}^2 & \sigma_{zy}^2 & \sigma_{zz}^2 \end{bmatrix}$$

where σ_{ii}^2 represents the variance of estimation errors in coordinates $i = (x, y, z)$, and the other elements represent the cross-correlation, indicating how they influence each other. The term Position error bound (PEB) is defined as the square root of the trace of matrix CRLB($\boldsymbol{\theta}$):

$$\text{PEB} = \sqrt{\sigma_{xx}^2 + \sigma_{yy}^2 + \sigma_{zz}^2}$$

Assuming the standard deviation of all measurements is σ, the relationship

$$\text{GDOP} = \frac{\text{PEB}}{\sigma}$$

holds, where GDOP refers to *Geometric Dilution of Precision*, a multiplica-

tive factor related to the geometry of the problem, specifically the positions of anchors and tags. In the following the GDOP is divided into two terms:

- *Vertical Dilution of Precision* (VDOP), related to the distance of the anchor plane from the tag plane (usually the z-axis), measured as VDOP = $\sqrt{\sigma_{zz}^2}$;
- *Horizontal Dilution of Precision* (HDOP), referring to misalignment error on the xy-plane, measured as HDOP = $\sqrt{\sigma_{xx}^2 + \sigma_{yy}^2}$.

3.3.1 Measurement campaign

The ultra-wideband localization system Sequitur, used in measurement campaigns, consists of proprietary hardware and software components. It was developed by Prof. Dardari's group at the University of Bologna in 2014 and is now commercialized by a company in the wireless systems sector. It was designed for indoor environments and logistics applications. For this purpose, the antenna was designed with an omnidirectional pattern to cover a larger area [116]. However, for the purpose of this thesis and for the proposed accuracy, this pattern is not optimal because it is affected by multipath reflections that degrade localization performance, as will be clarified later. Anchors and tags are active components capable of operating in both TDOA and TWR modes. For experimental tests, the TWR mode was chosen because it theoretically offers better performance.

At the hardware level, Sequitur allows the use of two different elements as tags: one called the tag and the other the minitag. While the former can operate in both modes, the latter supports only TDOA. Hence, there is a need to use tags, which are bulkier than minitags but the only ones capable of operating in TWR mode, shown in Fig. 3.32(b). Furthermore, this technique is decentralized, meaning the tag queries the anchors, obtains distance estimates, processes firmware with the localization algorithm, and therefore, the information is derived by the tag itself. In this mode, anchors only respond to tag queries.

The system allows setting up a zone where the algorithm can operate, called the localization area, by defining spatial boundaries. An important

(a) (b)

Figure 3.32: Photo of the positioning of the nodes still in a known position (a), close-up photo of the anchor/tag used(b).

consideration is to define this area using the plane of the anchors themselves as the boundary, as shown in Fig. 3.33, because there is a risk that the estimated point may be calculated not in its actual position but in a specular position relative to the anchor plane due to its geometry.

The measurement campaign reported aims to study an experimental analysis of an automatic docking system for the retrieval of large objects in harsh environments. Due to confidentiality agreements with the commissioning company, further details about the application cannot be disclosed. The main challenge lies in accurately localizing a tag placed outside the area bounded by the anchor nodes, where a high GDOP is encountered. The four anchors necessary for 3D localization were placed at the vertices of a square, with sides fixed at 0.5 and 1 meter to investigate the effect of two different distances. The power supply for the anchors is provided via micro USB port from a USB hub, which is then connected to the wall power outlet. The tag (to be located), on the other hand, is powered by a power bank. Communication between nodes and the PC occurs via an access point, a picture of the anchor setup is shown in Fig. 3.32. The SEQUITUR-Pi features a radio interface, which implements the IEEE 802.11.4a UWB standard. It offers four selectable frequency bands ranging from 3.5 GHz to 6.5 GHz, with adjustable data rates of 110 kbps, 850 kbps, and 6.8 Mbps. The device is fully compliant with FCC and ETSI UWB spectral mask regulations and provides

a ranging accuracy of up to 7 cm. Under favorable propagation conditions, it supports a transmission range of up to 200 meters at a data rate of 110 kbps.

First of all, the *mobility model* provided by the platform is studied to understand which one best fits the needs of the project. The mobility model in a localization system describes how devices or targets move within the area of interest. This model is essential for understanding and predicting the behavior of target nodes and for improving the effectiveness and accuracy of the localization system. In particular, the effect of two different models has been studied: the first uses a particle filter to predict the area where the tag is most likely to be found in the next moment and thus iteratively concentrates particles in this area. The second model, on the other hand, bases localization solely on the current measurement but still refers to particles distributed uniformly in the environment, without any information on the tag's dynamic model or memory of past estimates. What was observed during the "calibration" measurement campaign is that setting a too-large localization area with the first model does not pose problems, due to the properties of the particle filter, while with the second model, the estimated point tends to be very inaccurate and unstable. This is because the points, being limited in number (at most 6000), need to cover a too-large area, thus being present only in a few units per cubic meter, which is insufficient to intercept the likelihood function. Setting a localization area too small causes edge effects, making the position estimate too constrained and thus compromised. In Fig. 3.33, two tests performed with the two mobility models are shown, for anchors spaced one meter apart, with 6000 particles and a localization area large enough to avoid edge effects, i.e., $8m \times 6m \times 8m$ centered on the actual position of the tag. This means that there were, on average, 15 particles/m^3. The system allows devices to be provided with a calibration offset related to the distance between the tag and the anchor, aimed at compensating for any distance estimation offsets of the involved devices. This offset can be inserted using two parameters, defined for each node, $\mathrm{TX_{offset}}$ and $\mathrm{RX_{offset}}$. As was already evident from Fig. 3.33, the distance of the tag is underestimated. A detailed analysis was performed using the Sequitur software debugging tool. With this tool, it was possible to make the system

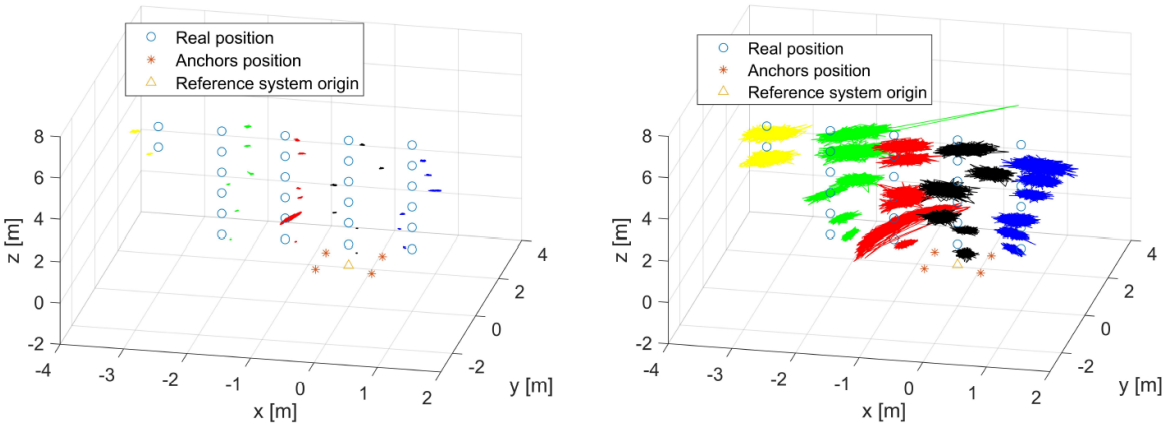

(a) (b)

Figure 3.33: Position measurements, comparison of mobility model 1 (a) and 3 (b), 6000 particles in a volume of 384 m^3. The blue circles represent the locations' real values assumed by the tag, the red asterisks the position of the anchors and the triangle the center of the reference system is yellow. The located points are divided by color in relation to the axis to which they refer.

measure the distance between two nodes at a time, particularly between the tag and the anchors, and then assign the offset to the latter, rather than to the tag. To do this, the offset must be set on the parameters TXoffset and RXoffset according to the following formulas:

$$\mathrm{TX}_{\mathrm{offset}} = 0.44 \cdot 2 \cdot (\text{real distance} - \text{measured distance}) \tag{3.6}$$

$$\mathrm{RX}_{\mathrm{offset}} = 0.56 \cdot 2 \cdot (\text{real distance} - \text{measured distance}) \tag{3.7}$$

where the coefficients 0.44 and 0.56 serve to divide the offset percentages as recommended by the documentation [117], and the coefficient 2 accounts for the fact that the TWR measurements, on which the distance calculations are based, refer to a double path, i.e., the signal's round trip, thus requiring doubling the difference between real and measured distance. Additionally, these measurements provide parameters such as Received Signal Strength Indicator (RSSI), like *accuracy*, which is a measure of the accuracy of the measurements, and like *quality*, which is a ratio between useful signal and noise, and transmission success rate. To understand whether it was possible to obtain more precise measurements by dynamically adjusting the

offset, the relationships between the offset, RSSI, and distance were observed. Measurements were collected for multiple anchors, both before and during the measurement campaigns described later. What was noticed is that it is not possible to identify an empirical law that predictably models the dependency of the offset on the easily measurable RSSI. For a fixed RSSI value, the offset tends to be very variable, even by tens of centimeters. Therefore, dynamic calibration does not seem to be a realistic hypothesis. However, it is noted that an offset is generally necessary, and in particular, these measurements confirm that the distance is underestimated. Calibration tends to improve accuracy around the point where it occurred but worsens it as one moves away from the calibration point, as confirmed in the measurement campaigns. Therefore, a possible approach could be to calibrate the anchors in the area of interest, accepting poorer localization results as one approaches the tag.

Since I cannot include photos of the setup, a drawing of it is shown in Fig. 3.34. First, the anchors were mounted on a wooden frame as shown in Fig. 3.32 (a), at the vertices of a square with a side length of 50 cm. In this case, five tags were mounted, spaced 30 cm apart from each other, and arranged on a beam aligned with the plane of the anchors, as depicted in Fig. 3.34 (b). Only one tag at a time was kept active to avoid interference. The tag positioned on the central axis of the anchors is subsequently referred to as T_1, with the numbering continuing in increasing order as the distance from the zero increases. The beam could be fixed at distances of 40, 70, 100, and 120 cm from the plane of the anchors. The parameters used in the Sequitur software are reported in Tab. 3.3.

Firstly, the calibration was performed on target T1 at a distance of one meter, then the control measurements were collected, i.e., the position data outside the tank, necessary to compare them with those acquired in the presence of water and to conclude the extent of the additional error. After completing the measurements outside the tank, the measurements inside the tank were carried out. These involved positioning the tags as close as possible to the water level (Fig. 3.35(b)), so the anchors tended to move closer to the tank edge, made of metal. This caused, as can be seen from Figs. 3.36 - 3.37 (red and green lines for outside and inside the tank respectively), an increase

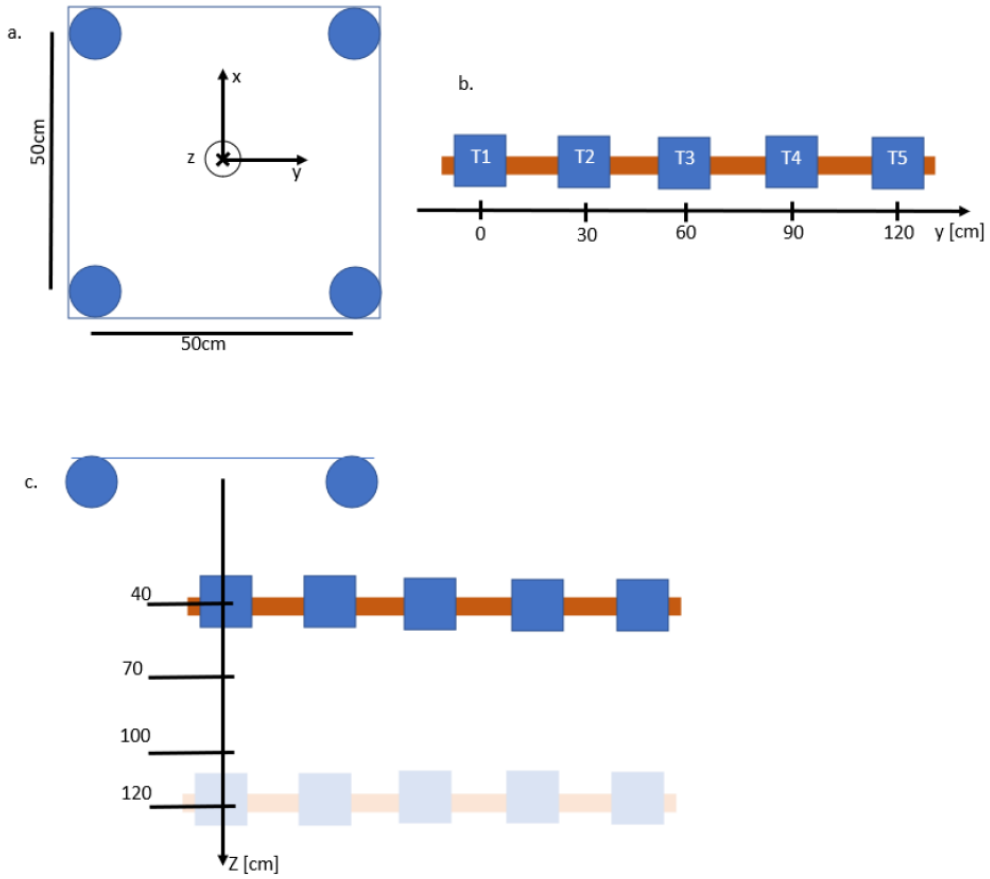

Figure 3.34: Detail of the positioning of the anchors (a) and tags (b). Point grid where to position the tag used in the third measurement campaign (c).

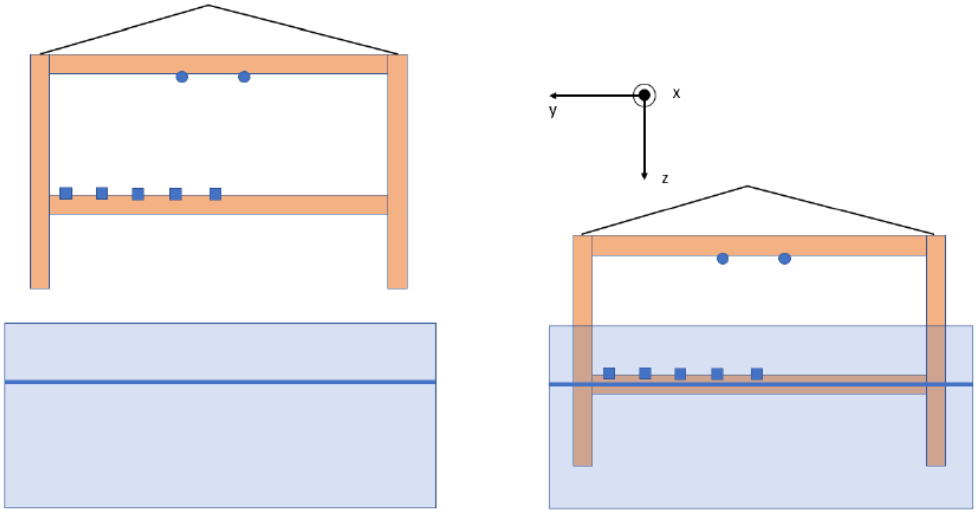

Figure 3.35: Frame positioning for dynamic measurements in the tank. Position outside the tank (a) and position of closest approach to the water (b). Blue circles and squares indicate the anchors and tags respectively, and the blue line indicates the water level.

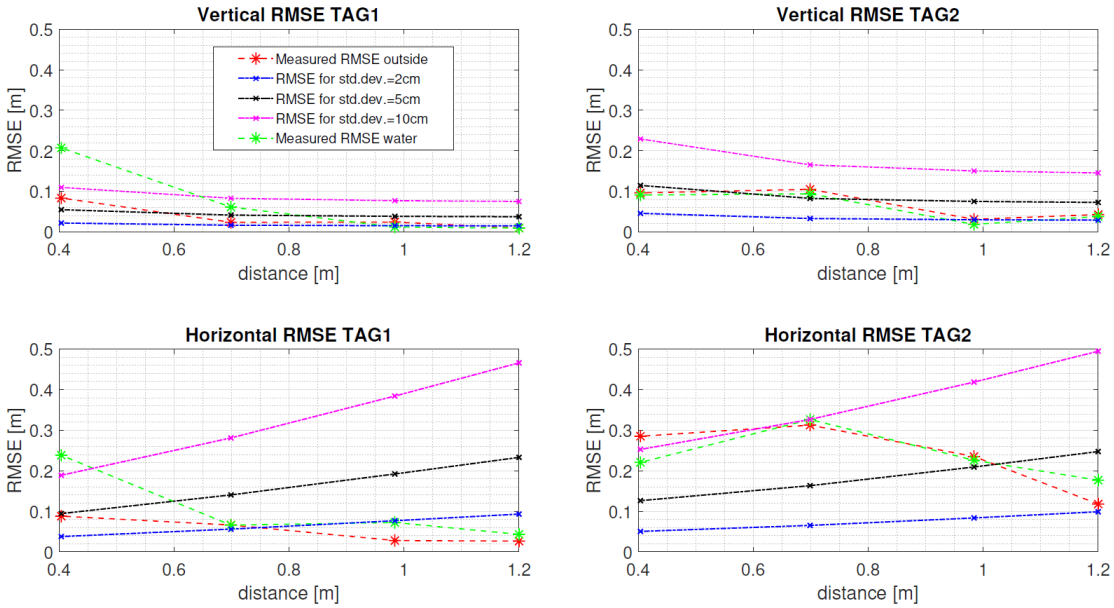

Figure 3.36: Vertical RMSE and Horizontal RMSE for Tag 1 (centered axis) and Tag 2 (axis offset by ($\Delta_y = 0.3$)m). Calibration was performed on Tag 1 at a distance of one meter.

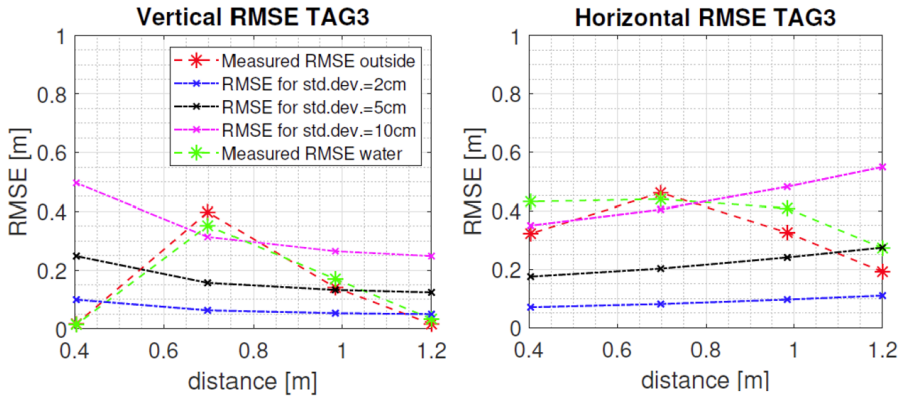

(a)

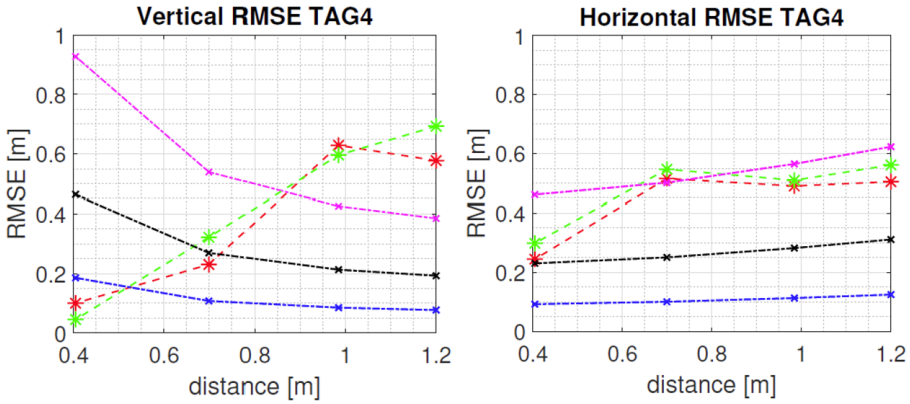

(b)

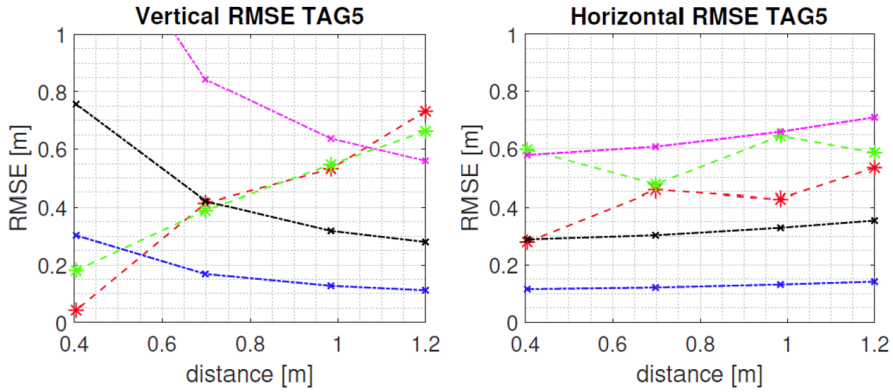

(c)

Figure 3.37: Vertical RMSE and Horizontal RMSE for (a) Tag 3 (axis offset by $\Delta y = 0.6$m), (b) Tag 4 (axis offset by $\Delta y = 1$m), (c) and Tag 5 (axis offset by $\Delta y = 1.20$m). Calibration was performed on Tag 1 at a distance of one meter.

Parameter	Value
Location particles	6000
Maximum anchor	4
Minimum anchors	4
Mobility model	1
Mobility std (x)	0.5 m/s
Mobility std (y)	0.5 m/s
Mobility std (z)	0.5 m/s
TOA estimation std	0.3
Calibration	1 m on central axis
Radio TX offset	44% of total offset
Radio RX offset	56% of total offset
Anchor distance	0.5 m
Number of anchors	4
Anchor orientation	Optimal
Power	Standard
Channel	5
Location	Outside tank vs Inside tank

Table 3.3: Parameters and Values UWB campaign.

in error for short distances. In general, however, the discrepancy between the RMSE calculated on the measurements outside and inside the tank is low, so the presence of fresh water does not seem to contribute significantly to the position estimation. The blue, black, and pink lines represent the theoretical RMSE with a standard deviation of 2 cm, 5 cm, and 10 cm, respectively. Referring to Tag 1 and Tag 2 of Fig. 3.36, it can be seen that the localization process results in vertical root-mean-square error (RMSE) errors in line with the theory, unlike when moving too far from the center of the anchor plane (Tag 3, Tag 4, and Tag 5 in Fig. 3.37), proving the limits of the calibration performed at one point. Referring instead to the error on the horizontal plane, it is generally greater than that obtained in the second test, usually residing beyond the curve of the ideal case with a standard deviation of 5 cm (black curve), except for the central axis. During this measurement campaign, dynamic measurements were also attempted, i.e., with the frame in motion but still at a fixed anchor-tag distance. This type of data was acquired both inside and outside the tank but with different

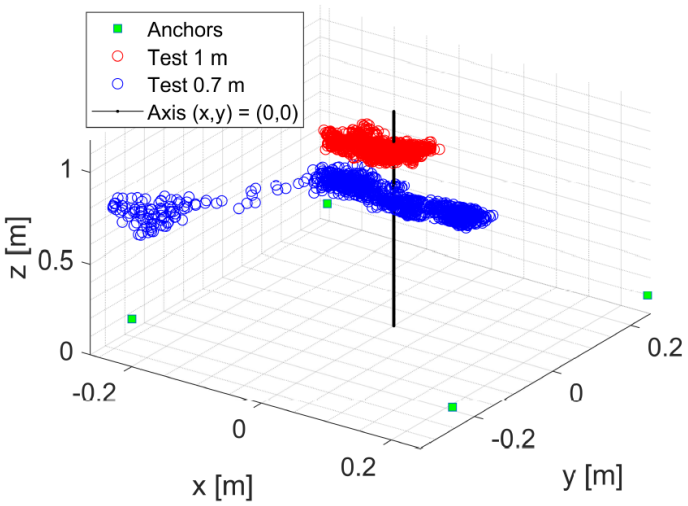

Figure 3.38: Dynamic test in the tank. Red and blue circles indicate the cases at a distance of 1m and 0.7m respectively, green squares indicate the anchors and the black line indicates the axis $(x, y) = (0, 0)$m. Ideally, we should have observed two points at positions $(x, y, z) = (0, 0, 1)$m and $(0, 0, 0.7)$m.

operational modes, involving only Tag 1. In the tank, the measurements were collected with the tag placed at one meter and 0.7 meters distance. The frame was raised and lowered for two cycles inside the tank using a remote-controlled overhead crane until the tags were at water level as shown in Fig. 3.35. Ideally, one expects to observe two fixed points in coordinates $(x, y, z) = (0, 0, 1)m$ and $(0, 0, 0.7)m$. The measurement result is shown in Fig. 3.38.

As the anchors were attached to the tag, they were moved closer to the tank edge, causing errors due to reflection phenomena, particularly, as shown in Fig. 3.39(b), around 40 and 100 seconds, i.e., when the tag was closest to the water and, therefore, with the anchors near the tank edge. While at one meter the error remains below 10 cm, the phenomenon is much more evident at 0.7 m, with a displacement reaching 35 cm in the y-coordinate alone. However, this behavior occurs only once every two times with particularly marked intensity. Subsequently, dynamic measurements were performed outside the tank. In these, the tag was detached from the frame, which was raised and lowered between 60 cm and 380 cm. Identifying the correct tag position to report errors, as well as preventing the frame from oscillating, was very dif-

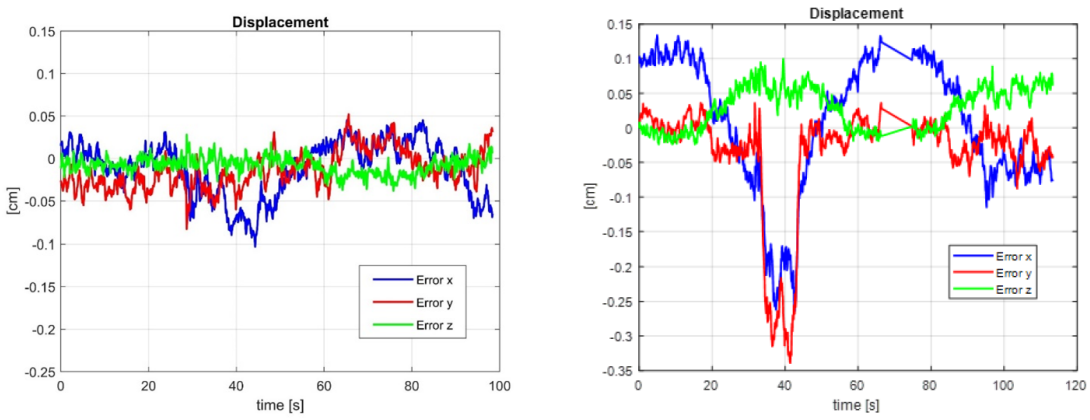

Figure 3.39: Dynamic test in the tank. Errors on the x, y, and z axes for the cases at 1m (a) and 0.7m (b) over time.

ficult, so one should expect unquantifiable systematic errors, not to mention that the oscillations of the plane then made the local reference system of the frame different from the global one. Without being able to measure all these factors instant by instant, the reported error measurements should be considered qualitative to get an idea of how the localization operates rather than precise and well-defined values to characterize the system. Here two cases are reported below: tag centered while keeping the frame as stable as possible and tag centered while trying to oscillate the frame. In Fig. 3.40, the green curve indicates the distance at which the anchor plane was from the tag. One can observe a spike in the error when the tag was at the closest position to the anchor plane, probably due to saturation phenomena, while the increase in error when the frame was at the highest position can be justified by unwanted oscillations or GDOP-related effects.

Error analysis

The work was carried out with anchors placed at the vertices of a square with a side length of 1 meter and, more interestingly, 0.5 meters, due to the possibility of using the system on a mobile support. The set objective was to achieve errors less than 10 cm near the point of greatest interest, i.e., where the target attachment would occur while relaxing the constraint during the

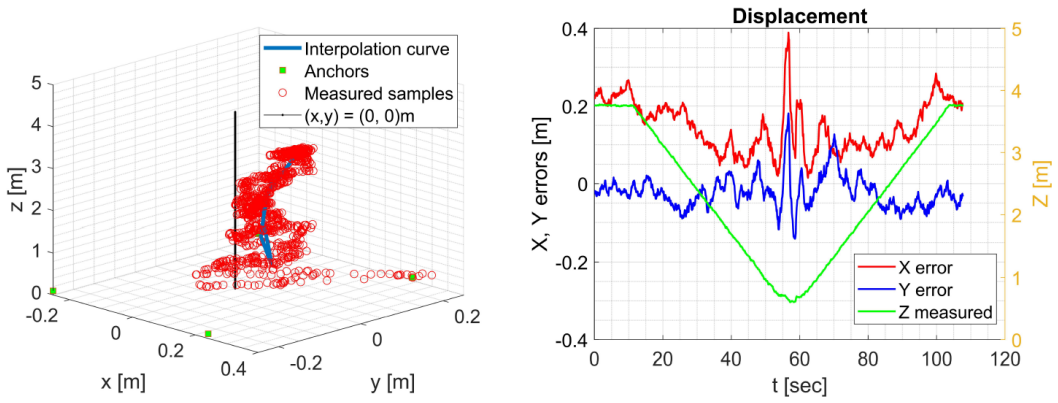

(a) (b)

Figure 3.40: Dynamic test outside the tank on the centered axis, limiting the frame oscillations. Measurement scenario (a) and corresponding errors in x and y (b).

approach phase. The tests conducted with the Sequitur localization system, given a very tight geometry, confirmed the superiority of the TWR mode for localization.

Calibration-related issues emerged from the various measurement campaigns. The ability to calibrate the system brought improvements, especially near the calibration point, but worsened the estimates when moving away from it. Therefore, calibrating the system at the point of maximum interest allowed for achieving the required precision, sacrificing it during the approach phase in accordance with the initial specifications. Assuming an optimal dynamic calibration, referred to as a possible deterministic function, better precision could have been achieved at every point.

Regarding the measurement campaigns, a significant impact on localization performance was observed in the presence of metal near the anchors when they were not properly oriented. To avoid these effects, the use of specially designed directive antennas for the environment and properly oriented can prevent the occurrence of strong reflection phenomena, thus improving localization.

The presence of freshwater does not significantly affect the measurements; however, it could be interesting to observe the effects in the presence of salt water. Although optical systems could yield better results, UWB technology has the ability to work even in low visibility conditions.

Chapter 4

Communication and localization algorithms for SREs

In this chapter, the algorithms developed during the PhD thesis are described, and the produced results are analyzed. Specifically, in Section 4.1, the algorithms for localization applications leveraging frequency-selective surfaces, called metaprisms, are presented. Section 4.1.1 discusses algorithms that utilize OFDM signals to achieve the frequency selectivity required by metaprisms, while Section 4.1.2 covers algorithms developed using FMCW signals for localization. Section 4.2 introduces the algorithms designed for applications leveraging SCMs. In particular: Section 4.2.1 focuses on efficient communication and beam tracking with multiple users equipped with SCMs. Section 4.2.2 explores grant-free channel access for users communicating with an access point. Section 4.2.3 presents high-accuracy localization of users equipped with SCMs, detailing two different architectural approaches. Finally, Section 4.3 describes the algorithms used for Radio-SLAM applications, explaining how the data acquired during measurement campaigns are processed.

4.1 NLOS Localization using metaprism

This section details the localization algorithms in NLOS conditions specifically developed for the use of metaprism, a frequency-selective metasurface described in Sec. 2.2. In particular, it is capable of achieving high levels of accuracy in estimating the position of a target or user in a fully passive manner and without the need for channel state information estimation. In the first subsection, the algorithms used for the 28 GHz and 300 GHz position estimation exploiting an OFDM-based beamsteering design are described, while in the second subsection are presented the algorithms for the 77 GHz localization estimation when the signal impinging on the metaprim is a FMCW chirp.

4.1.1 OFDM-based beamsteering design

In this section, the design of a metaprism is analyzed when the incident signal is an OFDM signal. Specifically, the goal is for each subcarrier of the OFDM signal incident on the metaprism to correspond to a different steering angle of the signal reflected by the metaprism. Then it is introduced a new approach described in [30] to localize user devices located in NLOS areas using a metaprism. By analyzing the spatial filtering of subcarriers in the OFDM signal transmitted by each user device, the base station can estimate the device's angle of view, distance, and subsequently its position.

Referring to Fig. 4.1, it is supposed a certain number of users are located in a region that is in NLOS with respect to the BS located at coordinates $\mathbf{p}_{\mathrm{BS}} = (d_{\mathrm{BS}}, \Theta_{\mathrm{BS}})$, where d_{BS} and Θ_{BS} are, respectively, the distance and the 3D angle of the BS with respect to the center $\mathbf{p}_0 = (0, 0, 0)$ of the metaprism, being $\Theta_{\mathrm{BS}} = (\theta_{\mathrm{BS}}, \phi_{\mathrm{BS}})$, with θ_{BS} and ϕ_{BS} representing the azimuth and elevation angles. No assumptions have been made regarding the BS, which is a single-antenna device. It is assumed that both the BS and the users are in LOS with reference to the metaprism. In the context of user localization, users transmit pilot symbols utilizing an OFDM modulation scheme across K available subcarriers, employing a multiple access protocol to prevent interference between users. It is important to note that this work does not delve into the analysis of various multiple access schemes. Instead, it will

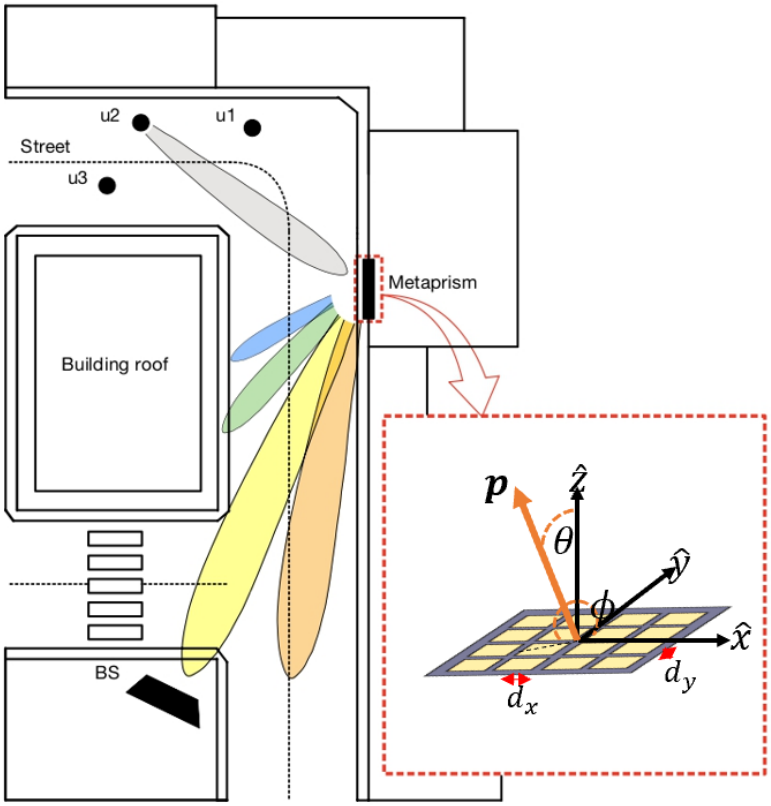

Figure 4.1: Typical scenario in which the signal transmitted by a user is reflected by the metaprism towards the base station. Each subcarrier component is reflected toward a different angle.

be focused on the localization of a single user as the central theme in the subsequent discussion. The user is located at position $\mathbf{p}_{\mathrm{u}} = (d_{\mathrm{u}}, \Theta_{\mathrm{u}})$, where $\Theta_{\mathrm{u}} = (\theta_{\mathrm{u}}, \phi_{\mathrm{u}})$. Denote by f_0 the carrier frequency, λ the corresponding wavelength, and by f_k the k-th subcarrier frequency within the bandwidth W.

It is supposed the metasurface lays in the $x-y$ plane consisting of $N \times M$ cells whose size is $d_x \times d_y$, where $d_x = d_y \approx \lambda/2$. Denote by $\mathbf{p}_{n,m} = \{x_n, y_m, 0\}$, the position of the nm-th cell, where $x_n = n\, d_x - N\, d_x/2$, with $n = 0, 1, \ldots N-1$, and $y_m = m\, d_y - M\, d_y/2$, with $m = 0, 1, \ldots M-1$. Considering the nm-th cell of the metaprism being characterized by the following frequency-selective reflection coefficient [118] as (2.11)

$$r_{nm}(f) = e^{j\Psi_{nm}(f)} \tag{4.1}$$

where $\Psi_{nm}(f)$ is the frequency-dependent reflection phase profile. According to the model in [118], and as reported in Eq. 2.14 - Sec. 2.2, $\Psi_{nm}(f)$ can be designed such that it exhibits a linear behavior with the frequency f, i.e.,

$$\Psi_{nm}(f) = \alpha_{nm} \cdot (f - f_{\mathrm{r}}) \tag{4.2}$$

where α_{nm} is a cell-dependent coefficient. According to (4.2), the frequency-dependent phase profile of the metaprism depends on the design of coefficients α_{nm}. As it will be shown, such a design allows the BS to infer the position of the user starting from the reception of the reflected signal. In the following, there are proposed two design criteria tailored to the operating condition of the system: i) users and BS located in the far-field region of the metaprism; ii) users and BS located in the near-field region.

i) Far-field scenario: Beamsteering design (BD) When both the user and the BS are in the LOS far-field region with respect to the metaprism, it is possible to discriminate only the angle of view of the user but not its distance from the metaprism. This can be done by properly designing the coefficients $\{\alpha_{nm}\}$ of the cells so that subcarrier-dependent beamsteering is obtained. In this way, the angle of the user is directly linked to the subcarriers and it can be estimated from their observations, as it will be explained later. The proposed criterium for designing the coefficients $\{\alpha_{nm}\}$ in (4.2) is

expressed by

$$\alpha_{nm} = a_0\, x_n + b_0\, y_m\,. \tag{4.3}$$

According to this model, in the following referred to as *beamsteering design (BD)*, α_{nm} increases incrementally based on the cell's coordinates, and a_0 and b_0 are two constants that need to be appropriately determined.

It is worth noticing that the user-metaprism subsystem is equivalent to a frequency-selective reflectarray antenna characterized by the following subcarrier-dependent AF

$$\begin{aligned} AF^{(k)}(\Theta) = \sum_{n=0}^{N-1}\sum_{m=0}^{M-1} \exp\Bigg(& j\frac{2\pi\, n\, d_x}{\lambda}\,\left(u_x(\Theta) + u_x(\Theta_{\mathrm{u}})\right) \\ &+ j\frac{2\pi\, m\, d_y}{\lambda}\,\left(u_y(\Theta) + u_y(\Theta_{\mathrm{u}})\right) + \jmath\Psi_{nm}(f_k)\Bigg) \end{aligned} \tag{4.4}$$

where the quantities $u_x(\Theta) = \sin(\theta)\cos(\phi)$ and $u_y(\Theta) = \sin(\theta)\sin(\phi)$ are defined. The array factor for a certain direction Θ indicates the intensity with which the k-th subcarrier of the signal incident on the metaprism generated by the user is reflected in that direction. From (4.2), (4.3) and by equating to zero the total phase shift in (4.4), it is easy to show that the angle of reflection $\Theta^{(k)} = \left(\theta^{(k)}, \phi^{(k)}\right)$ of the k-th subcarrier at frequency f_k of the incident OFDM signal is given by

$$\begin{aligned} u_x\left(\Theta^{(k)}\right) &= -u_x(\Theta_{\mathrm{u}}) - \frac{a_0\lambda}{2\pi}\,(f_k - f_0) \\ u_y\left(\Theta^{(k)}\right) &= -u_y(\Theta_{\mathrm{u}}) - \frac{b_0\lambda}{2\pi}\,(f_k - f_0)\,. \end{aligned} \tag{4.5}$$

Now, suppose the design of the metaprism is to ensure that it reflects the highest subcarrier of the user-generated signal ($k = K$) with angle $\theta^{(K)} = -\theta_{\mathrm{u}} - \theta_m$, for some angle θ_m, and $\phi^{(K)} = 0$. From (4.5), by setting $k = K$, the coefficients a_0 and b_0 become

$$a_0 = -4\pi/\lambda W\left(-\sin\left(\theta_{\mathrm{u}} + \theta_m\right) + \sin\left(\theta_{\mathrm{u}}\right)\right) \tag{4.6}$$

and $b_0 = 0$. With these values, the other subcarriers are reflected with different increasing angles in the range $\theta^{(k)} \in [\theta^{(K)}, \theta^{(1)}]$, where $\theta^{(1)}$ can be

obtained from (4.5) with $k = 1$, around the Snell's angle $-\theta_{\mathrm{u}}$. Thanks to the reciprocity of the metaprism, by exchanging θ_{u} with θ_{BS}, the same design corresponds to a metaprism that reflects the different subcarriers toward the users depending on the BS's angle θ_{BS}. Therefore, according to the angle θ_m, it is possible to design the desired angular span necessary to cover a specific NLOS area of interest. It is worth noting that the angle $\theta^{(k)}$ is monotonic with the OFDM subcarrier index k, leading to phase wrapping, yet this does not present any problem. Fig. 4.2 shows an example of the normalized AF in dB obtained from (4.4), with a metaprism designed using (4.6) with $\theta_m = 40^\circ$ so that the main lobe moves from -25° to -85°, considering a 50×50 cells metaprism, for the case of $K = 256$ and $K = 3300$ at $f_0 = 28$ GHz. For a fixed user's position (incident angle), it can be observed that as the number of subcarriers increases from $K = 256$ to $K = 3300$, the peaks of the equivalent AF become increasingly dense thus increasing the probability that the BS receives a sufficient amount of energy at least in one subcarrier. Notably, if the angle of the user is changed, a different subcarrier will be directed toward the BS. This is the phenomenon that will be exploited by the position estimator described later.

ii) Near-field scenario: Random design (RD) In near-field channel conditions, the plane wave propagation approximation is no longer valid and the beamsteering design criterium of the previous section cannot be applied because the cells of the metaprism do not share anymore the same angle of arrival/departure [119]. Therefore, the design of coefficients $\{\alpha_{nm}\}$ in (4.2) needs to be re-adapted to the near-field case. One option would be designing $\{\alpha_{nm}\}$ to obtain a focusing effect, as done in [118]. Unfortunately, this leads to a model with 3 parameters instead of 2 in (4.3) that does not give the necessary flexibility for localization purposes. For this reason, it is proposed to draw $\{\alpha_{nm}\}$ randomly from a uniform distribution (*Random design - RD*) as

$$\alpha_{nm} \sim \mathcal{UD}(0, 10^{-6}) \tag{4.7}$$

within the same range of values of the beamsteering design. The rationale behind the RD is based on the idea that assigning random values to the metaprism's coefficients guarantees a unique or nearly unique frequency pro-

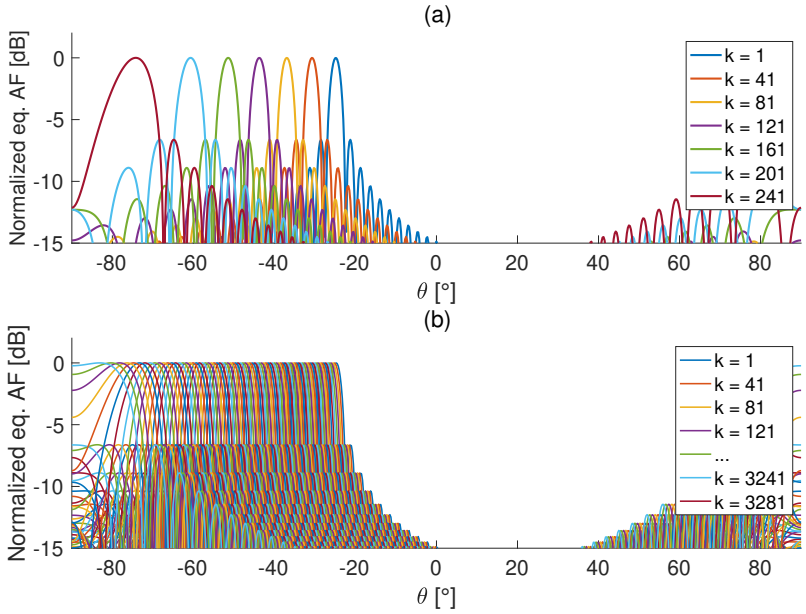

Figure 4.2: Normalized equivalent array factor (AF) for $K = 256$ subcarriers (a) and $K = 3300$ subcarriers (b) .

file for different user positions. By considering a large number of subcarriers and leveraging the randomness, the probability that two different positions have the same frequency profile is expected to decrease significantly. Unlike the BD approach, where the signal is reflected coherently towards a specific direction thus ensuring a certain array gain, the random design does not exploit the array gain, and the overall link budget tends to degrade.

Position Estimation

Considering both BS-metaprism and metaprism-UE Ricean channel models with Rice factor κ, the signal received by the BS at the k-th subcarrier can be written as

$$y_k = s_k(\mathbf{p}_\mathrm{u}) + v_k + n_k \tag{4.8}$$

for $k = 1, 2, \ldots, K$, where $s_k(\mathbf{p}_\mathrm{u})$ is the specular component of the useful signal at the k-th subcarrier which depends on the user's position $\mathbf{p}_\mathrm{u}$, whereas $n_k \sim \mathcal{CN}(0, \sigma^2)$ is the thermal noise sample, being $\sigma^2 = N_0 \Delta f$, N_0 the one-side noise power spectral density, and Δf the carrier spacing $\Delta f = W/K$.

The term v_k represents the diffuse component of the received signal and it is modeled as a complex Gaussian random variable, i.e., $v_k \sim \mathcal{CN}(0,\, \sigma_v^2)$. The useful specular component of the received signal $s_k(\mathbf{p}_\mathrm{u})$ is given by

$$s_k(\mathbf{p}_\mathrm{u}) = \sum_{n=0}^{N-1}\sum_{m=0}^{M-1} h_{mn}^{(k)}(\mathbf{p}_\mathrm{u})\, r_{mn}^{(k)}\, g_{mn}^{(k)}(\mathbf{p}_\mathrm{BS}) \times \sqrt{P_k \frac{\kappa}{1+\kappa}} x_k \tag{4.9}$$

where $r_{mn}^{(k)} = r_{mn}(f_k)$, $P_k = P_\mathrm{T}/K$ is the transmitted power allocated to each subcarrier, P_T the total transmitted power, and x_k is the pilot symbol, which is set to one, without loss of generality. $h_{mn}^{(k)}(\mathbf{p}_\mathrm{u})$ and $g_{mn}^{(k)}(\mathbf{p}_\mathrm{BS})$ are the channel gains at frequency f_k between the user and the nm-th cell of the metaprism and between the nm-th cell and the BS, respectively, given by

$$h_{mn}^{(k)}(\mathbf{p}_\mathrm{u}) = \frac{\sqrt{G_\mathrm{u}}\,\lambda}{4\pi|\mathbf{p}_\mathrm{u} - p_{mn}|} \exp\left(-j\frac{2\pi f_k}{c}|\mathbf{p}_\mathrm{u} - p_{mn}|\right) \tag{4.10}$$

$$g_{mn}^{(k)}(\mathbf{p}_\mathrm{BS}) = \frac{\sqrt{G_\mathrm{BS}}\,\lambda}{4\pi|\mathbf{p}_\mathrm{BS} - p_{mn}|} \exp\left(-j\frac{2\pi f_k}{c}|\mathbf{p}_\mathrm{BS} - p_{mn}|\right) \tag{4.11}$$

being c the speed of light, G_u and G_BS the antenna gains of the user and BS, respectively. According to the Ricean fading model, it is

$$\sigma_v^2 = |A_k|^2 P_\mathrm{T}/(1+\kappa), \tag{4.12}$$

having defined

$$A_k = \sum_{n=0}^{N-1}\sum_{m=0}^{N-1} h_{mn}^{(k)}(\mathbf{p}_\mathrm{u})\, r_{mn}^{(k)}\, g_{mn}^{(k)}(\mathbf{p}_\mathrm{BS})\,. \tag{4.13}$$

Since the profile $\{y_k\}$, for $k = 1, 2, \ldots, K$, of the received signal is a function of the user's position $\mathbf{p}_\mathrm{u}$, then it is possible to estimate $\mathbf{p}_\mathrm{u}$ from the observation of the y_k's. In this work, the Maximum Likelihood (ML) estimator, which can be expressed as

$$\widehat{\mathbf{p}}_\mathrm{u} = \arg\max_{\mathbf{p}_\mathrm{u}} \sum_{k=0}^{K-1} Re(y_k\, s_k^*(\mathbf{p}_\mathrm{u}))\,. \tag{4.14}$$

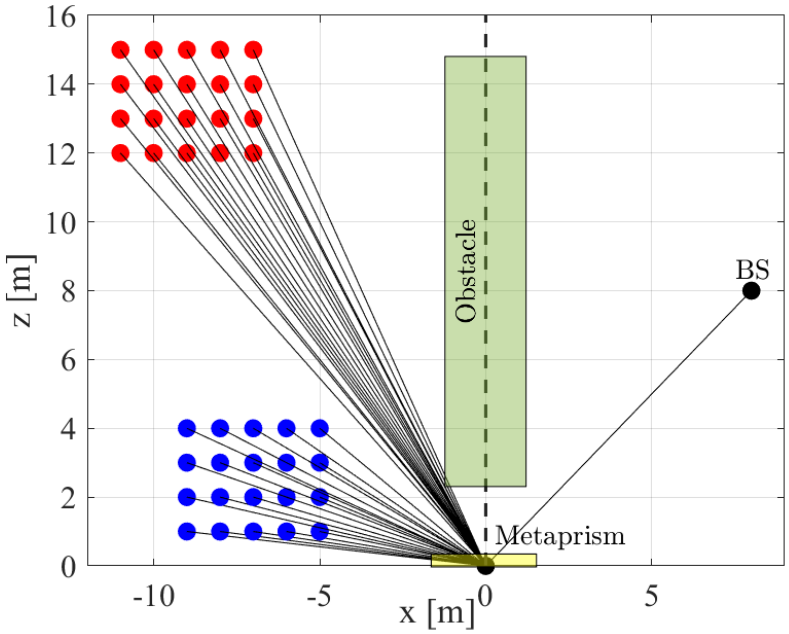

Figure 4.3: Users positions in scenario A (blue dots) and scenario B (red dots).

The ML in (4.14) corresponds to performing "fingerprinting" localization: the estimator compares the test profiles $\{s_k(\mathbf{p}_u)\}$, computed in all the test locations of the area of interest, with the profile of the received signal $\{y_k\}$, and chooses the position of the profile test pattern that most closely resembles that of the received signal. Obviously, the accuracy of the ML is strictly affected by the granularity of the test grid.

Numerical Results

In this section, some simulation examples are illustrated, addressing to validation of the proposed frequency-selective metasurface-aided localization schemes.

The two NLOS scenarios considered in the simulations are illustrated in Fig. 4.3. In this context, the red dots represent certain user positions within a given area, while the blue dots represent other user positions within another known area. The users are always in NLOS condition with the BS, due to the presence of a generic obstacle.

It is important to note that the Fraunhofer distance varies depending on the

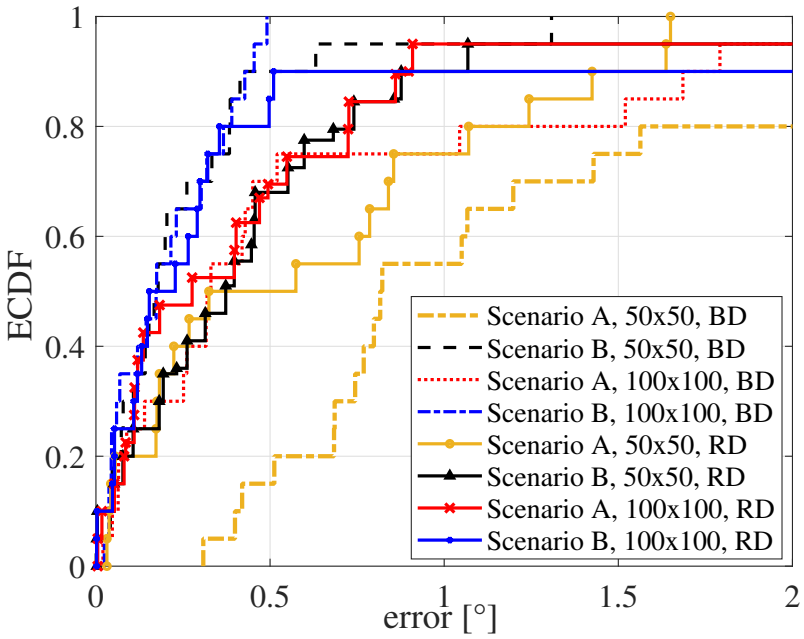

Figure 4.4: Angular ECDF varying the metasurface's size ($N \times M$). BD (beam-steering design); RD (random design). No fading.

dimensions of the metaprism considered, as $d_F = 2D^2/\lambda$, where D is the maximum size of the metaprism. To avoid any potential confusion between far and near-field conditions, the two NLOS scenarios will be referred to as *scenario A* for the red dots and *scenario B* for the blue dots.

The value of the simulation parameters resembles those of the mmWave 5G-NR wireless systems, i.e., $f_0 = 28\,\text{GHz}$, $P_T = 20\,\text{dBm}$, $G_{\text{BS}} = G_{\text{u}} = 6$ dB, bandwidth $W = 198\,\text{MHz}$, $K = 3300$, BS's position $\mathbf{p}_{\text{BS}} = \{8, 0, 8\}$ m, receiver's noise figure $F_{\text{noise}} = 3$ dB. The test grid step is equal to 0.1 m. For each system configuration and metaprism design criterium, a 200-iteration Monte Carlo simulation has been performed. The effect of the metaprism's size is investigated in Fig. 4.4 where the ECDFs of the angle estimation error is reported. As expected, by increasing the size from $N \times M = 50 \times 50$ (i.e., $26.7 \times 26.7\,\text{cm}^2$) to 100×100 (i.e., $53.5 \times 53.5\,\text{cm}^2$), also the performance improves thanks to better link budget and angular resolution. For the BD, the estimation error is minimal for users in scenario B, while for the RD, this difference is not so evident. The impact of fading can be analyzed in Fig. 4.5 for different values of the Rice factor κ. To avoid redundancy, only the case

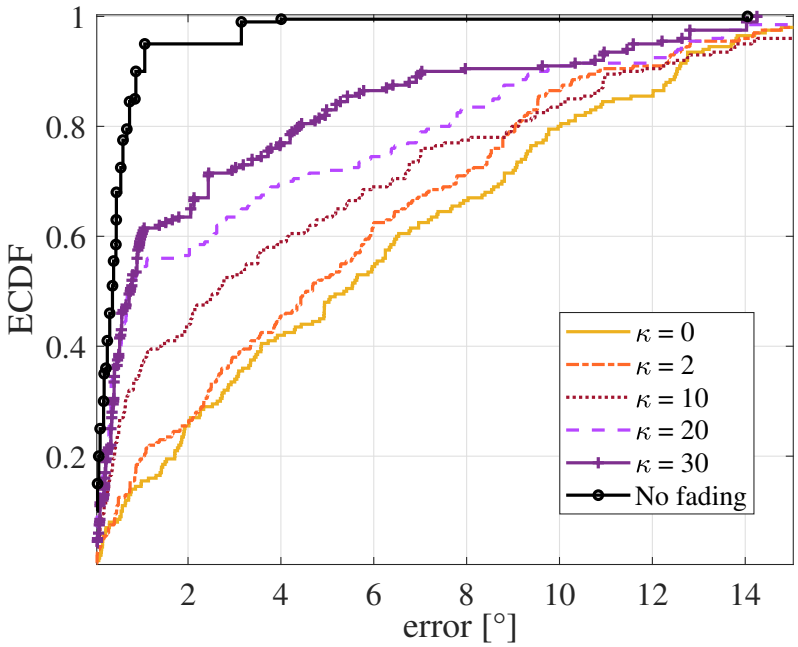

Figure 4.5: Angular ECDF by varying the Rice Factor κ in scenario B.

of scenario B for BD is reported, but the trend is the same for scenarios A and RD. As expected, with $\kappa = 0$ (Rayleigh fading), where the useful signal $s^{(k)}(\mathbf{p}_u)$ is null and only the noisy components are present, the estimation is not possible. In fact, the corresponding curve refers to the uncertainty associated with the spanned area whose size is a priori known. Vice versa, the curves related to higher values of κ indicate that the proposed scheme is effective in strong Ricean fading, which is typical at millimeter waves or higher frequencies.

The RD criterium opens the possibility to estimate not only the angle, as in the BD, but also the user's position, i.e., the angle and distance. This can be observed in Fig. 4.6 where the ECDFs of the position estimation error is reported for different configurations. The position estimation has a maximum error of less than 22 cm for scenario A and 35 cm for scenario B in 90% of locations.

OFDM-based localization at 300 GHz

In this part of the numerical results section the position estimation framework described above has been investigated at 300 GHz. The simulation

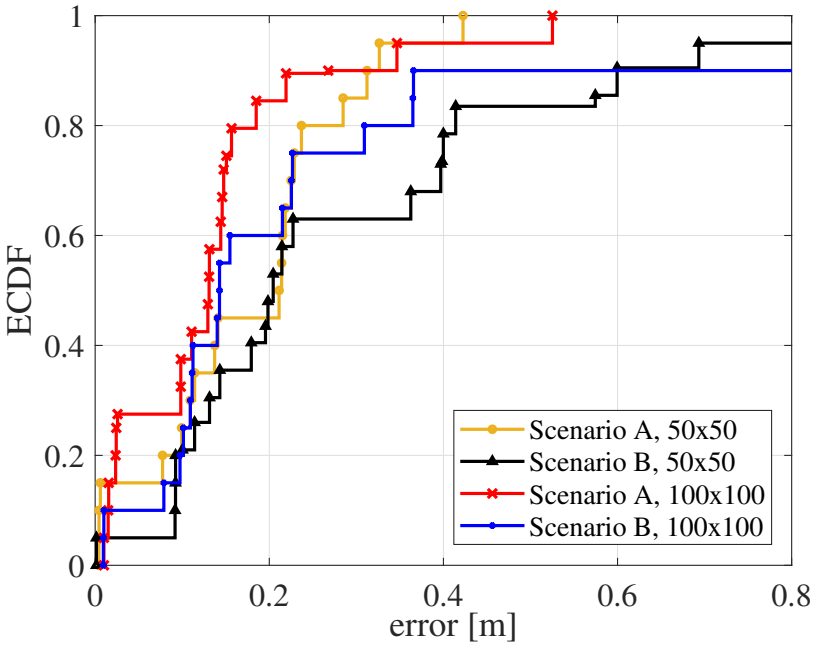

Figure 4.6: Position estimation error ECDF, random design, no fading.

parameters are given in Table 4.1 when not otherwise specified. The BS's position $\mathbf{p}_{\text{BS}} = \{3.5, 0, 3.5\}$ m. The position of the users and scenario are shown in Fig. 4.7. In this case, the context was industrial, and indeed in Fig. 4.7, the BS is referred to as a Access Point (AP), and the user is a robot, which can move within a known area, delineated in the figure. The distances and all simulation parameters have been scaled for operation at 300 GHz. The metaprism has been designed to provide an angular span from $\theta_0^1 = -15°$ to $\theta_0^K = -85°$ with an incident angle of $\theta_{\text{inc}} = 45°$. The test grid step is equal to 0.1 m. For each system configuration and metaprism design criterion, a 200-iteration Monte Carlo simulation has been performed.

The empirical cumulative distribution for the angular and position estimation are reported in Fig. 4.8. What the results show is that by changing the transmitted power and the number of subcarriers the performance does not change because the array factor is already dense with $K = 256$ subcarriers and the SNR is already favorable with $P_{\text{T}} = 10$ dBm. The results indicate less than 1° of angular error and 0.25 m of position error in 90% of the 200 Monte Carlo iterations thus showcasing the significant potential

Carrier frequency	$f_0 = 300\,\text{GHz}$
Total bandwidth	$W = 10\,\text{GHz}$
Number of subcarriers	$K = 256$
AP antenna gain	$G_T = 40\,\text{dBi}$
RX noise figure	$F = 8\,\text{dB}$
UE antenna gain	$G_R = 6\,\text{dBi}$
TX Power	$P_T = 10\,\text{dBm}$
Metaprism's size	100x100 cells (5x5 cm^2)

Table 4.1: System parameters.

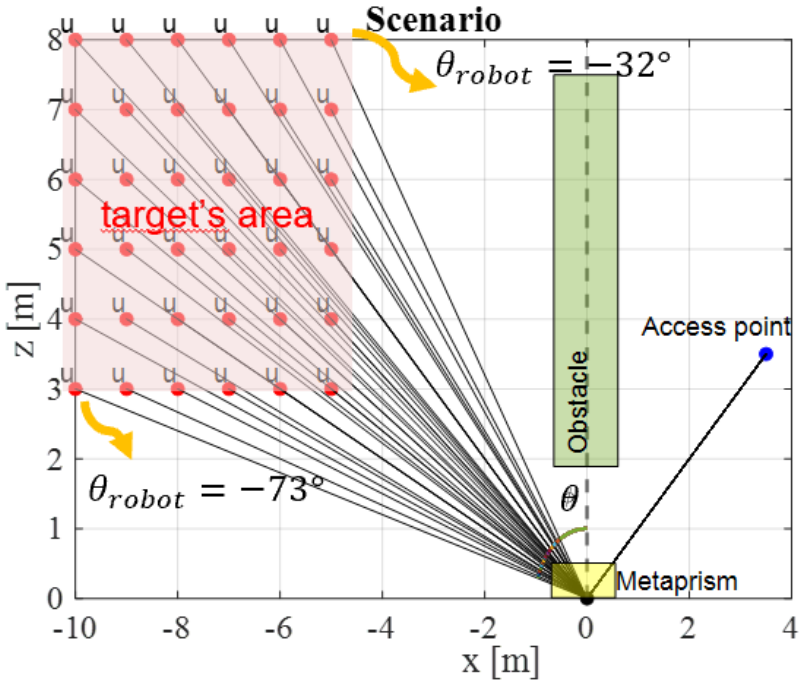

Figure 4.7: Simulation scenario of localization at 300 GHz

of the metaprism to aid the localization process in NLOS without significant complexity increase with respect to deploying additional BSs or using RISs [7, 11].

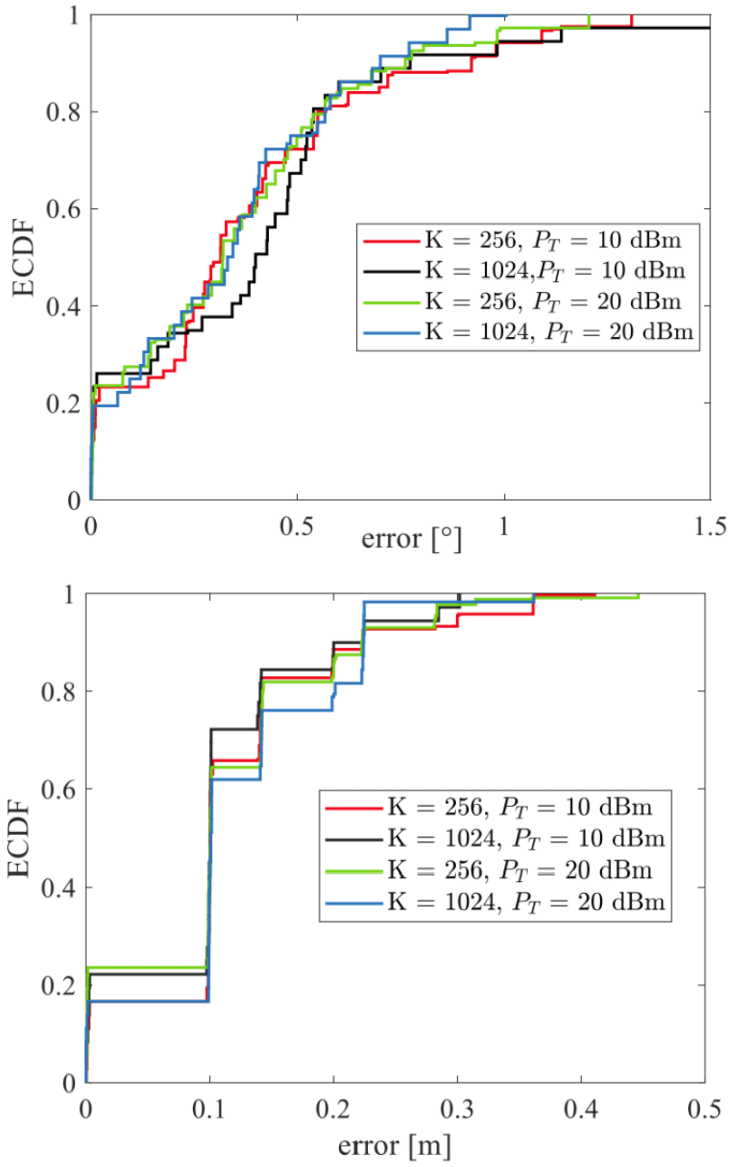

Figure 4.8: Angular and position Empirical cumulative distribution (ECDF)

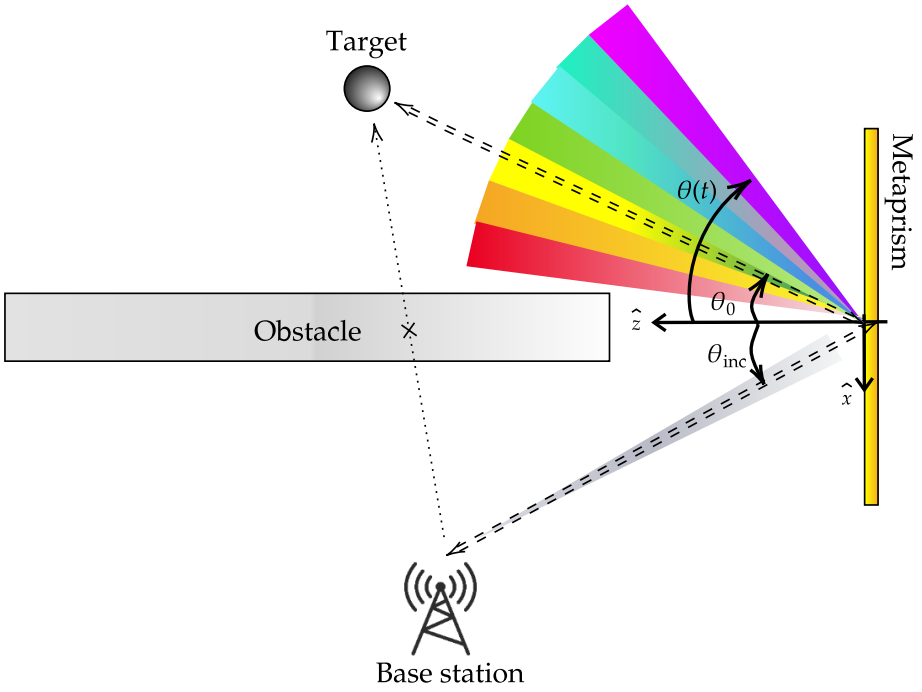

Figure 4.9: Reference scenario.

4.1.2 FMCW radar-based beamsteering design

In this section, it is shown how with a metaprism it is possible to detect the position of a target hidden by an obstacle using a standard FMCW signal. In particular, it is proposed an enhanced FMCW receiver capable of jointly estimating with high accuracy the range and angle of the target using a simple-single antenna FMCW radar. The reference scenario considered in this work is shown in Fig. 4.9, where a BS located at coordinates $\mathbf{p}_{\text{BS}}$ operating as a radar generates an FMCW signal to detect and localize a target at position $\mathbf{p}_{\text{T}}$ hidden by an obstacle. To accomplish this task, the BS exploits the reflection through a frequency-selective non-reconfigurable metasurface (the metaprism) which is supposed to be in LOS with respect to both the BS and the target, same assumption of the previous OFDM-based metaprism scheme. With reference to the normal of the metaprism, denote by θ_{inc} and θ_0, respectively, the angle of incidence of the signal generated by the BS and the angle of view of the target along the $x-z$ plane. No particular assumption is made on the BS' antenna that can be a single element or an

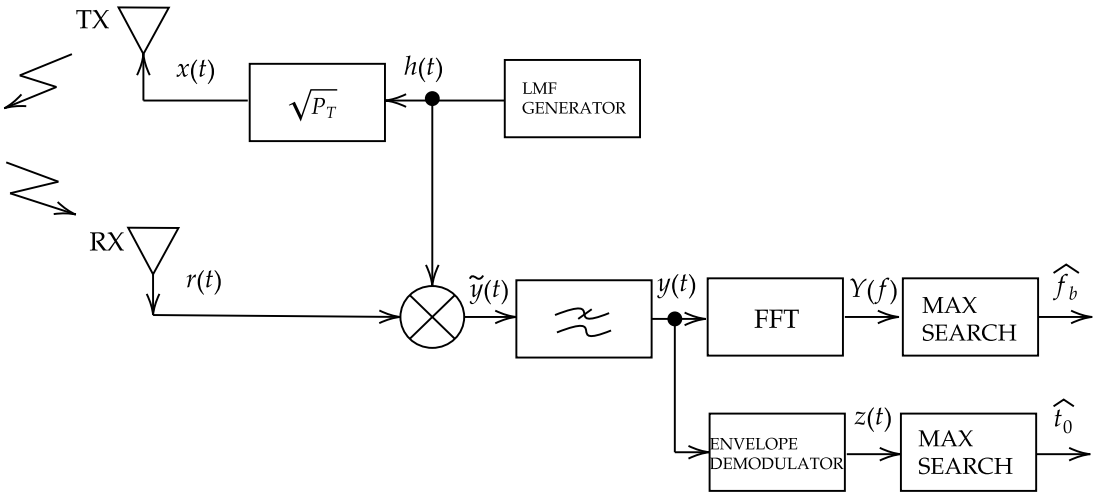

Figure 4.10: Modified FMCW transceiver.

array. The signal emitted by the FMCW radar is composed of one or more Linear Frequency Modulated (LFM) chirps, i.e., a sinusoidal signal whose frequency varies linearly starting from an initial frequency f_{start} and ending at the final frequency f_{stop}, thus covering the bandwidth $W = f_{\text{stop}} - f_{\text{start}}$ in a period of duration T (chirp time). The normalized chirp is given by [120]

$$h(t) = \text{rect}\left(\frac{t}{T}\right)\cos\left(2\pi f(t)\, t\right) \tag{4.15}$$

where $f(t) = f_{\text{r}} - W/2 + \beta t$ is the instantaneous frequency, with f_0 being the center frequency, β the slope of the FMCW signal, and $\text{rect}(x) = 1$, for $|x| < 0.5$, zero otherwise. The transmitted signal is $x(t) = \sqrt{2P_{\text{T}}}\, h(t)$, where P_{T} is the transmitted power.

As for the OFDM-based system, the metaprism is designed in such a way, for a given incident angle θ_{inc}, the FMCW signal emitted by the BS is reflected towards the angle $\theta(t) = \theta(f(t))$ depending on the instantaneous frequency $f(t)$ of the chirp. As a consequence, the frequency sweep of the chirp translates into an angle sweep of the reflected beam. Assuming the channel does not change within the chirp time, the signal backscattered by the target in the time interval in which the angle of the beam is close to θ_0 is reflected back towards the BS.

Then, a signal processing scheme capable of estimating both the target angle θ_0 and its distance r_0 from the metaprism, and hence its position, starting from the reflected signal, is proposed. The signal returned from a stationary target at the range distance r_0 and angle θ_0 is

$$r(t) = \sqrt{2p(t)}\cos(2\pi f(t-\tau)\,(t-\tau) + \phi_{\mathrm{R}}) + n(t) \tag{4.16}$$

where ϕ_{R} is the carrier phase, $n(t)$ is the AWGN with double-side power spectral density $N_0/2$, and $\tau = 2\,r_0/c$ is the round-trip propagation time with c being the speed of light.[1] $p(t)$ represents the instantaneous received power whose behavior is affected by the metaprism and the target, as it will be clarified in the following. The receiver at the BS is shown in Fig. 4.10.

As in conventional FMCW receivers, the received signal $r(t)$ is mixed with the normalized heterodyne signal generated by the LFM generator thus obtaining [120]:

$$\begin{aligned}\tilde{y}(t) =& r(t)\,h(t)\\ =& \sqrt{p(t)}\cos(2\pi(f(t-\tau)\,(t-\tau) - f(t)\,t)\; + \phi_{\mathrm{R}}) +\\ & \sqrt{p(t)}\cos(2\pi(f(t)\,t + f(t-\tau)(t-\tau)) + \phi_{\mathrm{R}}) + \tilde{w}(t)\end{aligned} \tag{4.17}$$

where $\tilde{w}(t) = n(t)\,h(t)$. The signal is then filtered by an ideal low-pass filter with bandwidth W. Note that the choice of W affects the maximum range detectable by the radar as well as the output SNR. After the low-pass filter, all the high-frequency terms are filtered out and the signal becomes

$$\begin{aligned}y(t) =& \sqrt{p(t)}\cos(2\pi(f(t-\tau)\,(t-\tau) - f(t)\,t)\; + \phi_{\mathrm{R}}) + w(t)\\ =& \sqrt{p(t)}\cos\left(4\pi\beta\,\tau\,t + \phi_{\mathrm{Y}}\right) + w(t)\,.\end{aligned} \tag{4.18}$$

having defined $\phi_{\mathrm{Y}} = 2\pi f_{\mathrm{r}}\tau - \pi W\tau - 2\pi\beta\tau^2$, and $w(t)$ the filtered version of $\tilde{w}(t)$. The last equation shows that the output yields a constant frequency

[1] In reality, τ accounts also for the extra delay due to the path between the BS and the metaprism. However, since this is a known quantity, it can always be subtracted then it is not considered in the following.

signal with a frequency of [120]

$$f_{\mathrm{b}} = f_{\mathrm{b}}(r_0) = 2\beta\tau = \frac{4\, r_0\, \beta}{c} \tag{4.19}$$

that depends on the target range r_0. Note that in a conventional FMCW radar setup, i.e., without the metaprism, the instantaneous received power $p(t)$ would be a constant during the reception of one chirp, that is,

$$p(t) = P_{\mathrm{R}}\, \mathrm{rect}\left(\frac{t-\tau}{T}\right) \tag{4.20}$$

where P_{R} is the received power given by the radar range equation. On the contrary, in the presence of the metaprism, the sinusoid in (4.18) results modulated because, due to the frequency-angular selectivity effect of the metaprism, the signal is reflected by the target only in the time interval close to t_0, being $t_0 \in [-T/2, T/2]$ the time instant at which the instantaneous frequency $f(t_0)$ corresponds to a reflection of the metaprism towards the target's angle θ_0, i.e., $\theta(t_0) \approx \theta_0$. The instantaneous received amplitude is modeled as a delayed version of the waveform $s(t)$ such that $\sqrt{p(t)} = s(t-t_0)$, where the shape of $s(t)$ depends on the target's position, size, and reflection characteristic, and $0 \leqslant s(t) \leqslant s(0)$, for $|t| > 0$. Therefore, (4.18) can be rewritten as

$$y(t) = s(t-t_0)\cos\left(2\pi f_b\, t + \phi_Y\right) + w(t)\,. \tag{4.21}$$

The output signal (4.21) can be processed in order to obtain an estimate of the target's range r_0 and angle of view θ_0. The estimate of the target's range r_0, through the estimate of f_{b}, can be obtained according to the classical scheme based on the Fourier transform of $y(t)$ (see the upper branch of the receiver in Fig. 4.10). In particular, the spectrum of (4.21) is

$$\begin{aligned} Y(f) = &\frac{1}{2} S(f-f_b) e^{-\jmath 2\pi f t_0 + \jmath\phi_y} + \\ &\frac{1}{2} S(f+f_b) e^{\jmath 2\pi f t_0 - \jmath\phi_y} + W(f) \end{aligned} \tag{4.22}$$

where $S(f)$ and $W(f)$ are the Fourier transforms of $s(t)$ and $w(t)$, respec-

tively. Specifically, the estimate of f_b can be simply obtained by locating the maximum of $|Y(f)|$. Since the resolution is related to the width of the central lobe of the spectrum around f_b, it is affected by the target position and its characteristics. The main difference with respect to the classical scheme is in the time-dependent power $p(t)$ which decreases the received energy. Regarding the angle θ_0, it affects the time instant t_0 at which the instantaneous receiver power $p(t)$ presents a peak. Therefore, it is possible to estimate it using the scheme depicted in the lower branch of the receiver in Fig. 4.10. It consists of an envelope demodulator of the signal $y(t)$ to extract the signal $s(t-t_0)$, that is,

$$z(t) \simeq s(t-t_0) + v(t) \tag{4.23}$$

followed by a delay estimator consisting of a maximum search, where $v(t)$ is AWGN with power spectral density $G_v(f) = N_0\,\mathrm{rect}(f/2W)$ [120,121]. With the estimated time t_0, the angle θ_0 of the signal backscattered from the target can be obtained as explained later.

It order to find a relationship between the instantaneous frequency of the FMCW radar chirp and the angle of reflection it is supposed that the signal transmitted by the BS impinges the metaprism with incident angle $\Theta_\mathrm{inc} = (\theta_\mathrm{inc}, 0)$ in the $x-z$ plane, such that $\phi = 0^\circ$. Thus, it is obtained that $u_x(\Theta) = \sin(\theta)$ and $u_y(\Theta) = 0$. Therefore (4.5) used in the OFDM case, it is not discretized in the frequency and θ_u is now θ_inc, it becomes

$$\sin(\theta) = -\sin(\theta_\mathrm{inc}) - \frac{a_0\lambda}{2\pi}\,(f - f_0) \tag{4.24}$$

from which the frequency-dependent angle of reflection can be determined

$$\theta(f) = \arcsin\left(-\sin(\theta_\mathrm{inc}) - \frac{a_0\lambda}{2\pi}\,(f - f_0)\right). \tag{4.25}$$

When illuminated by the chirp signal in (4.15), the reflected angle becomes time-dependent within the chirp duration T, that is,

$$\theta(t) = \arcsin\left(-\sin(\theta_\mathrm{inc}) - \frac{a_0\lambda}{2\pi}\,(\beta t - W/2)\right). \tag{4.26}$$

As an example, the coefficient is designed a_0 in (4.3) in such a way the incident signal from the BS is reflected towards the angle $\theta = -\theta_{\text{inc}} - \theta_{\text{m}}$, when the instantaneous frequency of the signal is $f_{\text{start}} = f_{\text{r}} - W/2$ (at the beginning of the chirp), and towards the angle $\theta = -\theta_{\text{inc}}$, when the instantaneous frequency is $f_{\text{stop}} = f_{\text{r}} + W/2$ (at the end of the chirp). Therefore, θ_{m} represents the desired angle span necessary to cover the intended NLOS area. From (4.25) it follows that

$$\begin{aligned} a_0 &= -\frac{2\pi}{\lambda(f_{\text{r}} - W/2 - f_0)} \left(-\sin(\theta_{\text{inc}} + \theta_{\text{m}}) + \sin(\theta_{\text{inc}})\right) \\ &= -\frac{4\pi}{\lambda W} \left(-\sin(\theta_{\text{inc}} + \theta_{\text{m}}) + \sin(\theta_{\text{inc}})\right) \end{aligned} \tag{4.27}$$

and $b_0 = 0$. These values can be used in (4.3) to obtain the design coefficient of each cell composing the metaprism.

To obtain an idea of the achievable performance bound in the estimation error variance of the angle θ_0 using the metaprism, the corresponding Cramer Rao Bound (CRB) is computed. Since θ_0 is obtained through the estimation of the intermediate parameter t_0, the first step is to compute the CRB on the estimation error variance of t_0 from the classical bound given by [122]

$$\text{CRLB}_{t_0} = \frac{N_0}{2\left(2\pi\right)^2 B_{\text{eff}}^2 E_s} = \frac{1}{8\pi^2 \text{SNR} B_{\text{eff}}^2} \tag{4.28}$$

where $B_{\text{eff}}^2 = \int_\infty f^2 \left|S\left(f\right)\right|^2 df / \int_\infty \left|S\left(f\right)\right|^2 df$ is the square of the effective bandwidth of $s(t)$, and the Signal-to-Noise Ratio (SNR) is defined as

$$\text{SNR} = \frac{E_s}{N_0} = \frac{1}{N_0} \int_T s^2(t)\, dt = \frac{1}{N_0} \int_T p(t)\, dt \tag{4.29}$$

where $p(t)$ is given by (4.35) explained later. Subsequently, the CRB of θ_0 can be obtained considering that $\text{CRLB}_{\theta_0} = \text{CRLB}_{t_0} \cdot \left(\partial\theta(t)/\partial t\right)^2$, being the derivative computed for $t = t_0$, where t_0 is the solution of (4.26) when $\theta(t_0)$ is set to θ_0, which gives

$$t_0 = \frac{W}{2\beta} - \left[\sin\left(\theta_0\right) + \sin\left(\theta_{\text{inc}}\right)\right] \frac{2\pi}{a_0 \lambda \beta}\,. \tag{4.30}$$

After some trigonometric manipulations and by defining $\mathrm{K} = a_0\lambda\beta/(2\pi)$, CRLB_{θ_0} becomes

$$\mathrm{CRLB}_{\theta_0} = \frac{\mathrm{K}^2/(8\pi^2\mathrm{SNR}B_{\mathrm{eff}}^2)}{\cos^2(\theta_{\mathrm{inc}}) - \mathrm{K}^2\left(\frac{W}{2\beta} - t_0\right)^2 + 2\mathrm{K}\sin(\theta_{\mathrm{inc}})\left(\frac{W}{2\beta} - t_0\right)} \tag{4.31}$$

Finally, by replacing (4.30) in (4.31) it is obtained

$$\mathrm{CRLB}_{\theta_0} = \frac{\mathrm{K}^2}{8\pi^2\mathrm{SNR}B_{\mathrm{eff}}^2\cos^2(\theta_0)}\,. \tag{4.32}$$

The last result indicates that the CRB on the estimation error variance of θ_0 worsens for large β and a_0, i.e., for fast frequency sweeps of the chirp and higher frequency selectivity of the metaprism. Moreover, the larger effective bandwidth is obtained for narrow power profiles $p(t)$, i.e., smaller target footprints in the angular domain (small target and/or far target), and for small angle of view θ_0.

Link budget analysis. Assuming the BS and the target in free-space condition with respect to the metaprism, the isotropic two-way channel gain accounting for the metaprism at frequency f is

$$G_0(f) = \frac{\lambda^4 G_{\mathrm{c}}^2 F(\theta_{\mathrm{inc}})\,F(\theta_0)}{(4\pi)^4}\left|\sum_{n=0}^{\mathrm{N}-1}\sum_{m=0}^{\mathrm{M}-1}\frac{\Gamma_{nm}(f)}{|\mathbf{p}_{\mathrm{BS}} - \mathbf{p}_{nm}||\mathbf{p}_{\mathrm{T}} - \mathbf{p}_{nm}|}\right.$$
$$\left.\exp\left(-j\frac{2\pi f}{c}\left(|\mathbf{p}_{\mathrm{BS}} - \mathbf{p}_{nm}| - |\mathbf{p}_{\mathrm{T}} - \mathbf{p}_{nm}|\right)\right)\right|^2 \tag{4.33}$$

where the sum accounts for the $N \cdot M$ elements of the metaprism along the x, y-directions. Γ_{nm} is modeled such that $|\Gamma_{nm}| = 1$ and $\angle\Gamma_{nm} = (f - f_0)(a_0 x_n + b_0 y_m)$. The power intercepted by the target having RCS σ_x is:

$$P_{\sigma_x}(f) = P_{\mathrm{T}}\,G_{\mathrm{T}}\,G_0(f)\,G_{\sigma_x}(f) \tag{4.34}$$

where G_{T} is the antenna gain of the BS, $G_{\sigma_x}(f) = G_{\sigma_x} = \sigma_x 4\pi/\lambda^2$ is the equivalent gain of the target considered as isotropic, as a first approximation.

Table 4.2: Parameters used in the simulation

Parameter	Symbol	Value
Carrier frequency	f_0	77 GHz
BS antenna gain	G_{T}	5 dB
Bandwidth	W	4 GHz
Chirp time	T	1 ms
Target radius	r	0.05 m
Receiver's noise figure	F_{noise}	3 dB
Test angles	θ_{test}	-(0:3:90)°
Parameter for F	q	0.57

So the power received by the radar becomes

$$P(f) = P_{\sigma_x}(f) G_{\mathrm{T}}\, G_0(f) = P_{\mathrm{T}} G_{\mathrm{T}}^2\, G_0(f)^2\, G_{\sigma_x}. \tag{4.35}$$

Note that during a frequency sweep, $p(t) = P(f(t))$, where $P(f)$ is given by (4.35).

Numerical Results

In this section, the evaluation of the angle estimation performance is reported. In the simulations, the target position was moved along an arc of 6 meters radius with angles ranging from 0 to -90°, with step 3°. The BS is at coordinates (3,0,3) m with respect to the reference system of Fig. 4.9. The metaprism was designed according to (4.27) with $\theta_{\mathrm{m}} = 40°$, thus spanning from -25° to -85° during a sweep of an FMCW chirp. The values of the parameters are shown in Tab. 4.2.

In Fig. 4.11, examples of the received signal $y(t)$ and its envelope $z(t)$ are shown for some target test angles. It can be seen that $y(t)$ is negligible for angles that do not belong to the design range of the metaprism, i.e., $[-25° : -85°]$. Also, for each test angle, the maximum of the envelope corresponds to the time instant in which the instantaneous reflection angle of the metaprism $\theta(f(t))$, given by (4.25) and (4.26), is equal to test angle θ_0. Subsequently, 1000 Monte Carlo iterations were considered to compute the RMSE of the angle estimation of the proposed receiver for each target position. Fig. 4.12 shows the RMSE for different sizes of the metaprism,

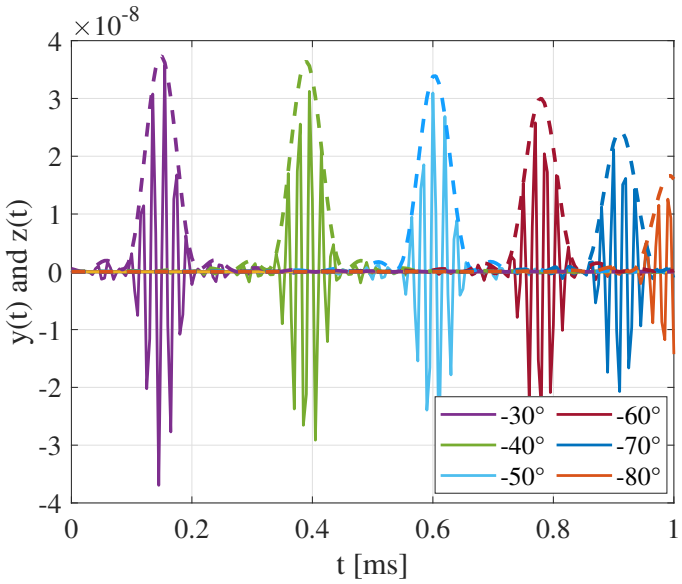

Figure 4.11: Received signal $y(t)$ (continuous line) and its envelope $z(t)$ (dashed line), with $P_{\mathrm{T}} = 15$ dBm and metaprim's size 20×50 cm^2.

in particular, from 10×50 cm^2 (i.e., $N = 53, M = 257$) to 20×100 cm^2 (i.e., $N = 103, M = 515$). What emerges is that the best estimate of the angle, in the range where the metaprism has been designed, is less than 10°. Moreover, lower values of RMSE can be obtained by increasing the size of the metaprism. The square root of the CRB on angle estimation is also reported for comparison. The gap with respect to the performance of the proposed receiver has to be ascribed to the fact that the CRB intrinsically assumes that $s(t)$ is perfectly known at the receiver, which is not typically the case in realistic situations. Fig. 4.13 investigates the impact of the transmitted power on the performance with a metaprism's size of 20×50 cm^2. The results show that it is possible to achieve an estimation accuracy better than 1° with a typical power of $P_{\mathrm{T}} = 20$ dBm. As regards the estimation of the range, simulation results indicate that, with the parameters considered, the RMSE of the range estimate is typically below 20 cm, thus confirming the capability of the proposed scheme to estimate both the angle and the range with high accuracy.

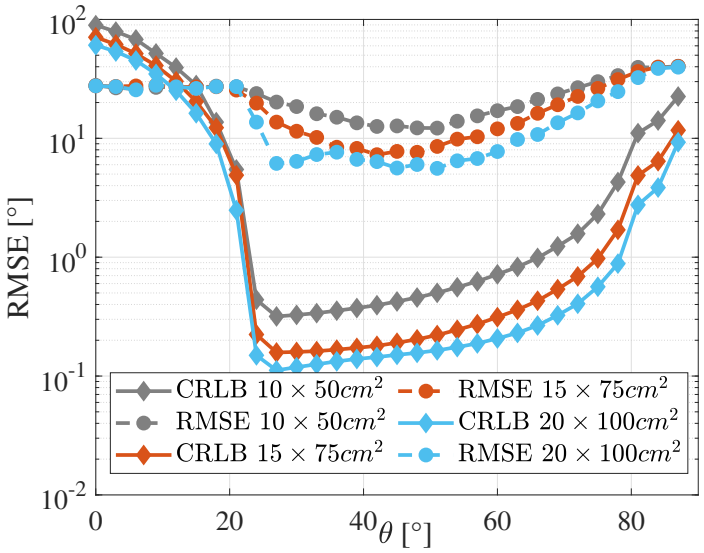

Figure 4.12: CRLB and RMSE results varying the size of the metaprism (MP) with fixed $P_{\mathrm{T}} = 15\,\mathrm{dBm}$.

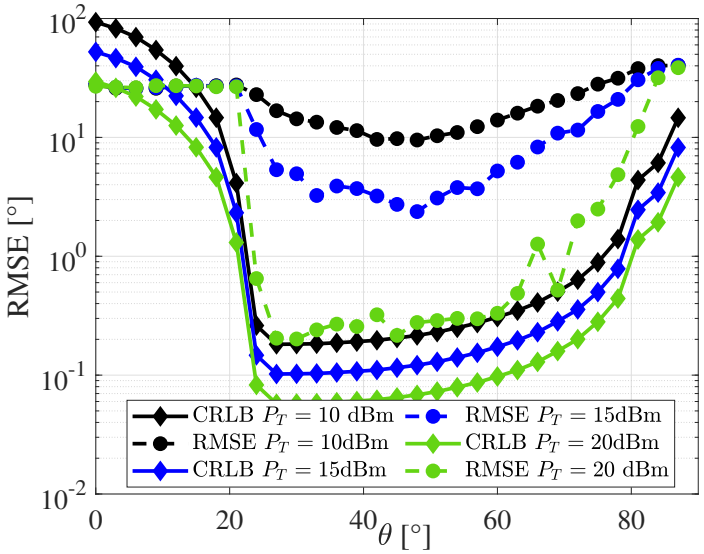

Figure 4.13: CRLB and RMSE results varying P_{T}. Metaprism's size: $20 \times 50\mathrm{cm}^2$.

4.2 SCMs for communication, media access control and localization purposes

To ensure high network capacity and ultra-massive communications, 6G wireless networks will exploit mmWave and THz bands, which will call for the adoption of (massive) MIMO systems to compensate for the increased path loss and manage high user densities [123]. Unfortunately, MIMO systems rely on complex and energy-hungry hardware and are characterized by high signalling overhead (e.g., for channel estimation) and slow beamforming procedures, which are at odds with many requirements of next-generation wireless networks. In fact, several applications envisioned for 6G, such as the creation of Digital Twins in Industrial Internet of Things (IIoT) environments and Vehicular-to-Everything (V2X) communications, will require low-complexity solutions, extremely short connection setup times, ultra-low latency [124] and the ability to track very fast channel variations [125, 126]. The state-of-the-art approaches either involve some computational effort on both sides, which affects hardware complexity and power consumption, or long training data/search time, resulting in increased latency. Clearly, these problems are exacerbated when the number of antennas is high, as expected in beyond 5G systems. In addition, at high frequencies, such as sub-THz/THz, technological constraints place several limitations on the flexibility in processing the signal sent/received by each individual antenna element, thus reducing the set of affordable methods and preventing their use in low-cost sensors.

Consequently, it is evident that the design of high-frequency MU-MIMO systems, incorporating large antenna arrays and involving simple and energy-efficient UEs (e.g., sensors), necessitates a paradigmatic and technological breakthrough. Such advancement should allow for the elimination of Analog-to-Digital converter (ADC) chains, while simultaneously preserving the inherent advantages offered by the MIMO channel, all the while prioritizing low-latency and extensive communication capabilities.

Having this objective in mind, the use of the SCMs, as studied in our works [32–35], introduces a methodology for establishing uplink MIMO communications without imposing any computational burden on the UE side or necessitating signalling procedures. This is accomplished in a blind and

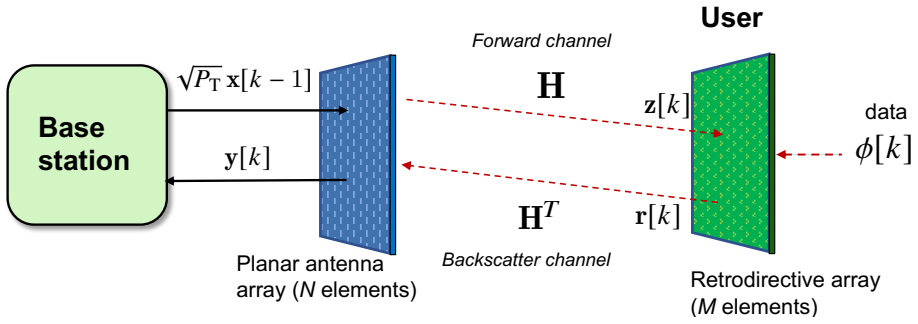

Figure 4.14: Single-user system model considering a UE equipped with a planar SCM communicating with a BS equipped with a planar antenna array thanks to retrodirective backscattering.

nearly optimal fashion during communication, without the need to explicitly estimate the CSI or resort to time-consuming beam alignment schemes. The procedure is based on three pillars:

- The availability of a retrodirective antenna (SCM) at the UE side, which is capable of reflecting the impinging signal along the direction of arrival (retrodirective backscattering), that is, towards the BS;

- The capability of the UE to modulate the phase of the reflected signal, according to the user's data, directly at EM level, thus enabling a low-complexity uplink communication;

- The availability of an algorithm running on the BS capable of jointly demodulating the received data and deriving the optimal precoding vector, i.e., enabling joint communication and beamforming, without any channel estimation or prior knowledge, thanks to the retrodirectivity property of the UE's antenna. The algorithm must also be able to dynamically adjust the beam orientation in response to any change in the position of the UE during the ongoing communication, thereby exhibiting tracking capabilities.

4.2.1 MU-MIMO communication using SCM

Single User Scenario

In this section the single-user uplink scenario is illustrated, shown in Fig. 4.14, with the purpose to illustrate the main idea behind the joint communication and beamforming using a SCM at the UE side. A BS, equipped with an antenna array of N elements, capable of full-duplex transmissions is considered. The design and characterization of the full-duplex front-end are beyond the scope of this work. Interested readers can find more details, e.g., in [127]. Alternatively, two separated antennas for the transmitter and receiver sections can be considered depending on application constraints. It is assumed a narrowband transmission with bandwidth W. It might represent, for instance, a sub-carrier or a resource block in an OFDM system. The UE is realized according to the scheme described in Sec. 2.3 and its SCM is composed of M elements.

Let $\sqrt{P_\mathrm{T}}\,\mathbf{x}[k] \in \mathbb{C}^{N\times 1}$ be the vector containing the signal transmitted by the N elements of the BS's antenna array, where P_T is the transmitted power and $\mathbf{x}[k]$ is a unit norm beamforming vector, i.e., the precoding vector, at the generic time interval k. At the startup, i.e., at $k = 0$, the optimal beamforming vector for the link with the given UE is not known by the BS, which therefore randomly generates a unit norm beamforming vector $\mathbf{x}[0]$. At the end of each time interval k, with $k \geqslant 1$, the beamforming vector $\mathbf{x}[k]$ will be iteratively updated, as described in detail later. The time interval T between time instants $k-1$ and k must be larger than twice the propagation delay τ_p. With some abuse of notation, in order to keep it simple, it is considered that the transmitted signal $\mathbf{x}[k-1]$ is received and retro-directed by the UE at time k, then collected by the BS[2] (see Fig. 4.14). Thus, the signal received by the UE is

$$\mathbf{z}[k] = \sqrt{P_\mathrm{T}}\,\mathbf{H}\,\mathbf{x}[k-1] + \boldsymbol{\eta}[k] \tag{4.36}$$

where $\mathbf{H} \in \mathbb{C}^{M\times N}$ denotes the channel matrix, and the signal retro-directed

[2]When describing the transmitted signal and the signal received/retro-directed by the UE, time instants k should be intended as intervals. Sampling is operated at the BS after standard matched filter processing of the signal in the last symbol interval of duration T.

by the UE, according to (2.27), is

$$\mathbf{r}[k] = g\, e^{\jmath\phi[k]}\, \mathbf{z}^*[k] = \sqrt{P_{\mathrm{T}}}\, g\, e^{\jmath\phi[k]}\, \mathbf{H}^*\, \mathbf{x}^*[k-1] + g\, \boldsymbol{\eta}^*[k] \tag{4.37}$$

being $\phi[k]$ the phase shift carrying the data generated by the UE in the k-th symbol time. Assuming channel reciprocity, at the BS side the received signal at time instant k, consisting of the feedback of the signal transmitted in the last symbol time, is

$$\begin{aligned}\mathbf{y}[k] =& \sqrt{P_{\mathrm{T}}}\, g\, e^{\jmath\phi[k]}\, \mathbf{H}^{\mathrm{T}}\mathbf{H}^*\mathbf{x}^*[k-1] + g\, \mathbf{H}^{\mathrm{T}}\, \boldsymbol{\eta}^*[k] + \mathbf{w}[k] \\ &+ \sqrt{P_{\mathrm{T}}}\, \mathbf{C}[k]\, \mathbf{x}[k-1]\end{aligned} \tag{4.38}$$

with $\mathbf{w}[k] \sim \mathcal{CN}\left(\mathbf{0}, \sigma_w^2 \mathbf{I}_N\right)$ being the AWGN at the receiver, $\sigma_w^2 = \kappa T_0 F_{\mathrm{AP}}\, W$, F_{AP} the BS' noise figure, and $\mathbf{C}[k]$ the stochastic clutter transfer function determining the signal backscattered by the surrounding environment [128]. The characterization of the clutter strongly depends on the environment. In the radar literature, the clutter is often modelled as homogeneous and with uncorrelated spatial intrinsic reflectivity [128], so $c_{i,j}[k] = [\mathbf{C}[k]]_{i,j}$ are independent, identically distributed (i.i.d.) random variables (RVs) with $c_{i,j}[k] \sim \mathcal{CN}\left(0, \sigma_c^2\right)$, $i, j = 1, 2, \ldots, N$. Regarding the time variability of the clutter, they are considered two extreme cases: fast clutter (*dynamic clutter*), for which matrices $\mathbf{C}[k]$ are considered i.i.d., and *static clutter*, where $\mathbf{C}[k]$ is considered to be almost constant (but still random) during the convergence process of the algorithms proposed, i.e., $\mathbf{C}[k] \simeq \mathbf{C}$. The effect of clutter on the algorithm is binary: below a certain threshold, it has no impact, but above the threshold the algorithm fails, making the user unobservable. Clutter intensity depends on factors like antenna number, transmitted power, and the specific scenario, making accurate modeling challenging. In the following, first it is analysed the dynamic clutter scenario, then the static case will be addressed.

In the presence of dynamic clutter, the last term in (4.38) results in a random vector $\mathbf{c}[k] = \sqrt{P_{\mathrm{T}}}\, \mathbf{C}[k]\, \mathbf{x}[k-1] \sim \mathcal{CN}\left(\mathbf{0}, P_{\mathrm{T}}\, \sigma_c^2 \mathbf{I}_N\right)$, which is uncorrelated with respect to the useful term. From (4.38) is obtained

$$\mathbf{y}[k] = e^{\jmath\phi[k]}\, \mathbf{A}^*\, \mathbf{x}^*[k-1] + \mathbf{n}^*[k] \tag{4.39}$$

where it has been defined $\mathbf{A} = \sqrt{P_{\mathrm{T}}}\, g\, \mathbf{H}^{\dagger}\mathbf{H} \in \mathbb{C}^{N\times N}$ and $\mathbf{n}^{*}[k] = g\, \mathbf{H}^{\mathrm{T}}\, \boldsymbol{\eta}^{*}[k] + \mathbf{w}[k] + \mathbf{c}[k]$, which includes all the noise terms. It is now convenient to introduce the eigenvalue decomposition of matrix $\mathbf{A}$

$$\mathbf{A} = \mathbf{V}\boldsymbol{\Lambda}\mathbf{V}^{\dagger} = \sum_{j=1}^{N} \lambda_j\, \mathbf{v}_j\, \mathbf{v}_j^{\dagger} \tag{4.40}$$

where $\boldsymbol{\Lambda} = \mathrm{diag}\{\lambda_1, \lambda_2, \ldots, \lambda_N\}$, being λ_j the jth eigenvalue with $\lambda_1 \geqslant \lambda_2 \geqslant \ldots, \geqslant \lambda_N$, and $\mathbf{v}_j$ is the jth eigenvector (direction) forming the jth column of matrix $\mathbf{V} \in \mathbb{C}^{N\times N}$. As a consequence, the generic vector $\mathbf{x}[k]$ at the k-th iteration can be decomposed as

$$\mathbf{x}[k] = \sum_{j=1}^{N} x_j[k]\, \mathbf{v}_j \tag{4.41}$$

being $x_j[k] = \mathbf{v}_j^{\dagger}\, \mathbf{x}[k]$ the projection of $\mathbf{x}[k]$ onto the jth direction $\mathbf{v}_j$. Analogously, the noise term can be expressed as

$$\mathbf{n}[k] = \sum_{j=1}^{N} n_j[k]\, \mathbf{v}_j \tag{4.42}$$

where $n_j \sim \mathcal{CN}\left(0, \sigma_j^2\right)$, with

$$\sigma_j^2 = \sigma_w^2 + P_{\mathrm{T}}\, \sigma_c^2 + \frac{\lambda_j\, g\, \sigma_\eta^2}{\sqrt{P_{\mathrm{T}}}}\,. \tag{4.43}$$

Based on the above, in the following it is introduced the iterative Algorithm 1, which is capable of automatically establishing joint communication and beamforming between the UE and the BS.

■ **Algorithm 1**. As appears in the pseudo-code of this procedure the process starts (step 0 of the pseudo-code) with the random generation of a guess unitary norm beamforming vector $\mathbf{x}[0]$. Obviously, any prior information (e.g., past transmission, UE position, etc.) can be exploited to speed up the process, therefore here it is implicitly considered a worst-case scenario. At the $(k-1)$-th iteration, with $k \geqslant 1$, the

Algorithm 1: Modified *Power Method* for joint communication and beamforming between UE - BS

0: *Initialization*: generate a guess unit norm beamforming vector $\mathbf{x}[0]$;
1: **for** $k = 1, \ldots, K$ **do**
2: transmit: $\sqrt{P_{\mathrm{T}}}\,\mathbf{x}[k-1]$; `// signal transmitted by the BS`
3: $\mathbf{z}[k] = \sqrt{P_{\mathrm{T}}}\,\mathbf{H}\,\mathbf{x}[k-1] + \boldsymbol{\eta}[k]$; `// signal received by the UE`
4: $\mathbf{r}[k] = g e^{\jmath\phi[k]} \mathbf{z}^*[k]$; `// signal retro-directed by the UE`
5: receive: $\mathbf{y}[k] = e^{\jmath\phi[k]}\,\mathbf{A}^*\,\mathbf{x}^*[k-1] + \mathbf{n}^*[k]$; `// signal received by the BS`
6: $\mathbf{x}[k] = \mathbf{y}^*[k]/\|\mathbf{y}[k]\|$; `// beamforming vector update`
7: $u[k] = \mathbf{x}^{\dagger}[k-1]\,\mathbf{x}[k]$; `// decision variable`
8: $\widehat{\phi}[k] = \mathsf{detection}\,(-\arg\{u[k]\})$; `// data detection`
end

BS transmits the current version of the beamforming vector, $\mathbf{x}[k-1]$ (step 2), which is then received by the UE (step 3). The latter reflects the received signal along the direction of arrival (thanks to the conjugation operation), modulating its phase based on the data intended for the BS (step 4). Specifically, at the UE, information data is associated with the phase sequence $\{\phi[k]\}_{k=1}^{K}$, forming a packet of length K symbols ($K = \infty$ in case of continuous transmission), according to any phase-based signalling scheme (e.g., BPSK, QPSK, ...).

The BS receives back the response at time instant k from the UE and the environment according to (4.38) (step 5). Then, a normalized and conjugated version of the received vector $\mathbf{y}[k]$ is computed (step 6) and used as the updated beamforming vector $\mathbf{x}[k]$ in the subsequent iteration. Information data is extracted by the BS at each iteration by correlating the current received vector with the previous beamforming vector $\mathbf{x}^{\dagger}[k-1]$, thus forming the decision variable $u[k]$ (step 7); the decision on the modulation symbol conveyed by $\widehat{\phi}[k]$ at the k-th time instant is obtained by means of the function $\mathsf{detection}(\cdot)$, according to the adopted modulation scheme (step 8). Here, symbol-level synchronization between the UE and the BS is assumed.[3] It is worth noticing that data demodulation is operated while the BS is transmitting its

[3]Symbol-level synchronization is not required for the algorithm to converge, but it is necessary to decode the data.

precoding vector, thanks to the full-duplex BS assumption.[4]

In the absence of noise and data, the processing operated in Algorithm 1 corresponds to the *Power Method*, or *Von Mises Iteration*, which allows to estimate the strongest eigenvector of a square matrix $\mathbf{A}$, described by the recurrence relation [129]

$$\mathbf{x}[k] = \frac{\mathbf{A}\,\mathbf{x}[k-1]}{\|\mathbf{A}\,\mathbf{x}[k-1]\|} \tag{4.44}$$

being $\mathbf{x}[0]$ an approximation of the dominant eigenvector or a random vector. For $k \to \infty$, the direction of $\mathbf{x}[k]$ converges to that of the dominant eigenvector. This means that $\mathbf{x}[k]$ tends to the direction of the top eigenvector of the modified round-trip channel $\mathbf{H}^{\dagger}\mathbf{H}$. Note that, because of the conjugation operated by the SCM, $\mathbf{H}^{\dagger}\mathbf{H}$ is not the round-trip channel, which is given, instead, by $\mathbf{H}^{\mathrm{T}}\mathbf{H}$. For this reason, here it is called *modified round-trip channel*.

Now, the convergence of Algorithm 1 in the absence of noise is investigated, then the investigation by introducing the noise and deriving the time evolution of the SNR is also reported.

Convergence in the absence of noise

In this case, it is

$$\mathbf{x}[k] = \frac{\mathbf{y}^{*}[k]}{\|\mathbf{y}[k]\|} = \frac{\mathbf{A}\,e^{-\jmath\phi[k]}\mathbf{x}[k-1]}{\|\mathbf{A}\,e^{-\jmath\phi[k]}\mathbf{x}[k-1]\|}\,. \tag{4.45}$$

[4]While a half-duplex implementation is possible, it requires the TX to switch to the RX mode before the earliest reflected signal arrives at the BS, which depends on the (usually) unknown UE-BS distance. This necessitates a shorter TX time, reducing energy accumulation within a symbol time and resulting in a lower SNR compared to full-duplex. Thus, despite the complexity, the full-duplex implementation remains the more appealing choice.

By unwrapping $k-1$ times the recursion in (4.45) it is

$$\mathbf{x}[k] = \frac{\mathbf{A}^k \, e^{-\jmath \sum_{i=1}^{k} \phi[i]} \mathbf{x}[0]}{\left\| \mathbf{A}^k \, e^{-\jmath \sum_{i=1}^{k} \phi[i]} \mathbf{x}[0] \right\|} \tag{4.46}$$

and

$$\begin{aligned} \mathbf{y}^*[k] &= \mathbf{A}^k \, e^{-\jmath \sum_{i=1}^{k} \phi[i]} \mathbf{x}[0] = e^{-\jmath \sum_{i=1}^{k} \phi[i]} \sum_{j=1}^{N} \lambda_j^k x_j[0] \, \mathbf{v}_j \\ &= \lambda_1^k e^{-\jmath \sum_{i=1}^{k} \phi[i]} \left(x_1[0]\mathbf{v}_1 + \sum_{j=2}^{N} \left(\frac{\lambda_j}{\lambda_1} \right)^k x_j[0]\mathbf{v}_j \right) . \end{aligned} \tag{4.47}$$

By substituting (4.47) in (4.46) and letting k grow, it is obtained

$$\begin{aligned} \mathbf{x}[k] = & \frac{e^{-\jmath \sum_{i=1}^{k} \phi[i]} \left(x_1[0]\mathbf{v}_1 + \sum_{j=2}^{N} \left(\frac{\lambda_j}{\lambda_1} \right)^k x_j[0]\mathbf{v}_j \right)}{\left\| x_1[0]\mathbf{v}_1 + \sum_{j=2}^{N} \left(\frac{\lambda_j}{\lambda_1} \right)^k x_j[0]\mathbf{v}_j \right\|} \\ & \xrightarrow{k \to \infty} \mathbf{v}_1 \, e^{-\jmath \sum_{i=1}^{k} \phi[i]} \end{aligned} \tag{4.48}$$

which converges to the top eigenvector $\mathbf{v}_1$ with convergence rate related to λ_2/λ_1. It is worth noticing that the complex scalar $e^{-\jmath \sum_{i=1}^{k} \phi[i]}$, being a multiplicative factor for all components of $\mathbf{v}_1$, does not make the (asymptotic) direction of $\mathbf{x}[k]$ divert from that of $\mathbf{v}_1$. Later in the numerical results, it will be shown that only a few iterations are needed to approach the asymptotic value, that is, to perform optimum beamforming, under common channel conditions. As far as the demodulation is concerned, from (4.48) it immediately follows that asymptotically (practically, in a few iterations) the decision variable $u[k]$ is

$$u[k] = \mathbf{x}[k-1]^\dagger \, \mathbf{x}[k] = e^{-\jmath \phi[k]} \tag{4.49}$$

and the k-th phase information $\phi[k]$ can be retrieved.

Convergence with the noise

Now the noise is reintroduced and it is evaluated the SNR at the discrete time k (i.e., in the k-th iteration) for the demodulation of the data associated

with the phase. In the presence of the noise, (4.45) reads

$$\mathbf{x}[k] = \frac{\mathbf{y}^*[k]}{\|\mathbf{y}[k]\|} = \frac{\mathbf{A}\, e^{-\jmath\phi[k]}\mathbf{x}[k-1] + \mathbf{n}[k]}{\|\mathbf{A}\, e^{-\jmath\phi[k]}\mathbf{x}[k-1] + \mathbf{n}[k]\|} \tag{4.50}$$

where

$$\mathbf{y}^*[k] = \sum_{j=1}^{N} \mathbf{v}_j \left(\lambda_j x_j[k-1] e^{-\jmath\phi[k]} + n_j[k]\right) . \tag{4.51}$$

Note that the term carrying the information (i.e., the phase $\phi[k]$) also includes the noise from the previous iterations, which is contained in $x_j[k-1]$. The decision variable $u[k]$ at the k-th symbol is proportional to the product

$$\begin{aligned} u[k] &\propto \mathbf{x}^\dagger[k-1]\, \mathbf{y}^*[k] \\ &= \mathbf{x}^\dagger[k-1]\, \mathbf{A}\, e^{-\jmath\phi[k]}\mathbf{x}[k-1] + \mathbf{x}^\dagger[k-1]\, \mathbf{n}[k] \\ &= e^{-\jmath\phi[k]} \sum_{j=1}^{N} \lambda_j \left|x_j[k-1]\right|^2 + \mathbf{x}^\dagger[k-1]\, \mathbf{n}[k] \end{aligned} \tag{4.52}$$

in which the first term is the useful one, as it contains the phase $\phi[k]$, and the second term represents the noise. In the following analysis, it is considered the particular case in which the noise generated by the SCM and seen by the receiver is negligible compared to the other two noise components, i.e., $\sigma_j^2 \simeq \sigma^2$, with $\sigma^2 = \sigma_w^2 + P_{\mathrm{T}}\, \sigma_c^2 \;\; \forall j$, which is reasonable considering it is attenuated by the UE-BS channel. Therefore, considering that by construction $\|\mathbf{x}[k]\|^2 = 1$, the SNR at the input of the detector for the k-th time instant is

$$\mathsf{SNR}^{(\mathrm{dec})}[k] = \frac{\left(\sum_{j=1}^{N} \lambda_j \;\left|x_j[k-1]\right|^2\right)^2}{\sigma^2} . \tag{4.53}$$

Note that $\left|x_j[k-1]\right|^2 / \left\|\mathbf{x}[k-1]\right\|^2 = \left|x_j[k-1]\right|^2$ represents the fraction of the total power (useful plus noise) transmitted by the UE associated with direction $\mathbf{v}_j$ at the discrete time $k-1$. Then, at the end of the k-th time interval, the SNR (at the BS) along the direction $\mathbf{v}_j$ is given by

$$\mathsf{SNR}_j[k] = \frac{\lambda_j^2 \left|x_j[k-1]\right|^2}{\sigma^2} . \tag{4.54}$$

Therefore, it can be rewritten (4.53) as a function of $\mathsf{SNR}_j[k]$ as

$$\mathsf{SNR}^{(\mathrm{dec})}[k] = \left(\sum_{j=1}^{N} \frac{\mathsf{SNR}_j[k]}{\sqrt{\mathsf{SNR}_j^{(\max)}}} \right)^2 \tag{4.55}$$

where

$$\mathsf{SNR}_j^{(\max)} = \frac{\lambda_j^2}{\sigma^2} \tag{4.56}$$

represents the maximum SNR along the direction $\mathbf{v}_j$, i.e., the SNR it would obtain if all the power were concentrated in the direction $\mathbf{v}_j$. The goal is now to determine an iterative expression for $\mathsf{SNR}^{(\mathrm{dec})}[k]$, which drives the signal demodulation performance, and evaluate the convergence condition for the Algorithm 1 proposed. Considering (4.51), the fraction of the total power that is associated with direction $\mathbf{v}_j$ at the beginning of time interval k can be written as

$$|x_j[k]|^2 = \frac{\lambda_j^2 \, |x_j[k-1]|^2 + \sigma^2}{\sum_{i=1}^{N} \left(\lambda_i^2 \, |x_i[k-1]|^2 + \sigma^2 \right)} \, . \tag{4.57}$$

Then, by inverting (4.54) and plugging $|x_j[k]|^2$ at both the left-hand and right-hand sides of (4.57), the following iterative formula for $\mathsf{SNR}_j[k]$ is obtained

$$\begin{aligned} \mathsf{SNR}_j[k] &= \frac{\lambda_j^2 \left(\mathsf{SNR}_j[k-1] + 1 \right)}{\sigma^2 \left[\sum_{i=1}^{N} \left(\mathsf{SNR}_i[k-1] + 1 \right) \right]} \\ &= \mathsf{SNR}_j^{(\max)} \frac{\mathsf{SNR}_j[k-1] + 1}{N + \sum_{i=1}^{N} \mathsf{SNR}_i[k-1]} \end{aligned} \tag{4.58}$$

for $k \geqslant 2$, where

$$\mathsf{SNR}_j[1] = \mathsf{SNR}_j^{(\max)} \, |x_j[0]|^2 \, . \tag{4.59}$$

Denote by $r = \mathrm{rank}\,(\mathbf{A})$ the rank of matrix $\mathbf{A}$, i.e., the rank of the channel. In the particular case of a channel that has rank $r = 1$ (e.g., a far-field LOS

channel with negligible multipath), (4.55) is given by

$$\mathsf{SNR}^{(\mathrm{dec})}[k] = \frac{\left(\mathsf{SNR}_1[k]\right)^2}{\mathsf{SNR}_1^{(\max)}} \tag{4.60}$$

with the SNR at the k-th time instant along direction $\mathbf{v}_1$ in (4.58) expressed as

$$\mathsf{SNR}_1[k] = \mathsf{SNR}_1^{(\max)} \frac{\mathsf{SNR}_1[k-1]+1}{N+\mathsf{SNR}_1[k-1]}\,. \tag{4.61}$$

The rank-1 case allows an easy evaluation of the convergence value. Following the approach proposed in [32], the solution at the equilibrium of the recursive expression in (4.61) can be found by solving

$$x = b\frac{x+1}{a+x} \tag{4.62}$$

with $a = N$ and $b = \mathsf{SNR}_1^{(\max)}$. When $b \gg a$, the solution is $x \simeq b - a \simeq b \gg 1$, whereas $x \simeq b/a \ll 1$ when $b \ll a$. In the particular case of $a = b$ it is $x = \sqrt{b}$. Therefore, if $\mathsf{SNR}_1^{(\max)}/N \gg 1$, at the convergence it is $\mathsf{SNR}^{(\mathrm{dec})}[k] \simeq \mathsf{SNR}_1^{(\max)}$, which takes the role of asymptotic SNR corresponding to the optimum beamforming vector for a channel with $r = 1$. Note that, if $\mathbf{x}[0]$ is randomly chosen, it is $|x_j[0]|^2 \simeq 1/N$, and hence at the first iteration (i.e., at the system bootstrap) it is $\mathsf{SNR}_1[1] \simeq \mathsf{SNR}_1^{(\max)}/N$. Therefore, the ratio $\mathsf{SNR}_1^{(\mathrm{boot})} = \mathsf{SNR}_1^{(\max)}/N$ is referred to as *bootstrap* SNR. When the bootstrap SNR is much less than one, convergence is still achieved, but with $\mathsf{SNR}^{(\mathrm{dec})}[k] \ll 1$. It is worth noticing that the convergence value does not depend on the initial random guess $\mathbf{x}[0]$, but only on the bootstrap SNR. It is interesting to investigate the implications of the above results in simple scenarios, such as in free space. In this case, the generic element of the channel matrix $\mathbf{H}$ related to the channel between the ith element of the BS's antenna and the jth antenna of the SCM, is

$$h_{i,j} = \frac{\sqrt{G_{\mathrm{BS}}\, G_{\mathrm{SCM}}}\,\lambda}{4\pi\, d_{i,j}} e^{-\jmath\frac{2\pi d_{i,j}}{\lambda}} \tag{4.63}$$

where $d_{i,j}$ is the distance, λ is the wavelength, G_{BS} and G_{SCM} are the gain of the elements of the BS's antenna and the SCM's antenna, respectively. As an example, with reference to Fig. 2.6, in far-field $\mathbf{v}_1$ takes the form of (2.24), that is, the beam steering vector pointing towards the direction Ψ, being Ψ the direction of arrival of the BS signal with respect to the UE. At the UE side, after conjugation, the retro-directed signal in (2.27) has direction of departure Ψ, which means that the signal reflected by the SCM points back to the BS. More specifically, assuming the BS and the SCM are in paraxial configuration ($\Psi = 0$), the first eigenvalue of $\mathbf{A}$ is given by [130]

$$\lambda_1 \simeq \frac{\sqrt{P_{\mathrm{T}}}\, g\, N\, M\, G_{\mathrm{BS}}\, G_{\mathrm{SCM}}\, \lambda^2}{(4\pi\, d)^2}\,. \tag{4.64}$$

As a consequence, the maximum and bootstrap SNRs become, respectively,

$$\mathsf{SNR}_1^{(\mathrm{max})} = \frac{P_{\mathrm{T}}\, g^2\, N^2\, M^2\, G_{\mathrm{BS}}^2\, G_{\mathrm{SCM}}^2\, \lambda^4}{\sigma^2\ (4\pi\, d)^4} \tag{4.65}$$

$$\mathsf{SNR}_1^{(\mathrm{boot})} = \frac{P_{\mathrm{T}}\, g^2\, N\, M^2\, G_{\mathrm{BS}}^2\, G_{\mathrm{SCM}}^2\, \lambda^4}{\sigma^2\ (4\pi\, d)^4}\,. \tag{4.66}$$

Remarks: The last equations show that, due to the backscattering nature of the communication, the path loss increases with the distance to the power of four, as happens with radio frequency identification (RFID) systems based on backscatter modulation [131]. On the other hand, such large path loss can be compensated by increasing the number of antenna elements N and M at the BS and UE, respectively. Increasing N and M is beneficial also for the bootstrap SNR, even though M has a higher impact than N. Another way to compensate for the path loss is to fix the areas of the BS and UE and increase the frequency. In this way, since the area of the BS's antenna is equal to $A_{\mathrm{BS}} = N\lambda^2/4$ and the area of the UE's antenna is equal to $A_{\mathrm{SCM}} = M\lambda^2/4$, (4.65) becomes

$$\mathsf{SNR}_1^{(\mathrm{max})} = \frac{P_{\mathrm{T}}\, g^2\, 16 A_{\mathrm{BS}}^2 G_{\mathrm{BS}}^2\, 16 A_{\mathrm{SCM}}^2 G_{\mathrm{SCM}}^2}{\lambda^4 \sigma^2\ (4\pi\, d)^4} \tag{4.67}$$

which highlights that, by keeping the area of the antenna arrays constant,

the SNR increases with the fourth power of the frequency, and hence our scheme is particularly suitable for high-frequency implementations.

The proposed system works independently of the channel characteristics (far-field, near-field, free-space, multipath, ...), and number of antenna elements, and it is completely blind as it does not require any explicit channel estimation. The result is the fast establishment of a single-layer MIMO communication link with an extremely simple UE which does not require any ADC chain. It also allows channel tracking provided that the channel dynamics are not faster than the convergence speed, which depends on the ratio λ_2^2/λ_1^2 and the symbol time T, as it will be investigated in the numerical results. The latter could be significantly small as it is lower bounded by the propagation round-trip time ($< 100\,\text{ns}$ in indoor environments) and the BS computational capacity.

It is worth noticing that when the channel has rank $r = 1$, the resulting Algorithm 1 is capacity-optimal. When $r > 1$, the scheme is not capacity-optimal because the SCM is intrinsically single-layer so that only one out of r potential data streams that could be established between the BS and the UE is exploited (lower spectral efficiency). However, it corresponds to the optimal single-layer beamforming scheme in the SNR maximization sense [132]. As a consequence, it contributes to maximizing and reducing the fluctuations of the SNR at the decision variable thus providing the maximum diversity gain. This is achieved with extremely low complexity with respect to classical implementations, which require CSI estimation and analog/digital beamforming.

Notice that the precoding vector $\mathbf{x}[k]$, transmitted at the instant k, determines the shape of the beam according to classic antenna array theory. At the beginning of the Algorithm 1, i.e. at $k = 0$, the beam takes a random shape because the sensor's position is unknown, and consequently, $\mathbf{x}[0]$ is chosen randomly. During the iterative algorithm, the shape of the transmitted beam evolves from a random shape to the top right eigenvector of the channel. In free-space conditions, this corresponds to beam steering toward the intended user, whereas in a more complex propagation setting (e.g., with multipath), it might take a more articulated shape. In Fig. 4.15, a graphical example of the evolution of the beam's shape is illustrated in the free-space

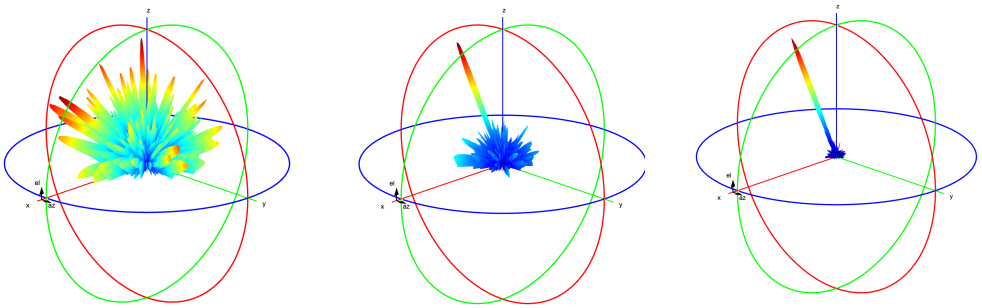

(a) (b) (c)

Figure 4.15: Evolution of the beam's shape at time $k = 1$ (a), $k = 2$ (b), and $k = 3$ (c).

condition. Note that the beam converges very fast to the final shape.

Analysis with static clutter

In the presence of static clutter, for which $\mathbf{C}[k] \simeq \mathbf{C}$, the term $\sqrt{P_\mathrm{T}}\,\mathbf{C}\,\mathbf{x}[k-1]$ in (4.38) is no longer uncorrelated with respect to the first term and it cannot be considered as additive noise. As a consequence, the iterative Algorithm 1 will converge to the strongest eigenvector of matrix $\tilde{\mathbf{A}} = \mathbf{A} + \sqrt{P_\mathrm{T}}\,\mathbf{C}$ instead of $\mathbf{v}_1$, i.e., that of matrix $\mathbf{A}$ associated with the UE. In the presence of strong clutter caused, for instance, by scatterers located close to the BS, it might happen that the largest eigenvector of $\tilde{\mathbf{A}}$ corresponds to a beam steering towards the scatterers instead of the UE. A general analysis of the problem appears prohibitive due to the presence of a random matrix. However, it is possible to derive a worst-case asymptotic condition on σ_c^2 for a large number N of antennas at the BS. Specifically, the worst-case scenario is that where the subspaces spanned by $\mathbf{A}$ and $\mathbf{C}$ are disjoint, meaning, for instance, that the UE and the scatterers are located far away from each other. On the contrary, if $\mathbf{A}$ and $\mathbf{C}$ had a common subspace, the strongest eigenvector of $\tilde{\mathbf{A}}$ would be likely partially steered toward the UE then making the communication still possible. Under the worst-case assumption, Algorithm 1 fails to converge to $\mathbf{v}_1$ in favor of the strongest eigenvector of $\mathbf{C}$ if $\lambda_1 < \sqrt{P_\mathrm{T}}\lambda_1^{(\mathrm{c})}$, where λ_1 and $\lambda_1^{(\mathrm{c})}$ are the largest eigenvalues of $\mathbf{A}$ and $\mathbf{C}$, respectively. Being

$\mathbf{C}$ a random matrix, the previous inequality has to be intended as an event that requires a statistical characterization. From the Tracy-Widom law, it is known that the largest eigenvalue of a random matrix of size N with i.i.d. Gaussian entries having variance σ_{c}^2 converges almost surely to the value $2\sigma_{\mathrm{c}}^2\sqrt{N}$ for increasing N [133]. Therefore, Algorithm 1 will converge to $\mathbf{v}_1$ if the following condition holds

$$\sigma_{\mathrm{c}}^2 < \frac{\lambda_1^2}{4\,P_{\mathrm{T}}\,N} = \sigma_{\mathrm{t}}^2\,. \tag{4.68}$$

In the non-worst-case scenario, condition (4.68) is still valid even though conservative. It is interesting to point out that λ_1^2 increases with N^2 (see, for instance, (4.64)), then the threshold σ_{t}^2 increases with N, meaning that Algorithm 1 can be made more robust to static clutter by increasing the number of antennas at the BS.

Single User Scenario Numerical Results

Here some numerical examples to investigate the performance of the proposed SCM-based joint communication and beamforming scheme are reported. The values of the system parameters adopted for the analysis and the simulations are those reported in Table 4.3, if not otherwise specified. The BS, equipped with a planar array deployed along the xy-plane, is located at $(0, 0, 0)$ [m]. Both free-space and more realistic 3GPP TR 38.901 channel models [134] have been considered in the simulations, the latter with a delay spread of 9 ns. In particular, among the NLOS channel models provided in [134] (Clustered Delay Line (CDL)-A, CDL-B, and CDL-C), CDL-C is chosen because it features higher path delays than CDL-B and more evenly distributed over time than CDL-A. Concerning LOS channel models (CDL-D, CDL-E), it has opted for CDL-E because it features higher path delays than CDL-D. There is more focus on the CDL-C, as the NLOS condition is more challenging.

These results are obtained by using the Algorithm 1 in the presence of dynamic clutter. The UE is located at $(0, 0, 10)$ [m] with a SCM deployed along the xy-plane. In Fig. 4.16(a), the evolution of $\mathsf{SNR}^{(\mathrm{dec})}[k]$ is shown in static free-space condition for two values of the transmitted power, $P_{\mathrm{T}} =$

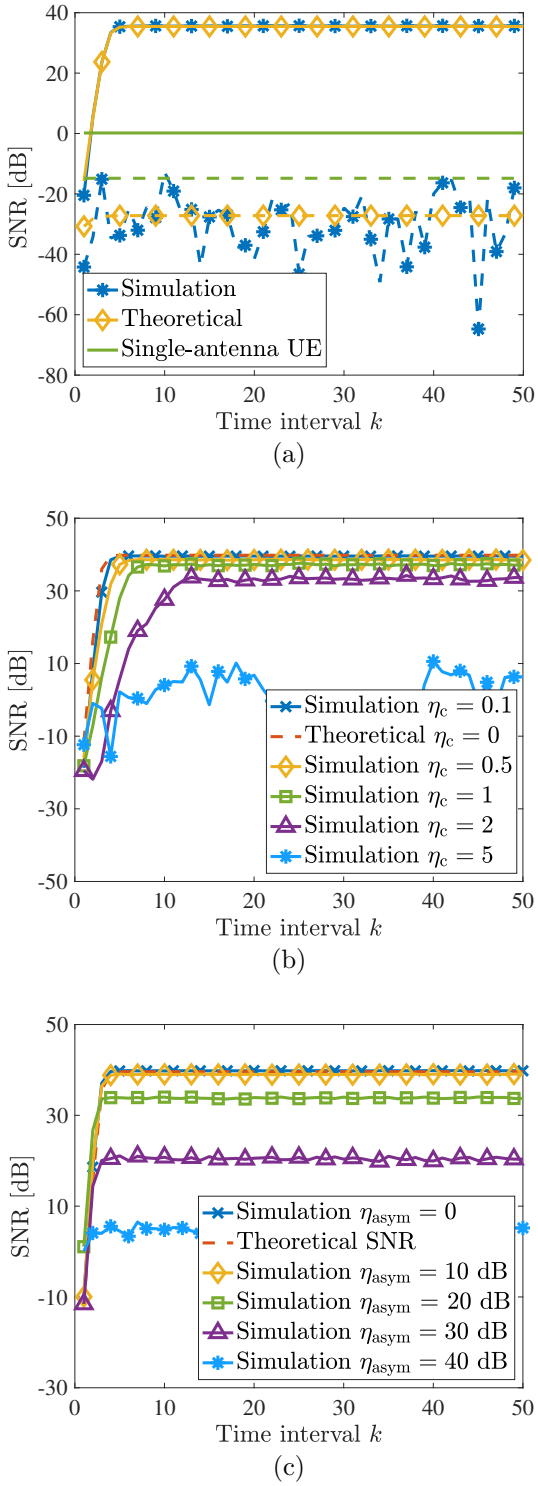

Figure 4.16: Free space propagation. (a) Dynamic clutter. Continuous lines $P_T = -30\,\text{dBm}$; dashed lines $P_T = -45\,\text{dBm}$. (b) Effect of static clutter, $P_T = -30\,\text{dBm}$. (c) Effect of channel non-reciprocity, $P_T = -30\,\text{dBm}$.

Table 4.3: Parameters used in the analysis and the simulations.

Parameter	Symbol	Value
Carrier frequency	f_{c}	28 GHz
BS antenna element gain	G_{BS}	0 dB (isotropic)
SCM antenna element gain	G_{SCM}	0 dB (isotropic)
SCM backscatter gain	g	29 dB
Bandwidth	W	240 kHz
Symbol time	T	4.2 μs
Total TX power	P_{T}	-30 dBm
SCM noise figure	F_{SCM}	3 dB
BS noise figure	F_{AP}	3 dB
BS antenna elements	N	20×20 ($10\times10\,\mathrm{cm}^2$ planar array)
SCM antenna elements per UE	M	10×10 ($5\times5\,\mathrm{cm}^2$ planar array)
Dynamic clutter	σ_c^2	$2\cdot10^{-15}$
Static clutter	η_{c}	0
Path-loss exponent	β	2 (free-space/LOS), 2.5 (NLOS)

$-30\,\mathrm{dBm}$ and $P_{\mathrm{T}} = -45\,\mathrm{dBm}$, corresponding to $\mathsf{SNR}^{(\mathrm{boot})} = 10.3\,\mathrm{dB}$, and $\mathsf{SNR}^{(\mathrm{boot})} = -4.7\,\mathrm{dB}$, respectively. Simulation results are compared with the theoretical ones obtained by evaluating (4.55). From the plots, it can be clearly noticed that when $\mathsf{SNR}_1^{(\mathrm{boot})} > 0\,\mathrm{dB}$ the SNR converges to $\mathsf{SNR}_1^{(\mathrm{max})}$, given by (4.65), within 4-5 time intervals (i.e., 4-5 iterations of the algorithm), whereas it converges to very low values when $\mathsf{SNR}_1^{(\mathrm{boot})} < 0\,\mathrm{dB}$. The SNRs that would be obtained with a single-antenna backscattering UE is also given as a reference (the green flat curves) in order to emphasize the large gain introduced by the SCM and the antenna array at the BS, despite the large path loss experienced at the considered carrier frequency (28 GHz) and the two-way backscatter channel. In Fig. 4.16(b), the effect of static clutter is investigated for different values of the ratio $\eta\mathrm{c} = \sigma_{\mathrm{c}}^2/\sigma_{\mathrm{t}}^2$ for one realization of the clutter matrix $\mathbf{C}$. As long as η_{c} overcomes 1, the performance degrades rapidly until a complete lack of convergence, as it can be seen for $\eta_{\mathrm{c}} = 5$, indicating that the beam focuses on the strong clutter instead of on the user. The impact of channel non-reciprocity caused, for instance, by asymmetric SCMs, is reported in Fig. 4.16(c). Non-reciprocity has been simulated by substituting $(\mathbf{H}+\mathbf{R})^{\dagger}$ to $\mathbf{H}^{\dagger}$ in the backward channel, where $\mathbf{R}$ is modeled as a random matrix with zero mean complex Gaussian elements and variance

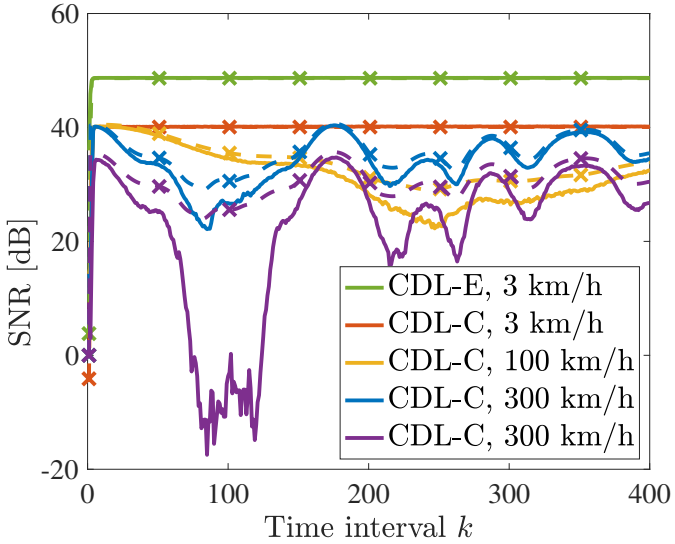

Figure 4.17: Transients of the SNR for the single-user scenario. Dynamic clutter. LOS/NLOS 3GPP channel models. Continuous lines refer to simulation results; dashed lines with markers refer to theoretical curves. Transmitted power $P_{\mathrm{T}} = -10$ dBm; curves for CDL-C at 300 km/h with $P_{\mathrm{T}} = -15$ dBm.

σ^2_{asym}. Plots for different ratios $\eta_{\mathrm{asym}} = \sigma^2_{\mathrm{asym}}\, N\, M/\|\mathbf{H}\|^2_{\mathrm{F}}$ are shown, being $\|\mathbf{H}\|_{\mathrm{F}}$ the Frobenius norm of matrix $\mathbf{H}$. The results indicate that the proposed scheme is very robust to forward-backward channel asymmetries until η_{asym} remains below N (26 dB).

Results with more realistic, time-variant, multipath 3GPP channel models, namely the CDL models [134], are shown in Fig. 4.17 for $P_{\mathrm{T}} = -10$ dBm and $P_{\mathrm{T}} = -15$ dBm. In particular, the LOS CDL-E and the NLOS CDL-C channel models [134] have been considered for different speeds from 3 km/h up to 300 km/h. The behaviour of the SNR assuming perfect estimation of the top eigenvector, i.e., $\mathsf{SNR}_1^{(\mathrm{max})}$, is reported for comparison (see the *theoretical* curves plotted with a dashed style).[5] The results demonstrate the capability of Algorithm 1 to track the fading evolution at very high speed as long as $\mathsf{SNR}_1^{(\mathrm{boot})} = \mathsf{SNR}_1^{(\mathrm{max})}/N \gg 1$. When $\mathsf{SNR}_1^{(\mathrm{boot})} < 1$, i.e., $\mathsf{SNR} < 26$ dB (note that $10\log_{10} N = 26$), because of fading, the algorithm

[5]Being the channel time-variant, also $\mathsf{SNR}_1^{(\mathrm{max})}$ becomes time variant during the transmission of a packet.

stops tracking until $\mathsf{SNR} > 26\,\mathrm{dB}$ again, showing a fast recovery. This can be explained by considering that the Doppler frequency at a speed of $v = 300\,\mathrm{km/h}$ is $f_\mathrm{d} = f_0\, v/c = 7.8\,\mathrm{kHz}$, corresponding to a coherence time of roughly $T_\mathrm{c} \approx 1/f_\mathrm{d} = 128\,\mu\mathrm{s}$, which is much more than the symbol time $T = 4.2\,\mu\mathrm{s}$. Since $f_\mathrm{d} \ll f_0$, in our analysis, the effect of Doppler frequency shift in the SCM response characterization is neglected. It can also be observed that the range of fading variation during tracking is relatively narrow, approximately 10 dB. This limited range is a consequence of the diversity gain intrinsic in the communication associated with the strongest eigenvector. Moreover, it can be noticed that the initial transient to achieve the convergence in NLOS conditions (CDL-C), characterized by significant multipath components, is slightly larger than that of the LOS condition (CDL-E). However, it falls below 8-time intervals (i.e., $36\,\mu\mathrm{s}$), confirming that the proposed scheme achieves initial beamforming and link setup with extremely low latency. In any case, it is safe not to transmit data during the initial transient by setting to zero the phase $\phi[k]$ within the preamble, that is, for $k = 1, 2, \ldots, K_p$, with K_p larger than the expected transient duration.

Multi User Scenario

Consider now the scenario shown in Fig. 4.18, in which there are U users equipped with the proposed SCMs with the aim of establishing up to L parallel Multi-User MIMO (MU-MIMO) links. Denote with $\mathbf{H}^{(1)}$, $\mathbf{H}^{(2)}$, ..., $\mathbf{H}^{(U)} \in \mathbb{C}^{M\times N}$ the channel matrices related to the U links between the BS and the users. For further convenience, it can be defined as the total channel matrix $\mathbf{H}$ of size $MU \times N$

$$\mathbf{H} = \begin{bmatrix} \mathbf{H}^{(1)} \\ \mathbf{H}^{(2)} \\ \cdots \\ \mathbf{H}^{(U)} \end{bmatrix} \tag{4.69}$$

and the matrix $\mathbf{A} \in \mathbb{C}^{N\times N}$ as

$$\mathbf{A} = \sqrt{P_\mathrm{T}}\, g\, \mathbf{H}^\dagger \mathbf{H}\,. \tag{4.70}$$

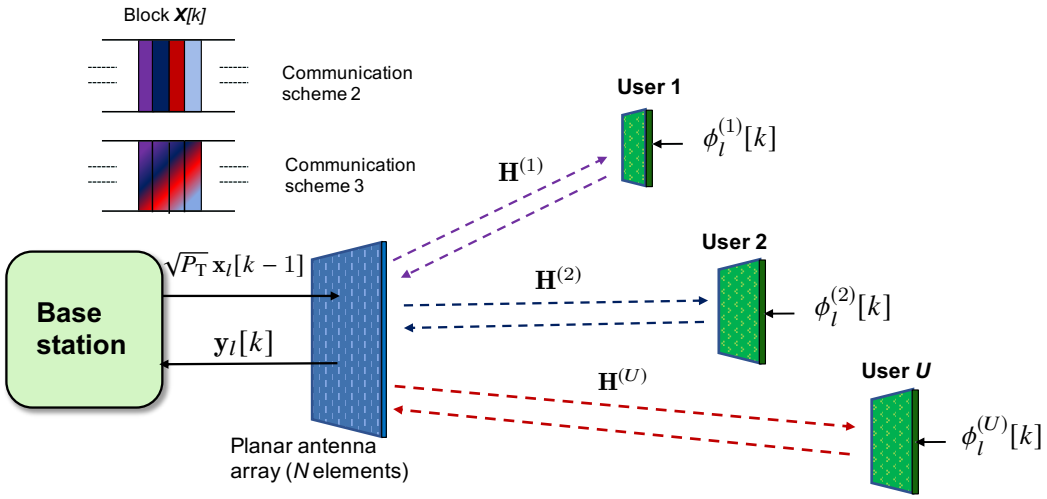

Figure 4.18: Multi-user system model. On the top-left, an example of the block composition in Algorithms (here Communication schemes) 2 and 3. In the former, the estimated eigenvectors are sent in sequence, thus addressing each user sequentially. In the latter, a linear combination of all the estimated eigenvectors is sent, thus addressing all the users simultaneously.

Note that $\mathbf{A} = \sum_{u=1}^{U} \mathbf{A}^{(u)}$, with $\mathbf{A}^{(u)} \in \mathbb{C}^{N\times N}$ given by

$$\mathbf{A}^{(u)} = \sqrt{P_T}\, g\, \left(\mathbf{H}^{(u)}\right)^{\dagger} \mathbf{H}^{(u)} \tag{4.71}$$

for $u = 1, 2, \ldots, U$. Define $r^{(u)} = \operatorname{rank}\left(\mathbf{A}^{(u)}\right)$, and $\mathbf{v}_i^{(u)}$ the ith eigenvector of $\mathbf{A}^{(u)}$, with $i = 1, 2, \ldots, r^{(u)}$. Note that now P_T represents the total transmitted power. Let it be assumed that the subspaces spanned by $\mathbf{H}^{(u)}$ are orthogonal, and so those by $\mathbf{A}^{(u)}$, for $u = 1, 2, \ldots, U$. This implies that $\mathbf{A}^{(u)}\, \mathbf{v}_i^{(p)} = 0$, $\forall p \neq u$ and $i = 1, 2, \ldots, r^{(p)}$. As a consequence, the top eigenvectors $\{\mathbf{v}_j\}$ of $\mathbf{A}$ are given by the eigenvectors $\mathbf{v}_i^{(u)}$, i.e., $\mathbf{v}_j = \mathbf{v}_i^{(u)}$, where

$$j = j(u, i) = \sum_{n=1}^{u-1} r^{(n)} + i \tag{4.72}$$

with $u = 1, 2, \ldots U$, $i = 1, 2, \ldots, r^{(u)}$, and $\sum_{u=1}^{U} r^{(u)} \leqslant N$. This means that each user is associated with a dedicated subset of eigenvectors of $\mathbf{A}$. For instance, in free-space and far-field conditions, each eigenvector will correspond to one user. In such a case, if the BS was capable of estimating the

$L \leqslant U$ strongest eigenvectors, then the optimal MU-MIMO communication with L out of U users would be established. More in general, to establish a communication link with U UEs, L must be larger than U because the same data stream generated by one UE affects multiple directions $\mathbf{v}_i^{(u)}$ that might not be ordered in terms of associated eigenvalues. In this case, it is supposed the data streams are reordered by the higher layers of the protocol stack. Without loss of generality, in the rest of the discussion is supposed the top-L eigenvectors of $\mathbf{A}$ correspond to distinct UEs, i.e., $\mathbf{v}_j = \mathbf{v}_1^{(j)}$, for $j = 1, 2, \ldots, L$, and $L \leqslant U$. The above disjoint assumption might correspond to the situation where users are located at different positions and a large number of antennas are used on both sides in a rich scattering scenario, as in massive MIMO systems (thus exploiting favorable propagation conditions). In practical contexts, such an assumption might not be exactly satisfied thus generating interference between users. This phenomenon will be investigated in the numerical results.

In the following, the approach considered in the previous subsection is extended to estimate the L strongest eigenvectors of $\mathbf{A}$.

Beamforming vector estimation with no data transmission

The first case considered is where no data are transmitted, and the purpose is to estimate the L-top eigenvectors of $\mathbf{A}$ forming the columns of matrix $\mathbf{V}_L$ which contains the first L-left columns of $\mathbf{V}$. This can be accomplished by customizing to our case the block version of the Power Method [129], also known as *Orthogonal Iteration*, to account for the operation performed by the SCM. The algorithm, presented below as Algorithm 2 along with its accompanying pseudo-code, exemplifies how this adaptation is implemented.

■ **Algorithm 2**. The scheme starts at iteration $k = 0$ with the generation of a random unitary matrix $\mathbf{X}[0] \in \mathbb{C}^{N \times L}$ (step 0 of the pseudo-code). Each iteration of this algorithm (*for* loop in step 2) consists of the consecutive transmission of the L columns $\mathbf{x}_l[k]$, $l = 1, 2, \ldots, L$, of matrix $\mathbf{X}[k] \in \mathbb{C}^{N \times L}$ (*block*) (step 3). It is worth noticing that, since L transmissions occur in each iteration, the total number of transmissions (time intervals) after k iterations is kL. In particular, the signal received by the SCM of the uth UE during the lth transmission interval

Algorithm 2: Modified *Block Power method* for a multi-user scenario. No data transmission.

0: *Initialization*: generate a random unitary matrix $\mathbf{X}[0] \in \mathbb{C}^{N \times L}$;
1: **for** $k = 1, \ldots, K$ **do**
  2: **for** $l = 1, \ldots, L$ **do**
    3: transmit: $\sqrt{P_{\mathrm{T}}}\,\mathbf{x}_l[k-1]$; `// signal transmitted by the BS`
    4: $\mathbf{z}_l^{(u)}[k] = \sqrt{P_{\mathrm{T}}}\,\mathbf{H}^{(u)}\,\mathbf{x}_l[k-1] + \boldsymbol{\eta}_l^{(u)}[k]$; `// signal received by the UE`
    5: $\mathbf{r}_l^{(u)}[k] = g\left(\mathbf{z}_l^{(u)}[k]\right)^*$; `// signal retro-directed by the UE`
    6: $\mathbf{y}_l[k] = \mathbf{H}^{\mathrm{T}}\mathbf{r}_l[k] + \mathbf{w}_l[k] + \mathbf{c}_l[k]$; `// signal received by the BS`
  end
  7: $\mathbf{Q} = \mathsf{QR}\left(\mathbf{Y}^*[k]\right)$; QR decomposition of $\mathbf{Y}^*[k] = \{\mathbf{y}_l^*[k]\}_{l=1}^{L}$; `// QR decomposition`
  8: $\mathbf{X}[k] = \mathbf{Q}$, where $\mathbf{X}[k] = \{\mathbf{x}_l[k]\}_{l=1}^{L}$; `// beamforming vectors update`
end

of the k-th iteration is

$$\mathbf{z}_l^{(u)}[k] = \sqrt{P_{\mathrm{T}}}\,\mathbf{H}^{(u)}\,\mathbf{x}_l[k-1] + \boldsymbol{\eta}_l^{(u)}[k] \tag{4.73}$$

where $\boldsymbol{\eta}_l^{(u)}[k] \sim \mathcal{CN}\left(\mathbf{0}, \sigma_\eta^2 \mathbf{I}_M\right)$ is the noise at the uth SCM (step 4). By defining

$$\mathbf{r}_l[k] = \mathrm{vec}\left(\mathbf{r}_l^{(1)}[k], \ldots, \mathbf{r}_l^{(U)}[k]\right) \tag{4.74}$$

with

$$\mathbf{r}_l^{(u)}[k] = g\left(\mathbf{z}_l^{(u)}[k]\right)^* \tag{4.75}$$

denoting the signal retro-directed by the uth UE (step 5), the signal

received by the BS at the lth time interval (step 6) can be written as

$$\begin{aligned}\mathbf{y}_l[k] =&\mathbf{H}^{\mathrm{T}}\mathbf{r}_l[k] + \mathbf{w}_l[k] + \sqrt{P_{\mathrm{T}}}\,\mathbf{C}\,\mathbf{x}_l[k-1] \\ =&\sum_{u=1}^{U}\left(\mathbf{A}^{(u)}\right)^{*}\mathbf{x}_l^{*}[k-1] \\ &+ g\sum_{u=1}^{U}\left(\mathbf{H}^{(u)}\right)^{\mathrm{T}}\left(\boldsymbol{\eta}^{(u)}[k]\right)^{*} + \mathbf{w}_l[k] + \mathbf{c}_l[k] \\ =&\mathbf{A}^{*}\mathbf{x}_l^{*}[k-1] + g\sum_{u=1}^{U}\left(\mathbf{H}^{(u)}\right)^{\mathrm{T}}\left(\boldsymbol{\eta}^{(u)}[k]\right)^{*} \\ &+ \mathbf{w}_l[k] + \mathbf{c}_l[k] \end{aligned} \tag{4.76}$$

for $l = 1, 2, \ldots, L$, where $\mathbf{w}_l[k] \sim \mathcal{CN}\left(\mathbf{0}, \sigma_w^2\mathbf{I}_N\right)$, and $\mathbf{c}_l[k] \sim \mathcal{CN}\left(\mathbf{0}, P_{\mathrm{T}}\,\sigma_c^2\mathbf{I}_N\right)$.

At each iteration, the L received vectors are gathered into the matrix $\mathbf{Y}[k] = \{\mathbf{y}_l[k]\}_{l=1}^{L}$, then, according to the Block Power method [129], the receiver performs a QR decomposition to obtain an updated version of matrix $\mathbf{X}[k]$ that will contain a set of L orthogonal vectors (step 7). In the absence of noise, the Block Power method ensures that for large k, the matrix $\mathbf{X}[k]$ (updated in step 8) converges towards $\mathbf{V}_L$, which contains the L top eigenvectors of $\mathbf{A}$ [129].

Algorithm 2 could be used as part of a protocol in which, first, an unmodulated preamble of length K_p is sent to estimate the beamforming vectors $\mathbf{V}_L$ at the BS and, second, data is transmitted by keeping the estimated beamforming vectors fixed to $\mathbf{X}[K_p]$ throughout the data packet transmission time, assuming the channel remains static. The first step must be repeated periodically according to the rate of change of the channel, which implies some overhead due to the preamble.

Differently from Algorithm 1, Algorithm 2 cannot be used to transmit data and track channel variations simultaneously because, upon convergence, $\mathbf{X}[k]$ will contain the set of eigenvectors which are orthogonal and hence only one user per symbol time would be addressed following a TDMA-like scheme (see Fig. 4.18). This would correspond to an increased complexity, as each user should modulate the SCM according to a slotted protocol, as well as

Algorithm 3: Modified *Block Power method* for a multi-user scenario with data transmission.

Initialization: generate a guess unitary matrix $\mathbf{V}[0] = \mathbf{X}[0] \in \mathbb{C}^{N \times L}$;
$\mathbf{P}[0] = \mathbf{I}_L$;
for $k = 1, 2, \ldots, K$ **do**
  for $l = 1, 2, \ldots, L$ **do**
    transmit : $\sqrt{P_{\mathrm{T}}}\,\mathbf{x}_l[k-1]$; `// signal transmitted by the BS`
    $\mathbf{z}_l^{(u)}[k] = \sqrt{P_{\mathrm{T}}}\,\mathbf{H}^{(u)}\,\mathbf{x}_l[k-1] + \boldsymbol{\eta}_l^{(u)}[k]$; `// signal received by the UE`
    $\mathbf{r}_l^{(u)}[k] = g e^{\jmath\phi_l^{(u)}[k]} \left(\mathbf{z}_l^{(u)}[k]\right)^*$; `// signal retro-directed by the UE`
    $\mathbf{y}_l[k] = \mathbf{H}^{\mathrm{T}}\mathbf{r}_l[k] + \mathbf{w}_l[k] + \mathbf{c}_l[k]$, with $\mathbf{r}_l[k] = \mathrm{vec}\left(\mathbf{r}_l^{(1)}[k], \ldots, \mathbf{r}_l^{(U)}[k]\right)$; `// signal received by the BS`
  end
  $\mathbf{F} = \mathbf{V}^{\dagger}[k-1]\,\mathbf{Y}^*[k]$; `// separate the contribution from each user`
  $f_{n,l} = f_{n,l}/p_{n,l}[k-1], \quad l, n = 1, 2, \ldots L$; `// de-embed the scrambling matrix of the BS from` $\mathbf{F}$
  $\widehat{\Phi}[k] = \mathsf{detection}\,(-\arg\{\mathbf{F}\})$; `// phase estimation for each user`
  $\mathbf{D} = \exp\left(\jmath\widehat{\Phi}[k]\right)$; `// reconstruct the phase matrix`
  $\mathbf{E} = \left(\mathbf{P}[k-1] \odot \mathbf{D}^*\right)^{-1}$; `//`
  $\mathbf{B} = \mathbf{Y}^*[k]\,\mathbf{E}$; `// de-embed the data of the users and the scrambling matrix`
  $\mathbf{Q} = \mathsf{QR}\,(\mathbf{B})$; `// QR decomposition`
  $\mathbf{V}[k] = \mathbf{Q}$; `// eigenvectors update`
  $\mathbf{V}[k] = \alpha_{\mathrm{f}}\mathbf{V}[k] + (1 - \alpha_{\mathrm{f}})\mathbf{V}[k-1]$; `// temporal filtering`
  Generate $\mathbf{P}[k]$; `// full rank unitary random matrix`
  $\mathbf{X}[k] = \mathbf{V}[k]\,\mathbf{P}[k]$; `// scramble the eigenvectors matrix`
end

to a reduction of the spectral efficiency of a factor L, i.e. number of user estimated.

Joint Beamforming and data transmission

Algorithm 3 is capable of handling simultaneous UEs' transmissions, as well as tracking the channel.

■ **Algorithm 3**. The main idea underlying Algorithm 3 (refer to the accompanying pseudo-code) is to transmit, at each iteration, a full-rank linear combination of the estimated eigenvectors (*scrambling*) rather than transmitting them sequentially. This is achieved by multiplying

the matrix $\mathbf{X}[k]$ with a full-rank unitary matrix $\mathbf{P}$ (*scrambling* matrix). By adopting this approach, all users can be simultaneously addressed, enabling continuous transmission without sacrificing spectral efficiency. Unfortunately, due to the scrambling process performed by the BS on the transmitted signal and the phase modulation $\left\{\phi_l^{(u)}[k]\right\}$ introduced by the UEs in the retro-directed signal (step 6 of the pseudo-code), the Block Power method fails to converge to $\mathbf{V}_L$. Therefore, prior to the QR decomposition, the BS must de-embed the users' data (contained in $\mathbf{D}$) and the scrambling matrix $\mathbf{P}$ from the received signal $\mathbf{Y}[k]$. This task is accomplished by multiplying $\mathbf{Y}[k]$ by matrix $\mathbf{E} = (\mathbf{P}[k-1] \odot \mathbf{D}^*)^{-1}$, as exemplified in steps 11, 12, and 13 of the provided pseudo-code. Once the "cleaned" matrix $\mathbf{B}$ has been obtained in step 13, its QR decomposition can be performed (step 14), leading to the derivation of the updated estimate of $\mathbf{V}_L$ (step 15).

To enhance the scheme's resilience against interference among users when the orthogonality assumption on the channels is violated, a straightforward approach involves applying a time filtering operation to the updated eigenvector matrix $\mathbf{V}[k]$ using a forgetting factor $0 \leqslant \alpha_{\mathrm{f}} \leqslant 1$ (step 16). The new full-rank unitary matrix $\mathbf{P}$ is then generated (step 17) and used to scramble $\mathbf{V}_L$ before transmission (step 18).

As will be shown later in the numerical results, Algorithm 3 is capable of establishing automatically and simultaneously up to L data links without the need for channel estimation. In free-space and far-field conditions, it realizes an optimal MU-MIMO scheme which does not require any processing at the UE as well as any ADC chain. Importantly, since L parallel links are established, no reduction in the spectral efficiency is introduced when L users are simultaneously active. Concerning the computational complexity of Algorithm 3, it is mainly determined by the QR decomposition, so it is $\mathsf{O}(N^3)$ and it involves only the BS.

Multi User Scenario Numerical Results

A scenario with 4 users located at coordinates $(0, -4, 7)$ [m], $(4, 0, 6)$ [m], $(-4, 0, 5)$ [m], $(0, 4, 4)$ [m], as shown in Fig. 4.19, is investigated when

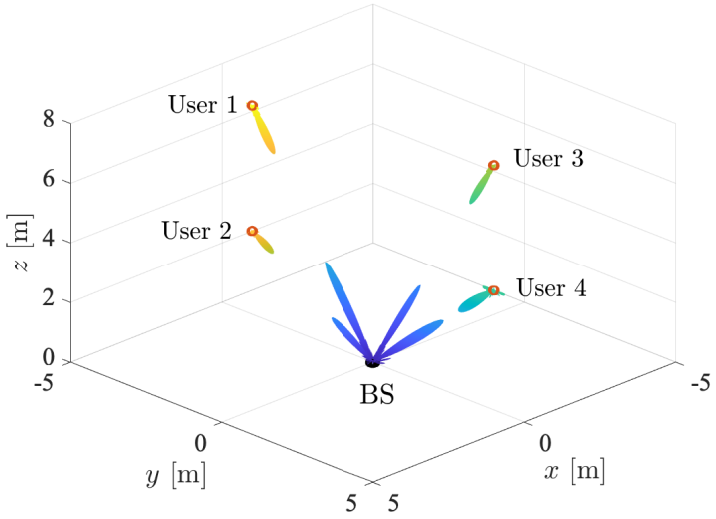

Figure 4.19: Multi-user scenario with the final equivalent array factors in free space.

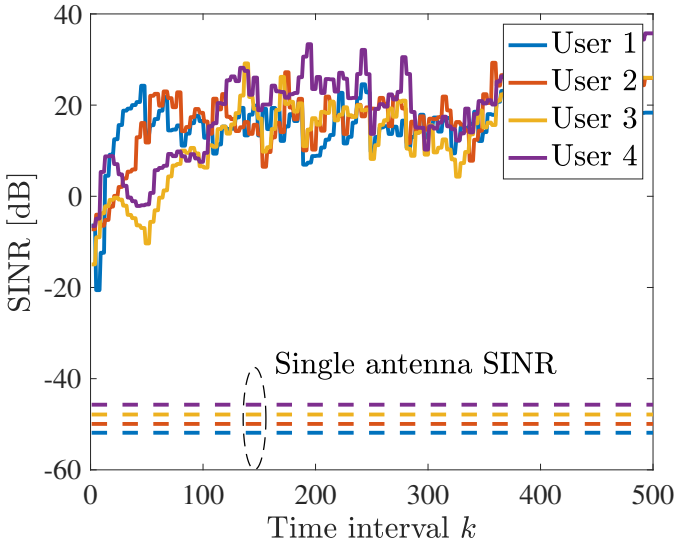

Figure 4.20: Multi-user scenario. Transient of the signal-to-interference-noise ratio (SINR) in free space (continuous lines). Comparison with the single-antenna case (dashed lines). $P_{\mathrm{T}} = -30\,\mathrm{dBm}$.

Algorithm 3 is adopted. A forgetting factor $\alpha_{\mathrm{f}} = 0.3$ and a preamble of $K_p = 40$ symbols (with scrambling matrix $\mathbf{P} = \mathbf{I}_L$) have been chosen as a trade-off between convergence speed and robustness to inter-user interference.

Indeed, in a multi-user scenario, it is possible for channels to lack orthogonality, resulting in interference between users. Consequently, the key metric to be examined in this context is the signal-to-interference-noise ratio (SINR).

In Fig. 4.19, the resulting equivalent array factor at the BS and the 4 UEs at the convergence is also reported in the case of free-space propagation. The equivalent array factor at UE side has been evaluated by computing $(\mathbf{H}\,\mathbf{V}[k])^*$ at the convergence, whereas at the BS side, it has been obtained starting from the beamforming vector $\mathbf{V}[k]$. As expected, for each column of $\mathbf{V}[k]$, the BS generates a beam pointing towards the corresponding user. On the UEs side, the backscatter signal is redirected towards the BS, as it can be noticed in Fig. 4.19.

An example of transient of the SINR is reported in Fig. 4.20 for a total power $P_{\mathrm{T}} = -30\,\mathrm{dBm}$ in free-space conditions. Compared with the transient where only one user is considered, as in Fig. 4.16(a), a slower convergence and a noisier behavior are observed, mainly due to the presence of inter-user interference caused by the non-perfect orthogonality between the different users's channels. The SINR has been evaluated as the ratio between the power from the intended user associated with its strongest eigenvector and the power of the other users' components projected onto the same eigenvector (plus noise).

In Fig. 4.21(a), the empirical Cumulative Density Function (CDF) of the SINR is reported by simulating 100 Monte Carlo iterations for $P_{\mathrm{T}} = -30\,\mathrm{dBm}$ and $P_{\mathrm{T}} = -45\,\mathrm{dBm}$ in free space. Clearly, the more the curves are shifted to the right, the better the conditions. While with $P_{\mathrm{T}} = -30\,\mathrm{dBm}$ all the 4 users present a significant SINR in most cases, with $P_{\mathrm{T}} = -45\,\mathrm{dBm}$, only user 4 has relatively good performance because it is the closest to the BS while the other users experience a SINR which goes below the bootstrap SNR in most of the realizations. The results obtained in the ideal case where no inter-user interference is present are also reported for comparison in order to highlight the impact of non-perfect orthogonality between users that, in this scenario, is dominant and might generate important SINR fluctuations. Inter-user interference can be made negligible by significantly increasing the number of antennas to create the conditions for favorable propagation, as well-known from massive MIMO theory.

Finally, Fig. 4.21(b) shows the empirical CDF of the SINR for $P_{\mathrm{T}} = -10\,\mathrm{dBm}$ and $P_{\mathrm{T}} = -20\,\mathrm{dBm}$ by considering 100 different realizations of the CDL-C NLOS channel model Also in this case, results indicate the effectiveness of the proposed multi-user scheme even in the presence of strong multipath and inter-user interference.

4.2.2 Grant-free Random Access with SCMs

In modern IIoT environments, there is a simultaneous need to meet several stringent requirements, including ultra-low latency ($< 100\,\mu$s), low jitter ($\approx 1 - 2\,\mu$s), ultra-massive access (10^7 sensors/km^2), high energy efficiency, and low complexity [135–137]. This type of industrial scenario is the one envisioned by the European projects in which my research group is involved (TIMES [138] and 6G-SHINE [139]). The traffic generated in massive Machine Type Communications (mMTCs) is often sporadic and random, with short packets as small as 16-32 bytes. To address these challenges, grant-free random access (GFRA) schemes are employed, where sensors transmit as soon as they have data ready, bypassing traditional coordination mechanisms like scheduling and retransmissions typically handled by the AP.

In this context, the role of the *Access Point*, which was previously referred to as the BS in earlier sections, becomes crucial. Similarly, what was previously termed the UE is now the *sensor*. GFRA schemes generally utilize single-antenna sensors with a single-RF chain, and a multi-antenna AP - forming an uplink single-input multiple-output (SIMO) configuration - and it has shown the capability to mitigate inter-sensor interference significantly [140–144]. This is particularly effective when the number of antennas at the AP increases, as demonstrated in [145].

Therefore, the technology of SCM can be applied to various purposes, including GFRA, providing a robust framework for analyzing and optimizing these complex scenarios. However, while most GFRA schemes are SIMO-based, there is growing interest in exploring high-frequency bands like mmWave and THz for IIoT communications. These frequencies necessitate the use of massive antenna arrays with narrow beams on both the AP and sensor sides, transitioning towards a true MIMO scheme. This approach not only com-

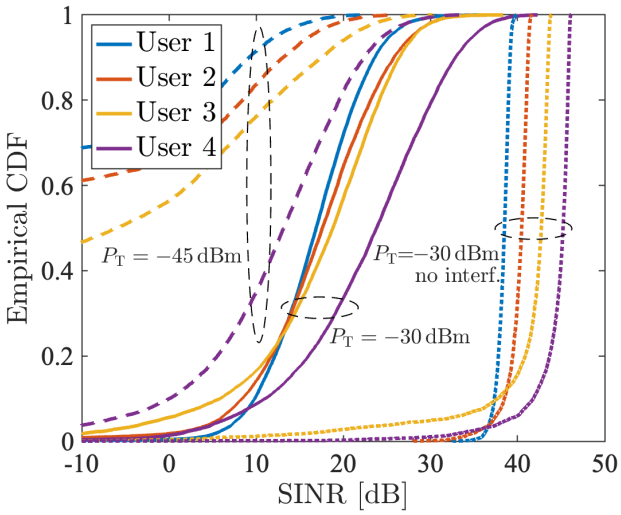

(a) Free space propagation.

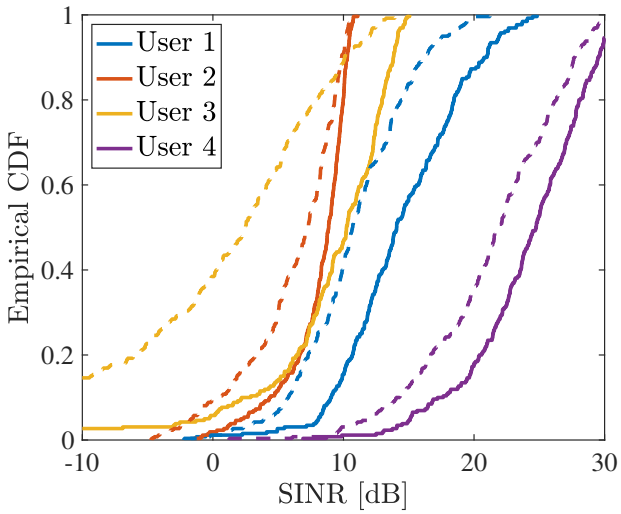

(b) NLOS CDL-C channel model. Continuous lines are for $P_T = -10$ dBm; dashed lines are for $P_T = -20$ dBm.

Figure 4.21: Empirical CDFs of the SINR in multi-user scenario.

pensates for high path loss but also improves spatial filtering and security. Nevertheless, this shift to MIMO introduces challenges, particularly in CSI estimation, which becomes difficult with the limited preamble lengths required by GFRA.

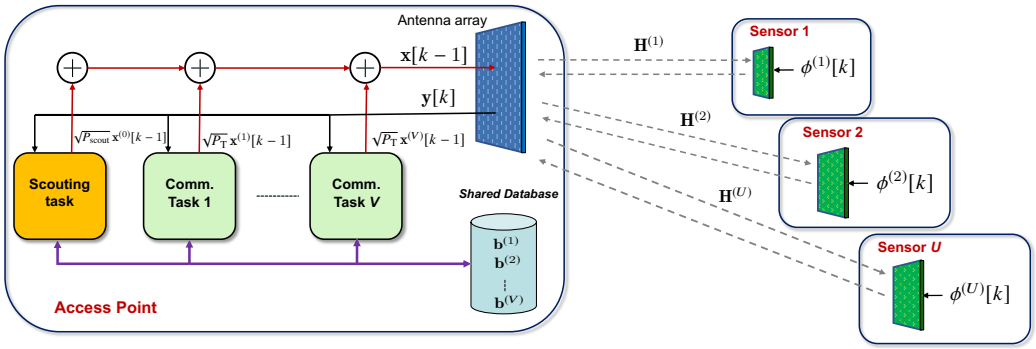

Figure 4.22: Scheme of the proposed grant-free MIMO access, the sensors are equipped with SCMs.

In this section, it will be considered a scenario in which a large number of asynchronous sensors deployed in the environment generate packets randomly. This study is considered the worst-case situation where each packet is generated by a distinct sensor located at a different location so that the reception of each packet requires the fast detection of the new sensor and the fast estimation of the beamforming vector at the AP without any a priori information. For this reason, in what follows it will be interchanged freely the terms packets and sensors. Note that in such a scenario, all the approaches relying on statistical/long-term CSI and/or sensors activity pattern estimation are highly inefficient or not applicable (e.g., [146]). Suppose that, at the generic time interval, there are U asynchronous active (i.e., transmitting) sensors. Denote with $\mathbf{H}^{(1)}, \mathbf{H}^{(2)}, \dots \mathbf{H}^{(U)} \in \mathbb{C}^{M\times N}$ the channel matrices related to the U links between the AP and the active sensors. For further convenience, the corresponding modified round-trip channels are defined as $\mathbf{A}^{(u)} = g\left(\mathbf{H}^{(u)}\right)^{\dagger}\mathbf{H}^{(u)} \in \mathbb{C}^{N\times N}$, for $u = 1, 2, \dots, U$. Note that the modified round-trip channel is defined similarly to (4.71), but in the GFRA treatment, the term for power P_{T} is not included as two different power values will be used depending on the task, as explained later. In addition, it is denoted with $\mathbf{v}_i^{(u)}$ and $\lambda_i^{(u)}$, respectively, the i-th eigenvector and eigenvalue of $\mathbf{A}^{(u)}$, with $i = 1, 2, \dots, r^{(u)}$, where $r^{(u)} = \text{rank}\left(\mathbf{A}^{(u)}\right)$.

The main idea of the proposed grant-free MIMO access scheme is sketched in Fig. 4.22 and described in the following. The AP has several tasks running in parallel. In particular, one task, namely the *Scouting Task*, is always ac-

tive and its purpose is to discover any newly transmitted[6] packet from a new active sensor and estimate the corresponding, possibly optimal, beamforming vector at the AP. Once a new packet is detected, the estimated beamforming vector, denoted as $\mathbf{b}^{(v)}$, is appended to a *Shared Database* that contains all the estimated beamforming vectors, indexed by v, related to the packets being decoded at that moment. In addition, a dedicated task, denoted as *Communication Task*, is initiated, and associated with the new packet. This task is responsible for decoding the packet until its completion. When the packet is over, i.e., the sensor stops backscattering, the associated Communication Task is terminated, and the corresponding beamforming vector is removed from the Shared Database. As it will be explained later if $r^{(u)} > 1$, then the same packet transmitted by the u-th sensor might be decoded using different orthogonal beamforming vectors, each of them associated with a different eigenvalue of $\mathbf{A}^{(u)}$. As a consequence, the size of the Shared Database, and then the number V of instantiated Communication Tasks, might be in general equal or larger than the number U of currently active sensors, that is, $V \geqslant U$. In the following, let $u = f(v)$ represent the function that associates the packet currently being decoded by the v-th Communication Task with the index u of the corresponding sensor that generated it. According to the scheme in Fig. 4.22, the Scouting Task and the V Communication Tasks generate, respectively, the beamforming vectors $\sqrt{P_{\text{scout}}}\,\mathbf{x}^{(0)}[k-1]$ and $\sqrt{P^{(v)}}\,\mathbf{x}^{(v)}[k-1] = \sqrt{P^{(v)}}\,\mathbf{b}^{(v)}$, $v = 1, 2, \dots V$, which are summed up to form the actual transmitted vector $\mathbf{x}[k-1]$ at time $k-1$, that is,

$$\mathbf{x}[k-1] = \sum_{u=0}^{V} \sqrt{P^{(v)}}\,\mathbf{x}^{(v)}[k-1] \tag{4.77}$$

where $P^{(0)} = P_{\text{scout}}$ and $\mathbf{x}^{(0)}[k-1]$ are, respectively, the transmitted power and the current beamforming vector used by the Scouting Task. Without loss of generality, it can be assumed that all the Communication Tasks transmit with the same power P_{T}, so $P^{(v)} = P_{\text{T}}$, $v = 1, 2, \dots V$, even though power control schemes can be easily implemented to minimize the overall transmit-

[6]For the sake of simplicity it can be said improperly that the sensor starts transmitting, whereas more precisely it starts backscattering the signal sent by the AP.

ted power. The signal received by the SCM of the u-th sensor during the k-th transmission interval is

$$\begin{aligned}\mathbf{z}^{(u)}[k] &= \mathbf{H}^{(u)}\,\mathbf{x}[k-1] + \boldsymbol{\eta}^{(u)}[k] \\ &= \mathbf{H}^{(u)} \sum_{l=0}^{V} \sqrt{P^{(l)}}\,\mathbf{x}^{(l)}[k-1] + \boldsymbol{\eta}^{(u)}[k] \end{aligned} \tag{4.78}$$

where $\boldsymbol{\eta}^{(u)}[k] \sim \mathcal{CN}\left(\mathbf{0}, \sigma_\eta^2\,\mathbf{I}_M\right)$ is the noise experienced by the SCM of the u-th sensor. Again, it resembles (4.73), but modified for the context. In (4.78), the channel matrix $\mathbf{H}^{(0)}$ characterizes the communication link between the AP and a potential new sensor during the scouting process. More in general, $u \in \mathcal{U}$, where $\mathcal{U}$ is defined as the set $\{0, 1, 2, \ldots, U\}$, if a new sensor is detected; otherwise, $\mathcal{U} = \{1, 2, \ldots, U\}$. According to (2.27), the signal backscattered by the u-th sensor is $\mathbf{r}^{(u)}[k] = g\,e^{\jmath\phi^{(u)}[k]}\left(\mathbf{z}^{(u)}[k]\right)^*$, then the signal received by the AP at the k-th time interval is given by the contributions from all sensors and can be written as

$$\begin{aligned}\mathbf{y}[k] &= \sum_{u\in\mathcal{U}} \left(\mathbf{H}^{(u)}\right)^T \mathbf{r}^{(u)}[k] + \mathbf{w}[k] \\ &= \sum_{u\in\mathcal{U}} e^{\jmath\phi^{(u)}[k]} \left(\mathbf{H}^{(u)}\right)^T \left(\mathbf{H}^{(u)}\right)^* \sum_{l=0}^{V} g\sqrt{P^{(l)}}\left(\mathbf{x}^{(l)}[k-1]\right)^* \\ &\qquad + \mathbf{n}[k] \\ &= \sum_{u\in\mathcal{U}} e^{\jmath\phi^{(u)}[k]} \left(\mathbf{A}^{(u)}\right)^* \sum_{l=0}^{V} \sqrt{P^{(l)}}\left(\mathbf{x}^{(l)}[k-1]\right)^* + \mathbf{n}[k] \end{aligned} \tag{4.79}$$

where $\mathbf{A}^{(0)} = g\left(\mathbf{H}^{(0)}\right)^\dagger \mathbf{H}^{(0)}$, $\mathbf{n}[k] = \mathbf{w}[k] + \sum_{u\in\mathcal{U}}\left(\mathbf{H}^{(u)}\right)^T\left(\boldsymbol{\eta}^{(u)}[k]\right)^*$ and $\left\{\phi^{(u)}[k]\right\}$ is the phase carrying the current data transmitted by the u-th active sensor. All the tasks have access to the received vector $\mathbf{y}[k]$.

The Shared Database (see Fig. 4.22), containing all the estimated beamforming vectors $\mathbf{B} = \left\{\mathbf{b}^{(1)}, \mathbf{b}^{(2)}, \cdots, \mathbf{b}^{(V)}\right\}$ associated with the packets currently being decoded, serves a dual purpose: *i)* the v-th beamforming vector $\mathbf{b}^{(v)}$ is used by the v-th Communication Task to address the sensor with index $u = f(v)$ until the end of the corresponding packet; *ii)* the set of beamforming vectors in $\mathbf{B}$ is used by the Scouting Task to perform the es-

Algorithm 4: Algorithm of the Scouting Task.

0: *Initialization*: generate a guess unitary norm beamforming vector $\mathbf{x}^{(0)}[0]$; $V = 0$;
1: **for** $k = 1, \ldots, \infty$ **do**
  2: If the Shared Database has been updated, then generate a random unitary norm vector $\mathbf{x}^{(0)}[k-1]$ orthogonal to $\mathbf{B}$ //
  3: transmit: $\sqrt{P_{\text{scout}}}\,\mathbf{x}^{(0)}[k-1]$ //
  4: receive: $\mathbf{y}[k]$ //
  5: $\mathring{\mathbf{y}}[k] = \mathsf{orthogonalize}(\mathbf{y}[k], \mathbf{B})$ //
  6: $\mathbf{x}^{(0)}[k] = (\mathring{\mathbf{y}}[k])^* / \|\mathring{\mathbf{y}}[k]\|$ `// beamforming vector update`
  7: $\gamma[k] = \|\mathring{\mathbf{y}}[k]\|^2 / \sigma^2$ `// SNR computation`
  8: If $\gamma[k] > \gamma_{\text{dec}}$ and $\gamma[k]/\gamma[k-1] < \gamma_{\Delta}$, then a new packet has been detected, $V = V + 1$, a new dedicated Communication Task is allocated using $\mathbf{x}^{(0)}[k]$ as beamforming vector, and $\mathbf{b}^{(V)} = \mathbf{x}^{(0)}[k]$ is added to the Shared Database.
end

timation of the beamforming vector of a possibly newly transmitting sensor in a subspace orthogonal to that spanned by the vectors in $\mathbf{B}$ (i.e., in the null space of $\mathbf{B}$). The latter ensures that the vectors in $\mathbf{B}$ are orthogonal and hence all the tasks (Scouting and Communication) address orthogonal subspaces. As a final remark, it can be noted that the outlined analytical framework also accounts for potential misalignments of the beam reflected by sensors relative to the incident beam, due to the noise contribution in (4.78) that undergoes the conjugation operation fundamental to retrodirectivity. Likewise, the analysis incorporates the potential non-idealities in the beamforming vectors estimated by the AP, which are influenced by *i)* the presence of noise as well as by *ii)* sensor nodes oriented in non-orthogonal directions. The former affects the signal used by the AP for beamforming vectors' estimation, given by (4.79), while the latter ensures the beams are orthogonal to each other to avoid mutual interference, meaning that they may not be directed exactly toward the respective receivers. Remarkably, all these phenomena are accounted for in the numerical results where the outcomes of simulations will be presented.

Scouting Task

The pseudo-code of the algorithm executed by the Scouting Task is reported in Algorithm 4.

At the startup time $k = 0$, $\mathbf{x}^{(0)}[0]$ is initialized with a unitary norm random vector (step 0 of the pseudo-code). At the $(k-1)$-th iteration, with $k > 1$, the Scouting Task (see Algorithm 4) sends the current estimated beamforming vector, $\mathbf{x}^{(0)}[k-1]$ (step 3), and receives back the response at time k from the new sensor (if any) according to (4.79) (step 4). Before further processing, the received vector $\mathbf{y}[k]$ is made orthogonal to $\mathbf{B}$, that is,

$$\mathring{\mathbf{y}}[k] = \left(\mathbf{I} - \mathbf{B}\,\mathbf{B}^{\dagger}\right)\mathbf{y}[k] \tag{4.80}$$

in order to force the searching in the null space of $\mathbf{B}$ and hence not interfere with the currently active Communication Tasks (step 5). Then, a normalized and conjugated version of $\mathring{\mathbf{y}}[k]$ is computed (step 6) and used as the updated beamforming vector $\mathbf{x}^{(0)}[k]$ in the subsequent iteration.

Finally, let k^* represent the time instant a new sensor starts the transmission of a packet. The new packet is detected when the SNR $\gamma[k] = \|\mathring{\mathbf{y}}[k]\|^2/\sigma^2$, with $k > k^*$, satisfies $\gamma[k] > \gamma_{\text{dec}}$ and $\gamma[k]/\gamma[k-1] < \gamma_{\Delta}$ (steps 7 and 8). The first inequality checks that a certain level of energy has been received compared to the noise level, whereas the second one guarantees that (4.81) is close to the convergence, with the thresholds γ_{dec} and γ_{Δ} to be properly tuned.

The processing operated by Algorithm 4 is the modification of the well-known *Power Method* [129] that, in the absence of noise, interference, and the orthogonalization in (4.80), allows the estimation of the top-eigenvector of the square matrix $\mathbf{A} = \sum_{u\in\mathcal{U}} \mathbf{A}^{(u)}$, as described previously in Sec. 4.2.1. Here, differently from the classical Power Method, due to (4.80), the matrix seen by the iterative method is $\mathring{\mathbf{A}} = \left(\mathbf{I} - \mathbf{B}\,\mathbf{B}^{\dagger}\right)\mathbf{A}$, which determines the subspace under exploration by the Scouting Task, whose eigenvectors and eigenvalues are denoted by $\{\mathring{\lambda}_1, \mathring{\lambda}_2, \ldots, \mathring{\lambda}_{\mathring{r}}\}$ and $\{\mathring{\mathbf{v}}_1, \mathring{\mathbf{v}}_2, \ldots, \mathring{\mathbf{v}}_{\mathring{r}}\}$, respectively, where $\mathring{r} = \text{rank}\left(\mathring{\mathbf{A}}\right)$. Furthermore, whenever a modification is made to $\mathbf{B}$ (such as adding or removing elements), $\mathbf{x}^{(0)}[k]$ is reinitialized by generating a random vector that is subsequently made orthogonal to the vectors in $\mathbf{B}$,

according to (4.80), while ensuring it remains unitary. In particular, the beamforming vector is updated according to (step 6)

$$\mathbf{x}^{(0)}[k] = \frac{\mathring{\mathbf{y}}^{*}[k]}{\|\mathring{\mathbf{y}}[k]\|} \tag{4.81}$$

until a change on $\mathbf{B}$ occurs or a new packet is detected.

Obviously, the new sensor can be detected only if $\mathring{\mathbf{A}}$ and $\mathbf{A}^{(0)}$ share a not null subspace.

It has to be remarked that, in general, it is not guaranteed that $\mathring{\mathbf{v}}_1$ is referred to the channel between the AP and the new sensor. In fact, when the sensor and AP are in radiating near-field conditions, or in far-field in the presence of multipath, the channel might have a rank larger than one and the same sensor can be reached addressing different orthogonal subspaces [147].

In such cases, the Scouting Task is likely to converge to a subspace related to a sensor already under decoding but not yet included in $\mathbf{B}$, and hence a second Communication Task will be associated with that sensor. Duplicated packet decoding is not an issue as it can be easily solved by higher protocol layers. On the contrary, such a phenomenon might be beneficial as it creates a sort of eigenvector diversity.

If the packet generation of the new sensor is not simultaneous (at symbol time T level) to the generation of an already serving sensor, it is likely that all the significative secondary eigenvectors of $\mathring{\mathbf{A}}$ have been already explored when the new sensor starts its transmission, and $\mathbf{v}_1^{(0)}$ is effectively associated with the new sensor.

Communication Task

Once a new packet has been detected by the Scouting Task, a new Communication Task is activated whose algorithm is reported in Algorithm 5.

Denote with $k^{(v)}$ the time instant the packet is detected by the Scouting Task and the Communication Tasks starts, being v the index associated to the new packet generated by the u-th sensor, with $u = f(v)$, and with $\mathbf{b}^{(v)} = \mathbf{x}^{(0)}\left[k^{(v)}\right]$ the corresponding beamforming vector estimated through Algorithm 4 and stored in the Shared Database by the Scouting Task. The

Communication Task, for $k \geqslant k^{(v)}$ until the end of the packet, executes Algorithm 5 that, at each iteration, always transmits the same beamforming vector $\sqrt{P^{(v)}}\,\mathbf{x}^{(v)}[k-1]$, with $\mathbf{x}^{(v)}[k-1] = \mathbf{b}^{(v)}$ (step 2). Subsequently, according to (4.52) and (4.79), the decision variable is formed as (step 4)

$$\begin{aligned} u^{(v)}[k] &= \left(\mathbf{b}^{(v)}\right)^{\dagger} \mathbf{y}^{*}[k] \\ &= \sum_{i \in \mathcal{U}} e^{-\jmath\phi^{(i)}[k]} \left(\mathbf{b}^{(v)}\right)^{\dagger} \mathbf{A}^{(u)} \sum_{l=0}^{V} \sqrt{P^{(l)}}\,\mathbf{x}^{(l)}[k-1] \\ &\quad + \left(\mathbf{b}^{(v)}\right)^{\dagger} \mathbf{n}^{*}[k] \\ &= e^{-\jmath\phi^{(u)}[k]} \sum_{l=0}^{V} \sqrt{P^{(l)}} \left(\mathbf{b}^{(v)}\right)^{\dagger} \mathbf{A}^{(u)}\,\mathbf{x}^{(l)}[k-1] \\ &\quad + \sum_{i \in \mathcal{U},\, i \neq u}^{U} e^{-\jmath\phi^{(i)}[k]} \sum_{l=0}^{V} \sqrt{P^{(l)}} \left(\mathbf{b}^{(v)}\right)^{\dagger} \mathbf{A}^{(u)}\,\mathbf{x}^{(l)}[k-1] \\ &\quad + \left(\mathbf{b}^{(u)}\right)^{\dagger} \mathbf{n}^{*}[k] \end{aligned} \tag{4.82}$$

where $u = f(v)$. A decision on the transmitted phase $\phi^{(u)}[k]$ from the sensor with index $u = f(v)$ is made (step 5) based on the argument of $u^{(v)}[k]$ in (4.82) according to the mapping scheme considered. The first term in (4.82) represents the useful contribution. Equation (4.82) reveals that, in general, the decision variable is affected by the presence of interference from other sensors (second term), caused by potential not orthogonality of the sensors' channels, and thermal noise (third term). Finally, when $\gamma[k] = \left|u^{(v)}[k]\right|^2/\sigma^2 < \gamma_{\text{drop}}$, the end of the packet has been likely reached, and the task is deactivated (steps 6 and 7).

Numerical Results

Here some simulation results with the purpose of investigating the performance of the proposed scheme are reported. The values of the system parameters adopted for the analysis and the simulations are reported in Table 4.4, if not otherwise specified. The scenario considered, shown in Fig. 4.23, is composed of an AP, equipped with a Uniform Planar Array (UPA) deployed along the xy-plane, located at $(0, 0, 0)$ [m], and sensors generating very short

Algorithm 5: Algorithm of the v-th Communication Task.

0: *Initialization*: *active* = 1, $k = k^{(v)}$ // $k^{(v)}$ time instant of packet detection
1: **while** *active=1* **do**
2: transmit: $\sqrt{P^{(v)}}\,\mathbf{x}^{(v)}[k-1] = \sqrt{P^{(v)}}\,\mathbf{b}^{(v)}$ //
3: receive: $\mathbf{y}[k]$ //
4: $u^{(v)}[k] = \left(\mathbf{b}^{(v)}\right)^{\dagger}\,\mathbf{y}^{*}[k]$ // decision variable
5: $\widehat{\phi}[k] = \text{demodulation}\left(-\arg\left\{u^{(v)}[k]\right\}\right)$ // data demodulation
6: $\gamma[k] = \left|u^{(v)}[k]\right|^2/\sigma^2$ // SNR computation
7: If $\gamma[k] < \gamma_{\text{drop}}$, then beamforming vector $\mathbf{b}^{(v)}$ is removed from the Shared Database, and this task is de-instantiated
(*active* = 0, $V = V - 1$) //
$k = k + 1$;
end

Table 4.4: Parameters used in the simulation.

Parameter	**Symbol**	**Value**
Carrier frequency	f_{c}	100 GHz
AP antenna element gain	G_{BS}	0 dB (isotropic)
SCM cell gain	G_{SCM}	0 dB (isotropic)
SCM backscatter gain	g	20 dB
Bandwidth	W	10 MHz
Symbol time	T	100 ns
TX power	P_{T}	-5 dBm
Power boost scouting	$P_{\text{scout}}/P_{\text{T}}$	10 dB
SCM noise figure	F_{SCM}	3 dB
AP noise figure	F_{AP}	3 dB
AP antenna elements	N	30×30 ($4.5 \times 4.5\,\text{cm}^2$ UPA)
SCM cells per sensor	M	20×20 ($3 \times 3\,\text{cm}^2$ UPA)
Path loss exponent	β	2
Detection SNR threshold	γ_{dec}	30 dB
Delta SNR convergence	γ_{Δ}	5 dB
Drop SNR threshold	γ_{drop}	5 dB
Packet length	K	144 bits
Guard symbols	K_{g}	16 bits
Packet duration	$T_{\text{p}} = K\,T$	14.4 μs

packets of total length $K = 144$ bits (18 bytes payload). In particular, packets are generated randomly with exponentially distributed inter-arrival time with mean μ, corresponding to a total offered traffic $G = T_{\text{p}}/\mu$, where $T_{\text{p}} = K\,T$ is the packet duration. Each packet corresponds to a sensor whose position is generated randomly with uniform distribution within the area centered in

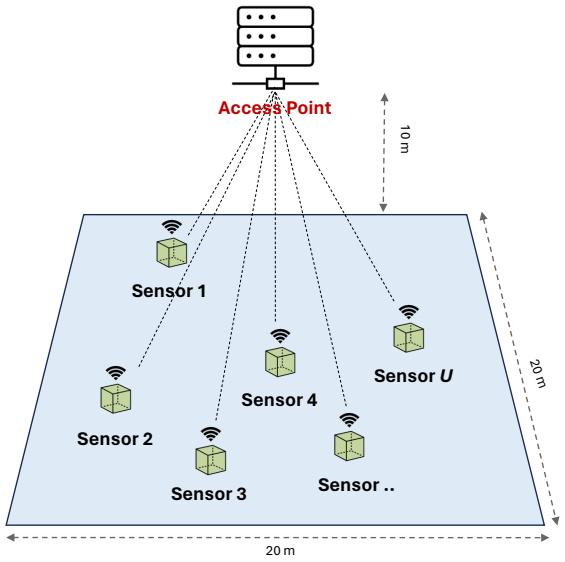

Figure 4.23: Simulated scenario.

$(0, 0, 10)$ [m] and size 20×20 [m^2]. The sensor's SCMs are supposed to lay on the xy-plane.

In Fig. 4.24(a), the time evolution of $\mathsf{SNR}_1[k]$ during the Scouting Task is shown for different bootstrap conditions in the case of rank-1 channel computed using (4.58), with $k^* = 1$. In the first 2 top curves, a random initial guess of the beamforming vector, corresponding to $\mathsf{SNR}_1[1] \simeq \mathsf{SNR}_1^{(\max)}/N$, was assumed, whereas the third curve is related to an even more unfavorable situation where $\mathsf{SNR}_1[1] = \mathsf{SNR}_1^{(\max)}/N^2$. The blue and green curves have been evaluated with $\mathsf{SNR}_1^{(\max)} = 35$ dB and $\mathsf{SNR}_1^{(\max)} = 25$ dB, respectively, to which a bootstrap SNR of 5.45 dB and -4.54 dB corresponds. It can be noticed that when the bootstrap SNR is larger than one, the SNR converges after a few steps to $\mathsf{SNR}_1^{(\max)}$ and the packet can be detected, whereas it converges to a very low SNR when the bootstrap SNR is less than one. From Fig. 4.24(a), it can also be concluded that the impact of the initial beamforming vector on the SNR evolution is marginal, and it does not affect the final value.

The situation with a rank-3 channel (e.g., due to multipath) is analyzed in Fig. 4.24(b), where the evolution of $\mathsf{SNR}_j[k]$, $j = 1, 2, 3$, is plotted for $\mathsf{SNR}_1^{(\max)} = 35$ dB, $\mathsf{SNR}_2^{(\max)} = 30$ dB, and $\mathsf{SNR}_3^{(\max)} = 25$ dB. As evident in

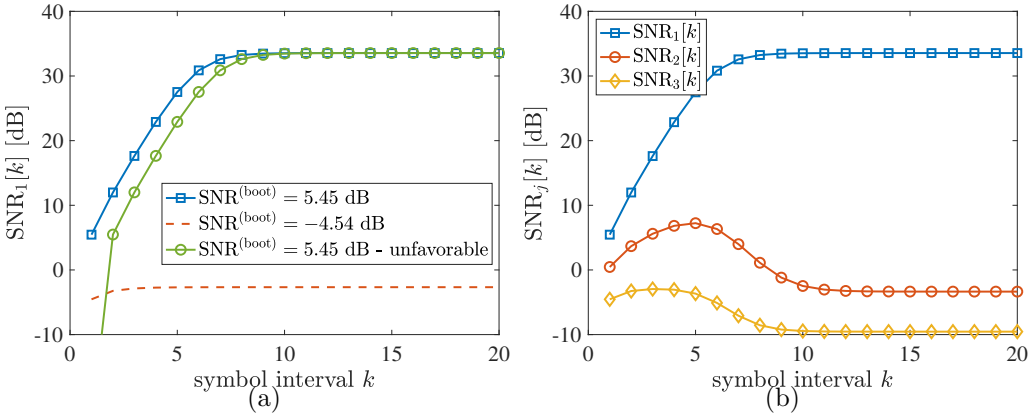

Figure 4.24: Time evolution of the SNR during the Scouting Task for different bootstrap conditions in the case of rank-1 channel (a) - $\mathsf{SNR}_1[k]$, and rank-3 channel (b) - $\mathsf{SNR}_j[k]$).

the figure, the proposed iterative method ensures the convergence to the top eigenvector of the channel (blue curve), whereas the components associated with the top-second and top-third eigenvectors vanish. Comparing the blue curves in Fig. 4.24(a) and Fig. 4.24(b), it can also be observed that the convergence speed to the top-eigenvector is only slightly affected by the channel rank. In all cases, the convergence time is below 10 time intervals. This suggests that a guard time of $K_{\text{g}} = 16$ symbols set to zero, inserted at the beginning of each packet and followed by the payload of 18 bytes, gives sufficient time to the Scouting Task to converge and detect the packet. Since the Scouting Task is the most critical one, it is of interest to investigate whether it benefits from an assignment of a power level P_{scout} higher than the power level P_{T} associated with the Communication Task. To this purpose, it is defined the power boost as $P_{\text{scout}}/P_{\text{T}}$. In Fig. 4.25(a), the packet error rate (PER), corresponding to $1 - \{\text{Probability of packet detection}\}$, as a function of the offered traffic G is shown for different scouting power boost levels in free space. The PER has been computed through Monte Carlo simulations terminated when at least 100 erroneous packets were counted. Observations reveal that the benefits of the power boost do not escalate indefinitely, indicating the presence of a discernible trade-off. Indeed, while increasing the power boost aids in detecting new packets by the Scouting Task, it may also

increase interference for packets already undergoing decoding, particularly in unfavorable propagation conditions. Simulations demonstrate that a power boost of 15 dB yields the lowest PER across all scenarios, yet satisfactory performance is still achieved with a lower boost level of 10 dB. Obviously, under favorable propagation (massive MIMO) the inter-sensor interference is minimized, and the determination of the power boost is less critical.

The impact of the transmitted power and channel models can be observed in Fig. 4.25(b). In particular, free-space and the LOS CDL-E multipath 3GPP channel models [134] with a delay spread of 9 ns have been considered. With multipath, slightly higher power levels are in general necessary to satisfy the link budget. The increase of the transmitted power lowers slightly the PER indicating that the performance is mainly limited by the inter-sensor interference caused by the non-orthogonality of the channels in this scenario. The curves denoted with baseline GFRA (BGFRA) will be described hereafter. Achieving favorable propagation, i.e., channel orthogonality, through a substantial increase of the antenna elements at the AP is one possible solution to mitigate or even eliminate the inter-sensor interference and hence significantly improve the performance. Another possible solution to mitigate the effect of the interference is to introduce a successive interference cancellation (SIC) algorithm, for instance, a non-orthogonal multiple access (NOMA) scheme.

To complete the study in the fairest manner, a comparison is also made with the structures proposed in the state of the art, which can be found in the Appendix.

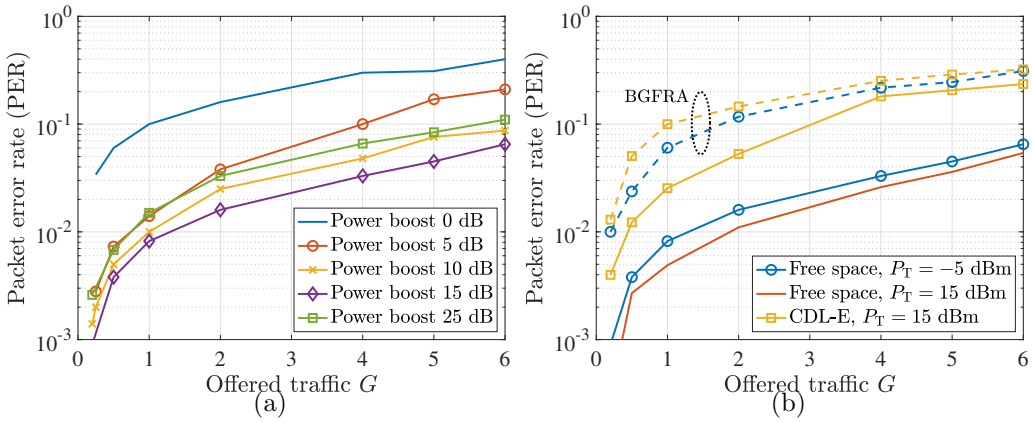

Figure 4.25: (a): Packet error rate as a function of the offered traffic G. Effect of the Scouting Task power boost. $P_T = -5$ dBm. Free space condition. (b): Packet error rate as a function of the of the offered traffic G for different transmitted power levels and channel models. Power boost 15 dB.

4.2.3 Real-time Localization Based on SCMs

To stay within the themes and scope of communication and localization for SRE in this thesis, it was interesting to explore how SCM technology could be leveraged for positioning applications. In [35], an application in vehicular networks is studied, where position information must be updated several times per second (high update rate) to adequately support control systems, and must be extremely current (ultra-low latency) to enable rapid responses even in high-speed scenarios [148–150]. When the demand for positioning is coupled with stringent energy efficiency and low complexity requirements, radio backscattering emerges as a viable solution [151–154]. Backscatter radios can be deployed onboard drone swarms for network-based positioning applications or as energy-autonomous tags (e.g., utilizing energy harvesting technologies) placed in the environment. In the latter case, these tags can serve as reference nodes (anchors) for the self-positioning of autonomous vehicles (navigation applications).

However, the primary drawback of backscatter radio is the significant path loss, as the signal traverses the propagation channel twice. This limits the operational range to just a few meters, as commonly observed in RFID applications [155]. These limitations are further exacerbated at higher frequencies

(mmWave/THz) [156], making traditional backscatter schemes impractical for achieving high-accuracy positioning in the aforementioned applications.

One possible solution to mitigate path loss, as already stated in the previous sections, is the adoption of MIMO techniques, involving the integration of multiple antennas on both nodes participating in the backscattering process (i.e., the emitter of the interrogation signal and the backscatter radio). However, this would require maintaining beam alignment, which contradicts the low-complexity nature of backscatter radio, where CSI estimation is not feasible. Therefore, it has been chosen to explore the application using the SCM technology presented in previous sections.

It is important to note that the localization of UEs is commonly achieved through the deployment of a set of reference nodes, referred to as *anchors*, positioned at fixed known locations. Anchors and UEs interact to estimate the characteristics of position-dependent signals, such as the AoA [157]. In the following, it is illustrated how SCMs can be exploited both at the UE and anchor sides, leading to different architectural solutions, each with its own set of advantages and disadvantages.

Before, effectively implementing the proposed architectures, specific building blocks, and dedicated methods are required. It is important to note that in both architectures, MIMO transceivers (MIMO TRXs) are adopted. Indeed, the adoption of multiple antennas is required to counteract the unfavorable path loss typical of backscatter communication as well as to allow the estimation of the signal's AoA. Thus, the same antenna array can be used for transmission and reception by exploiting a full-duplex radio implementation, as commonly considered in monostatic radar applications [158].

The primary challenge in both architectures is determining the beamforming vector at the MIMO TRX to direct the interrogation signal towards the SCM, also called RAA, whose direction remains unknown prior to AoA estimation. To tackle this challenge, it is proposed an iterative procedure inspired by [33] described in the previous section 4.2, leveraging the distinctive capability of SCMs to reflect the signal in the same direction it was received. Remarkably, the determination of the beamforming vector intrinsically provides the AoA of the backscattered signal, subsequently used for localization. Clearly, since a MIMO link is finally established, the communication benefits

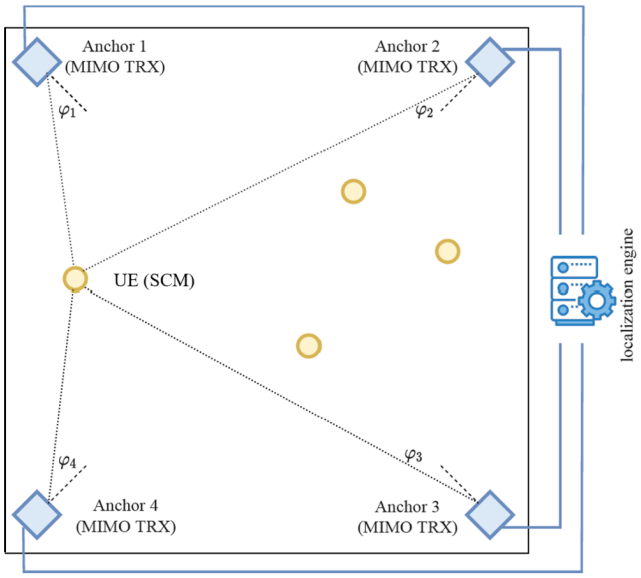

Figure 4.26: Localization of SCMs-equipped mobile UEs (yellow circles) by using array-equipped anchors (blue squares). Anchors are also labelled a MIMO transceivers (TRX).

from the MIMO gain to mitigate the high path loss.

Architecture 1 is designed as the configuration where SCMs are employed on mobile UEs, while anchor nodes use conventional antenna arrays (see Fig. 4.26), thus playing the role of MIMO TRXs. Conversely, *Architecture 2* involves SCMs for anchors while UEs are equipped with conventional antenna arrays, thus acting as MIMO TRXs (see Fig. 4.27).

Architecture 1 - SCM at the UE Side

Each mobile UE is equipped with an SCM (Fig. 4.26), while each anchor is equipped with a conventional array and is configured to transmit an interrogation signal, thus being a MIMO TRX. This signal is backscattered by the SCMs, which also embed their identifiers (IDs), and subsequently received by the same anchor. The anchor can then estimate the AoAs of the signals received by the SCMs and extract their ID using the scheme introduced in the following sections. Such information is then passed to a localization engine, which is in charge of estimating the UEs' positions based on the data received by all anchors. Once a sufficient number of AoA measurements are collected for a given SCM, the localization engine can localize the UEs, know-

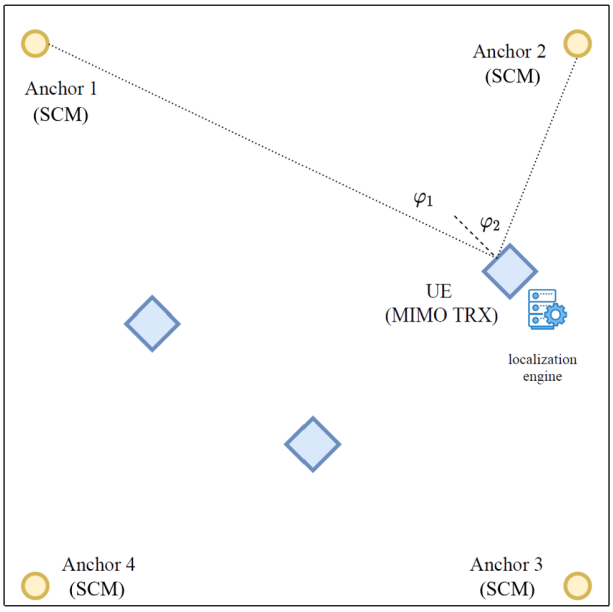

Figure 4.27: Navigation of array-equipped mobile UEs (blue squares) through the interaction with SCMs (yellow circles) used as anchor nodes. UEs are also labeled MIMO transceivers (TRX).

ing the anchors' positions and orientations. For example, at least two AoAs per UE are needed for unambiguous 2D localization. Clearly, the larger the number of AoA measurements for each UE, the better will be the localization accuracy.

To deal with measurement errors, the localization engine can fuse different AoAs estimates by leveraging, for instance, standard tools such as least squares or particle filtering.[7] Different anchors can access simultaneously the UEs by exploiting, for example, different frequencies, assuming a flat frequency response of the SCM within the signal bandwidth. The discrimination of the backscatter components associated with different UEs, can be realized by exploiting the antenna array spatial selectivity. This architecture is primarily tailored for network localization applications, enabling the network to gain comprehensive insights into the positions of all UEs within the scenario of interest. This encompasses a wide set of use cases such as asset and personnel tracking, logistics management, and more. The primary ad-

[7]The reader can refer to [157].

vantage of this architecture lies in the potential for remarkably simple UEs, as they require no processing capabilities on their side. Essentially, the UE solely engages in backscattering the incoming signal using the SCM and incorporating its ID in the reflected signal. Consequently, there is no need for complex RF chains or baseband components within the UEs, resulting in reduced costs and complexity as well as the possible exploitation of energy harvesting techniques making the UEs energy autonomous.

Architecture 2 - SCM at the Anchor Side

This architecture entails equipping each anchor node with an SCM, while UEs utilizes a conventional antenna array, thus being MIMO TRXs (Fig. 4.27). In contrast to Architecture 1, in this scenario, it is the anchor that responds to the interrogation signal emitted by the UE, leveraging retrodirectivity. Consequently, each UE must detect the presence of the SCM-equipped anchors, extracting their IDs, and estimate the AoAs of the retro-directed signals relative to its local coordinate system. A decentralized localization engine operates within each UE, enabling the estimation of its position.

This architecture is primarily suited for navigation purposes, resembling GNSS-like positioning, as the position computation occurs at the UE level. When considering vehicular networks, this architecture is particularly suited for the self-localization of autonomous vehicles (where no complexity constraints usually arise on-board vehicles) using simple, low-cost, and possibly energy autonomous reference tags (equipped with SCMs) deployed in the environment. In general, this architecture allows for reducing the complexity and cost of anchor infrastructure, which often serves as the primary barrier to introducing high-accuracy positioning systems like those based on UWB technology [157].

The different UEs can access simultaneously the SCM-based anchors by exploiting, for example, different frequencies. A given UE can address simultaneously different anchors thanks to the spatial discrimination allowed by the use of antenna arrays with a large number of antennas and the scheme.

A key distinction from Architecture 1 is that, in this scenario, localization information is immediately available at the UE itself. This minimizes latency in scenarios where UEs require prompt awareness of their positions. This is crucial when utilizing position information to feed navigation engines,

especially in autonomous driving applications involving vehicles, unmanned aerial vehicles (UAVs) and mobile robots. This architecture can be further improved by enabling the SCM-based anchors to transmit not only their ID but also their coordinates. This additional information can be utilized by the UE for localization without requiring prior knowledge of the anchors' deployment layout. Furthermore, in a practical system, multiple anchors can be seamlessly added without the need to update the anchor database at the UE side. *Remark:* In Architecture 1, the AoA estimation is performed by anchor nodes that are aware of the absolute reference system. In contrast, in Architecture 2, the orientation of the UE may be unknown and must be estimated to determine the UE's absolute coordinates. In this case, in fact, the UE localizes itself relative to its own local reference system rather than the absolute one. To map the result to an absolute reference system, the orientation of the UE must be known, either a priori or through additional sensors, such as an inertial sensor or a compass.

SCM Detection and AoA Estimation

Now a procedure for the MIMO TRX to estimate the AoA of the signal backscattered by an SCM using a blind iterative approach, guiding the MIMO TRX to direct its interrogation signal towards the SCM is reported. Subsequently, the scheme is extended to accommodate multiple SCM-based devices, allowing for simultaneous estimations. To begin, only two nodes are considered, namely, a MIMO TRX and an SCM. The MIMO TRX is equipped with a ULA comprising N elements, capable of full-duplex communications. The SCM, on the other hand, is realized as a uniform linear array consisting of M elements, without processing capabilities (refer to Fig. 4.28). Here, uniform linear arrays are considered for simplicity of explanation, although various array layouts can be explored. Both arrays are located in the far-field region of each other, separated by a distance d. The Angle of Departure (AoD) of the signal emitted by the MIMO TRX, when directed towards the SCM, is denoted as φ, while the AoA of the signal received at the SCM from the MIMO TRX is denoted as ψ.

The scheme proposed involves transmitting from the MIMO TRX to the

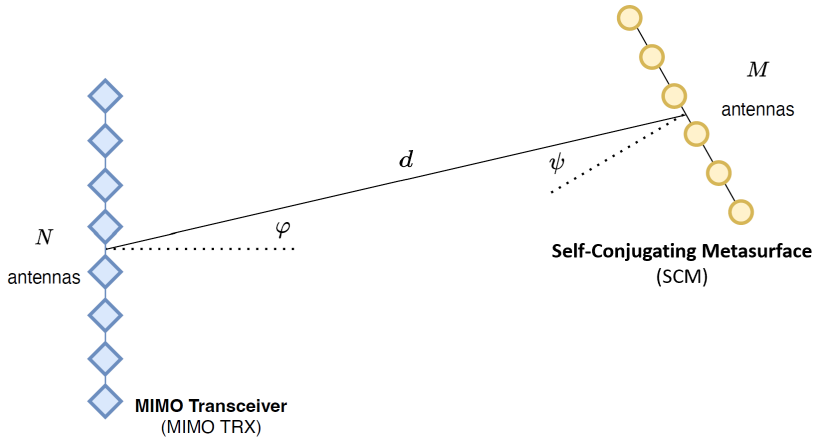

Figure 4.28: Geometry of the scenario. MIMO TRX equipped with a N-antennas ULA; SCM composed of M antennas organized as ULA.

SCM using a certain beamforming vector $\mathbf{x} \in \mathbb{C}^{N\times 1}$, ideally aligned with direction φ, as already described in the previous sections.

Let $\sqrt{P_{\mathrm{T}}}\,\mathbf{x}[k] \in \mathbb{C}^{N\times 1}$ be the vector containing the signal transmitted by the N elements of the MIMO TRX's antenna array, where P_{T} is the transmitted power and $\mathbf{x}[k]$ is the unit norm beamforming vector at the generic time interval k. At the other end of the communication link, consider a plane wave impinging on the SCM, the schematic representation of which is shown in Fig. 2.6, with an angle ψ with respect to its normal direction. At the m-th SCM antenna, the impinging wave accumulates a phase shift θ_m, with respect to the first antenna, is given by (2.18) described in Sec. 2.3.

By introducing the noise generated by the SCM, which is present in case it is implemented using active components [78, 97], the discrete-time signals at the input of the M antennas in the k-th time interval can be expressed by the formula (2.25).

Considering a free-space LOS scenario, and denoting with G_{BS} and G_{SCM} the gain of each antenna element at the MIMO TRX and SCM, respectively,

the channel matrix $\mathbf{H}$ takes the form

$$\begin{aligned}\mathbf{H}(\varphi,\psi) = \sqrt{G_{\mathrm{BS}}\,G_{\mathrm{SCM}}}\frac{\lambda}{4\pi d}&\underbrace{\begin{bmatrix}1\\ e^{-\jmath\frac{2\pi}{\lambda}\Delta\sin\psi}\\ \vdots\\ e^{-\jmath\frac{2\pi}{\lambda}(M-1)\Delta\sin\psi}\end{bmatrix}}_{\tilde{\mathbf{u}}(\psi)\in\mathbb{C}^{M\times 1}}\\ &\times\underbrace{\begin{bmatrix}1 & e^{-\jmath\frac{2\pi}{\lambda}\Delta\sin\varphi} & \dots & e^{-\jmath\frac{2\pi}{\lambda}(N-1)\Delta\sin\varphi}\end{bmatrix}}_{\tilde{\mathbf{v}}^{\top}(\varphi)\in\mathbb{C}^{1\times N}}\\ &= \sqrt{G_{\mathrm{BS}}\,G_{\mathrm{SCM}}}\frac{\lambda}{4\pi d}\tilde{\mathbf{u}}(\psi)\tilde{\mathbf{v}}^{\top}(\varphi)\end{aligned} \tag{4.83}$$

where it has been highlighted with $\mathbf{H}(\varphi,\psi)$ the dependence of the channel on the AoD φ at the MIMO TRX and AoA ψ at the SCM. It is worth noting that the channel matrix $\mathbf{H}(\varphi,\psi)$ depends on the angles φ and ψ (i.e., on the geometry of the scenario), regardless of whether the beamforming vector at the MIMO TRX's side $\mathbf{x}[k]$ corresponds to the beam steering vector in the direction φ (i.e., the optimal direction to convey power towards the SCM) or not.

By defining the vectors $\mathbf{u}(\psi) = \tilde{\mathbf{u}}(\psi)/\sqrt{M} \in \mathbb{C}^{M\times 1}$ and $\mathbf{v}(\varphi) = \tilde{\mathbf{v}}^{*}(\varphi)/\sqrt{N} \in \mathbb{C}^{N\times 1}$, it results

$$\mathbf{H}(\varphi,\psi) = \sqrt{NMG_{\mathrm{BS}}\,G_{\mathrm{SCM}}}\frac{\lambda}{4\pi d}\mathbf{u}(\psi)\mathbf{v}^{\dagger}(\varphi) \tag{4.84}$$

which has rank one since obtained as an outer product of two vectors $\mathbf{u}$ and $\mathbf{v}^{*}$. Notice that $\mathbf{u}$ and $\mathbf{v}$ are, respectively, the top left and right eigenvectors of matrix $\mathbf{H}(\varphi,\psi)$ and hence give the optimum beamforming vectors at the SCM side and at the MIMO TRX.[8] It can be introduced the singular-value decomposition (SVD) of $\mathbf{H}(\varphi,\psi)$ as $\mathbf{H}(\varphi,\psi) = \mathbf{U}\boldsymbol{\Sigma}\mathbf{V}^{\dagger}$ where $\boldsymbol{\Sigma}$ has a singular non-zero entry

$$\sigma_1 = \frac{\sqrt{NMG_{\mathrm{BS}}\,G_{\mathrm{SCM}}}\lambda}{4\pi d} \tag{4.85}$$

[8]Since $\mathbf{H}(\varphi,\psi)$ has rank one, $\mathbf{u}$ and $\mathbf{v}$ correspond to the only left and right eigenvectors associated with non-zero eigenvalues. In this sense, they are referred to as the top eigenvectors.

in its first element, $\mathbf{U}$ has $\mathbf{u}(\psi)$ as the first eigenvector (i.e., first column), and $\mathbf{V}$ has $\mathbf{v}(\varphi)$ as the first eigenvector (i.e., first column).

Assuming channel reciprocity, at the MIMO TRX side the received signal at time interval k, consisting of the feedback of the signal transmitted in the last time interval, is given by[9]

$$\begin{aligned}\mathbf{y}[k] =&\sqrt{P_{\mathrm{T}}}\, g\, e^{\jmath\phi[k]}\, \mathbf{H}^{\top}(\varphi,\psi)\, \mathbf{H}^{*}(\varphi,\psi)\, \mathbf{x}^{*}[k-1] \\ &+ g\, \mathbf{H}^{\top}(\varphi,\psi)\, \boldsymbol{\eta}^{*}[k] + \mathbf{w}[k]\end{aligned} \tag{4.86}$$

with $\mathbf{w}[k] \sim \mathcal{CN}(\mathbf{0}, \sigma_w^2 \mathbf{I}_N)$ being the AWGN at the receiver, and $\sigma_w^2 = \kappa T_0 F_{\mathrm{AP}}\, W$, where F_{AP} represents the MIMO TRX's noise figure. (4.86) is the same reported in (4.38), but here the dependence on the angles φ, ψ is shown. By defining $\mathbf{A}(\varphi) = \sqrt{P_{\mathrm{T}}}\, g\, \mathbf{H}^{\dagger}(\varphi,\psi)\mathbf{H}(\varphi,\psi) \in \mathbb{C}^{N\times N}$, according to (4.84) it results

$$\mathbf{A}(\varphi) = \sqrt{P_{\mathrm{T}}}\, gNMG_{\mathrm{BS}}G_{\mathrm{SCM}} \left(\frac{\lambda}{4\pi d}\right)^2 \mathbf{v}(\varphi)\mathbf{v}^{\dagger}(\varphi) \tag{4.87}$$

which depends only on the angle φ, thanks to the retrodirectivity property of the SCM. Moreover, $\mathbf{A}$ is proportional to the (modified) round-trip channel $\mathbf{H}^{\dagger}(\varphi,\psi)\mathbf{H}(\varphi,\psi)$, rather than the (true) round-trip channel $\mathbf{H}^{\top}(\varphi,\psi)\mathbf{H}(\varphi,\psi)$ as in conventional backscatter communications. Consequently, the eigenvectors of $\mathbf{A}$ are identical to the right-eigenvectors of $\mathbf{H}(\varphi,\psi)$. From (4.86) it is

$$\mathbf{y}[k] = e^{\jmath\phi[k]}\, \mathbf{A}^{*}(\varphi)\, \mathbf{x}^{*}[k-1] + \mathbf{n}^{*}[k] \tag{4.88}$$

where it can be defined $\mathbf{n}^{*}[k] = g\, \mathbf{H}^{\top}(\varphi,\psi)\, \boldsymbol{\eta}^{*}[k] + \mathbf{w}[k]$, as done in (4.39).

[9]For simplicity, in this model it is not considered the clutter, that is, the signal backscattered by the environment and not modulated by the SCM. The reader can refer to [33] for a discussion concerning the modeling of the clutter and its impact on communication.

Substituting (4.87) into (4.88) it is obtained (4.89):

$$\mathbf{y}[k] = \underbrace{\sqrt{P_{\mathrm{T}}}\, g\, e^{\jmath\phi[k]} MNG_{\mathrm{BS}}G_{\mathrm{SCM}} \left(\frac{\lambda}{4\pi d}\right)^2 \mathbf{v}^*(\varphi)\mathbf{v}^\top(\varphi)\mathbf{x}^*[k-1]}_{\tilde{\mathbf{y}}[k]\text{: useful term}} + \underbrace{g\sqrt{MNG_{\mathrm{BS}}G_{\mathrm{SCM}}}\frac{\lambda}{4\pi d}\mathbf{v}^*(\varphi)\mathbf{u}^\dagger(\psi)\boldsymbol{\eta}^*[k] + \mathbf{w}[k]}_{\text{noise term}} \tag{4.89}$$

In case of perfect beamforming, i.e., $\mathbf{x}[k-1] = \mathbf{v}(\varphi)$, the useful term $\tilde{\mathbf{y}}[k]$ in (4.89) becomes

$$\tilde{\mathbf{y}}[k] = \sqrt{P_{\mathrm{T}}}\, g\, e^{\jmath\phi[k]} MNG_{\mathrm{BS}}G_{\mathrm{SCM}} \left(\frac{\lambda}{4\pi d}\right)^2 \mathbf{v}^*(\varphi) \tag{4.90}$$

since $\mathbf{v}^\top\mathbf{v}^* = 1$, thus corresponding to a plane wave of power proportional to $P_{\mathrm{T}}\, M^2N^2/\mathcal{L}^2(d)$ impinging with AoA φ, where

$$\mathcal{L}(d) = \left(\frac{4\pi d}{\lambda}\right)^2 \tag{4.91}$$

is the link loss for a distance d in free space. Notice that due to the backscattering communication type, the path loss increases with the distance to the power of four, as happens in RFID systems [159]. On the other hand, thanks to the adoption of multiple antennas on both sides, such large path loss can be compensated by increasing the number of antenna elements N and M at the MIMO TRX and SCM, respectively (beamforming gain).

The scheme proposed for SCM detection, identification, and AoA estimation operates iteratively. As shown in the pseudocode for this procedure (Algorithm 6), to which the reader is referred, the process starts (step 1 of the pseudocode) with the generation of a random unitary beamforming vector $\mathbf{x}[0]$, which the MIMO TRX uses at startup when the locations of SCMs are still unknown.

The iterative procedure, which occurs with discrete time steps indexed by $k \geqslant 1$ (step 2), can then begin with the MIMO TRX transmitting the beamforming vector $\sqrt{P_{\mathrm{T}}}\,\mathbf{x}[k-1]$ (step 3). The SCM, upon receiv-

Algorithm 6: SCM detection and AoA estimation

0: *Initialization*: generate a random unitary norm beamforming vector $\mathbf{x}[0]$;
1: **for** $k = 1, \ldots, \infty$ **do**
  2: transmit: $\sqrt{P_{\mathrm{T}}}\,\mathbf{x}[k-1]$; `// signal transmitted`
  3: receive: $\mathbf{y}[k] = e^{\jmath\phi[k]}\,\mathbf{A}^*(\varphi)\,\mathbf{x}^*[k-1] + \mathbf{n}^*[k]$; `// signal received`
  4: update the beamforming vector: $\mathbf{x}[k] = \mathbf{y}^*[k]/\|\mathbf{y}[k]\|$; `// beamforming update`
  5: $u[k] = \mathbf{x}^\dagger[k-1]\,\mathbf{y}^*[k]$; `// decision variable`
  6: estimate the SNR: $\gamma[k] = |u[k]|^2/\sigma_w^2$; `// SNR estimation`
  7: **if** $\gamma[k] > \eta_1$ *and* $\gamma[k]/\gamma[k-1] < \eta_2$ **then**
    8: $\bar{k} = k$;
    9: $\mathbf{q} = \mathrm{DFT}\left[\mathbf{x}[\bar{k}]\right]$; `// DFT computation`
    10: $\widehat{\varphi} = \arcsin\left(\frac{2}{N}\,\mathrm{argmax}_{i\in\{1,2,\ldots,N\}}\,\{|q_i|\}\right)$; `// AoA estimation`
    // Start of ID detection
    11: **for** $j = 1, \ldots, K$ **do**
      12: $k = k + 1$;
      13: transmit: $\sqrt{P_{\mathrm{T}}}\,\mathbf{x}[\bar{k}]$; `// signal transmitted`
      14: receive: $\mathbf{y}[k] = e^{\jmath\phi[k]}\,\mathbf{A}^*(\varphi)\,\mathbf{x}^*[\bar{k}] + \mathbf{n}^*[k]$; `// signal received`
      15: $u[k] = \mathbf{x}^\dagger[\bar{k}]\,\mathbf{y}^*[k]$; `// decision variable`
      16: decode the symbol: $\widehat{\phi}[j] = \mathsf{demodulation}\,(-\arg\{u[k]\})$; `// symbol detection`
    end
    17: extract the packet ID: $\left\{\widehat{\phi}[j]\right\}_{j=1,\ldots,K}$; `// packet ID extraction`
    // End of ID detection
  end
end

ing $\mathbf{z}[k] = \sqrt{P_{\mathrm{T}}}\mathbf{H}\mathbf{x}[k-1] + \boldsymbol{\eta}[k]$ (see (4.36)), backscatters it in the direction of arrival, as a result of the conjugation operation. Additionally, it introduces a phase modulation based on the data to be transmitted to the MIMO TRX, resulting in the reflected signal $\mathbf{r}[k] = g\,e^{\jmath\phi[k]}\mathbf{z}^*[k]$ (see (4.37)). The MIMO TRX then receives the retro-directed and modulated response $\mathbf{y}[k] = e^{\jmath\phi[k]}\,\mathbf{A}^*(\varphi)\,\mathbf{x}^*[k-1] + \mathbf{n}^*[k]$, as described by (4.88) (step 4).

At the MIMO TRX, a normalized and conjugated version of the received vector $\mathbf{y}[k]$ is computed (step 5) as $\mathbf{x}[k] = \frac{\mathbf{y}^*[k]}{\|\mathbf{y}[k]\|}$. This vector will be used as the updated beamforming vector $\mathbf{x}[k]$ in the next iteration. This adjustment makes the beamforming vector steer toward the SCM. In principle, the

updated beamforming vector should immediately align with the SCM. However, due to the presence of noise and multipath, the alignment may require more than one iteration to be completed.

The decision variable $u[k] = \mathbf{x}^{\dagger}[k-1]\,\mathbf{y}^{*}[k]$, which depends on $e^{-\jmath\phi[k]}$, is then computed[10] (step 6) allowing also to estimate the SNR $\gamma[k] = |u[k]|^2/\sigma_w^2$ experienced in the current iteration by the MIMO TRX (step 7). If $\gamma[k]$ exceeds a specific detection threshold η_1, i.e., $\gamma[k] = |u[k]|^2/\sigma_w^2 > \eta_1$, and there is no significant increase in received power compared to the previous iteration, i.e., $\gamma[k]/\gamma[k-1] < \eta_2$, where η_1 and η_2 are empirically tuned thresholds, then the SCM is detected (step 8). In fact, the first inequality checks that a certain level of energy has been received compared to the noise level, whereas the second one guarantees that convergence is approximately reached.

If this is the case, the MIMO TRX assumes that the transient interval — during which the beamforming vector is iteratively adjusted to point toward the SCM — is over and that the vector is now accurately aligned with the SCM. Therefore, the current time index $\bar{k}$ is "frozen" (step 9) and the AoA estimation is carried out (steps 10 and 11). Specifically, the AoA estimate $\widehat{\varphi}$ of φ concerning the detected SCM is obtained as[11]

$$\widehat{\varphi} = \arcsin\left(\frac{2}{N}\,\mathrm{argmax}_{i\in\{1,2,\ldots,N\}}\,\{|q_i|\}\right) \tag{4.92}$$

where $\mathbf{q} = \{q_i\}$ is the Discrete Fourier Transform (DFT) of the beamforming vector corresponding to the detected SCM, that is

$$\mathbf{q} = \mathrm{DFT}\left[\mathbf{x}[\bar{k}]\right]\,. \tag{4.93}$$

To identify the detected SCM, the MIMO TRX must now extract its ID from the backscattered signal. In fact, this ID is encoded in a unique pseudo noise (PN) sequence of length K symbols, which the SCM transmits cyclically by modulating the backscattered signal. Of course, only during the transmission of the interrogation signal from the MIMO TRX, such PN sequence correspond to a physical modulated signal. In this regard, Fig. 4.29 shows

[10] In fact, in the absence of noise, it is easy to show from (4.39) that $u[k] = \mathbf{x}^{\dagger}[k-1]\,\mathbf{y}^{*}[k] \propto e^{-\jmath\phi[k]}$, being $\mathbf{x}^{\dagger}[k-1]\,\mathbf{x}[k-1] = 1$.

[11] An array spacing $\Delta = \lambda/2$ is assumed.

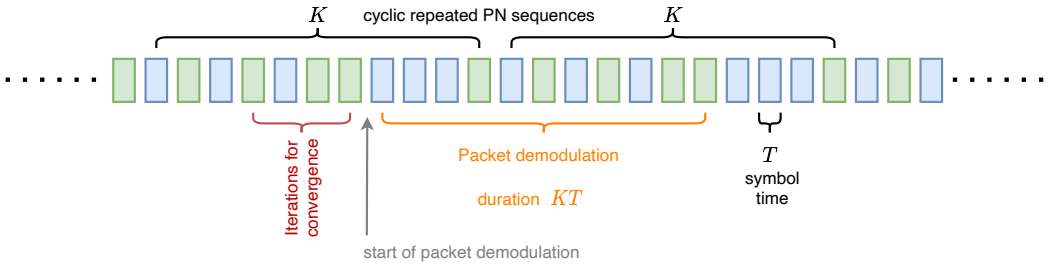

Figure 4.29: Cyclic transmission of the SCM's ID. Time evolution.

the sequence of K symbols, out of a binary alphabet, that corresponds to the backscatter modulation cyclically realized at the SCM. The identification task is performed in steps 12 to 18, where the MIMO TRX:

- transmits always using the optimum beamforming vector $\mathbf{x}[i]$ (step 14);
- receives the backscattered signal carrying the ID information in $\phi[k]$ (step 15);
- creates the decision variable $u[k]$ (step 16);
- finally, determines the modulation symbol conveyed by $\phi[k]$ through a suitable demodulation scheme applied to $u[k]$, depending on the modulation alphabet (step 17).

Once all the K components of the ID have been collected (step 19), the MIMO TRX can finally assign an identity to the SCM transmitting from the direction given by the estimated AoA.

Summarizing, the iterative process here proposed allows the MIMO TRX to transmit according to the optimum beamforming vector pointing towards the SCM. Therefore, the AoD of the signal from the MIMO TRX coincides with the AoA of the signal received from the SCM, thus enabling angle-based localization. This is realized by exploiting the processing gain offered by the N antennas at the MIMO TRX and the M antennas at the SCM, but without explicit channel estimation, and adopting backscattering. **Remark:** It is worth noting that the strategy described above is based on the transmission of narrowband signals, which is beneficial in terms of spectrum usage efficiency. This aspect is becoming increasingly important as future wireless

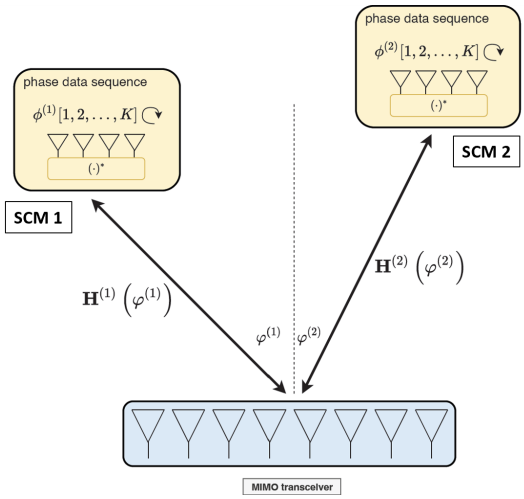

Figure 4.30: Communication and AoA estimation with multiple SCMs sending packets of K bytes cyclically.

technologies are expected to support both communication and localization (sensing) services, possibly sharing the same RF front-end and the same frequency band. However, classical high-accuracy localization techniques are based on the estimation of the TOA or TDOA of the signals, whose resolution is related to the bandwidth. Centimeter-level accuracy requires the availability of roughly 1 GHz of bandwidth with consequent reduction of potential communication throughput. Moreover, time-based approaches are very sensitive to clock mismatches between the involved devices thus making them not really appealing for IoT applications [29]. Therefore, any localization technique capable of providing high-accuracy positioning with minimal usage of bandwidth and simple hardware on the device side is, in general, more attractive. Along this direction, our scheme does not require a wideband signal as it relies on AoA estimation. In addition, the backscatter nature of our scheme significantly simplifies the complexity of the user and does not suffer from clock mismatches.

Extension to Multiple SCM-based Devices

Now, it is assumed that there are P SCM-based devices in the environment. These devices can either be mobile UEs in Architecture 1 or fixed anchors in Architecture 2. In the same environment, there are also devices equipped

with a standard antenna array (MIMO TRX), which emit interrogation signals to detect the presence of the P SCM-based devices and estimate their corresponding AoAs (see Fig. 4.30).

In LOS channel conditions, the process of detecting the presence of the P SCMs by a MIMO TRX is equivalent to determining the top eigenvectors of the P channels $\mathbf{A}^{(p)}$, $p = 1, 2, \ldots, P$, between the MIMO TRX and the P SCMs. The formulas are the ones described in 4.2.1.

In this regard, the iterative scheme proposed in Algorithm 6, which is limited to the estimation of only the top eigenvector, can be extended to estimate the P top eigenvectors of $\mathbf{A} = \sum_{p=1}^{P} \mathbf{A}^{(p)}\left(\varphi^{(p)}\right)$, as already described in Sec. 4.2.1. Nevertheless, if the SCMs are positioned at distinct angles and the number of antennas is increased by employing massive arrays (massive MIMO), the channels $\mathbf{A}^{(p)}$ tend to become orthogonal. This situation approaches the so-called *favorable propagation* [160], which, strictly speaking, occurs when the channels $\mathbf{A}^{(p)}$ are orthogonal [161]. Under this condition, once the top eigenvector of $\mathbf{A}$ has been estimated, the detection of the second top eigenvector can be achieved using the same scheme described in Algorithm 6, provided that the iterative search is conducted in a space orthogonal to that spanned by the top eigenvector. To elaborate further, let's consider a matrix $\mathbf{B}$ that collects all the previously discovered top eigenvectors. At Step 5 of the algorithm described in Algorithm 6, the following operation is performed:

$$\mathbf{x}[k] = \frac{\left(\mathbf{I} - \mathbf{B}\,\mathbf{B}^{\dagger}\right)\mathbf{y}^{*}[k]}{\left\|\left(\mathbf{I} - \mathbf{B}\,\mathbf{B}^{\dagger}\right)\mathbf{y}^{*}[k]\right\|} \tag{4.94}$$

so that, before further processing, the updated beamforming vector $\mathbf{x}[k]$ is adjusted to be orthogonal to $\mathbf{B}$. This ensures that the subsequent search is conducted within the null space of $\mathbf{B}$, preventing the detection of previously identified eigenvectors (i.e., already detected SCM-based devices). This procedure is the same as that performed by the Scouting Task of the GFRA application, described in the previous section. In a more general scenario where the favorable propagation condition is not perfectly achieved, the top eigenvectors of $\mathbf{A}$ may not precisely align with the top eigenvectors of $\mathbf{A}^{(p)}$ [32,33]. This can result in interference among SCM-based devices and subsequent performance degradation for demodulation and AoA estimation.

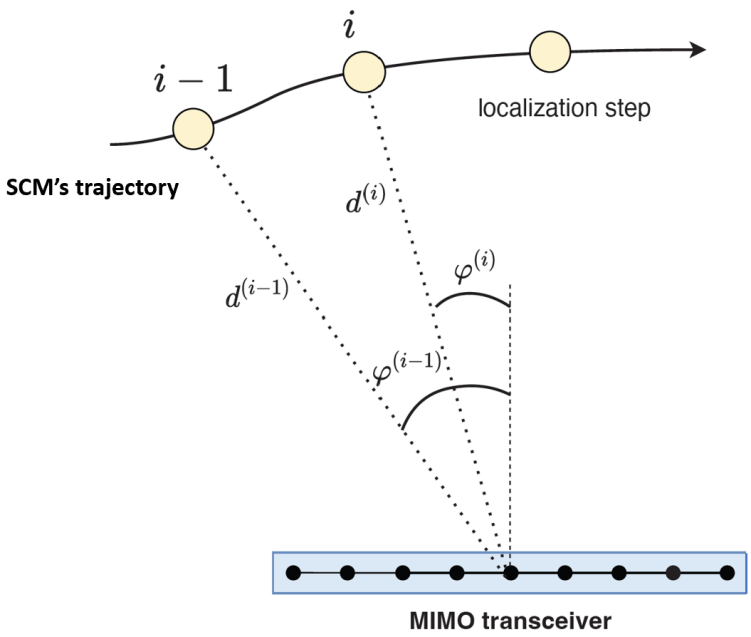

Figure 4.31: Localization of the SCM in a dynamic scenario.

Channel Tracking

Consider now the localization task in a dynamic scenario, where one of the two nodes (e.g., the SCM) moves along a certain trajectory (see Fig. 4.31). The iterative scheme described in Algorithm 6 is executed at specific points of the trajectory, namely, the localization steps. Specifically, at the i-th localization step an AoA estimate (after SCM detection) and a data packet consisting of K symbols (e.g., the node's ID) are obtained. Referring to Fig. 4.31, the SCM is observed at an angle $\varphi^{(i)}$ with respect to the MIMO TRX and located at a distance $d^{(i)}$ during the i-th localization step. Specifically, τ denotes the time interval between two consecutive localization steps. Thus, it can be defined the maximum localization update rate as $\mathcal{R} = 1/\tau$, assuming that a sufficient number of angular measurements is collected at the i-th localization step to obtain an unambiguous location estimate.

To speed up the convergence of the proposed iterative scheme, rather than randomly choosing an initial beamforming vector $\mathbf{x}^{(i)}[0]$ at the i-th localization step, it may be more convenient to use the last available estimated beamforming vector $\mathbf{x}^{(i-1)}[\bar{k}]$ at the previous localization step (i.e., $i-1$),

thus assuming $\mathbf{x}^{(i)}[0] = \mathbf{x}^{(i-1)}[\bar{k}]$. Since, according to this choice, the estimated beamforming vectors are re-used and updated iteratively during the movement of the node, such a strategy is defined as *channel tracking*.

Now it is defined, for further convenience, the SNR along the first direction at the startup for the i-th localization step; this is the key parameter determining the convergence speed of the scheme. Specifically, it can be defined *startup SNR* so that $\mathsf{SNR}_{\text{start}}^{(i)} = \mathsf{SNR}_{1}^{(i)}[0]$ for the localization step i. It can be assumed that at the localization step $i-1$ the convergence to $\mathsf{SNR}_{1,\max}$ was achieved. Next, the last beamforming vector $\mathbf{x}^{(i-1)}[K]$ of localization step $i-1$ is used as first beamforming vector $\mathbf{x}^{(i)}[0]$ of localization step i. In such a case, the SNR along the first direction at the startup for the localization step i, which determines the convergence speed, can be written as

$$\mathsf{SNR}_{\text{start}}^{(i)} = \gamma\, \mathsf{SNR}_{1,\max}^{(i-1)} \tag{4.95}$$

where γ reflects the change in the SNR between the two positions when adopting the previous beamforming vector. In particular, it can be decomposed γ as the product of two factors, i.e., $\gamma = \xi\rho$; the coefficient $\rho \leqslant 1$ indicates the correlation between the channels related to the localization steps $i-1$ and i, while $\xi \lesseqgtr 1$ indicates the difference in terms of path loss. The term ρ can be obtained as the cross-correlation coefficient between the beamforming vectors corresponding to angles $\varphi^{(i-1)}$ and $\varphi^{(i)}$, that are, $\mathbf{v}(\varphi^{(i-1)})$ and $\mathbf{v}(\varphi^{(i)})$ as

$$\rho = \left| < \mathbf{v}(\varphi^{(i)}), \mathbf{v}(\varphi^{(i-1)}) > \right| . \tag{4.96}$$

The term ξ can be written as the ratio between the path loss at positions $i-1$ and i, thus it is $\xi = \mathcal{L}(d^{(i-1)})/\mathcal{L}(d^{(i)})$ according to (4.91) when considering a free space scenario. If $\mathsf{SNR}_{1,\max}^{(i)}/N \gg 1$ it is obtained convergence at the maximum SNR for the localization step i, which is $\mathsf{SNR}_{1,\max}^{(i)} = \xi\, \mathsf{SNR}_{1,\max}^{(i-1)}$.

The choice of using the previous convergence beamforming vector is beneficial only if the corresponding startup SNR is larger than that obtained with the random guess $\mathbf{x}^{(i)}[0]$ at the i-th localization step. In fact, when selecting randomly the first beamforming vector $\mathbf{x}^{(i)}[0]$, it is obtained the value $\mathsf{SNR}_{1,\text{boot}}^{(i)} = \mathsf{SNR}_{1,\max}^{(i)}/N$ as the starting point of the iterative proce-

dure. Formalizing, the choice is beneficial if

$$\mathsf{SNR}_{\text{start}}^{(i)} = \xi\rho\,\mathsf{SNR}_{1,\max}^{(i-1)} > \mathsf{SNR}_{1,\text{boot}}^{(i)} = \frac{\mathsf{SNR}_{1,\max}^{(i)}}{N}\,. \tag{4.97}$$

However, since it holds that $\mathsf{SNR}_{1,\max}^{(i)} = \xi\,\mathsf{SNR}_{1,\max}^{(i-1)}$ (i.e., the SNR obtained when considering the optimum beamforming vector at each location) the criterion (4.97) becomes

$$\rho > \frac{1}{N}\,. \tag{4.98}$$

It is very important to underline that the convenience is experienced in the number of iterations needed to reach convergence (i.e., convergence speed); no differences are obtained in terms of probability of convergence to the maximum SNR, since this is determined only by the bootstrap SNR value.

From (4.98), it could be inferred that a large number of antennas N at the MIMO TRX is beneficial for ensuring faster convergence (i.e., that a larger number of antennas can allow to tolerate highly decorrelated channels between localization steps $i-1$ and i). However, it is important to note that the correlation coefficient ρ itself strongly depends on the number of antennas N. For instance, consider a scenario where there is a small movement of the SCM orthogonal to the MIMO TRX's array normal direction. In such a case, the primary source of change in the SNR arises from the differing optimal combinations of phase values at the two positions, leading to $\gamma \approx \rho$. Consider for simplicity $\varphi(i-1) = 0$ (i.e., SCM on the MIMO TRX's normal direction at localization step $i-1$), and the SCM moving with constant speed v transversal to the MIMO TRX's normal direction. When operating with half-wavelength spaced ULAs, it is

$$\begin{aligned}\mathbf{v}_1^{(i-1)} &= \frac{1}{\sqrt{N}}\left[1, 1, \dots 1\right] \;\in \mathbb{C}^{N\times 1} \\ \mathbf{v}_1^{(i)} &= \frac{1}{\sqrt{N}}\left[1, e^{\jmath\pi\sin\varphi^{(i)}}, \dots, e^{\jmath\pi(N-1)\sin\varphi^{(i)}}\right] \;\in \mathbb{C}^{N\times 1}\end{aligned} \tag{4.99}$$

thus it can be written

$$\rho = \frac{1}{N}\left|\sum_{n=0}^{N-1} e^{-\jmath\pi n\sin\varphi^{(i)}}\right| \approx \operatorname{sinc}\left(\frac{N\sin\varphi^{(i)}}{2}\right). \tag{4.100}$$

In order to obtain a simple condition for determining the advantage of using the previous beamforming vector in the dynamic scenario, the sinc function can be approximated using its Taylor expansion around the origin, i.e., $\mathrm{sinc}\,(x) \approx 1 - \frac{\pi^2 x^2}{3!}$ and consider $\sin\varphi^{(i)} \approx \tan\varphi^{(i)} = v\tau/d^{(i)}$ obtaining for (4.98)

$$1 - \frac{\pi^2 N^2 v^2 \tau^2}{24\left(d^{(i)}\right)^2} > \frac{1}{N}\,. \tag{4.101}$$

Then, by inverting (4.101), it follows that the choice of using the previous beamforming vector is beneficial with respect to a random guess to ensure faster convergence only if

$$v < \frac{2d^{(i)}\sqrt{6(N-1)}}{\pi\tau N\sqrt{N}}\,. \tag{4.102}$$

When such a condition is not met, the channel variations between localization steps $i-1$ and i are too significant, and relying on the previous beamforming vector proves ineffective. In such cases, a random guess can ensure faster convergence.

According to (4.102), the larger the number of antennas N, the lower the maximum tolerated speed. In fact, a large number of antennas causes the channel to quickly decorrelate when moving from one position to another. Interestingly, it is worth noting that the convergence speed is not affected by M, i.e., the number of antennas at the SCM. Thus, this parameter can be increased to improve the link budget without encountering convergence constraints in dynamic scenarios.

In order to characterize the potential of tracking the channel by exploiting the last available beamforming vector, it is considered a numerical example considering a variable number N of antennas and $\tau = 100\,ms$. Fig. 4.32 shows the maximum speed for the SCM in order to benefit from using the previous beamforming vector according to (4.102). It is possible to notice that, as the number of antennas increases, the maximum speed decreases. Moreover, if the SCM is close to the MIMO TRX the speed limit is lower since the channel changes faster its angular correlation (larger variation in angle φ for a given transversal movement). It is worth noticing that if the speed is larger than that reported in Fig. 4.32, convergence is still guaranteed

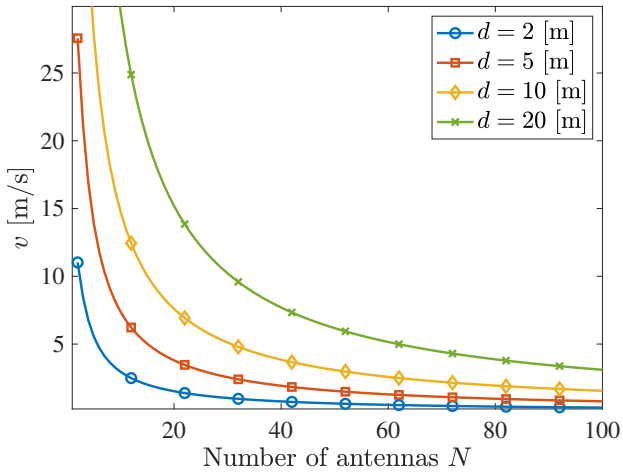

Figure 4.32: Maximum speed to make the channel tracking effective for improving the convergence speed of the proposed scheme.

if the bootstrap SNR satisfies $\mathsf{SNR}^{(i)}_{\text{start}}/N \gg 1$; however, using a random guess would be more effective (higher startup SNR thus faster convergence).

Numerical Results

In this section, the performance of the proposed localization strategies for both Architecture 1 and Architecture 2 are investigated. The simulation parameters, detailed below, are identical in both cases. Simulations are performed in the 2D scenario depicted in Fig. 4.33, where two UEs (U1 and U2) move along the red trajectories in the xz - plane. Four anchors are also positioned in this scenario. The SCMs, whether at the UE side or the anchor side depending on the architecture being investigated, consist of square uniform planar arrays with 20×20 antenna elements arranged in the xy - plane. MIMO TRXs consist also of uniform planar arrays featuring 10×10 antenna elements, deployed in the xy - plane. According to the scheme outlined in Algorithm 6, MIMO TRXs employ the signals backscattered by the SCMs to estimate their AoAs. Notice that, despite localization being realized on a plane, both fixed and mobile antennas (including SCMs) are assumed as 2D panels; this choice does not affect the angular resolution but improves the link budget thanks to additional SNR gain. The parameters used in the

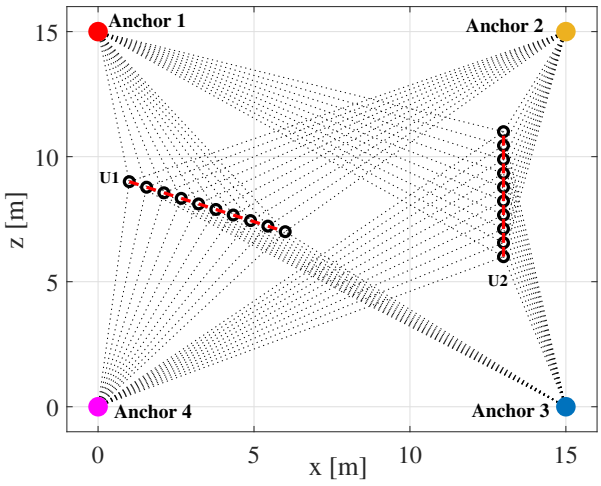

Figure 4.33: Simulated scenario: two users (U1 and U2) moving along the red trajectories, and four anchors. Black circles indicate the locations corresponding to the localization steps given a certain localization update rate $\mathcal{R}$.

Table 4.5: Parameters used in the simulations.

Parameter	**Symbol**	**Value**
Carrier frequency	f_{c}	$28\,GHz$
Bandwidth	W	$10\,MHz$
Symbol time	T	$190\,ns$
TX power	P_{T}	$0\,dBm$
Path loss exponent	β	2
MIMO TRX antenna gain	G_{A}	$0\,dBi$ (isotropic)
SCM antenna gain	G_{SCM}	$0\,dBi$ (isotropic)
SCM backscatter gain	g	$0\,dB$ or $10\,dB$
SCM/MIMO TRX noise figure	F	$3\,dB$
SCM antenna elements	M	20×20 $(10.7 \times 10.7\,cm^2)$
MIMO TRX antenna elements	N	10×10 $(5.36 \times 5.36\,cm^2)$
SNR detection threshold	η_1	$30\,dB$
SNR convergence threshold	η_2	$3\,dB$
ID length	K	40 symbols
Localization update time-step	τ	$100\,ms$
Speed of UEs	v	$0.54\,m/s$
UE's trajectory length	L	$5.39\,m$

simulations, unless otherwise specified, are reported in Tab. 4.5.

Localization Error Analysis - Architecture 1

Depending on the channel condition and SNR, one or more anchors (i.e., MIMO TRXs) in the scenario can detect the presence of the SCMs (i.e., UEs) at each localization step and obtain the associated AoA estimates. Then, the AoA estimates are fused using a least-square approach as described in [162], yielding an estimate $\widehat{\mathbf{p}} = [\widehat{x}, \widehat{z}]$ of the position $\mathbf{p} = [x, z]$, in accordance with the geometry depicted in Fig. 4.33.

As a preliminary assessment of the proposed system performance, Monte Carlo simulations are conducted with a single UE (U1 in Fig. 4.33). The results are reported in Fig. 4.34, which shows the ECDF of the absolute localization error $\epsilon = |\widehat{\mathbf{p}} - \mathbf{p}|$ under different conditions, obtained over 100 Monte Carlo iterations. Specifically, a user moving with a speed of $v = 0.54]m/s$ along a straight trajectory of length $L = 5.39]m$, and a localization update rate $\mathcal{R} = 10Hz$ (i.e., $\tau = 100ms$), thus corresponding to 100 discrete localization steps along the trajectory is considered. The results refer to various operating conditions, including:

- An ideal LOS channel (free-space) and a realistic 3GPP CDL-E channel [134];
- The exploitation of passive ($g = 0\,dB$) and active ($g = 10\,dB$) SCMs;
- The adoption of a random beamforming vector (b.v. in the plot legends) as initialization of the proposed scheme, or the last available beamforming vector, according to the channel tracking strategy presented in Sec. 4.2.3.

When focusing on the impact of the channel, it is evident from Fig. 4.34 that the best performance is achieved with free-space LOS conditions (dashed lines), owing to the absence of multipath propagation. In this case, deviations in the AoA estimate from the true angle primarily result from measurement noise. Performance deteriorates slightly when considering the 3GPP CDL-E channel (continuous lines), due to multipath effects. Generally, the localization error remains below $5\,cm$ and $10\,cm$ in 90% of cases for the free-space channel (dashed lines) and CDL-E channel (continuous line), respectively. The same figure also illustrates the impact of path loss on performance. It is

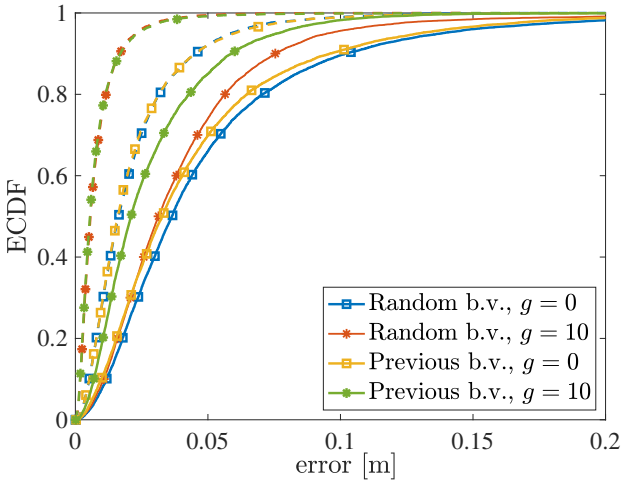

Figure 4.34: ECDF of the absolute localization error for Architecture 1. Dashed lines (- -) are for the free-space LOS channel; continuous lines (–) are for the 3GPP CDL-E channel.

evident that leveraging active SCMs (red/green lines) reduces the localization error, primarily due to increased received power and consequently more robust AoA estimation.

When considering the channel tracking mechanism proposed in Sec. 4.2.3, no differences in performance are observed for the free-space LOS channel. This is expected, as channel tracking primarily facilitates faster convergence compared to randomly generating the initial beamforming vector. However, this aspect is not captured by the results shown in Fig. 4.34, which concern positioning errors. Contrarily, when a realistic multipath channel is considered, leveraging the previous beamforming vector (i.e., utilizing the channel tracking mechanism) results in a reduction in localization error. In fact, when the beamforming vector is randomly generated at each localization step, there is a chance that the AoA estimator locks onto a multipath component, potentially leading to more significant errors compared to starting the iterative algorithm from the previous, possibly correct, AoA estimate.

The impact of the array size on the AoA estimation and, consequently, on localization accuracy is shown in Fig. 4.35, which depicts the ECDF of the absolute localization error as the number of SCM elements varies. The simulations are carried out for both users moving along the trajectories shown

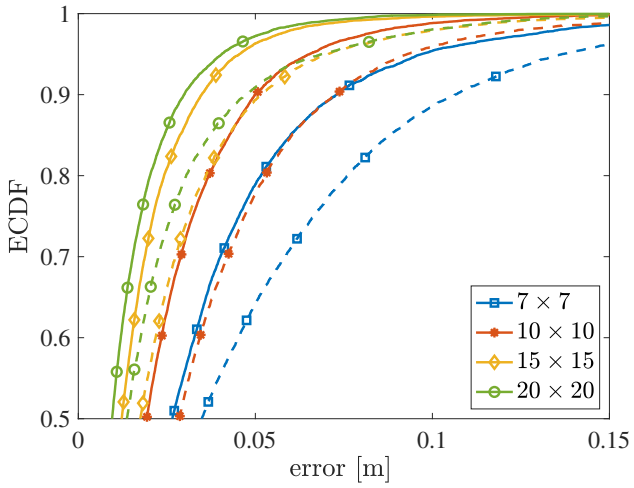

Figure 4.35: ECDF of the absolute localization error for U1 (continuous lines) and U2 (dashed lines) in Architecture 1, varying the size $M \times M$ of the SCM.

in Fig. 4.33. Performance improves with an increasing number of antenna elements, due to the dual benefits of higher SNR (larger number of observations with additional antenna elements) and a larger aperture, which results in enhanced angular resolution.

Localization Error Analysis - Architecture 2

When considering Architecture 2, it is the UE that transmits the interrogation signal, which is then backscattered by SCM-equipped anchors. Therefore, it is the UE that estimates the AoA of the received signals relative to its own reference system. In this section, the focus is on Architecture 2 and on the investigation of the performance of localization strategy in the scenario depicted in Fig. 4.33, concentrating on U1.

In Fig. 4.36, the ECDF of the absolute angle estimation error relative to each of the 4 anchors is shown. This figure was obtained with 100 Monte Carlo cycles along the trajectory, varying the gain of the backscattered signal g, with a LOS channel, and without utilizing the beamforming vector from the previous step. Fig. 4.36 shows that the accuracy of angular estimation is generally below one degree with the proposed setup. The highest accuracy is achieved by anchors 1 and 4, which are closest to U1. As for Architecture 1, increasing the gain g of the SCMs significantly reduces the error.

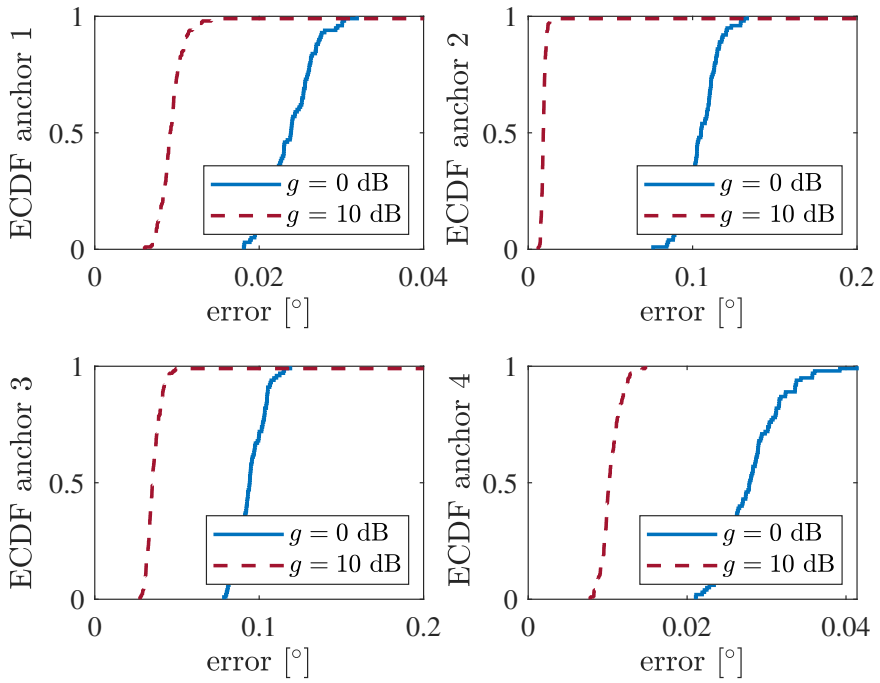

Figure 4.36: ECDF of the angle estimation error in Architecture 2 for U1.

Regarding the estimation of the UE's position in Architecture 2 according to a global reference system, it is already pointed out that this is possible only if the UE knows the coordinates of the anchors and its own orientation. Fig. 4.37 shows the ECDF of the absolute localization error when assuming that the UE experiences a residual random error on its own orientation, obtained from external sensors. Specifically, this error is modeled as Gaussian with zero mean and variance σ^2. As it can be noticed, increasing the UE orientation error deteriorates the performance due to the mismatch between the local and global reference systems. While higher SCM gain g can be adopted in general to ameliorate the performance in the absence of residual orientation error ($\sigma^2 = 0°$), the presence of an orientation error outweighs the benefits of the SCM gain (the corresponding curves are overlapped for $\sigma^2 > 0°$ in Fig. 4.37). The blue curves also demonstrate that the two architectures exhibit a comparable performance.

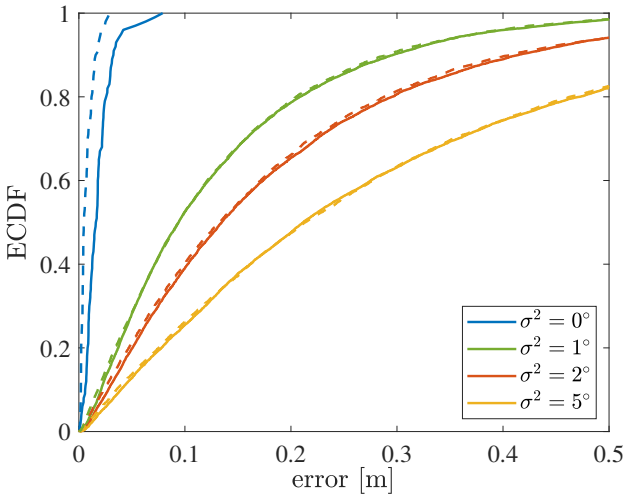

Figure 4.37: ECDF of the absolute localization in Architecture 2, considering a residual random error with variance σ^2 on the UE orientation. Continuous lines (–) are for $g = 0dB$; dashed lines (- -) are for $g = 10dB$.

Convergence Analysis

The impact of the channel tracking mechanism, introduced in Sec. 4.2.3, is further investigated in Fig. 4.38, which refers to Architecture 1. This figure presents the ECDF of the number of iterations required for UEs' detection relative to Anchor 4 (located at the bottom-left in Fig. 4.33). The LOS free-space channel is here considered (similar outcomes are achieved with the 3GPP channel model).

A noticeable difference in the number of iterations required for convergence is observed between using a random beamforming vector (blue/red lines) and the last available beamforming vector (yellow/green lines) as initialization of the proposed estimation scheme. The results demonstrate that utilizing the previous beamforming vector yields consistent improvement in terms of the number of iterations needed for convergence. This improvement is particularly significant for U2, which is the farthest from Anchor 4, thus experiencing highly correlated channels from one localization step to the other (as discussed in Sec. 4.2.3). Remarkably, when exploiting the previous beamforming vector, the convergence time is halved for $g = 0dB$.

These results also offer insights into the localization update rate $\mathcal{R}$. While being set $\mathcal{R} = 10Hz$ in the simulations, much higher values could have been

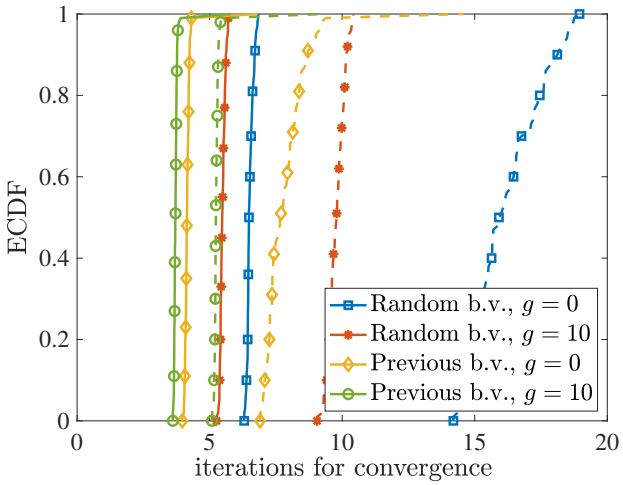

Figure 4.38: Number of iterations required for detection relative to anchor 4, by varying the SCM gain and the use of the previous/random beamforming vector. Dashed lines (- -) are for U2; continuous lines (–) are U1.

chosen, as the lower limit on this parameter is determined by the packet size K. In fact, the time elapsed between consecutive localization steps must be greater than KT (see Fig. 4.29), which corresponds to the duration of the ID transmission. Depending on the number of SCMs in the environment, to ensure the discrimination of each ID a certain number of different PN sequences must be available. By assuming, as an example, the adoption of maximum length sequences, a packet length of $K = 1023$ symbols allows discriminating 60 different SCMs, while a packet length of $K = 8191$ symbols allows discriminating 630 different SCMs [152]. These values lead to a maximum localization update rate $\mathcal{R}$ of roughly $10kHz$ and $1]kHz$, respectively, which is larger than today's real time locating systems (RTLSs), that usually provide tens of update per second. In fact, in this case, scalability is much simpler than in time-based RTLSs, where multiple users are usually interrogated sequentially. Since convergence is realized in a few iterations (e.g., 10 is a typical value according to Fig. 4.38) the detection/estimation time results are generally negligible with respect to the ID duration.

In addition to offering a very high localization update rate, the proposed solution offers several advantages over currently available solutions, such as UWB-based RTLSs; in fact, it can work with narrowband transmissions, no

synchronization is required as for time-difference-of-arrival based systems, and no clock drift is experienced. Consequently, UWB-based RTLSs results in a more complex anchor localization calibration process compared to our scheme [29]. Moreover, being the SCMs backscattering devices, energy harvesting techniques can be included to make them energy autonomous.

4.3 Radio-Simultaneous Localization and Mapping at THz

In this section, the proposed R-SLAM approach tailored to a mobile device offering THz-based radar functionalities is introduced. First, the formalization of the problem statement and then the description of the processing chain that, starting with raw radar measurements, leads to the estimation of the user's trajectory and the automatic mapping of the environment are reported. The procedure, algorithms, and results presented in this section refer to the measurements described in Sec. 3.2.

A 2D scenario is considered in which the state of a mobile user at the (discrete) time instant k, with time step T_{F}, is denoted by

$$\mathbf{x}_k = [x_k, y_k, \dot{x}_k, \dot{y}_k, \theta_k, \dot{\theta}_k]^T \tag{4.103}$$

which accounts for the user's position coordinates (x_k, y_k), orientation θ_k and their variation speeds $(\dot{x}_k, \dot{y}_k)$ and $\dot{\theta}_k$, respectively. Moreover, the absolute pose of the user is denoted by

$$\mathbf{p}_k = [x_k, y_k, \theta_k]^T. \tag{4.104}$$

The objective is to devise a processing chain that, starting from raw measurements provided by the THz radar, is capable of estimating in real-time the trajectory of the mobile user up to time k, i.e., the sequence of states $\mathbf{x}_{[1:k]}$ (and therefore of poses $\mathbf{p}_{[1:k]}$), as well as the map of the surrounding environment.

Classical solutions to the joint localization and mapping problem are typically found in the realm of SLAM algorithms, which have been extensively explored in the literature in the context of laser-based measurement sources. In this case, however, the final objective must be achieved starting from radio measurements, which requires ad hoc strategies that fall within the far less investigated R-SLAM field. Radio signals backscattered by the environment have to be properly processed in order to infer the map of the scenario and, simultaneously, track the position of the user. In the following, each step of

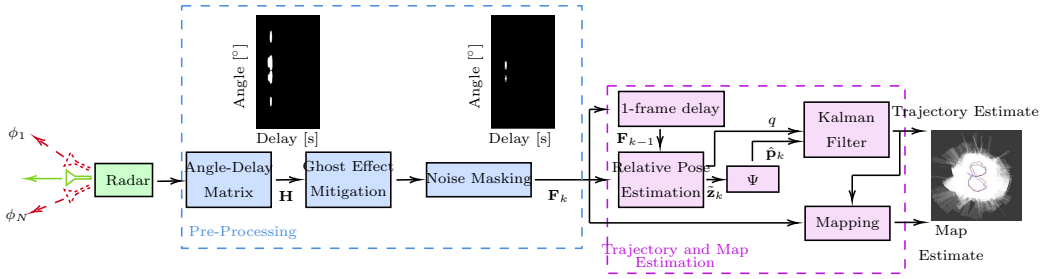

Figure 4.39: R-SLAM: Proposed processing chain. Ψ denotes the operations of (4.114)-(4.116) that transform the relative pose $\tilde{\mathbf{z}}_k = [\tilde{dx}, \tilde{dy}, \tilde{d\theta}]^T$ on the absolute pose $\hat{\mathbf{p}}_k$. Possible implementations of the "Pose Estimation" block are depicted in Figs. 4.41-4.42.

the processing chain is discussed, which is depicted in Fig. 4.39. In order to keep the discussion general, I will not focus on a particular radar technology, but rather it can be supposed that the radar equipment provides the sampled CIRs of the two-way channel for a set $\{\phi_1, \phi_2, \ldots, \phi_N\}$ of N angular directions. These can be obtained, for example, using a MIMO radar where the signal emitted by the transmitting antennas and backscattered by the environment is collected by an array of receiving antennas [163]. Such outcomes are then processed as described below. How the sampled CIRs were obtained through measurements made in a real environment in the 300 GHz band will be explained in Sec. 3.2.

The radar sounder outputs are assumed of M samples, with sampling time T_s (time resolution), of the backscatter CIR for N different angles of view ϕ_n uniformly distributed in the range $[-90°, 90°]$. The magnitudes of these samples are gathered into the *Angle-Delay* matrix

$$\mathbf{H} = \{|h_{n,m}|\},\ n = 1, 2, \ldots, N,\ m = 1, 2, \ldots, M \tag{4.105}$$

so that the n-th row of $\mathbf{H}$ contains the magnitudes of M (noisy) samples of the CIR in the angular direction ϕ_n. In particular, for a given angular direction ϕ_n, $|h_{n,m}|$ refers to the time instant $t_m = T_\mathrm{min} + (m-1)\,T_\mathrm{s}$, $m = 1, 2, \ldots, M$, with T_min denoting the minimum two-way propagation delay which is considered to remove the contribution of the direct coupling between the transmitting and receiving antennas of the radar. Clearly, by converting propagation

delays into distances between the radar and the reflecting objects, the generic element $|h_{n,m}|$ corresponds to a range $d_m = d_{\min} + (m-1)\,d$ in the angular direction ϕ_n, where $d_{\min} = c\,T_{\min}/2$ is the minimum detection distance, $d = c\,T_{\mathrm{s}}/2$, and c is the speed of light. Ideally, an antenna oriented in a given direction should only receive signals coming from the same direction, i.e., reflected from objects intercepted by the antenna axis. This property is a peculiar feature of laser-based radars (Lidars) because of the extremely narrow laser beam. Unfortunately, even though very narrow beams can be realized at THz frequencies, unwanted sidelobes of the antenna's radiation pattern might catch also echoes coming from other directions, then making R-SLAM much more challenging than classical Lidar-based SLAM. In fact, the radar might erroneously infer the presence of an object in the direction where the main beam of the antenna is oriented due to echoes coming from other directions, thus showing ghost artifacts [164]. As shown in Fig. 4.39, to mitigate this phenomenon a ghost-effect mitigation (GEM) procedure is performed, which operates on each column $\mathbf{h}_m$ of $\mathbf{H}$, with $m = 1, 2, \ldots, M$. In particular, for each column vector

$$\mathbf{h}_m = [|h_{1,m}|, |h_{2,m}|, \ldots, |h_{n,m}|, \ldots |h_{N,m}|]^T \tag{4.106}$$

of $\mathbf{H}$ (that is, for each distance from the radar), the maximum value is determined as

$$\hat{h}_m = \max(\mathbf{h}_m) \tag{4.107}$$

where $\hat{h}_m$ corresponds to the strongest echo detected at the considered distance. Then, a threshold is defined as

$$\xi_m^{(\mathsf{GEM})} = \eta_{\mathrm{CL}} \cdot \hat{h}_m, \quad 0 < \eta_{\mathrm{CL}} \leqslant 1 \tag{4.108}$$

such that, for each column vector $\mathbf{h}_m$, it has been operate as follows

$$|h_{n,m}| = \begin{cases} |h_{n,m}| & \text{if} \quad |h_{n,m}| \geqslant \xi_m^{(\mathsf{GEM})} \\ 0 & \text{if} \quad |h_{n,m}| < \xi_m^{(\mathsf{GEM})} \end{cases}. \tag{4.109}$$

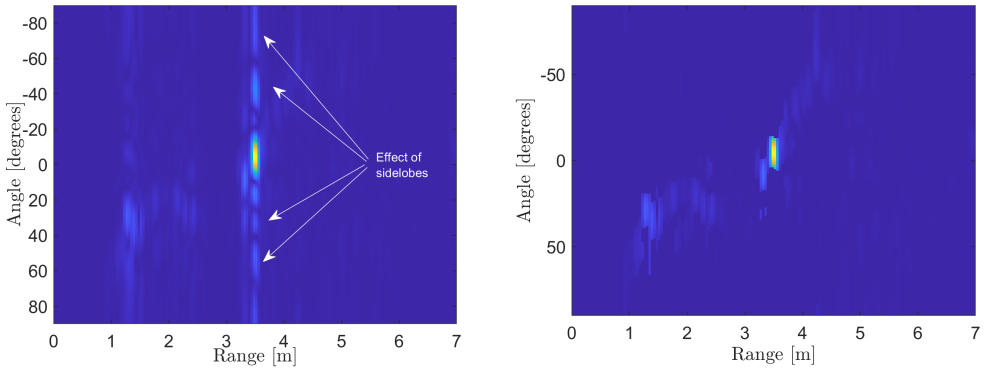

(a) **H** matrix before the GEM procedure. (b) **H** matrix after the GEM procedure.

Figure 4.40: Impact of the GEM procedure. Single obstacle located at three meters in front of the radar working at 77 GHz with $\eta_{\mathrm{CL}} = 0.4$.

In other words, by properly defining the parameter η_{CL}, which depends on the sidelobes level, and hence, on the antenna radiation pattern, it is possible to mitigate the presence of artifacts. The rationale behind the GEM method proposed is that it is unlikely that multiple obstacles are present exactly at the same distance from the radar, whereas echoes captured by sidelobes appear exactly at the same distance. Fig. 4.40 shows an example of the beneficial impact of the GEM algorithm on a matrix **H** obtained from measurements taken in the 77 GHz band. Although in this work the measurements are taken in the $[235 - 320]$ GHz band, it has been purposely switched to the 77 GHz band for the purpose of generating Fig. 4.40 to better highlight the ghost artifact phenomenon, which is visually more evident in the millimeter-wave band because of the lower resolution of the radar.

Another important impairment affecting the accuracy of measurements is the background noise, either received by the antenna or generated by the radar circuitry itself. Radars usually mitigate its impact by running a NM algorithm that eliminates all the signal components that fall below a certain masking threshold. In our case, the NM algorithm operates as follows. First, it detects the peak of the matrix **H**, that is,

$$h_{\max} = \max(\mathbf{H})\,. \tag{4.110}$$

Then, similarly to the GEM algorithm, it requires to define the threshold

$$\xi^{(\mathsf{NM})} = \eta_{\mathrm{CF}} \cdot h_{\max}, \quad 0 < \eta_{\mathrm{CF}} \leqslant 1 \tag{4.111}$$

where η_{CF} is a properly chosen parameter that depends on the background noise and it can be based, for instance, on the constant false alarm rate (CFAR) strategy [163]. Given this threshold, the matrix $\mathbf{H}$ is cleaned of the unwanted noise contribution as follows

$$|h_{n,m}| = \begin{cases} |h_{n,m}| & \text{if} \quad |h_{n,m}| \geqslant \xi^{(\mathsf{NM})} \\ 0 & \text{if} \quad |h_{n,m}| < \xi^{(\mathsf{NM})} \end{cases}. \tag{4.112}$$

As shown in Fig. 4.39, after undergoing the GEM and NM processings, the response to matrix $\mathbf{H}$ is denoted as $\mathbf{F}_k$ and is referred to as *frame*. The subscript k has been introduced to emphasize that a new frame is generated each time the radar performs a complete scan of the environment, which occurs at time instants $k\,T_{\mathrm{F}}$. As evident in Fig. 4.39, as soon as a new frame $\mathbf{F}_k$ is generated, it is passed to the subsequent stage, which is in charge of updating the estimates of the mobile user's trajectory and of the environment map. As shown in Fig. 4.39, the estimation of the user's trajectory is performed by means of a Kalman filter on the basis of the pose estimates $\hat{\mathbf{p}}_k$ obtained by comparing the current frame $\mathbf{F}_k$ with that of the previous time instant, $\mathbf{F}_{k-1}$. In this regard, it is worth emphasizing that $\mathbf{F}_k$ and $\mathbf{F}_{k-1}$ are two-dimensional representations of the scanned area (in polar coordinates), hence they can be meant as "radar images" of the sensed environment in successive instants. This suggested to derive the pose estimates by means of algorithms that were initially conceived for image processing.

The specific pose estimation algorithms considered in this manuscript, which represent one of the major contributions of this work, deserve detailed descriptions. In any case, whatever pose estimation algorithm is adopted, $\hat{\mathbf{p}}_k$ is derived starting from the estimated relative pose vector

$$\tilde{\mathbf{z}}_k = [\tilde{dx}, \tilde{dy}, \tilde{d\theta}]^T \tag{4.113}$$

whose elements are the estimated horizontal shift, vertical shift, and rotation

of the current pose with respect to the previous one, all referenced to the radar-based coordinate system, as well as a quality indicator $q \in [0,1]$ of the estimates. It should be emphasized that $\tilde{\mathbf{z}}_k$ refers to the local coordinate system of the mobile user, i.e., the radar point of view, therefore it has to be transformed into the absolute coordinate system by considering the latest available estimate of the mobile user's rotation $\hat{\theta}_{k-1}$, that is,

$$\mathbf{z}_k = \mathbf{U}(\hat{\theta}_{k-1})\,\tilde{\mathbf{z}}_k \tag{4.114}$$

where

$$\mathbf{U}(\theta) = \begin{bmatrix} \cos\theta & \sin\theta & 0 \\ -\sin\theta & \cos\theta & 0 \\ 0 & 0 & 1 \end{bmatrix} \tag{4.115}$$

denotes the rotation matrix of angle θ. Given $\mathbf{z}_k$, and the previous absolute pose estimate, denoted by $\hat{\mathbf{p}}_{k-1} = [\hat{x}_{k-1}, \hat{y}_{k-1}, \hat{\theta}_{k-1}]^T$, the current raw absolute pose estimate is

$$\hat{\mathbf{p}}_k = \hat{\mathbf{p}}_{k-1} + \mathbf{z}_k\,. \tag{4.116}$$

The processing steps outlined in (4.114), (4.115), and (4.116) are represented in Fig. 4.39 by the block labelled Ψ, which receiving as input $\tilde{\mathbf{z}}_k$ generates as output $\hat{\mathbf{p}}_k$. The latter is then passed to the Kalman filter, which is in charge of the trajectory estimation accounting for the user's mobility model and the quality of the relative pose estimates. In this regard, when it comes to tracking algorithms, it is customary to consider a Markovian state-space model to describe the evolution of the state, which is based on the following second-order kinematic linear model [165, 166]

$$\mathbf{x}_{k+1} = \mathbf{A}\,\mathbf{x}_k + \mathbf{w}_k \tag{4.117}$$

where

$$\mathbf{A} = \begin{bmatrix} \mathbf{I}_2 & T_{\mathrm{F}}\,\mathbf{I}_2 & \mathbf{0}_2 \\ \mathbf{0}_2 & \mathbf{I}_2 & \mathbf{0}_2 \\ \mathbf{0}_2 & \mathbf{0}_2 & \tilde{\mathbf{A}} \end{bmatrix} \tag{4.118}$$

is the transition matrix and $\mathbf{w}_k \sim \mathcal{N}(\mathbf{0}_{1\times 6}; \mathbf{Q})$ is the process noise whose

covariance matrix $\mathbf{Q}$ is [166]

$$\mathbf{Q} = \begin{bmatrix} w_0 \frac{T_\mathrm{F}^3}{3} \mathbf{I}_2 & w_0 \frac{T_\mathrm{F}^2}{2} \mathbf{I}_2 & \mathbf{0}_2 \\ w_0 \frac{T_\mathrm{F}^2}{2} \mathbf{I}_2 & w_0 T_\mathrm{F} \mathbf{I}_2 & \mathbf{0}_2 \\ \mathbf{0}_2 & \mathbf{0}_2 & \tilde{\mathbf{Q}} \end{bmatrix} \tag{4.119}$$

with $\mathbf{I}_N$ and $\mathbf{0}_N$ being respectively $N \times N$ identity and zero matrices, w_0 being the power spectral density of the linear acceleration noise, and with

$$\tilde{\mathbf{A}} = \begin{bmatrix} 1 & T_\mathrm{F} \\ 0 & 1 \end{bmatrix}, \qquad \tilde{\mathbf{Q}} = \begin{bmatrix} \omega_\theta \frac{T_\mathrm{F}^3}{3} & \omega_\theta \frac{T_\mathrm{F}^2}{2} \\ \omega_\theta \frac{T_\mathrm{F}^2}{2} & \omega_\theta T_\mathrm{F} \end{bmatrix} \tag{4.120}$$

where w_θ is the power spectral density of the angular acceleration noise (process noise), which depends on the expected mobility of the user [166]. The evolution of the absolute state $\mathbf{x}_k$ can be tracked by means of a Kalman filter, fed step-by-step with the current raw absolute pose estimate, $\hat{\mathbf{p}}_k$, using the following observation model

$$\hat{\mathbf{p}}_k = \mathbf{B}\,\mathbf{x}_k + \boldsymbol{\nu}_k \tag{4.121}$$

where

$$\mathbf{B} = \begin{bmatrix} 1 & 0 & 0 & 0 & 0 & 0 \\ 0 & 1 & 0 & 0 & 0 & 0 \\ 0 & 0 & 0 & 0 & 1 & 0 \end{bmatrix} \tag{4.122}$$

and $\boldsymbol{\nu}_k \sim \mathcal{N}(\mathbf{0}_3; \mathbf{R})$ is the estimation noise modeled as Gaussian random vector with covariance matrix [166]

$$\mathbf{R} = \mathrm{diag}\left(\sigma_x^2/q^2, \sigma_y^2/q^2, \sigma_\theta^2/q^2\right) \tag{4.123}$$

that accounts for the reliability q of the current relative pose estimate, being $\sigma_x^2 = \sigma_y^2$, and σ_θ^2 the estimation noise power expected by the specific relative pose estimator. At each time instant k, the Kalman filter provides an estimate $\hat{\mathbf{x}}_k$ of the state $\mathbf{x}_k$ as well as its covariance matrix. Concerning the mapping task, in this work an *occupancy grid* approach to represent the indoor environment [167] is employed. This approach involves dividing the

scenario into a fine grid of cells and solving the problem of determining the occupancy probability of each cell by utilizing measurements and estimated trajectories. In particular, for each cell, the likelihood of its occupancy must be calculated on the basis of the collected observations.

According to [24], the actual map at time instant k can be represented as a vector of cells as[12]

$$\mathbf{m}_k \triangleq \left[m_{1,k},\, \ldots, m_{i,k},\, \ldots,\, m_{N_{\mathsf{cell}},k}\right]^{\mathsf{T}} \in \mathbb{B}^{N_{\mathsf{cell}}} \tag{4.124}$$

where $m_{i,k} \in \mathbb{B}$ represents the true occupancy of the i-th cell ($m_{i,k} = 0$ denotes an empty cell, whereas $m_{i,k} = 1$ denotes an occupied cell), $\mathbb{B}$ is the Boolean domain, and N_{cell} is the total number of considered cells. In the sequel, it is considered a stationary map, that is $\mathbf{m}_k = \mathbf{m}$, $\forall k$.

The goal of the mapping algorithm is to infer (4.124) by computing the maximum of the *a-posteriori* probability mass function (*belief*) given the history of frame observations and the estimated trajectories (see Fig. 4.39). Denoting with $b_k(m_i)$ the belief of occupancy of the i-th cell at time instant k, the following steps are performed:

- *Initialization:* If no prior map information is available, a possible initialization is $b_0(m_i) = 0.5$, corresponding to a complete uncertainty, $\forall i = 1, 2, \ldots, N_{\mathsf{cell}}$.

- *Scan vector generation:* The cleaned Angle-Range matrix $\mathbf{F}_k$, which is obtained as the output of the GEM and NM processing at the time instant k, is passed to the mapping algorithm (the Mapping block in Fig. 4.39), whose first task is to generate a 1-by-N vector of ranges $\mathbf{v}_k$ similar to the one provided by a Lidar scan. Specifically, $\mathbf{v}_k$ contains only one range value of the current *frame* $\mathbf{F}_k$ for each considered steering angle, i.e., $\mathbf{v}_k = \left[v_1^{(k)}, v_2^{(k)}, \ldots, v_N^{(k)}\right]$, with $v_n^{(k)}$ being the range of the object (if any) seen at the angle ϕ_n by the radar. This result is achieved by comparing each row of the current frame, i.e., $\mathbf{f}_n = [|h_{n,1}|, |h_{n,2}|, \cdots |h_{n,M}|]$ of $\mathbf{F}_k$, with a suitable threshold $0 < \eta_{\mathrm{SV}} \leqslant 1$. The distance corresponding to the first element which

[12]The map might be time-varying due to moving obstacles, such humans or mobile furniture (e.g., chairs).

exceeds $\eta_{\mathrm{SV}} \cdot f_{\max}$, with $f_{\max}$ being the maximum value in $\mathbf{f}_n$, is saved in $\mathbf{v}_k$.

Similarly, the angles ϕ_n are collected into the angle vector $\boldsymbol{\phi} = [\phi_1, \phi_2, \ldots, \phi_N]$. The final scan vector at time instant k is given by $\mathbf{s}_k = \left[\mathbf{v}_k^T, \boldsymbol{\phi}^T\right]$.

- *Log-Odd Update:* Starting from $\mathbf{s}_k$, the beliefs are updated following a classic occupancy grid algorithm [167]. To avoid numerical instability during calculations, a practical solution is to map the belief into the log-odd quantity

$$\ell_k\left(m_i\right) \triangleq \log\left(\frac{b_k(m_i)}{1-b_k(m_i)}\right). \forall\, i = 1, 2, \ldots, N_{\mathsf{cell}} \tag{4.125}$$

Since the belief can be expressed as in [166, Eq. 12], and by embedding all the prior information into the term $\ell_{k-1}\left(m_i\right)$, (4.125) becomes:

$$\begin{aligned}\ell_k\left(m_i\right) =& \log\left(\frac{p\left(\mathbf{s}_k|m_i=1\right)}{p\left(\mathbf{s}_k|m_i=0\right)}\right) + \ell_{k-1}\left(m_i\right) \\ & \forall\, i = 1, \ldots, N_{\mathsf{cell}}\end{aligned} \tag{4.126}$$

where $p\left(\mathbf{s}_k|m_i=1\right)$ ($p\left(\mathbf{s}_k|m_i=0\right)$) is the likelihood function considering the current scan $\mathbf{s}_k$ given the presence of an occupied (empty) cell in m_i. In our case, $p\left(\mathbf{s}_k|m_i=1\right)$ can take two values, that is 0.9 when the polar coordinates of the ith cell are present inside the scan vector $\mathbf{s}_k$, and 0.1 otherwise. Finally, the likelihood of having an empty cell is simply given by

$$p\left(\mathbf{s}_k|m_i=0\right) = 1 - p\left(\mathbf{s}_k|m_i=1\right)\,. \tag{4.127}$$

In (4.126) it has been assumed that each cell is independent of all the others (including adjacent cells) as for laser observations. Nevertheless, inter-cell correlations can be considered in the observation model to further refine the mapping process [168].

As a concluding statement regarding the above-described algorithm, it can be underlined that the resulting map is obtained by considering the

complete history of measurements collected from distinct radar positions. By capitalizing on the spatial diversity inherent in measurements obtained from various locations, this approach effectively mitigates potential issues stemming from signal blockage, suboptimal antenna radiation patterns, and low reflective characteristics of objects.

In the following, the details of the algorithms considered for estimating the relative pose are presented, specifically referring to the Pose Estimation block in Fig. 4.39. Firstly, the *Laser Scan Matching* algorithm [169] is introduced, commonly adopted in Lidar-based systems, which is considered here as a benchmark. Then, inspired by the possibility of employing algorithms typically used for image processing, a modified version of the *Fourier-Mellin* algorithm is proposed, specifically adapted to operate with signals provided by a THz radar. Finally, a simplified version of the *Fourier-Mellin*-based algorithm that, having lower computational complexity, is better suited for use in portable devices implementing R-SLAM is reported.

Laser Scan Matching Algorithm This methodology was conceived for Lidar-based systems and it is here considered as a benchmark [169]. When fed with laser scans, it has been proved to achieve real-time loop closure and 5 cm resolution [169].

According to this algorithm, the user's relative pose in the current instant k, given by (4.113), is derived starting from the current and the previous scan vectors $\mathbf{s}_k$ and $\mathbf{s}_{k-1}$, which are compared to estimate the corresponding translation increments $(\tilde{dx}, \tilde{dy})$ and rotation increment $\tilde{d\theta}$ using a grid-based search.[13] Specifically, the *Laser Scan Matching* algorithm converts $\mathbf{v}_k$, $\mathbf{v}_{k-1}$ and $\boldsymbol{\phi}$ into probabilistic grids and finds the pose between the two scans by correlating their grids [169]. The interested reader is referred to [170] for additional details on the strategy adopted by the algorithm to speed up the computation.

Fourier-Mellin-based Algorithm With the goal of achieving improved performance compared to the *Laser Scan Matching* algorithm, in this work

[13]The scan vectors $\mathbf{s}_k$ and $\mathbf{s}_{k-1}$ on which the *Laser Scan Matching* algorithm operates are derived.

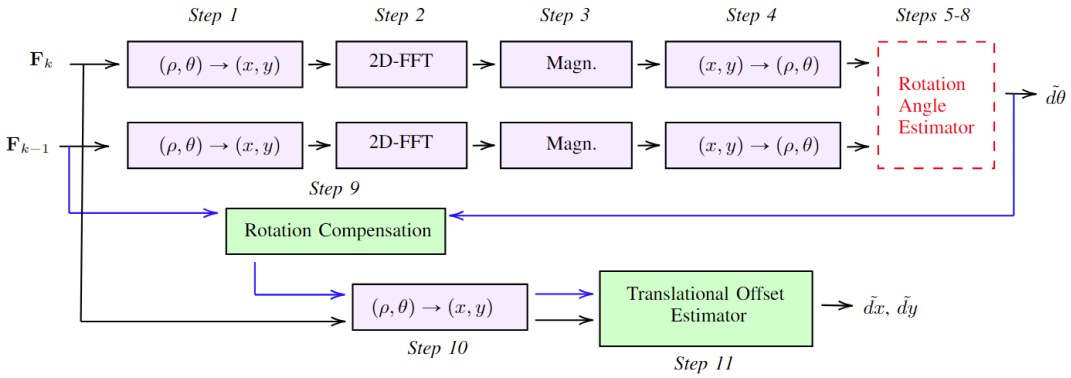

Figure 4.41: Relative pose estimation implemented using the Fourier-Mellin-based algorithm. The output is the relative pose $\tilde{\mathbf{z}}_k = [d\tilde{x}, d\tilde{y}, d\tilde{\theta}]^T$. The details of the "Rotation Angle Estimator" are depicted in Fig. 4.42.

is proposed to estimate the relative pose between two consecutive frames $\mathbf{F}_k$ and $\mathbf{F}_{k-1}$ by means of the Fourier-Mellin algorithm [171, 172], which is an FFT-based method used to register[14] two different images searching for the optimal match in the frequency domain. In particular, the objective of the algorithm is to decouple the translation and rotation effects in order to facilitate their estimation.

This algorithm, which was designed to operate on Cartesian images, is here applied to consecutive *frames* in polar coordinates, which in fact can be interpreted as "radio images" of the environment. For the sake of clarity, in the following, it will be highlighted the dependence of the elements of $\mathbf{F}_k$ on the distance ρ and the angle θ by treating the frame as a two-dimensional function $\mathbf{F}_k(\theta, \rho)$. It is worth pointing out, in this regard, that ρ and θ are here meant as continuous variables, in contrast with the corresponding discrete variables d_m and ϕ_n introduced before. This choice is aimed at simplifying the notation in the following analysis, the discrete version of which was implemented in the test bed.

The algorithm proposed consists of the main steps shown in Figs. 4.41-4.42, which are described hereafter.

- *Step 1.* The current and previous frames $\mathbf{F}_k(\theta, \rho)$ and $\mathbf{F}_{k-1}(\theta, \rho)$, which

[14] Image registration is an image processing technique used to align multiple scenes into a single integrated image, compensating rotations, translations and different scaling.

clearly refer to a polar coordinate system, are converted into the corresponding images $\mathbf{C}_k(x, y)$ and $\mathbf{C}_{k-1}(x, y)$ in Cartesian coordinates.

- *Step 2.* Given $\mathbf{C}_k(x, y)$ and $\mathbf{C}_{k-1}(x, y)$, the corresponding 2D Fourier transforms $\boldsymbol{\mathcal{F}}_k(\xi, \eta)$ and $\boldsymbol{\mathcal{F}}_{k-1}(\xi, \eta)$ are computed. Assuming that $\mathbf{C}_k(x, y)$ is a perfectly (i.e., not affected by noise and artifacts) rotated and translated replica of $\mathbf{C}_{k-1}(x, y)$, that is

$$\begin{aligned}\mathbf{C}_k(x, y) = \mathbf{C}_{k-1}(&x\cos(d\theta) + y\sin(d\theta) - dx, -x\sin(d\theta) \\ &+ y\cos(d\theta) - dy)\end{aligned} \tag{4.128}$$

where (dx, dy) are the translational offsets and $d\theta$ is the rotation angle from instant $k-1$ to instant k, the relation between the corresponding 2D Fourier transforms is:

$$\begin{aligned}\boldsymbol{\mathcal{F}}_k(\xi, \eta) = e^{-j2\pi(\xi dx + \eta dy)}\boldsymbol{\mathcal{F}}_{k-1}(&\xi\cos(d\theta) + \eta\sin(d\theta), \\ &- \xi\sin(d\theta) + \eta\cos(d\theta)).\end{aligned} \tag{4.129}$$

- *Step 3.* Given (4.129), the relation between the magnitudes of $\boldsymbol{\mathcal{F}}_k(\xi, \eta)$ and $\boldsymbol{\mathcal{F}}_{k-1}(\xi, \eta)$ is

$$\begin{aligned}\mathbf{M}_k(\xi, \eta) = \mathbf{M}_{k-1}(&\xi\cos(d\theta) + \eta\sin(d\theta), \\ &- \xi\sin(d\theta) + \eta\cos(d\theta)).\end{aligned} \tag{4.130}$$

From (4.130) one can argue that the magnitude is translation invariant, as it does not depend on (dx, dy). It turns out, therefore, that possible differences between $\mathbf{M}_k(\xi, \eta)$ and $\mathbf{M}_{k-1}(\xi, \eta)$ are found to be solely dependent on the rotation $d\theta$.

- *Step 4.* By expressing (4.130) in polar coordinates, it immediately results

$$\mathbf{M}_k(\theta, \rho) = \mathbf{M}_{k-1}(\theta - d\theta, \rho) \tag{4.131}$$

that represents a convenient formulation for the derivation of the rotation angle $d\theta$. Actually, converting the magnitudes from Cartesian

to polar coordinates makes it possible to represent rotations as translations in the angular domain, as evident in (4.131), thus allowing to exploit the translation property of the Fourier transform, as explained in Step 5.

- *Step 5.* By denoting $\boldsymbol{\mathcal{M}}_k(\mu,\nu)$ and $\boldsymbol{\mathcal{M}}_{k-1}(\mu,\nu)$ the 2D Fourier transforms of $\mathbf{M}_k(\theta,\rho)$ and $\mathbf{M}_{k-1}(\theta,\rho)$, respectively, it results

$$\boldsymbol{\mathcal{M}}_k(\mu,\nu) = \boldsymbol{\mathcal{M}}_{k-1}(\mu,\nu)\, e^{-j2\pi\nu d\theta} \tag{4.132}$$

that features the nice property of having the rotation angle $d\theta$ included only in the exponential function, which can be easily isolated, as shown in Step 6.

- *Step 6.* By defining the cross-power spectrum $\mathsf{CPS}_k(\mu,\nu)$ of $\mathbf{M}_k(\theta,\rho)$ and $\mathbf{M}_{k-1}(\theta,\rho)$ as

$$\mathsf{CPS}_k(\mu,\nu) = \frac{\boldsymbol{\mathcal{M}}_k(\mu,\nu)\,\boldsymbol{\mathcal{M}}^*_{k-1}(\mu,\nu)}{|\boldsymbol{\mathcal{M}}_k(\mu,\nu)\,\boldsymbol{\mathcal{M}}^*_{k-1}(\mu,\nu)|} \tag{4.133}$$

it immediately follows

$$\mathsf{CPS}_k(\mu,\nu) = e^{-j2\pi\nu d\theta}. \tag{4.134}$$

- *Step 7.* Taking the inverse Fourier transform of (4.134) yields a Dirac δ-function centered at $d\theta$.

- *Step 8.* Finding the location where the maximum of the inverse Fourier transform occurs, allows to derive an estimation $\tilde{d\theta}$ of the rotation angle $d\theta$. When dealing with less-than-perfect images, the peak amplitude can serve as a quality indicator q for assessing the accuracy of the relative pose estimation to be used in (4.123).

- *Step 9.* Given $\tilde{d\theta}$, it is now possible to apply such rotation to $\mathbf{F}_{k-1}(\theta,\rho)$, thus obtaining $\widetilde{\mathbf{F}}_{k-1}(\theta,\rho)$, which (ideally) is aligned in the angle domain with $\mathbf{F}_k(\theta,\rho)$.

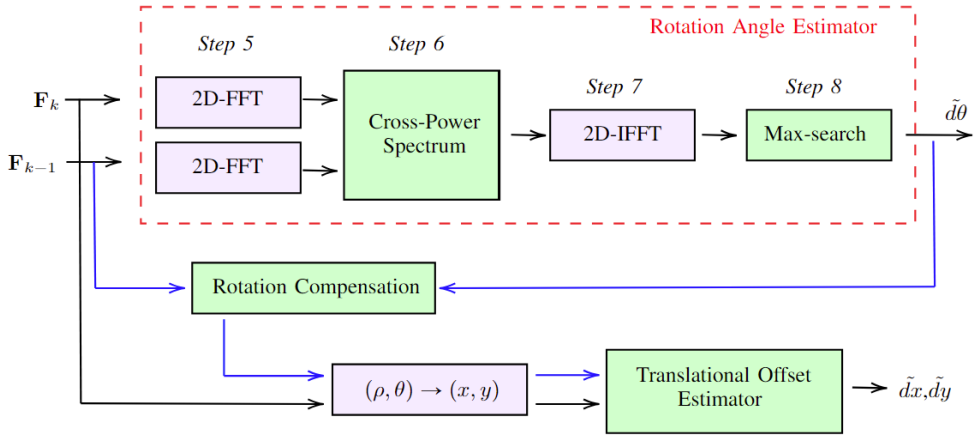

Figure 4.42: Relative pose estimation implemented using the simplified Fourier-Mellin algorithm. The output is the relative pose $\tilde{\mathbf{z}}_k = [\tilde{dx}, \tilde{dy}, \tilde{d\theta}]^T$.

- *Step 10.* The angle-compensated $\widetilde{\mathbf{F}}_{k-1}(\theta, \rho)$ is then converted from polar to Cartesian coordinates, thus becoming $\widetilde{\mathbf{F}}_{k-1}(x, y)$, in preparation for the comparison with $\mathbf{F}_k(x, y)$.

- *Step 11.* After Steps 9 and 10, $\mathbf{F}_k(x, y)$ is (ideally) a translated replica of $\widetilde{\mathbf{F}}_{k-1}(x, y)$. The estimation $(\tilde{dx}, \tilde{dy})$ of the translation offset (dx, dy) can now be derived following the same procedure adopted to estimate the rotation angle $d\theta$, starting from Step 5 to Step 8. To avoid confusing the reader with an overly complicated diagram, these steps have been incorporated into the *Translational Offset Estimator* block of Fig. 4.41, whose inputs, however, are $\mathbf{F}_k(x, y)$ and $\widetilde{\mathbf{F}}_{k-1}(x, y)$.

Simplified Fourier-Mellin Algorithm Considering that THz R-SLAM is intended as an additional feature for future portable devices, the objective of minimizing computational effort and, subsequently, energy consumption led us to develop a simpler, in principle less accurate, version of the above described Fourier-Mellin-based algorithm. The basic idea of this new version is to make the rotation-angle estimator (see the dashed red box in Fig. 4.41) work directly on $\mathbf{F}_k(\theta, \rho)$ and $\mathbf{F}_{k-1}(\theta, \rho)$, rather than on the magnitude of their Fourier transforms. This means that the steps from 1 to 4 of the

original algorithm are skipped, thus leading to the much simpler block scheme shown in Fig. 4.42. The assumption that makes the simplified algorithm sufficiently accurate is that, passing from $\mathbf{F}_{k-1}(\theta, \rho)$ to $\mathbf{F}_k(\theta, \rho)$, the impact of translations is much lower than the impact of rotations so that the *Rotation Angle Estimator* is not significantly affected by translations. This requires that a sufficiently small sampling time T_s is chosen.

Regarding the complexity of the Fourier-Mellin and simplified Fourier-Mellin algorithms, it mainly depends on the number of FFTs involved. Given that the complexity of each FFT is $\mathcal{O}(N \log N)$, where N represents the data size, the Fourier-Mellin algorithm requires 5 FFT computations for each pose estimation, while the simplified Fourier-Mellin algorithm requires only 3 FFT computations, resulting in a lower overall complexity for the latter.

Despite its simplicity, the numerical results section 4.3.1 demonstrates that the simplified algorithm exhibits similar, and in some cases better, performance compared to the Fourier-Mellin-based algorithm.

Remark 1: The block diagram shown in Fig. 4.39 includes blocks that are specific to the THz band, as well as others that can also be used in the mmWave range. In particular, the macro-block denoted as *Trajectory and Map Estimation*, which incorporates the Fourier-Mellin algorithm, is specifically designed to leverage the ranging and angular accuracy of THz radars. This is because the Fourier-Mellin algorithm requires a fairly accurate radar image of the environment, which is difficult to obtain with mmWave radars. Contrarily, the blocks labeled as *Ghost Effect Mitigation* and *Noise Masking* could also be used to implement mmWave R-SLAM, provided that their parameters are appropriately adjusted.

Remark 2: It is important to highlight that the entire procedure described above relies on the estimation of the impulse response of the backscatter channel, which ultimately consists of the CSI. As a result, this approach remains applicable regardless of the waveform utilized or the specific methodology employed to derive the CSI estimate. Indeed, the derivation of the CSI is the basis for most of the (de)modulation schemes proposed for ISAC (e.g., for OFDM).

Table 4.6: Trajectory estimation RMSE for different approaches and scenarios.

	Scenario A	Scenario B	Scenario C
FM	5.7 mm	15 cm	24 cm
SFM	5 mm	15 cm	12 cm
LSM	6.5 cm	3.3 cm	74 cm

4.3.1 R-SLAM Experimental Performance

In this section, the performance of the R-SLAM algorithms using the radar measurements described in Sec. 3.2 as input are investigated. Since the state $\mathbf{x}_k$ of the radar at instant k is estimated starting from relative pose estimations, the final estimated trajectory and map will be relative to its initial position. The lower sections of Figs. 4.43, 4.44, and 4.45 show the estimated trajectories derived from measurements taken in the corresponding scenarios depicted in the upper sections of the same figures. These estimated trajectories are then compared to the ground-truth trajectory, represented by the cyan curve. To define the ground-truth trajectory, a reference system was established within the area, with its origin $\mathbf{p}_0 = (x = 0, y = 0)$ aligned with position #1. The actual coordinates of the radar's placement were determined thanks to the positioner and a laser meter, ensuring an accuracy of 1 mm. To aid the reader's comprehension of the measurement environment, let us clarify that the wall with the open door in Fig. 3.27(a) corresponds to the rightmost vertical wall in Figs. 4.43 (top), 4.44 (top) and 4.45 (top), whereas the wall behind the wide desk in Fig. 3.27(b) corresponds to the upper horizontal wall in Figs. 4.43 (top), 4.44 (top) and 4.45 (top).

The radar trajectories have been estimated using the *Fourier-Mellin-based* (FM), *Simplified Fourier-Mellin* (SFM), and the *Laser Scan Matching* (LSM) algorithms for the relative pose estimation. A summary of the trajectory estimation RMSE for different approaches and scenarios are reported in Table 4.6. The RMSE was calculated using the measured coordinates and those estimated by the algorithm as

$$\mathsf{RMSE} = \sqrt{\frac{1}{N}\sum_{i=1}^{N}\|\mathbf{p}_i - \hat{\mathbf{p}}_i\|^2} \tag{4.135}$$

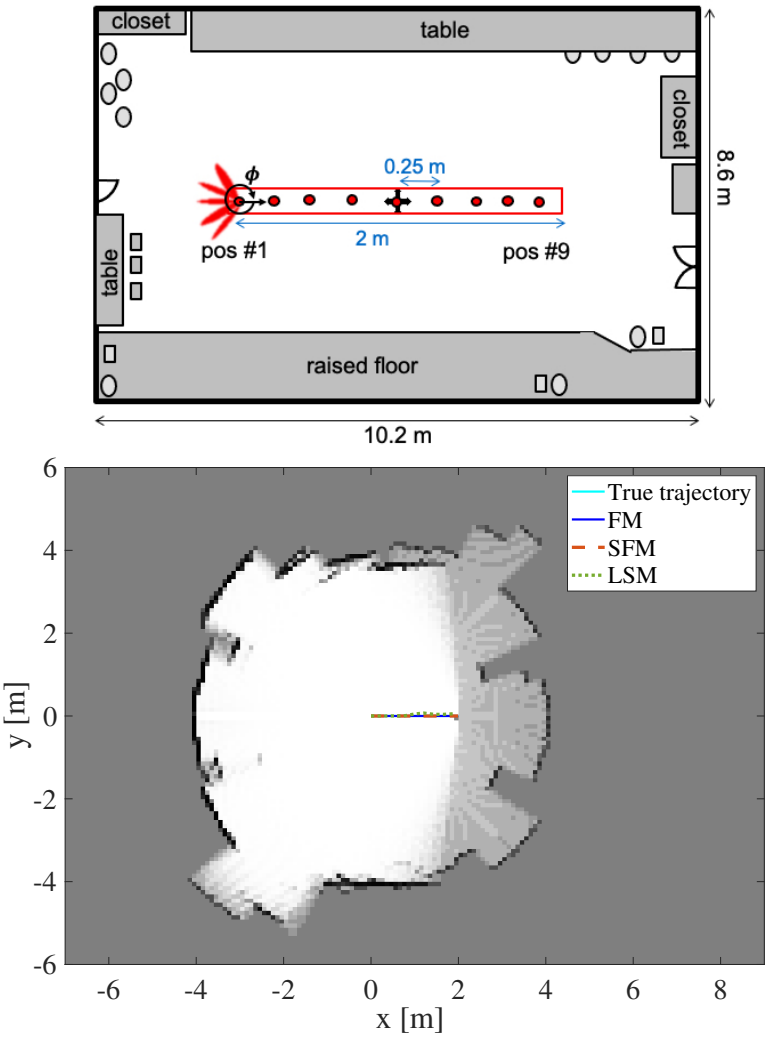

Figure 4.43: Measurement Scenario A (top); Estimated trajectories and map (bottom).

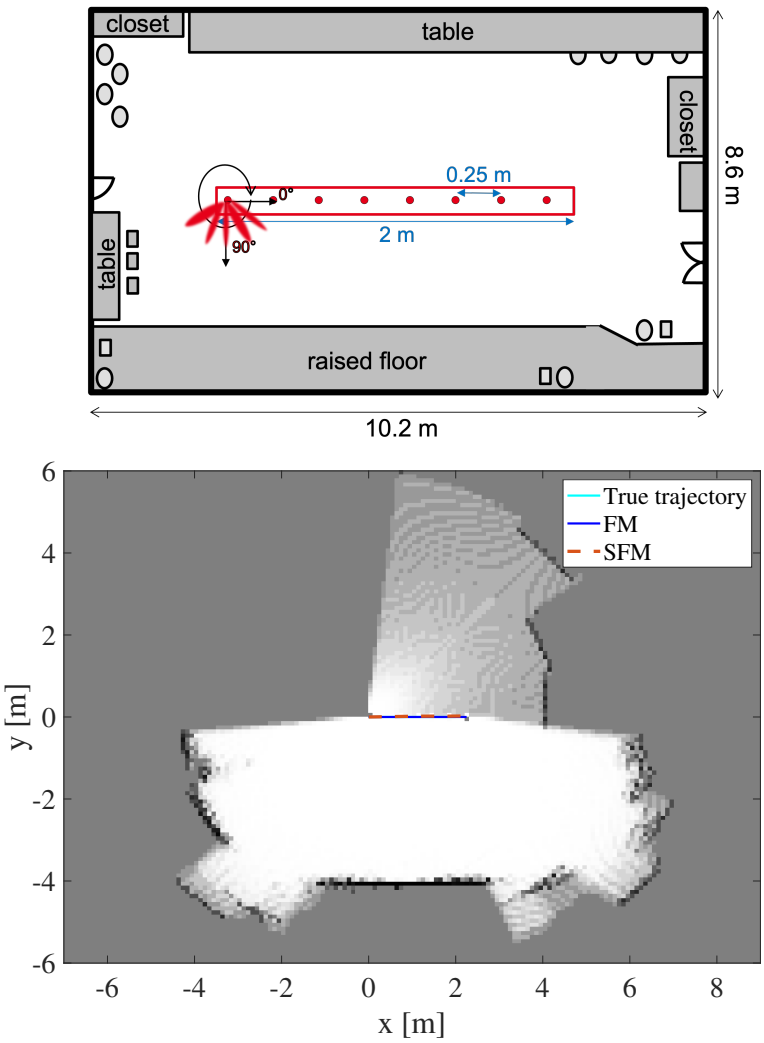

Figure 4.44: Measurement Scenario B (top); Estimated trajectories and map (bottom).

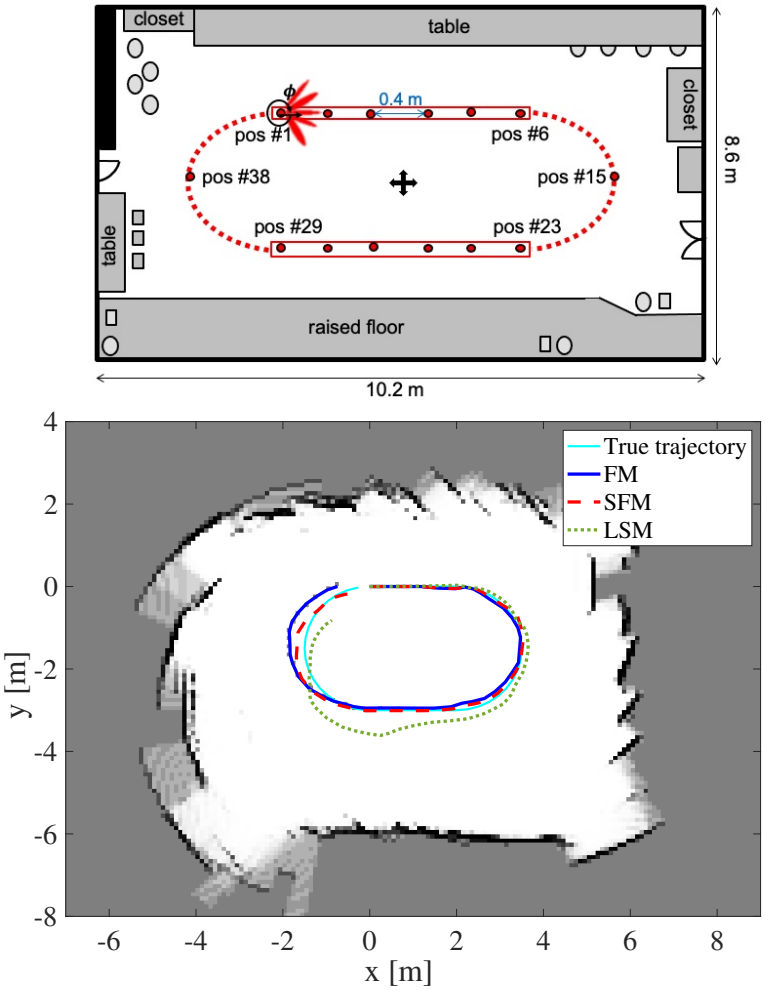

Figure 4.45: Measurement Scenario C (top); Estimated trajectories and map (bottom).

with N being the number of positions considered in each measurement campaign, $\mathbf{p}_i$ and $\hat{\mathbf{p}}_i$ the ith true and estimated positions of the radar, respectively.

All algorithms provide the best trajectory estimation performance in Scenario A depicted in Fig. 4.43 (the three estimated trajectories appear overlaid with the true trajectory), with a RMSE of 5.7 mm (FM), 5 mm (SFM), and 6.5 cm (LSM). According to the achieved results, the millimeter-level accuracy achieved with FM and SFM is of great interest.

Somewhat more challenging is Scenario B in Fig. 4.44, where the same trajectory is followed while keeping the radar pointed perpendicular to the direction of movement. In this case, the relative pose relies mainly on CIR variations in the angular domain that might be difficult to recognize because variations in the incident angle of the electromagnetic waves on walls typically correspond to significant backscatter intensity fluctuations. As a consequence, the RMSEs are higher than those obtained in Scenario A, that is 15 cm (FM), 15 cm (SFM), and 3.3 cm (LSM), denoting a higher sensitivity of FM and SFM algorithms to this effect.

Finally, a more elaborated trajectory following an oval path is considered in Scenario C (Fig. 4.45), where simultaneous translations and rotations are present. The RMSEs of the trajectory estimation for the three algorithms are 24 cm (FM), 12 cm (SFM), and 74 cm (LSM). Surprisingly, the SFM algorithm outperforms the others, while the LSM algorithm exhibits a relatively high estimation error. This result can be attributed to the fact that, although FM should theoretically provide the best estimate of the relative pose, this holds true only in the case of perfect images, that is, those that precisely correspond to rotated and translated versions of each other. Unfortunately, radar images are far to be perfect because of multipath, noise, and the above-mentioned backscatter intensity fluctuations that create several artifacts. Since FM and the LSM algorithms involve many more processing steps than SFM, the latter proves to be more robust to artifacts.

As far as the mapping is regarded, the color of the estimated map in Figs. 4.43 (bottom), 4.44 (bottom) and 4.45 (bottom) represents the occupancy status: black, grey, and white cells indicate the value of the belief at the end of the mapping process, being equal to 1 (occupied), 0.5 (complete

uncertainty), or 0 (empty), respectively. Mapping has been obtained starting from the FM trajectory estimate. In fact, since all algorithms achieved cm-level accuracies, the maps obtained with SFM and LSM show no significant differences visually. As evident, the estimated maps are consistent with the actual shape of the considered scenario.

In conclusion, these experimental results validate the feasibility of R-SLAM using backscattered signals in the THz band collected by a mobile radar. Furthermore, they demonstrate the potential to achieve cm-level localization accuracy without the need for any dedicated infrastructure.

Conclusion

This doctoral thesis is set in a futuristic context where the signal propagation environment is no longer passive and uncontrollable but aims to become a smart, programmable, and active entity. To achieve this Smart Radio Environment (SRE), certain enabling technologies, such as Reconfigurable Intelligent Surface (RIS), are used. RISs are capable of re-radiating the incident signal at an angle different from that predicted by Snell's law, following a generalized form of the reflection angle. This is made possible through the careful design of the intelligent surface, which is discussed in detail in Chapter 2.1 of this thesis.

When the surface is no longer reconfigurable, and thus does not require active components in its design, yet still manages to achieve a reflection angle different from Snell's law, it is referred to as a metasurface. This thesis investigates frequency-selective metasurfaces in Chapter 2.2, where the metasurface responds with a distinct reflection angle depending on the frequency of the incident signal. Furthermore, metasurfaces that exploit the property of retroreflectivity are examined in Chapter 2.3. These surfaces are capable of reflecting the signal back in the same direction as the incident one, without the need for specific active components.

In Chapter 3, the study focuses on how SRE applications can move beyond theoretical and simulation-based approaches to achieve practical, real-world implementation. Specifically, Chapter 3.1 addresses the validation of two RISs from the company NEC, one operating at 5.3 GHz and the other at 3.47 GHz. The measurement campaigns aimed to identify malfunctions in both boards. For the first RIS, variations in the phase profile - also known as the codebook in technical terms - produced changes, though not the expected ones. For the second RIS, however, it appeared to not respond at all

to changes in the phase profile.

For the 5.3 GHz RIS, additional measurements were conducted at the antenna laboratory in Aalborg, one of the most advanced facilities in the world, equipped with some of the largest anechoic chambers. Their daily work involves measuring 3D radiation patterns of RISs. They also confirmed that the RIS did not behave as expected, likely due to structural scattering from the ground plane being overlooked during the design phase, in addition to phase shifters not providing the anticipated angular shift.

Regarding the second RIS at 3.47 GHz, there were communication issues with the company from the start. They were unable to explain why the unit cells were spaced at a distance different from $\lambda/2$, despite their documentation specifying such spacing, or why the cells had a preferred polarization and were not square, unlike the other RIS. The company informed us that they were not directly involved in the antenna design, making technical communication and support difficult from the outset.

Chapter 3.2 then continues with the description of the measurement campaign that provided the first proof-of-concept for the personal radar concept, a milestone technology for indoor radio imaging and infrastructure-less systems at THz frequencies, specifically at 300 GHz. A quasi-monostatic radar setup was used, which collected and measured the channel frequency responses for each measurement by capturing the backscattered signal from the environment.

Finally, a UWB application for localization purposes is presented in Chapter 3.3. The work was conducted with anchors placed at the vertices of a square with sides of 0.5 m, in view of the potential use of the system on a mobile platform. In addition, the system was tested in two challenging environments emulated during measurement campaigns, collecting data in the presence of reflections and water. The goal was to achieve errors smaller than 10 cm near the point of greatest interest, where the target would be engaged while relaxing this constraint during the approach phase. The tests conducted with the Sequitur localization system revealed that calibrating the system at the point of maximum interest allowed the required accuracy to be achieved, though at the cost of sacrificing accuracy during the approach phase, in line with the initial specifications. As expected, a strong impact

on localization performance was observed when metal was present near the anchors, especially when they were not properly oriented. To mitigate these effects, the use of directive antennas designed specifically for the environment and properly oriented can prevent these strong reflection phenomena, thus improving localization accuracy.

Chapter 4 concludes by describing the algorithms developed in this doctoral thesis and presenting the numerical results obtained from simulations for each different application. In particular, Chapter 4.1 focuses on localization algorithms that leverage metaprisms to localize a user in NLOS conditions. The numerical results obtained at millimeter-wave frequencies with an OFDM incident signal demonstrate that the system can achieve an angle estimation error of approximately 2°, and a position estimation error of less than 40 cm in 90% of the cases analyzed.

At 300 GHz, the results indicate an angular error of less than 1° and a position error of 0.25 m in 90% of the 200 Monte Carlo iterations, demonstrating the significant potential of the metaprism to aid the localization process in NLOS scenarios. This is achieved without a substantial increase in complexity compared to deploying additional base stations or utilizing RIS. In the second subchapter 4.1.2 dedicated to metaprisms, an FMCW radar is presented, which leverages a metaprism to enable target localization in NLOS conditions. A modified FMCW receiver structure is proposed, capable of simultaneously estimating both the angle and range of the target using a conventional chirp signal. The results demonstrate that highly accurate angle and range estimates can be achieved once again, without the need for reconfigurable metasurfaces or multiple antennas at the base station.

Subchapter 4.2 discusses the algorithms developed for utilizing SCMs in the context of communication, channel access, and localization, thereby situating this work within various facets of SRE.

In the context of communication, it has been proposed the adoption of modulating SCMs as a means to realize ultra-low complexity uplink MIMO communications based on retrodirective backscattering. Thanks to the iterative algorithms introduced in this work, inspired by Power Methods, the BS is able to derive and track optimal beamforming vectors for the round-trip channel between the BS and UE.

It has been demonstrated that in multi-user MIMO scenarios, UEs can automatically establish parallel communication links with the BS in a blind manner, without the need for ADC chains, explicit channel estimation, or time-consuming beamforming and alignment schemes. An analytical characterization of the SNR evolution during the iterations has been derived, allowing for the identification of the conditions necessary to achieve a robust SNR at convergence, even in the presence of strong static clutter. Numerical results indicate that MIMO communications can be established automatically after just a few iterations, with latency on the order of microseconds, even when utilizing very large antenna arrays. Moreover, the system can effectively track rapid channel variations in realistic dynamic scenarios characterized by multipath propagation.

After, it is presented the adoption of SCMs to achieve low-complexity MIMO GFRA communications by leveraging retro-directive backscattering. The AP can estimate the optimal beamforming vector for the round-trip channel between the AP and the sensor, thereby establishing optimal single-layer MIMO communication. Numerical results demonstrate that MIMO communications can be established after just a few iterations, with setup times on the order of microseconds and no jitter, even when utilizing very large antenna arrays in the presence of realistic multipath channels. Related to this work, the Appendix also includes a comparison of the proposed scheme with existing solutions in the state-of-the-art, with particular emphasis on the performance achieved by our scheme when NOMA algorithms are applied. Finally, there are reported two network architectures aimed at localizing mobile devices by harnessing the presence of SCMs, which can be integrated either within the network infrastructure or directly onboard the mobile devices themselves. The proposed iterative scheme works on top of the two envisioned network architectures, which enables fast beam-forming and AoA estimation, without requiring any channel estimation procedure. Specifically, the full MIMO gain is obtained, thus overcoming the main drawback of backscattering-based solutions caused by the two-way path loss, which can be detrimental when working at mmWave/THz. This results in simple, cost-effective, and energy-efficient devices, as no dedicated signaling or onboard signal processing capability for devices equipped with the SCM is

needed. Additionally, an enhanced version of the proposed scheme capable of tracking the channel in the presence of mobile devices is described. This improvement yields even faster AoA estimation when the mobile speed remains below a certain threshold. Numerical results investigate both the localization accuracy and speed of convergence of the proposed scheme in free space channel conditions as well as when multipath affects the propagation. The results show that the proposed solution manages to keep the localization error at the centimeter level using narrowband signals and only a few anchor nodes while achieving a high localization update rate and very low latency, essential requirements in dynamic vehicular contexts.

Finally, the last part of Chapter 4 is dedicated to R-SLAM algorithms based on Fourier-Mellin transforms, along with a simplified version that can operate with signals generated by a mobile radar. The numerical results demonstrate the feasibility of infrastructure-less localization and mapping using a personal radar, particularly in the context of smart radio environments and 6G systems, where integrated communication, localization, and mapping capabilities will be essential.

Several potential directions for future research emerge from this thesis. One key direction is the implementation of metaprism technology. A major advantage of this technology is that it does not require significant resources or expensive equipment, thereby reducing the economic entry barrier and making it accessible to small and medium-sized enterprises. Furthermore, it can be deployed without signaling overhead or external power supply and operates transparently to the wireless protocol. Now, groups are working on possible implementations of the metaprism with whom we collaborate. Moreover, the equivalent scattering model utilized in this work for the metaprism does not account for two aspects in characterizing the operation of a realistic reflecting metasurface: the specular component associated with the structural scattering of the metaprism and the EM mutual coupling between closely spaced unit cells. These aspects can be further explored later. Similarly, also regarding the work on SCM, the missing part is precisely the realization of such a device and its use in measurement campaigns to validate the developed algorithms.

In fact, conducting experimental tests of the algorithms presented in var-

ious real-world scenarios will be crucial. These experiments will validate the theoretical models and provide insights into practical challenges, such as variability in phase shifts across different cells. Testing under diverse conditions will not only assess the robustness of the proposed solutions but also facilitate iterative improvements based on empirical data.

Appendix

Comparison of the GFRA scheme proposed in Sec. 4.2.2 with Baseline Solutions

The goal is to highlight the differences between the work presented in Sec. 4.2.2 and the existing literature on GFRA and metasurface-based BackCom schemes, while clarifying the strengths and weaknesses of this proposed SCM-based solution. In particular:

- **SCM-based vs Baseline Massive MIMO GFRA**

  Some might argue that a potential drawback of the proposed scheme based on backscatter communication, in comparison to conventional GFRA schemes, is the increased path loss resulting from the two-way channel. This observation might lead to the conclusion that the proposed SCM-based scheme may not be suitable for operation in high-frequency bands, such as mmWaves or even THz. On the contrary, as it will be analyzed in the following, this is a wrong conclusion.

  A typical GFRA scheme employs single antenna sensors with a single RF chain and possibly a multi-antenna AP, i.e., an uplink SIMO configuration, even though it is often referred to as "massive MIMO", as already outlined in the Introduction. In this scenario, each sensor employs a preamble from a limited set of orthogonal sequences for detection and channel estimation purposes at the AP. As a consequence, for a given preamble length, the performance is bounded by the limited number of available preambles [141]. Moreover, in traditional GFRA systems, the benefit of path loss recovery, made possible in principle by the MIMO technology, cannot be practically achieved when dealing with sensing nodes. In fact, a MIMO solution is in general not feasible

for two main reasons: *i)* if sensors are only transmitting, they do not have a chance to perform beamforming because of the lack of CSI; *ii)* even though sensors were equipped also with a receiver, the complexity required for estimating the CSI and performing beamforming, including the need for an antenna array with phase shifters and signaling overhead, might not be affordable, especially at high frequencies. Therefore, in order to perform a fair comparison, it is taken into account a SIMO BGFRA system which is supposed to have a complexity similar to that of the proposed SCM-based scheme. For simplicity, it is considered free space propagation, and compared the SCM-based and BGFRA schemes by fixing the size of the AP antenna array $A_{\mathrm{AP}} \simeq N\lambda^2/4$ and the sensor SCM size $A_{\mathrm{SCM}} \simeq M\lambda^2/4$, assuming antenna elements are spaced apart of $\lambda/2$. Under this condition, from (4.61) the maximum SNR can be expressed as a function of the antenna sizes, yielding

$$\begin{aligned}\mathsf{SNR}^{(\mathrm{SCM})} &= \frac{P_{\mathrm{T}}\, g^2\, N^2\, M^2\, G_{\mathrm{AP}}^2\, G_{\mathrm{SCM}}^2\, \lambda^4}{\sigma^2\ (4\pi d)^4} \\ &= \frac{P_{\mathrm{T}}\, g^2\, 16 A_{\mathrm{AP}}^2 G_{\mathrm{AP}}^2\, 16 A_{\mathrm{SCM}}^2 G_{\mathrm{SCM}}^2}{\lambda^4 \sigma^2\ (4\pi d)^4}\,. \end{aligned} \tag{4.136}$$

The last equation highlights that by maintaining a constant area for the antenna arrays, the SNR increases with the fourth power of the frequency (i.e., the inverse of λ), despite the greater propagation loss associated with higher frequencies. For the BGFRA scheme, the maximum achievable SNR (perfect CSI estimate), assuming the gain of the sensor's transmitting antenna is equal to G_{SCM}, is

$$\mathsf{SNR}^{(\mathrm{BGFRA})} = \frac{P_{\mathrm{T}}\, N\, G_{\mathrm{AP}}\, G_{\mathrm{SCM}}\, \lambda^2}{\sigma^2\ (4\pi d)^2} = \frac{4\, P_{\mathrm{T}}\, A_{\mathrm{AP}}\, G_{\mathrm{AP}}\, G_{\mathrm{SCM}}}{\sigma^2\ (4\pi d)^2} \tag{4.137}$$

which is constant with the frequency. Comparing (4.136) and (4.137), it is $\mathsf{SNR}^{(\mathrm{SCM})} > \mathsf{SNR}^{(\mathrm{BGFRA})}$ when

$$f_{\mathrm{c}} > c\sqrt{4\pi d}\,\alpha^{-\frac{1}{4}} \tag{4.138}$$

where $\alpha = g^2\, 64\, A_{\mathrm{AP}}\, G_{\mathrm{AP}}\, A_{\mathrm{SCM}}^2 G_{\mathrm{SCM}}$ and c is the speed of light. The

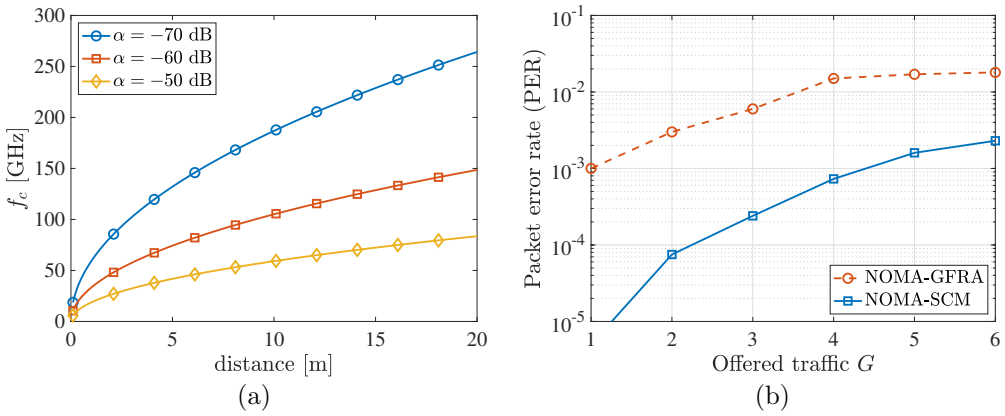

Figure 4.46: (a): Carrier frequency above which our SCM-based scheme provides a more favorable link budget compared to a SIMO BGFRA scheme using the parameters in Table I. Free-space condition. (b): Comparison between NOMA-SCM and NOMA-GFRA. $P_{\mathrm{T}} = -5\,\mathrm{dBm}$. Free-space condition.

previous inequality provides the condition on the carrier frequency under which our backscatter-based SCM scheme leads to a more favorable link budget than that of a BGFRA scheme.

In Fig. 4.46(a), the discriminating carrier frequency given in (4.138) is plotted for $\alpha = -70, -60, -50\,\mathrm{dB}$ corresponding, respectively, to the values in Table I for $g = 0, 10, 20\,\mathrm{dB}$. Obviously, the same values can be obtained through different combinations of the factors determining α such as the antenna size. The area above each curve represents the frequency/distance combinations for which our scheme is more advantageous in terms of link budget. As it can be observed, despite its backscatter nature, the two-way path loss is compensated and overcome by the two-way MIMO antenna gain making our scheme particularly appealing when working at high frequencies and/or small distances. In terms of performance comparison, it is considered as a reference to the analysis carried out in [141] for the BGFRA. Assuming a perfect CSI estimation, a preamble length equal to K_{g} (same overhead as our scheme) chosen randomly among all possible $K_{\mathrm{p}} = 2^{K_{\mathrm{g}}}$ preambles, a binary phase-shift keying (BPSK) uncoded modulation, the packet

error probability (PEP) can be computed as

$$P_e = 1 - P_{\mathrm{nc}}(K_{\mathrm{p}}) \prod_{k=K_{\mathrm{g}}+1}^{K} \left(1 - \frac{1}{2}\mathrm{erfc}\left(\sqrt{\mathrm{SINR}_k}\right)\right) \tag{4.139}$$

where $\mathrm{erfc}(\cdot)$ is the complementary error function, SINR_k is the SINR of the k-th received symbol, and $P_{\mathrm{nc}}(K_{\mathrm{p}})$ represents the probability of no preamble collision given by [141]

$$P_{\mathrm{nc}}(K_{\mathrm{p}}) = \left(1 - \frac{1}{K_{\mathrm{p}}}\right)^{N_{\mathrm{i}}} \tag{4.140}$$

with N_{i} being the number of interfering packets. SINR_k and N_{i} have been obtained under the same simulation scenario whose parameters are listed in Table I. As it can be noticed in (4.139), the packet error probability is affected by both the probability of preamble collision and the probability of correct packet detection.

In Fig. 4.25(b), the PEP of the BGFRA scheme is compared with the PER of the SCM scheme under the same conditions. It can be observed that due to preamble collision and a less favorable link budget, as explained before, the BGFRA scheme provides a worse performance compared to the backscatter SCM-based scheme. Through a more detailed numerical investigation of the components of (4.139), it has been found that the dominant performance degradation factor is given by preamble collisions rather than non-perfect channel orthogonality which is similar for both schemes since they work in the same scenario. Preamble collisions can be reduced by increasing the size of the preamble at the expense of a significant overhead when short packet transmission is considered. While the performance of BGFRA is compromised by pilot collisions, our approach is only limited by non-perfect orthogonality stemming from geometric configuration. In the case of quasi-perfect orthogonality, for instance by going massive with the number of antennas, the performance of our scheme would perform similarly to the single-sensor scenario whereas BGFRA schemes would be still limited by preamble collision.

- **NOMA-based SCM and GFRA**
  As anticipated, the impact of the interference caused by non-perfect channel orthogonality can be mitigated by introducing a NOMA scheme as recently considered in state-of-the-art GFRA algorithms [173]. Specifically, this can be done by applying a SIC algorithm during the Communication Task which is in charge of decoding all the packets that are significantly colliding in the same channel subspace spanned by the precoding vector associated with that Communication Task. To this end, the Communication Task is kept active until the last colliding packet has been solved or the SIC fails. To get an idea on the benefits brought by the inclusion of a NOMA scheme, in Fig. 4.46(b), the PER of a NOMA-powered SCM scheme is reported in comparison with a NOMA-based GFRA. The NOMA scheme considered is power-based in which a packet is considered decoded if the SINR is higher than the threshold $\Gamma = 4\,\text{dB}$ [174]. The system parameters are the same as those in Fig. 4.25b in free-space condition. As expected, NOMA has a similar impact on the performance improvement in both schemes, being the SCM superior thanks to its more favorable link budget at high frequencies.

- **SCM vs BackCom Solutions**

  Metasurface-based BackCom communications have several similarities with our SCM-based scheme, but also profound differences. Both are based on the backscatter modulation of a source RF signal, then they are characterized by the same two-way link budget and, in principle, by similar performance provided that the metasurface in the BackCom system is optimally configured and the AP has obtained a good estimate of the CSI [175]. The main difference relies on the fact that to configure the metasurface, the CSI of the MIMO cascade channel must be estimated, and this typically takes a time proportional to the number of antenna elements [176]. Moreover, according to the estimated CSI, the AP must configure the metasurface in order to realize a suitable beamforming back to the AP which requires a dedicated control channel as well as additional complexity and energy consumption at the

sensor. On the other hand, BackCom allows for multi-layer MIMO in case multiple sensors are co-located in the same metasurface, whereas our scheme realizes a single-layer MIMO (i.e., a single data stream). In summary, current BackCom schemes are not well suited for GFRA using short packets and low-complexity sensors, especially in dynamic scenarios.

- **Complexity and Scalability Considerations**

  From the computational complexity point of view, the Scouting Task is primarily driven by the orthogonalization operation in (4.80), which exhibits a complexity of $\mathcal{O}(NV)$, where N is the number of the AP's antennas and V represents the number of sensors transmitting simultaneously. Conversely, the complexity of the Communication Task is $\mathcal{O}(N)$, involving the computation of the decision variable. With V active Communication Tasks, the overall complexity remains at $\mathcal{O}(NV)$. Both the Scouting and Communication Tasks involve elementary operations whose number is proportional to the number N of antennas at the AP but not to the number of cells M at the SCM. Therefore, M can be considered as a useful degree of freedom that can be exploited to improve the link budget, and hence the $\mathsf{SNR}^{(\mathrm{boot})}$, without any drawback in terms of algorithm's complexity. Obviously, the complexity would significantly increase if a NOMA scheme is employed to improve the performance. Nevertheless, such an increase is the same one would obtain in conventional NOMA-based GFRA solutions. In terms of scalability with the number of sensors, this scheme is not different from conventional multi-user MIMO systems. In particular, scalability can be addressed in two ways. Firstly, by increasing the number of antennas, resulting in narrower beams and more favorable propagation (massive MIMO). This reduces interference issues and allows for targeting a larger number of devices. Secondly, when the number of antennas is fixed, leveraging NOMA techniques to discriminate between users interfering with each other, as discussed before. As already mentioned, the key advantage of our solution compared to conventional multi-user MIMO systems is that the sensor node does not

require any dedicated circuitry (such as RF chains, Digital-to-Analog Converters (DACs), phase shifters, etc.) or signal processing capability (e.g., for CSI estimation) to perform beamforming.

List of Figures

1.1 Radio Environment vs Smart Radio Environement concept. . . 8
1.2 Personal radar concept [26]. 10

2.1 Schematic representations of the desired behavior for the anomalous reflection. 16
2.2 3D geometry explanation of a reconfigurable surface composed of elementary cells. 20
2.3 Overview of the signal's cascade channel from the TX (BS) to the RX (UE). 21
2.4 Schematic drawings of different operations with an RIS. 24
2.5 Equivalent model of the cell. 26
2.6 Schematic representation of a SCM. 29
2.7 Schematic representation and principle of active and passive retrodirective arrays proposed as TX/RX antenna by the UE. 30
2.8 Principle scheme of a modulating self-conjugating metasurface (SCM)-based MIMO communication. 35

3.1 RIS Controller layout 39
3.2 Codebook (Ψ_{nm}) for a FF assumption incident wave (a) and for a NF incident wave (b) with TX and RX placed in the same azimuth plane, the RX is normal to the RIS, while the TX is tilted of 30°. ($\theta_i = 30°, \phi_i = 270°, \theta_r = 0°, \phi_r = 0°$) . . . 40
3.3 Photos of the setup from the first measurement campaign conducted in the corridor of the Cesena campus at the University of Bologna 41
3.4 Schematic of the geometry for the first measurement campaign 41

3.5 Power delay profile first measurement campaign ($\theta_i = 5^\circ, \phi_i = 270^\circ$and $\theta_r = 30^\circ, \phi_i = 180^\circ$) 42
3.6 Experimental setup tested by NEC [98] 43
3.7 Photos of the setup from the second indoor and outdoor measurement campaigns conducted at the Cesena campus of the University of Bologna 43
3.8 Schematic of the geometry for the indoor and outdoor measurement campaigns, resembling the NEC setup 44
3.9 Power delay profile indoor measurement campaign with NEC setup ($\theta_i = 33^\circ, \phi_i = 270^\circ$and $\theta_r = 3^\circ, \phi_i = 90^\circ$) 45
3.10 Power delay profile outdoor measurement campaign with NEC setup ($\theta_i = 33^\circ, \phi_i = 270^\circ$and $\theta_r = 3^\circ, \phi_i = 90^\circ$) 45
3.11 SATIMO testing setup for antenna characterization. 47
3.12 Experimental setup for RIS testing. 48
3.13 RIS reference coordinate system (a) and anechoic chamber reference system (b). 48
3.14 3D radiation pattern of the RIS setup (a) and elevation cut of the radiation pattern at $\phi = 90^\circ$ (b), setting $\theta_r = 0^\circ$, $\phi_r = 110^\circ$, $\theta_i = 14^\circ$, $\phi_i = 270^\circ$. 49
3.15 Setup equal to the one tested by NEC. 49
3.16 Measurements results obtained with codebook provided by NEC, 3D radiation pattern (a) and 2D cut (b). 50
3.17 Measurements results, 3D radiation pattern (a) and 2D cut (b) with $\theta_i = 33^\circ$, $\phi_i = 271^\circ$, $\theta_r = 10^\circ$, $\phi_r = 180^\circ$. 51
3.18 Measurements results obtained with RIS in absorption mode, 3D radiation pattern (a) and 2D cut (b). 51
3.19 RF switch and microstrips and relative length of the associated delay lines, and the resulting phase shifts [98]. 52
3.20 Setup in order to test the phase shifter functionality 53
3.21 Measured phase as a function of the phase configuration applied to all cells 54

3.22 Codebook (Ψ_{nm}) for a FF assumption incident wave (a) and for a NF incident wave (b) with TX and RX placed in the same azimuth plane, the RX is 4 m distant to the RIS, with $\theta_r = 30°$, $\phi_r = 180°$ while the TX is tilted of 3° in the elevation plane. ($\theta_i = 3°, \phi_i = 270°$) 56
3.23 Picture of the setup for the RIS 3.47 GHz test. The TX is positioned at a distance of $d = 3.75$ m, with $\theta_i = 3°$ and $\phi_i = 270°$. The RX is located 4 meters from the RIS, with $\theta_r = 30°$ and $\phi_r = 180°$. 56
3.24 Power delay profile for different codebook assumptions in NF and FF cases and RIS turned off. 57
3.25 Testing each unit cell of the RIS with a voltmeter to ensure that the correct configuration is sent to each cell. 58
3.26 Measurement setup scheme. 60
3.27 Pictures of the environment. 61
3.28 Normalized CIRs for all steering angles at position #15 of Campaign C (a), with delays mapped into distances; polar representation of the normalized PADP at position #15 of Scenario C compared to the actual map of the environment (b). 62
3.29 Empirical CDFs of the delay spread and angular spread for all the positions of Campaign A (top), Campaign B (middle), and Campaign C (bottom). 64
3.30 Angle of Arrival localization principle. 68
3.31 Angle of Arrival localization principle, with RSS, TOA and TWR techniques. 69
3.32 Photo of the positioning of the nodes still in a known position (a), close-up photo of the anchor/tag used(b). 72
3.33 Position measurements, comparison of mobility model 1 (a) and 3 (b), 6000 particles in a volume of 384 m^3. The blue circles represent the locations' real values assumed by the tag, the red asterisks the position of the anchors and the triangle the center of the reference system is yellow. The located points are divided by color in relation to the axis to which they refer. 74

3.34 Detail of the positioning of the anchors (a) and tags (b). Point grid where to position the tag used in the third measurement campaign (c). 76
3.35 Frame positioning for dynamic measurements in the tank. Position outside the tank (a) and position of closest approach to the water (b). Blue circles and squares indicate the anchors and tags respectively, and the blue line indicates the water level. 77
3.36 Vertical RMSE and Horizontal RMSE for Tag 1 (centered axis) and Tag 2 (axis offset by ($\Delta_y = 0.3$)m). Calibration was performed on Tag 1 at a distance of one meter. 77
3.37 Vertical RMSE and Horizontal RMSE for (a) Tag 3 (axis offset by $\Delta y = 0.6$m), (b) Tag 4 (axis offset by $\Delta y = 1$m), (c) and Tag 5 (axis offset by $\Delta y = 1.20$m). Calibration was performed on Tag 1 at a distance of one meter. 78
3.38 Dynamic test in the tank. Red and blue circles indicate the cases at a distance of 1m and 0.7m respectively, green squares indicate the anchors and the black line indicates the axis $(x, y) = (0, 0)$m. Ideally, we should have observed two points at positions $(x, y, z) = (0, 0, 1)$m and $(0, 0, 0.7)$m. 80
3.39 Dynamic test in the tank. Errors on the x, y, and z axes for the cases at 1m (a) and 0.7m (b) over time. 81
3.40 Dynamic test outside the tank on the centered axis, limiting the frame oscillations. Measurement scenario (a) and corresponding errors in x and y (b). 82

4.1 Typical scenario in which the signal transmitted by a user is reflected by the metaprism towards the base station. Each subcarrier component is reflected toward a different angle. . . 85
4.2 Normalized equivalent array factor (AF) for $K = 256$ subcarriers (a) and $K = 3300$ subcarriers (b) 89
4.3 Users positions in scenario A (blue dots) and scenario B (red dots). 91
4.4 Angular ECDF varying the metasurface's size ($N \times M$). BD (beamsteering design); RD (random design). No fading. . . . 92

4.5 Angular ECDF by varying the Rice Factor κ in scenario B. . 93
4.6 Position estimation error ECDF, random design, no fading. . 94
4.7 Simulation scenario of localization at 300 GHz 95
4.8 Angular and position Empirical cumulative distribution (ECDF) 96
4.9 Reference scenario. 97
4.10 Modified FMCW transceiver. 98
4.11 Received signal $y(t)$ (continuous line) and its envelope $z(t)$ (dashed line), with $P_{\mathrm{T}} = 15$ dBm and metaprim's size 20×50 cm^2. 105
4.12 CRLB and RMSE results varying the size of the metaprism (MP) with fixed $P_{\mathrm{T}} = 15\,\mathrm{dBm}$. 106
4.13 CRLB and RMSE results varying P_{T}. Metaprism's size: $20 \times 50\mathrm{cm}^2$. 106
4.14 Single-user system model considering a UE equipped with a planar SCM communicating with a BS equipped with a planar antenna array thanks to retrodirective backscattering. 108
4.15 Evolution of the beam's shape at time $k = 1$ (a), $k = 2$ (b), and $k = 3$ (c). 120
4.16 Free space propagation. (a) Dynamic clutter. Continuous lines $P_{\mathrm{T}} = -30\,\mathrm{dBm}$; dashed lines $P_{\mathrm{T}} = -45\,\mathrm{dBm}$. (b) Effect of static clutter, $P_{\mathrm{T}} = -30\,\mathrm{dBm}$. (c) Effect of channel non-reciprocity, $P_{\mathrm{T}} = -30\,\mathrm{dBm}$. 122
4.17 Transients of the SNR for the single-user scenario. Dynamic clutter. LOS/NLOS 3GPP channel models. Continuous lines refer to simulation results; dashed lines with markers refer to theoretical curves. Transmitted power $P_{\mathrm{T}} = -10$ dBm; curves for CDL-C at 300 km/h with $P_{\mathrm{T}} = -15$ dBm. 124
4.18 Multi-user system model. On the top-left, an example of the block composition in Algorithms (here Communication schemes) 2 and 3. In the former, the estimated eigenvectors are sent in sequence, thus addressing each user sequentially. In the latter, a linear combination of all the estimated eigenvectors is sent, thus addressing all the users simultaneously. . . 126

4.19 Multi-user scenario with the final equivalent array factors in free space. 132
4.20 Multi-user scenario. Transient of the SINR in free space (continuous lines). Comparison with the single-antenna case (dashed lines). $P_{\mathrm{T}} = -30\,\mathrm{dBm}$. 132
4.21 Empirical CDFs of the SINR in multi-user scenario. 135
4.22 Scheme of the proposed grant-free MIMO access, the sensors are equipped with SCMs. 136
4.23 Simulated scenario. 144
4.24 Time evolution of the SNR during the Scouting Task for different bootstrap conditions in the case of rank-1 channel (a) - $\mathsf{SNR}_1[k]$, and rank-3 channel (b) - $\mathsf{SNR}_j[k]$). 145
4.25 (a): Packet error rate as a function of the offered traffic G. Effect of the Scouting Task power boost. $P_{\mathrm{T}} = -5\,\mathrm{dBm}$. Free space condition. (b): Packet error rate as a function of the of the offered traffic G for different transmitted power levels and channel models. Power boost 15 dB. 147
4.26 Localization of SCMs-equipped mobile UEs (yellow circles) by using array-equipped anchors (blue squares). Anchors are also labelled a MIMO transceivers (TRX). 149
4.27 Navigation of array-equipped mobile UEs (blue squares) through the interaction with SCMs (yellow circles) used as anchor nodes. UEs are also labeled MIMO transceivers (TRX). 150
4.28 Geometry of the scenario. MIMO TRX equipped with a N-antennas ULA; SCM composed of M antennas organized as ULA. 153
4.29 Cyclic transmission of the SCM's ID. Time evolution. 159
4.30 Communication and AoA estimation with multiple SCMs sending packets of K bytes cyclically. 160
4.31 Localization of the SCM in a dynamic scenario. 162
4.32 Maximum speed to make the channel tracking effective for improving the convergence speed of the proposed scheme. . . . 166

4.33 Simulated scenario: two users (U1 and U2) moving along the red trajectories, and four anchors. Black circles indicate the locations corresponding to the localization steps given a certain localization update rate $\mathcal{R}$. 167

4.34 ECDF of the absolute localization error for Architecture 1. . . 169

4.35 ECDF of the absolute localization error for U1 (continuous lines) and U2 (dashed lines) in Architecture 1, varying the size $M \times M$ of the SCM. 170

4.36 ECDF of the angle estimation error in Architecture 2 for U1. . 171

4.37 ECDF of the absolute localization in Architecture 2, considering a residual random error with variance σ^2 on the UE orientation. Continuous lines (–) are for $g = 0dB$; dashed lines (- -) are for $g = 10dB$. 172

4.38 Number of iterations required for detection relative to anchor 4, by varying the SCM gain and the use of the previous/random beamforming vector. Dashed lines (- -) are for U2; continuous lines (–) are U1. 173

4.39 R-SLAM: Proposed processing chain. Ψ denotes the operations of (4.114)-(4.116) that transform the relative pose $\tilde{\mathbf{z}}_k = [\tilde{dx}, \tilde{dy}, \tilde{d\theta}]^T$ on the absolute pose $\hat{\mathbf{p}}_k$. Possible implementations of the "Pose Estimation" block are depicted in Figs. 4.41-4.42. 176

4.40 Impact of the GEM procedure. Single obstacle located at three meters in front of the radar working at 77 GHz with $\eta_{\mathrm{CL}} = 0.4$. 178

4.41 Relative pose estimation implemented using the Fourier-Mellin-based algorithm. The output is the relative pose $\tilde{\mathbf{z}}_k = [\tilde{dx}, \tilde{dy}, \tilde{d\theta}]^T$. The details of the "Rotation Angle Estimator" are depicted in Fig. 4.42. 185

4.42 Relative pose estimation implemented using the simplified Fourier-Mellin algorithm. The output is the relative pose $\tilde{\mathbf{z}}_k = [\tilde{dx}, \tilde{dy}, \tilde{d\theta}]^T$.188

4.43 Measurement Scenario A (top); Estimated trajectories and map (bottom). 191

4.44 Measurement Scenario B (top); Estimated trajectories and map (bottom). 192

4.45 Measurement Scenario C (top); Estimated trajectories and map (bottom). 193
4.46 (a): Carrier frequency above which our SCM-based scheme provides a more favorable link budget compared to a SIMO BGFRA scheme using the parameters in Table I. Free-space condition. (b): Comparison between NOMA-SCM and NOMA-GFRA. $P_{\mathrm{T}} = -5\,\mathrm{dBm}$. Free-space condition. 205

Bibliography

[1] R. I. M. 2370-0, "IMT traffic estimates for the years 2020 to 2030," *Radiocommunication Sector of ITU*, Jul. 2015.

[2] K. B. Letaief, W. Chen, Y. Shi, J. Zhang, and Y.-J. A. Zhang, "The roadmap to 6G: AI empowered wireless networks," *IEEE communications magazine*, vol. 57, no. 8, pp. 84–90, 2019.

[3] M. D. Renzo, M. Debbah, D.-T. Phan-Huy, A. Zappone, M.-S. Alouini, C. Yuen, V. Sciancalepore, G. C. Alexandropoulos, J. Hoydis, H. Gacanin, *et al.*, "Smart radio environments empowered by reconfigurable AI meta-surfaces: An idea whose time has come," *EURASIP Journal on Wireless Communications and Networking*, vol. 2019, no. 1, pp. 1–20, 2019.

[4] D. Dardari, "Reconfigurable Electromagnetic Environments: A General Framework," *IEEE Journal on Selected Areas in Communications*, 2024.

[5] H. Zhang, N. Shlezinger, F. Guidi, D. Dardari, and Y. C. Eldar, "6G wireless communications: From far-field beam steering to near-field beam focusing," *IEEE Communications Magazine*, vol. 61, no. 4, pp. 72–77, 2023.

[6] N. González-Prelcic, M. F. Keskin, O. Kaltiokallio, M. Valkama, D. Dardari, X. Shen, Y. Shen, M. Bayraktar, and H. Wymeersch, "The integrated sensing and communication revolution for 6G: Vision, techniques, and applications," *Proceedings of the IEEE*, 2024.

[7] F. Jiang, A. Abrardo, K. Keykhosravi, H. Wymeersch, D. Dardari, and M. Di Renzo, "Two-Timescale Transmission Design and RIS Optimization for Integrated Localization and Communications," *IEEE Transactions on Wireless Communications*, vol. 22, no. 12, pp. 8587–8602, 2023.

[8] A. Guerra, F. Guidi, D. Dardari, and P. M. Djurić, "Near-field tracking with large antenna arrays: Fundamental limits and practical algorithms," *IEEE Transactions on Signal Processing*, vol. 69, pp. 5723–5738, 2021.

[9] A. Elzanaty, A. Guerra, F. Guidi, D. Dardari, and M.-S. Alouini, "Toward 6g holographic localization: Enabling technologies and perspectives," *IEEE internet of things magazine*, vol. 6, no. 3, pp. 138–143, 2023.

[10] S. Palmucci, A. Guerra, A. Abrardo, and D. Dardari, "Two-timescale joint precoding design and RIS optimization for user tracking in near-field MIMO systems," *IEEE Transactions on Signal Processing*, 2023.

[11] D. Dardari, N. Decarli, A. Guerra, and F. Guidi, "LOS/NLOS near-field localization with a large reconfigurable intelligent surface," *IEEE Transactions on Wireless Communications*, vol. 21, pp. 4282–4294, June 2022.

[12] G. Bartoli, A. Abrardo, N. Decarli, D. Dardari, and M. Di Renzo, "Spatial multiplexing in near field MIMO channels with reconfigurable intelligent surfaces," *IET Signal Processing*, vol. 17, no. 3, p. e12195, 2023.

[13] P. Yang, Y. Xiao, M. Xiao, and S. Li, "6G wireless communications: Vision and potential techniques," *IEEE network*, vol. 33, no. 4, pp. 70–75, 2019.

[14] D. Dardari and N. Decarli, "Holographic communication using intelligent surfaces," *IEEE Communications Magazine*, vol. 59, no. 6, pp. 35–41, 2021.

[15] C. Huang, A. Zappone, G. C. Alexandropoulos, M. Debbah, and C. Yuen, "Reconfigurable intelligent surfaces for energy efficiency in wireless communication," *IEEE transactions on wireless communications*, vol. 18, no. 8, pp. 4157–4170, 2019.

[16] Y. Liu, X. Liu, X. Mu, T. Hou, J. Xu, M. Di Renzo, and N. Al-Dhahir, "Reconfigurable intelligent surfaces: Principles and opportunities," *IEEE communications surveys & tutorials*, vol. 23, no. 3, pp. 1546–1577, 2021.

[17] M. Issa and H. Artail, "Using reflective intelligent surfaces for indoor scenarios: Channel modeling and RIS placement," in *2021 17th International Conference on Wireless and Mobile Computing, Networking and Communications (WiMob)*, pp. 277–282, IEEE, 2021.

[18] J. A. Hodge, K. V. Mishra, Q. M. Nguyen, and A. I. Zaghloul, "Generalized polarization-space modulation in reconfigurable intelligent surfaces," in *2020 54th Asilomar Conference on Signals, Systems, and Computers*, pp. 712–717, IEEE, 2020.

[19] S. Lin, B. Zheng, G. C. Alexandropoulos, M. Wen, M. Di Renzo, and F. Chen, "Reconfigurable intelligent surfaces with reflection pattern modulation: Beamforming design and performance analysis," *IEEE transactions on wireless communications*, vol. 20, no. 2, pp. 741–754, 2020.

[20] T. Sharma, A. Chehri, and P. Fortier, "Reconfigurable intelligent surfaces for 5G and beyond wireless communications: A comprehensive survey," *Energies*, vol. 14, no. 24, p. 8219, 2021.

[21] B. Amjad, Q. Z. Ahmed, P. I. Lazaridis, M. Hafeez, F. A. Khan, and Z. D. Zaharis, "Radio SLAM: A review on radio-based simultaneous localization and mapping," *IEEE Access*, vol. 11, pp. 9260–9278, 2023.

[22] W. Morris, I. Dryanovski, J. Xiao, *et al.*, "3D indoor mapping for micro-UAVs using hybrid range finders and multi-volume occupancy grids," in *RSS 2010 workshop on RGB-D: Advanced Reasoning with Depth Cameras, Zaragoza, Spain*, vol. 2, p. 1, 2010.

[23] B. Alsadik and S. Karam, "The simultaneous localization and mapping (SLAM)-An overview," *Journal of Applied Science and Technology Trends*, vol. 2, no. 02, pp. 147–158, 2021.

[24] F. Guidi, A. Guerra, and D. Dardari, "Personal mobile radars with millimeter-wave massive arrays for indoor mapping," *IEEE Trans. Mobile Comput.*, vol. 15, no. 6, pp. 1471–1484, 2015.

[25] A. Guerra, F. Guidi, and D. Dardari, "Millimeter-wave personal radars for 3D environment mapping," in *2014 48th Asilomar Conference on Signals, Systems and Computers*, pp. 701–705, IEEE, 2014.

[26] A. Guerra, "Location and Map Awareness Technologies in Next Wireless Networks," 2016.

[27] K. Rikkinen, P. Kyosti, M. E. Leinonen, M. Berg, and A. Parssinen, "THz radio communication: Link budget analysis toward 6G," *IEEE Communications Magazine*, vol. 58, no. 11, pp. 22–27, 2020.

[28] H. Tataria, M. Shafi, A. F. Molisch, M. Dohler, H. Sjöland, and F. Tufvesson, "6G wireless systems: Vision, requirements, challenges, insights, and opportunities," *Proceedings of the IEEE*, vol. 109, no. 7, pp. 1166–1199, 2021.

[29] D. Dardari, A. Conti, U. Ferner, A. Giorgetti, and M. Z. Win, "Ranging With Ultrawide Bandwidth Signals in Multipath Environments," *Proceedings of the IEEE*, vol. 97, no. 2, pp. 404–426, 2009.

[30] M. Lotti, G. Calesini, and D. Dardari, "NLOS localization exploiting frequency-selective metasurfaces," in *ICC 2024-IEEE International Conference on Communications*, IEEE, 2024.

[31] M. Lotti and D. Dardari, "Metaprism-aided NLOS target localization," in *2023 31st European Signal Processing Conference (EUSIPCO)*, pp. 895–899, IEEE, 2023.

[32] D. Dardari, M. Lotti, N. Decarli, and G. Pasolini, "Establishing MIMO communications automatically using self-conjugating metasur-

faces," in *ICC 2023-IEEE International Conference on Communications*, pp. 1286–1292, IEEE, 2023.

[33] D. Dardari, M. Lotti, N. Decarli, and G. Pasolini, "Establishing multi-user MIMO communications automatically using retrodirective arrays," *IEEE Open Journal of the Communications Society*, 2023.

[34] D. Dardari, M. Lotti, N. Decarli, and G. Pasolini, "Grant-free random access with backscattering self-conjugating metasurfaces," *IEEE Transactions on Cognitive Communications and Networking*, 2024.

[35] M. Lotti, N. Decarli, G. Pasolini, and D. Dardari, "Real-time localization based on mimo backscattering from retro-directive antenna arrays," *IEEE Transactions on Vehicular Technology*, pp. 1–16, 2025.

[36] M. Lotti, G. Pasolini, A. Guerra, F. Guidi, M. Caillet, R. D'Errico, and D. Dardari, "Radio simultaneous localization and mapping in the terahertz band," in *WSA 2021; 25th International ITG Workshop on Smart Antennas*, pp. 1–6, VDE, 2021.

[37] M. Lotti, G. Pasolini, A. Guerra, F. Guidi, R. D'Errico, D. Dardari, *et al.*, "Radio SLAM for 6G systems at THz frequencies: Design and experimental validation," *IEEE journal of selected topics in signal processing*, vol. 17, pp. 834–849, 2023.

[38] G. C. Trichopoulos, P. Theofanopoulos, B. Kashyap, A. Shekhawat, A. Modi, T. Osman, S. Kumar, A. Sengar, A. Chang, and A. Alkhateeb, "Design and evaluation of reconfigurable intelligent surfaces in real-world environment," *IEEE Open Journal of the Communications Society*, vol. 3, pp. 462–474, 2022.

[39] J.-B. Gros, V. Popov, M. A. Odit, V. Lenets, and G. Lerosey, "A reconfigurable intelligent surface at mmwave based on a binary phase tunable metasurface," *IEEE Open Journal of the Communications Society*, vol. 2, pp. 1055–1064, 2021.

[40] V. R. J. Velez, J. P. C. B. B. Pavia, N. M. B. Souto, P. J. A. Sebastião, and A. M. C. Correia, "Performance Assessment of a RIS-Empowered

Post-5G/6G Network Operating at the mmWave/THz Bands," *IEEE Access*, vol. 11, pp. 49625–49638, 2023.

[41] G. C. Alexandropoulos, A. Clemente, S. Matos, R. Husbands, S. Ahearne, Q. Luo, V. Lain-Rubio, T. Kürner, and L. M. Pessoa, "Reconfigurable intelligent surfaces for thz: Hardware design and signal processing challenges," in *2024 18th European Conference on Antennas and Propagation (EuCAP)*, pp. 1–5, 2024.

[42] M. Nemati, J. Park, and J. Choi, "RIS-assisted coverage enhancement in millimeter-wave cellular networks," *IEEE Access*, vol. 8, pp. 188171–188185, 2020.

[43] E. Moro, I. Filippini, A. Capone, and D. De Donno, "Planning MmWave access networks with reconfigurable intelligent surfaces," in *2021 IEEE 32nd Annual International Symposium on Personal, Indoor and Mobile Radio Communications (PIMRC)*, pp. 1401–1407, IEEE, 2021.

[44] Ö. Özdogan, E. Björnson, and E. G. Larsson, "Using intelligent reflecting surfaces for rank improvement in MIMO communications," in *ICASSP 2020-2020 IEEE International Conference on Acoustics, Speech and Signal Processing (ICASSP)*, pp. 9160–9164, IEEE, 2020.

[45] V. Degli-Esposti, E. M. Vitucci, M. Di Renzo, and S. A. Tretyakov, "Reradiation and scattering from a reconfigurable intelligent surface: A general macroscopic model," *IEEE Transactions on Antennas and Propagation*, vol. 70, no. 10, pp. 8691–8706, 2022.

[46] A. Díaz-Rubio and S. A. Tretyakov, "Acoustic metasurfaces for scattering-free anomalous reflection and refraction," *Physical Review B*, vol. 96, no. 12, p. 125409, 2017.

[47] H. Zhang, H. Zhang, B. Di, K. Bian, Z. Han, and L. Song, "Metalocalization: Reconfigurable intelligent surface aided multi-user wireless indoor localization," *IEEE Transactions on Wireless Communications*, vol. 20, no. 12, pp. 7743–7757, 2021.

[48] E. Čišija, A. M. Ahmed, A. Sezgin, and H. Wymeersch, "RIS-aided mmWave MIMO radar system for adaptive multi-target localization," in *2021 IEEE Statistical Signal Processing Workshop (SSP)*, pp. 196–200, IEEE, 2021.

[49] L. Yang, J. Yang, W. Xie, M. O. Hasna, T. Tsiftsis, and M. Di Renzo, "Secrecy performance analysis of RIS-aided wireless communication systems," *IEEE Transactions on Vehicular Technology*, vol. 69, no. 10, pp. 12296–12300, 2020.

[50] M. Wijewardena, T. Samarasinghe, K. T. Hemachandra, S. Atapattu, and J. S. Evans, "Physical layer security for intelligent reflecting surface assisted two–way communications," *IEEE Communications Letters*, vol. 25, no. 7, pp. 2156–2160, 2021.

[51] M. A. ElMossallamy, H. Zhang, L. Song, K. G. Seddik, Z. Han, and G. Y. Li, "Reconfigurable intelligent surfaces for wireless communications: Principles, challenges, and opportunities," *IEEE Transactions on Cognitive Communications and Networking*, vol. 6, no. 3, pp. 990–1002, 2020.

[52] R. Liu, M. Li, H. Luo, Q. Liu, and A. L. Swindlehurst, "Integrated sensing and communication with reconfigurable intelligent surfaces: Opportunities, applications, and future directions," *IEEE Wireless Communications*, vol. 30, no. 1, pp. 50–57, 2023.

[53] R. P. Sankar, S. P. Chepuri, and Y. C. Eldar, "Beamforming in integrated sensing and communication systems with reconfigurable intelligent surfaces," *IEEE Transactions on Wireless Communications*, 2023.

[54] I. A. Buriak, V. O. Zhurba, G. S. Vorobjov, V. R. Kulizhko, O. K. Kononov, and O. Rybalko, "Metamaterials: Theory, classification and application strategies (review)," *Journal of Nano- and Electronic Physics*, vol. 8, no. 4, 2016.

[55] C. L. Holloway, E. F. Kuester, J. A. Gordon, J. O'Hara, J. Booth, and D. R. Smith, "An overview of the theory and applications of metasurfaces: The two-dimensional equivalents of metamaterials," *IEEE Antennas and Propagation Magazine*, vol. 54, pp. 10–35, April 2012.

[56] S. V. Hum and J. Perruisseau-Carrier, "Reconfigurable reflectarrays and array lenses for dynamic antenna beam control: A review," *IEEE transactions on antennas and propagation*, vol. 62, no. 1, pp. 183–198, 2013.

[57] H. Yang, X. Cao, F. Yang, J. Gao, S. Xu, M. Li, X. Chen, Y. Zhao, Y. Zheng, and S. Li, "A programmable metasurface with dynamic polarization, scattering and focusing control," *Scientific reports*, vol. 6, no. 1, pp. 1–11, 2016.

[58] I. Alamzadeh, G. C. Alexandropoulos, and M. F. Imani, "Intensity-only OMP-based Direction Estimation for Hybrid Reconfigurable Intelligent Surfaces," in *2023 IEEE International Symposium on Antennas and Propagation and USNC-URSI Radio Science Meeting (USNC-URSI)*, pp. 01–02, IEEE, 2023.

[59] D. Demmer, F. Foglia Manzillo, S. Gharbieh, M. Śmierzchalski, R. D'Errico, J.-B. Doré, and A. Clemente, "Hybrid precoding applied to multi-beam transmitting reconfigurable intelligent surfaces (T-RIS)," *Electronics*, vol. 12, no. 5, p. 1162, 2023.

[60] N. Shlezinger, G. C. Alexandropoulos, M. F. Imani, Y. C. Eldar, and D. R. Smith, "Dynamic metasurface antennas for 6G extreme massive MIMO communications," *IEEE Wireless Communications*, vol. 28, no. 2, pp. 106–113, 2021.

[61] I. Alamzadeh, G. C. Alexandropoulos, N. Shlezinger, and M. F. Imani, "A reconfigurable intelligent surface with integrated sensing capability," *Scientific reports*, vol. 11, no. 1, p. 20737, 2021.

[62] Y. Liu, X. Mu, J. Xu, R. Schober, Y. Hao, H. V. Poor, and L. Hanzo, "STAR: Simultaneous transmission and reflection for 360° coverage by

intelligent surfaces," *IEEE Wireless Communications*, vol. 28, no. 6, pp. 102–109, 2021.

[63] M. Di Renzo, A. Zappone, M. Debbah, M.-S. Alouini, C. Yuen, J. de Rosny, and S. Tretyakov, "Smart radio environments empowered by reconfigurable intelligent surfaces: How it works, state of research, and the road ahead," *IEEE Journal on Selected Areas in Communications*, vol. 38, no. 11, pp. 2450–2525, 2020.

[64] M. Haghshenas, P. Ramezani, M. Magarini, and E. Björnson, "Parametric channel estimation with short pilots in RIS-assisted near-and far-field communications," *IEEE Transactions on Wireless Communications*, 2024.

[65] W. Tang, M. Z. Chen, X. Chen, J. Y. Dai, Y. Han, M. Di Renzo, Y. Zeng, S. Jin, Q. Cheng, and T. J. Cui, "Wireless Communications with Reconfigurable Intelligent Surface: Path Loss Modeling and Experimental Measurement," *IEEE transactions on wireless communications*, vol. 20, no. 1, pp. 421–439, 2020.

[66] S. W. Ellingson, "Path loss in reconfigurable intelligent surface-enabled channels," pp. 829–835, 2021.

[67] S. V. Hum and J. Perruisseau-Carrier, "Reconfigurable reflectarrays and array lenses for dynamic antenna beam control: A review," *IEEE Transactions on Antennas and Propagation*, vol. 62, pp. 183–198, Jan 2014.

[68] D. R. Smith, O. Yurduseven, L. P. Mancera, P. Bowen, and N. B. Kundtz, "Analysis of a waveguide-fed metasurface antenna," *Phys. Rev. Applied*, vol. 8, p. 054048, Nov 2017.

[69] C. Pfeiffer and A. Grbic, "Metamaterial Huygens' surfaces: Tailoring wave fronts with reflectionless sheets," *Phys. Rev. Lett.*, vol. 110, p. 197401, May 2013.

[70] M. Selvanayagam and G. V. Eleftheriades, "Circuit modeling of Huygens surfaces," *IEEE Antennas and Wireless Propagation Letters*, vol. 12, pp. 1642–1645, 2013.

[71] S. B. Glybovski, S. A. Tretyakov, P. A. Belov, Y. S. Kivshar, and C. R. Simovski, "Metasurfaces: From microwaves to visible," *Physics Reports*, vol. 634, pp. 1 – 72, 2016.

[72] N. Mohammadi Estakhri and A. Alù, "Wave-front transformation with gradient metasurfaces," *Phys. Rev. X*, vol. 6, p. 041008, Oct 2016.

[73] V. S. Asadchy, M. Albooyeh, S. N. Tcvetkova, A. Díaz-Rubio, Y. Ra'di, and S. A. Tretyakov, "Perfect control of reflection and refraction using spatially dispersive metasurfaces," *Phys. Rev. B*, vol. 94, p. 075142, Aug 2016.

[74] C. A. Balanis, *Antenna Theory: analysis and design*. New Jersey, USA: Wiley, 2016.

[75] A. Tayebi, J. Tang, P. R. Paladhi, L. Udpa, S. S. Udpa, and E. J. Rothwell, "Dynamic beam shaping using a dual-band electronically tunable reflectarray antenna," *IEEE Transactions on Antennas and Propagation*, vol. 63, pp. 4534–4539, Oct 2015.

[76] A. Abrardo, D. Dardari, and M. Di Renzo, "Intelligent reflecting surfaces: Sum-rate optimization based on statistical position information," *IEEE Transactions on Communications*, vol. 69, pp. 7121–7136, Oct 2021.

[77] E. Basar and H. V. Poor, "Present and Future of Reconfigurable Intelligent Surface-Empowered Communications [Perspectives]," *IEEE Signal Processing Magazine*, vol. 38, pp. 146–152, Nov. 2021.

[78] Z. Zhang, L. Dai, X. Chen, C. Liu, F. Yang, R. Schober, and H. V. Poor, "Active RIS vs. passive RIS: which will prevail in 6G?," *IEEE Trans. Wireless Commun.*, vol. 71, pp. 1707–1725, Mar. 2023.

[79] R. Long, Y.-C. Liang, Y. Pei, and E. G. Larsson, "Active reconfigurable intelligent surface-aided wireless communications," *IEEE Transactions on Wireless Communications*, vol. 20, no. 8, pp. 4962–4975, 2021.

[80] R. Fara, D.-T. Phan-Huy, P. Ratajczak, A. Ourir, M. Di Renzo, and J. De Rosny, "Reconfigurable intelligent surface-assisted ambient backscatter communications: Experimental assessment," in *2021 IEEE International Conference on Communications Workshops (ICC Workshops)*, pp. 1–7, 2021.

[81] X. Jia, X. Zhou, D. Niyato, and J. Zhao, "Intelligent reflecting surface-assisted bistatic backscatter networks: Joint beamforming and reflection design," *IEEE Transactions on Green Communications and Networking*, 2021.

[82] Y.-C. Liang, R. Long, Q. Zhang, J. Chen, H. V. Cheng, and H. Guo, "Large intelligent surface/antennas (LISA): Making reflective radios smart," *Journal of Communications and Information Networks*, vol. 4, no. 2, pp. 40–50, 2019.

[83] J. Zuo, Y. Liu, L. Yang, L. Song, and Y.-C. Liang, "Reconfigurable intelligent surface enhanced noma assisted backscatter communication system," *IEEE Transactions on Vehicular Technology*, vol. 70, no. 7, pp. 7261–7266, 2021.

[84] M. Hua, Q. Wu, L. Yang, R. Schober, and H. V. Poor, "A novel wireless communication paradigm for intelligent reflecting surface based symbiotic radio systems," *IEEE Transactions on Signal Processing*, vol. 70, pp. 550–565, 2022.

[85] V. S. Asadchy, A. Díaz-Rubio, S. N. Tcvetkova, D.-H. Kwon, A. Elsakka, M. Albooyeh, and S. A. Tretyakov, "Flat engineered multichannel reflectors," *Phys. Rev. X*, vol. 7, p. 031046, Sep 2017.

[86] C. Shen, A. Díaz-Rubio, J. Li, and S. A. Cummer, "A surface impedance-based three-channel acoustic metasurface retroreflector," *Applied Physics Letters*, vol. 112, 04 2018. 183503.

[87] M. Kalaagi and D. Seetharamdoo, "Multiangle retrodirective cascaded metasurface," *Journal of Applied Physics*, vol. 126, 09 2019. 104901.

[88] M. Kalaagi and D. Seetharamdoo, "Fano resonance based multiple angle retrodirective metasuface," in *2020 14th European Conference on Antennas and Propagation (EuCAP)*, pp. 1–4, 2020.

[89] R. Miyamoto and T. Itoh, "Retrodirective arrays for wireless communications," *IEEE Microwave Magazine*, vol. 3, pp. 71–79, Mar. 2002.

[90] C. Pon, "Retrodirective array using the heterodyne technique," *IEEE Transactions on Antennas and Propagation*, vol. 12, no. 2, pp. 176–180, 1964.

[91] R. Miyamoto, Y. Qian, and T. Itoh, "A retrodirective array using balanced quasi-optical FET mixers with conversion gain," in *1999 IEEE MTT-S International Microwave Symposium Digest (Cat. No.99CH36282)*, vol. 2, pp. 655–658 vol.2, 1999.

[92] E. Sharp and M. Diab, "Van Atta reflector array," *IRE Transactions on Antennas and Propagation*, vol. 8, no. 4, pp. 436–438, 1960.

[93] C. Allen, K. Leong, and T. Itoh, "A negative reflective/refractive "meta-interface" using a bi-directional phase-conjugating array," in *IEEE MTT-S International Microwave Symposium Digest, 2003*, vol. 3, pp. 1875–1878 vol.3, 2003.

[94] A. R. Katko, S. Gu, J. P. Barrett, B.-I. Popa, G. Shvets, and S. A. Cummer, "Phase conjugation and negative refraction using nonlinear active metamaterials," *Phys. Rev. Lett.*, vol. 105, p. 123905, Sep 2010.

[95] J. G. Hester and M. M. Tentzeris, "A mm-wave ultra-long-range energy-autonomous printed RFID-enabled Van-atta wireless sensor: At the crossroads of 5G and IoT," in *2017 IEEE MTT-S International Microwave Symposium (IMS)*, pp. 1557–1560, 2017.

[96] S. Yen and D. Filipovic, "Co-polarized retrodirective array with active enhancement," in *2020 IEEE International Symposium on Antennas*

and Propagation and North American Radio Science Meeting, pp. 425–426, 2020.

[97] J.-F. Bousquet, S. Magierowski, and G. G. Messier, "A 4-GHz active scatterer in 130-nm CMOS for phase sweep amplify-and-forward," *IEEE Transactions on Circuits and Systems I: Regular Papers*, vol. 59, no. 3, pp. 529–540, 2012.

[98] M. Rossanese, P. Mursia, A. Garcia-Saavedra, V. Sciancalepore, A. Asadi, and X. Costa-Perez, "Design and validation of scalable reconfigurable intelligent surfaces," *Computer Networks*, vol. 241, p. 110208, 2024.

[99] "Agilent e5062a datasheet." https://www.testequipmenthq.com/datasheets/Agilent-E5062A-Datasheet.pdf.

[100] "Alltest narda 643 datasheet." https://docs.alltest.net/manual/Alltest-Narda-643-Datasheet.pdf, 2016.

[101] "Tdk hrn-0118 horn antenna datasheet." https://www.tdkrfsolutions.tdk.com/images/uploads/data-sheets/TDK-HRN-0118.pdf, 2016.

[102] I. F. Akyildiz, J. M. Jornet, and C. Han, "TeraNets: ultra-broadband communication networks in the terahertz band," *IEEE Wireless Commun.*, vol. 21, no. 4, pp. 130–135, 2014.

[103] G. Pasolini, A. Guerra, F. Guidi, N. Decarli, and D. Dardari, "Crowd-based cognitive perception of the physical world: Towards the Internet of Senses," *Sensors*, vol. 20, no. 9, p. 2437, 2020.

[104] D. Dardari, R. D'Errico, G. Pasolini, F. Guidi, A. Guerra, A. Clemente, and M. Lotti, "Personal radars for radio imaging and infrastructure-less localization (primeloc)," /, 2019.

[105] K. Haneda, J. Järveläinen, A. Karttunen, M. Kyrö, and J. Putkonen, "A Statistical Spatio-Temporal Radio Channel Model for Large Indoor Environments at 60 and 70 GHz," *IEEE Transactions on Antennas and Propagation*, vol. 63, no. 6, pp. 2694–2704, 2015.

[106] B. Fleury, "First- and second-order characterization of direction dispersion and space selectivity in the radio channel," *IEEE Trans. Inf. Th.*, vol. 46, no. 6, pp. 2027–2044, 2000.

[107] M. Lotti, M. Caillet, and R. D'Errico, "Comparison of Indoor Channel Characteristics for Sub-THz Bands from 125 GHz to 300 GHz," in *Proc. 16th European Conf. on Antennas and Propagation (EuCAP)*, pp. 1–5, 2022.

[108] M. Lotti, M. Caillet, and R. D'Errico, "Multiband sub-THz double angular characterization in indoor scenario," *IEEE Trans. Antennas Propag.*, vol. 71, no. 2, pp. 1747–1756, 2023.

[109] F. C. Commission *et al.*, "Revision of part 15 of the commission's rules regarding ultra-wideband transmission systems," *FIRST REPORT AND ORDER FCC 02-48*, 2002.

[110] M. Z. Win, D. Dardari, A. F. Molisch, W. Wiesbeck, and W. Jinyun Zhang, "History and applications of uwb," in *Institute of Electrical and Electronics Engineers*, 2009.

[111] D. Dardari, P. Closas, and P. M. Djurić, "Indoor tracking: Theory, methods, and technologies," *IEEE transactions on vehicular technology*, vol. 64, no. 4, pp. 1263–1278, 2015.

[112] B. D. Anderson and J. B. Moore, *Optimal filtering*. Courier Corporation, 2005.

[113] F. Gustafsson, "Particle filter theory and practice with positioning applications," *IEEE Aerospace and Electronic Systems Magazine*, vol. 25, no. 7, pp. 53–82, 2010.

[114] S. Gezici, Z. Tian, G. B. Giannakis, H. Kobayashi, A. F. Molisch, H. V. Poor, and Z. Sahinoglu, "Localization via ultra-wideband radios: a look at positioning aspects for future sensor networks," *IEEE signal processing magazine*, vol. 22, no. 4, pp. 70–84, 2005.

[115] D. B. Jourdan, D. Dardari, and M. Z. Win, "Position error bound for uwb localization in dense cluttered environments," *IEEE transactions on aerospace and electronic systems*, vol. 44, no. 2, pp. 613–628, 2008.

[116] "Decawave dwm1000 datasheet." https://www.decawave.com/sites/default/files/resources/DWM1000-Datasheet-V1.6.pdf, 2016.

[117] "Decawaveaps014: Antenna delay calibration of dw1000- based products and systems." https://www.decawave.com/wp-content/uploads/2018/08/aps014-antennadelaycalibrationofdw1000-basedproductsandsystems_v1.01.pdf, 2018.

[118] D. Dardari and D. Massari, "Using metaprisms for performance improvement in wireless communications," *IEEE Transactions on Wireless Communications*, vol. 20, no. 5, pp. 3295–3307, 2021.

[119] D. Dardari, N. Decarli, A. Guerra, and F. Guidi, "LOS/NLOS near-field localization with a large reconfigurable intelligent surface," *IEEE Trans. on Wireless Commun.*, 2021.

[120] M. C. Budge and S. R. German, *Basic RADAR analysis*. Artech House, 2020.

[121] H. Taub and D. L. Schilling, *Principles of communication systems*. McGraw-Hill Higher Education, 1986.

[122] H. L. Van Trees, *Detection, estimation, and modulation theory, part I*. John Wiley & Sons, 2004.

[123] O. L. López, N. H. Mahmood, H. Alves, C. M. Lima, and M. Latva-aho, "Ultra-low latency, low energy, and massiveness in the 6G era via efficient CSIT-limited scheme," *IEEE Communications Magazine*, vol. 58, no. 11, pp. 56–61, 2020.

[124] H. Viswanathan and P. E. Mogensen, "Communications in the 6G era," *IEEE access*, vol. 8, pp. 57063–57074, 2020.

[125] M. Noor-A-Rahim, Z. Liu, H. Lee, M. O. Khyam, J. He, D. Pesch, K. Moessner, W. Saad, and H. V. Poor, "6G for vehicle-to-everything (V2X) communications: Enabling technologies, challenges, and opportunities," *Proceedings of the IEEE*, vol. 110, no. 6, pp. 712–734, 2022.

[126] Z. Gong, F. Jiang, and C. Li, "Angle domain channel tracking with large antenna array for high mobility V2I millimeter wave communications," *IEEE Journal of Selected Topics in Signal Processing*, vol. 13, no. 5, pp. 1077–1089, 2019.

[127] A. H. Gazestani, S. A. Ghorashi, B. Mousavinasab, and M. Shikh-Bahaei, "A survey on implementation and applications of full duplex wireless communications," *Physical Communication*, vol. 34, pp. 121–134, 2019.

[128] J. R. Guerci, J. S. Bergin, R. J. Guerci, M. Khanin, and M. Rangaswamy, "A new MIMO clutter model for cognitive radar," in *2016 IEEE Radar Conference (RadarConf)*, pp. 1–6, 2016.

[129] G. H. Golub and H. A. van der Vorst, "Eigenvalue computation in the 20th century," *Journal of Computational and Applied Mathematics*, vol. 123, no. 1, pp. 35–65, 2000. Numerical Analysis 2000. Vol. III: Linear Algebra.

[130] D. Tse and P. Viswanath, *Fundamentals of Wireless Communication*. New York, NY: Cambridge University Press, 2005.

[131] D. Dardari, R. D'Errico, C. Roblin, A. Sibille, and M. Z. Win, "Ultrawide bandwidth RFID: The next generation?," *Proc. IEEE*, vol. 98, pp. 1570 –1582, Sep 2010. Special Issue on RFID - A Unique Radio Innovation for the 21st Century.

[132] E. G. Larsson and P. Stoica, *Space-Time Block Coding for Wireless Communications*. New York, USA: Cambdrige Univ. Press, 2003.

[133] R. Vershynin, "Introduction to the non-asymptotic analysis of random matrices," in *Compressed Sensing*, 2010.

[134] 3GPP, "Study on channel model for frequencies from 0.5 to 100 GHz (3GPP TR 38.901," tech. rep., 3GPP, 2019.

[135] W. Hao, G. Sun, M. Zeng, Z. Chu, Z. Zhu, O. A. Dobre, and P. Xiao, "Robust design for intelligent reflecting surface-assisted MIMO-OFDMA terahertz IoT networks," *IEEE Internet of Things Journal*, vol. 8, no. 16, pp. 13052–13064, 2021.

[136] Z. Liu, J. Liu, Y. Zeng, and J. Ma, "Covert wireless communication in IoT network: From AWGN channel to THz band," *IEEE Internet of Things Journal*, vol. 7, no. 4, pp. 3378–3388, 2020.

[137] S. Cavallero, N. Decarli, G. Cuozzo, C. Buratti, D. Dardari, and R. Verdone, "Terahertz networks for future industrial internet of things," *ITU Journal on Future and Evolving Technologies*, vol. 4, pp. 196–208, Mar. 2023.

[138] "TIMES EU Project." http://www.times6g.eu/.

[139] "6G-SHINE EU Project." https://6gshine.eu/.

[140] L. Valentini, M. Chiani, and E. Paolini, "Interference cancellation algorithms for grant-free multiple access with massive MIMO," *IEEE Trans. Wireless Commun.*, vol. 71, no. 8, pp. 4665–4677, 2023.

[141] J. Ding, D. Qu, H. Jiang, and T. Jiang, "Success probability of grant-free random access with massive MIMO," *IEEE Internet of Things Journal*, vol. 6, no. 1, pp. 506–516, 2018.

[142] J. Choi, "An approach to preamble collision reduction in grant-free random access with massive MIMO," *IEEE Trans. Wireless Commun.*, vol. 20, no. 3, pp. 1557–1566, 2020.

[143] A. Fengler, S. Haghighatshoar, P. Jung, and G. Caire, "Grant-free massive random access with a massive MIMO receiver," in *2019 53rd Asilomar Conference on Signals, Systems, and Computers*, pp. 23–30, IEEE, 2019.

[144] L. Liu, E. G. Larsson, W. Yu, P. Popovski, C. Stefanovic, and E. de Carvalho, "Sparse signal processing for grant-free massive connectivity: A future paradigm for random access protocols in the internet of things," *IEEE Signal Process. Mag.*, vol. 35, pp. 88–99, Sep. 2018.

[145] L. Liu and W. Yu, "Massive connectivity with massive MIMO - Part I: Device activity detection and channel estimation," *IEEE Trans. Signal Process.*, vol. 66, pp. 2933–2946, June 2018.

[146] A.-S. Bana, G. Xu, E. D. Carvalho, and P. Popovski, "Ultra reliable low latency communications in massive multi-antenna systems," in *2018 52nd Asilomar Conference on Signals, Systems, and Computers*, pp. 188–192, Oct 2018.

[147] N. Decarli and D. Dardari, "Communication modes with large intelligent surfaces in the near field," *IEEE Access*, vol. 9, pp. 165648–165666, 2021.

[148] M. Säily, O. N. C. Yilmaz, D. S. Michalopoulos, E. Pérez, R. Keating, and J. Schaepperle, "Positioning technology trends and solutions toward 6G," in *2021 IEEE 32nd Annual International Symposium on Personal, Indoor and Mobile Radio Communications (PIMRC)*, pp. 1–7, 2021.

[149] S.-W. Ko, H. Chae, K. Han, S. Lee, D.-W. Seo, and K. Huang, "V2X-based vehicular positioning: opportunities, challenges, and future directions," *IEEE Wireless Commun.*, vol. 28, pp. 144–151, Apr. 2021.

[150] N. Decarli, A. Guerra, C. Giovannetti, F. Guidi, and B. M. Masini, "V2X sidelink localization of connected automated vehicles," *IEEE J. Sel. Areas Commun.*, pp. 1–15, Oct. 2023.

[151] A. Motroni, A. Buffi, and P. Nepa, "A survey on indoor vehicle localization through RFID technology," *IEEE Access*, vol. 9, pp. 17921–17942, Jan. 2021.

[152] N. Decarli, F. Guidi, and D. Dardari, "Passive UWB RFID for tag localization: architectures and design," *IEEE Sensors J.*, vol. 16, pp. 1385–1397, March 2016.

[153] S. Zhang, W. Wang, S. Tang, S. Jin, and T. Jiang, "Robot-assisted backscatter localization for IoT applications," *IEEE Trans. Wireless Commun.*, vol. 19, pp. 5807–5818, Sep. 2020.

[154] N. Decarli, M. Del Prete, D. Masotti, D. Dardari, and A. Costanzo, "High-accuracy localization of passive tags with multisine excitations," *IEEE Trans. Microw. Theory Techn.*, vol. 66, pp. 5894–5908, Dec. 2018.

[155] R. Miesen, R. Ebelt, F. Kirsch, T. Schafer, G. Li, H. Wang, and M. Vossiek, "Where is the Tag?," *IEEE Microwave Mag.*, vol. 12, pp. 49–63, Dec. 2011.

[156] M. El-Absi, A. A. Abbas, A. Abuelhaija, F. Zheng, K. Solbach, and T. Kaiser, "High-accuracy indoor localization based on chipless RFID systems at THz band," *IEEE Access*, vol. 6, pp. 54355–54368, Sep. 2018.

[157] D. Dardari, P. Closas, and P. M. Djuric, "Indoor tracking: theory, methods, and technologies," *IEEE Trans. Veh. Technol.*, vol. 64, pp. 1263–1278, Apr. 2015.

[158] C. B. Barneto, S. D. Liyanaarachchi, M. Heino, T. Riihonen, and M. Valkama, "Full duplex radio/radar technology: the enabler for advanced Joint Communication and Sensing," *IEEE Wireless Commun.*, vol. 28, pp. 82–88, Feb. 2021.

[159] N. Decarli, F. Guidi, and D. Dardari, "A novel joint RFID and radar sensor network for passive localization: design and performance bounds," *IEEE J. Sel. Topics Signal Processing*, vol. 8, pp. 80–95, Feb. 2014.

[160] E. Björnson, J. Hoydis, and L. Sanguinetti, *Massive MIMO Networks: Spectral, Energy, and Hardware Efficiency.* Vol. 11, No. 3-4, pp. 154–655: IEEE Foundations and Trends in Signal Processing, 2017.

[161] H. Q. Ngo, E. G. Larsson, and T. L. Marzetta, "Aspects of favorable propagation in Massive MIMO," in *2014 22nd European Signal Processing Conference (EUSIPCO)*, pp. 76–80, 2014.

[162] A. Pages-Zamora, J. Vidal, and D. Brooks, "Closed-form solution for positioning based on angle of arrival measurements," in *The 13th IEEE International Symposium on Personal, Indoor and Mobile Radio Communications*, vol. 4, pp. 1522–1526 vol.4, 2002.

[163] M. C. Budge and S. R. German, *Basic Radar Analysis*. Second Edition, Artech House, 2020.

[164] F. Guidi, A. Guerra, D. Dardari, A. Clemente, and R. D'Errico, "Joint energy detection and massive array design for localization and mapping," *IEEE Trans. Wireless Commun.*, vol. 16, no. 3, pp. 1359–1371, 2016.

[165] Y. Bar-Shalom, X. R. Li, and T. Kirubarajan, *Estimation with applications to tracking and navigation: Theory algorithms and software*. John Wiley & Sons, 2004.

[166] D. Dardari, P. Closas, and P. M. Djurić, "Indoor tracking: Theory, methods, and technologies," *IEEE Trans. Veh. Tech.*, vol. 64, no. 4, pp. 1263–1278, 2015.

[167] S. Thrun, "Learning metric-topological maps for indoor mobile robot navigation," *Artificial Intelligence*, vol. 99, no. 1, pp. 21–71, 1998.

[168] A. Guerra, F. Guidi, J. Dall'Ara, and D. Dardari, "Occupancy grid mapping for personal radar applications," in *Proc. IEEE Stat. Signal Process. Workshop (SSP)*, pp. 766–770, 2018.

[169] W. Hess, D. Kohler, H. Rapp, and D. Andor, "Real-time loop closure in 2D LIDAR SLAM," in *2016 IEEE International Conference on Robotics and Automation (ICRA)*, pp. 1271–1278, 2016.

[170] J. Clausen, "Branch and Bound Algorithms-Principles and Examples," *Department of Computer Science, University of Copenhagen*, pp. 1–30, 1999.

[171] Qin-Sheng Chen, M. Defrise, and F. Deconinck, "Symmetric phase-only matched filtering of Fourier-Mellin transforms for image registration and recognition," *IEEE Trans. Pattern Analysis Machine Intelligence*, vol. 16, no. 12, pp. 1156–1168, 1994.

[172] B. S. Reddy and B. N. Chatterji, "An FFT-based technique for translation, rotation, and scale-invariant image registration," *IEEE Trans. Image Process.*, vol. 5, no. 8, pp. 1266–1271, 1996.

[173] M. B. Shahab, R. Abbas, M. Shirvanimoghaddam, and S. J. Johnson, "Grant-free non-orthogonal multiple access for IoT: A survey," *IEEE Communications Surveys & Tutorials*, vol. 22, no. 3, pp. 1805–1838, 2020.

[174] J. Choi, "NOMA-based random access with multichannel ALOHA," *IEEE J. Sel. Areas Commun.*, vol. 35, no. 12, pp. 2736–2743, 2017.

[175] Y.-C. Liang, Q. Zhang, J. Wang, R. Long, H. Zhou, and G. Yang, "Backscatter communication assisted by reconfigurable intelligent surfaces," *Proceedings of the IEEE*, vol. 110, no. 9, pp. 1339–1357, 2022.

[176] T. L. Jensen and E. De Carvalho, "An optimal channel estimation scheme for intelligent reflecting surfaces based on a minimum variance unbiased estimator," in *IEEE Int. Conf. Acoustics, Speech and Signal Processing*, pp. 5000–5004, 2020.

Acknowledgements

Il mio più sentito ringraziamento va al mio mentore, il Prof. Davide Dardari. Grazie, perché hai sempre avuto un'idea brillante o un consiglio tecnico perfetto al momento giusto, senza mai farmi sentire in difetto o abbandonata nella mia ricerca.

Vorrei poi ringraziare tutto il team dell'Università di Bologna e del CNR, con i quali ho lavorato in questi tre anni: Gianni, Anna, Francesco, Nicolò, Giulia, Caterina e tutti gli altri. La vostra collaborazione è stata preziosa e stimolante.

Ovviamente, non posso dimenticare i miei amici di sempre, quelli che nei momenti di sconforto hanno saputo rallegrarmi e che mi hanno accompagnato in questi tre anni importanti non solo dal punto di vista professionale, ma anche personale. Grazie, Amici.

Grazie ai miei nonni Iride ed Ivano, mio fratello Gian Luca e mio papà Flavio. Siete i miei cardini e pilastri. Vi ringrazio di esserci sempre e del farmi percepire il vostro orgoglio. Io ugualmente sono fiera di voi, che non vi siete mai arresi davanti agli imprevisti dell'alluvione e della vita, posso solo che imparare da voi.

Un sincero ringraziamento va anche ai miei suoceri. Anna Maria, che hai sempre tenuto Isacco durante le mie trasferte, e Orfeo, che hai costruito con grande precisione e maestria tutto ciò che ti chiedessi per le mie necessità di laboratorio.

Sappiate che tutti voi avete inciso profondamente ogni giornata di questo percorso, e vi ringrazio di non avermi mai lasciata sola.

Ringrazio infine i tre amori della mia vita. Isacco e Margherita, grazie per avermi resa mamma durante questo dottorato. Darvi la vita è stato come rinascere di nuovo; per voi provo un amore sconfinato, impossibile da descri-

vere. Vorrei che un giorno leggiate questo elaborato e sapeste che la mamma vi ha pensato e amato ogni giorno di queste campagne di misure, algoritmi, articoli. Non nego che sia stato difficile conciliare la vita professionale con quella personale, ma un vostro sorriso o un calcetto nella pancia mi hanno fatto sempre ricordare il motivo per il quale aveva senso raggiungere questo obiettivo.

Marco, sei l'uomo più speciale che io abbia mai conosciuto, ed io sono così fortunata ad averti al mio fianco. Non mi hai mai detto di no a nessuno dei miei progetti, non mi hai mai fatto mancare nulla come donna, mamma, ingegnere e moglie. In ogni singolo giorno di questa tesi mi hai sempre appoggiata, aiutata, ascoltata e, a volte, consolata. Grazie, davvero. Questo dottorato dovrebbe portare anche il tuo nome.

Marco, Isacco e Margherita, questa tesi è grazie a voi e per voi.